
A sharp view on the low-frequency radio sky

A sharp view on the low-frequency radio sky

Proefschrift

ter verkrijging van
de graad van Doctor aan de Universiteit Leiden,
op gezag van Rector Magnificus prof. mr. P. F. van der Heijden,
volgens besluit van het College voor Promoties
te verdedigen op woensdag 26 augustus 2009
klokke 13.45 uur

door

Hubertus Theodorus Intema

geboren te Leiden
in 1971

Promotiecommissie

Promotores: Prof. dr. H. J. A. Röttgering
Prof. dr. G. K. Miley

Overige leden: Prof. dr. A. G. de Bruyn (Rijksuniversiteit Groningen;
Stichting ASTRON, Dwingeloo)
Dr. W. D. Cotton (NRAO, Charlottesville VA, USA)
Prof. dr. M. A. Garrett (Universiteit Leiden;
Stichting ASTRON, Dwingeloo)
Prof. dr. K. H. Kuijken
Prof. dr. A.-J. van der Veen (Technische Universiteit Delft)

Voor mijn lieve vrouw

The front cover shows a composition of a VLA radio telescope (bottom), a part of the low-frequency radio sky at 153 MHz (top), and a representation of a phase screen model that was used to suppress the phase effects of the ionosphere on low-frequency radio observations (middle).

The back cover also shows a part of the 153 MHz radio sky.

Cover design by Cecile Intema.

Contents

1	Introduction	1
1.1	Large-scale structure formation	1
1.2	Cosmic radio sources	2
1.3	Low-frequency radio interferometry	3
1.4	This thesis	4
1.5	Future prospects	6
2	Ionospheric calibration of low-frequency radio interferometric observations using the peeling scheme I. Method description and first results	7
2.1	Introduction	8
2.2	Ionosphere and calibration	8
2.2.1	The ionosphere	8
2.2.2	Image plane effects	10
2.2.3	Ionospheric phase calibration	11
2.2.4	Proposed and existing ionospheric calibration schemes	13
2.3	Method	15
2.3.1	Instrumental phase calibration	17
2.3.2	Initial phase calibration and initial sky model	19
2.3.3	Peeling	20
2.3.4	Ionospheric phase screen model	22
2.3.5	Imaging	27
2.4	Applications	28
2.4.1	Data selection, preparation and processing	28
2.4.2	Phase calibration accuracy	31
2.4.3	Background noise	33
2.4.4	Source properties	34
2.5	Discussion and conclusions	44
2.6	Future work	46

2.7	Appendix: Derivation and interpolation of the KL base vectors	47
3	Ionospheric calibration of low-frequency radio interferometric observations using the peeling scheme II. Method extensions & application to a larger array	49
3.1	Introduction	50
3.2	Limitations of the single-layer ionosphere model	51
3.2.1	Ionospheric phase rotation	51
3.2.2	Single-layer ionosphere models	52
3.2.3	Phase errors induced by a single-layer ionosphere model	53
3.3	The multi-layer ionosphere model	57
3.3.1	Towards a multi-layer model	57
3.3.2	Ionospheric multi-layer phase screen model	59
3.3.3	Reconstruction of individual ionospheric model layers	61
3.4	Instrumental phase drift estimation	62
3.5	Applications	64
3.5.1	Data selection	64
3.5.2	Data reduction	65
3.5.3	Output image comparison	69
3.6	Discussion and conclusions	75
4	Deep low-frequency radio observations of the NOAO Boötes field	77
I.	Data reduction and catalog construction	77
4.1	Introduction	78
4.2	Observations and data reduction	79
4.2.1	Observations	79
4.2.2	Data reduction	80
4.3	Catalog construction	83
4.3.1	Source extraction	85
4.3.2	Completeness and contamination	85
4.3.3	Astrometric accuracy	87
4.3.4	Flux scale	88
4.4	Analysis	92
4.4.1	Differential source counts	92
4.4.2	Spectral indices	94
4.4.3	Identification fraction of radio sources versus spectral index	97
4.5	Conclusions and future plans	98
4.6	Appendix: A selection of 153 MHz radio source images	101
5	Low-frequency radio images of the galaxy cluster Abell 2256	103
5.1	Introduction	104
5.2	Observations and data reduction	105
5.2.1	Observations	105
5.2.2	Data reduction	107
5.2.3	Total intensity maps	112
5.2.4	Spectral index maps	115
5.3	Results	117

5.3.1	Large-scale flux distribution	117
5.3.2	Peripheral relic	117
5.3.3	Central halo	118
5.3.4	Sources A & B	118
5.3.5	Source F	121
5.4	Discussion	124
5.4.1	A radio phoenix in the cluster periphery	124
5.4.2	A radio phoenix at the cluster center?	126
5.4.3	Bent head-tail galaxies at the cluster center	127
5.5	Summary	128
6	Large-scale structure of Lyman break galaxies around a radio galaxy protocluster at $z \sim 4$	131
6.1	Introduction	132
6.2	Data reduction and sample selection	132
6.3	Analysis	133
6.3.1	Projected density distribution of bright LBGs	133
6.3.2	LBG overdensity in redshift space	133
6.3.3	Projected density distribution of all LBGs	135
6.3.4	LBG angular and spatial correlation	137
6.3.5	LBG void probability function	138
6.3.6	Protocluster volume density	138
6.4	Conclusions	139
	Bibliography	141
	Nederlandse samenvatting	151
	Curriculum vitae	159
	Nawoord / Acknowledgements	161

Introduction

1.1 Large-scale structure formation

The Universe has an estimated age of 13.7 billion years (Komatsu et al. 2009). Dedicated galaxy redshift surveys like the 2dFGRS and the SDSS (Colless et al. 2001; Abazajian et al. 2009) show that the millions of visible galaxies in the present Universe have organized themselves in a non-homogeneous, large-scale structure that is generally referred to as the cosmic web. From observations of the cosmic microwave background (CMB), it is derived that the matter distribution in the early universe (0.3 million years after the Big Bang) was very homogeneous, except for tiny fluctuations (e.g., Hinshaw et al. 2009). The deepest astronomical observations with large telescopes discovered distant galaxies and quasars (e.g., Fan et al. 2003; Iye et al. 2006) that were already in place when the Universe was less than one billion years old. Cosmologists try to understand how the initial, nearly homogeneous distribution of matter evolved into the current, clumpy structure that we observe in the present Universe. It is therefore important to gather observational evidence of the evolution of galaxies and the cosmic web in both the distant, young Universe and the local, present Universe.

The largest inhomogeneous structures observed in the local Universe are clusters that can consist of hundreds of galaxies. Typical sizes for rich clusters of galaxies in the present Universe are 5–30 Mpc (e.g., Bahcall 1988). Clusters appear to be connected by filaments, elongated galaxy distributions between clusters with lengths of 50 Mpc or more and widths of ~ 10 Mpc. The clusters and filaments are surrounded by empty voids.

The common paradigm of structure formation is that the primordial (CMB) density fluctuations (mostly dark matter) within a certain mass range became gravitationally unstable and collapsed into dense structures surrounded by voids of empty space (e.g., Peacock 2001). In the cold dark matter (Λ CDM) model of structure formation, density fluctuations have progressively larger amplitudes on smaller length scales. Therefore structure formation is expected to proceed in a ‘bottom-up’ manner, with stars forming earlier than galaxies, and galaxies forming earlier

than galaxy clusters (e.g., Yoshida 2009). Clusters occupy a special position in this hierarchy, since they are the largest objects that have had time to undergo gravitational collapse.

The Λ CDM model predicts biased formation of smaller-scale structure in larger-scale regions of enhanced mass density. It also predicts gradual growth of structure through mergers. These predictions seem to fit well to the observed clustering and merging activity of galaxies (e.g., Peebles 1980; Hwang & Chang 2009). Cosmological N-body simulations (e.g., Springel et al. 2005) show that also clusters undergo mergers. Observational evidence is accumulating that this is indeed the case (e.g., Kempner & Sarazin 2001, and references therein). The interplay between theory and observation should eventually lead to a complete picture of how galaxies and clusters came to take their present forms.

1.2 Cosmic radio sources

Existing optical and infrared telescopes are already probing the first billion years of the Universe. Planned observational programs are aimed at directly detecting light from objects even farther away. However, tracing the cosmic history from this epoch to the current is biased by selection effects due to extinction near the source (e.g., dust obscured star formation) or by cosmic extinction. Radio waves are generally not sensitive to extinction by gas or dust, and therefore provide an unbiased view on the early Universe. A typical sample of bright radio sources contains galaxies out to the largest distances, whereas a bright optical sample contains mostly nearby objects. Relatively few objects are bright enough radio emitters to be detectable across cosmic distances, but these objects do appear to have a direct relation to large-scale structure formation.

Radio galaxies are a subclass of active galactic nuclei (AGN), which are galaxy cores in which the central massive black hole ($10^{6-9} M_{\odot}$) accretes matter. AGN are hosted by very massive ellipticals ($10^{12-13} M_{\odot}$). AGN in the local Universe are rare, but much less so in the early Universe. Considering the short lifetime of radio sources (10–100 Myr), it is not unlikely that every massive galaxy may have gone through one or more radio-loud periods. The clumpy optical morphology of radio galaxies in the distant Universe (Pentericci et al. 1999) indicates that radio activity is triggered by matter accretion through mergers. Radio galaxies are found to be among the most massive galaxies in the distant Universe (e.g., Miley & De Breuck 2008), living in overdense regions of galaxies (Venemans et al. 2002; Miley et al. 2004). Therefore, distant radio galaxies are considered to be the signposts of cluster formation in the early Universe. The activity of radio-loud AGN is found to have a pronounced effect on the state of the intra-cluster medium (ICM) (e.g., Fabian et al. 2003). This feedback may play an important role in reducing the rate at which galaxies are formed (e.g., Croton et al. 2006).

There is a small fraction of clusters in the local Universe that emit detectable radio waves on megaparsec (Mpc) scales. These clusters have relatively large X-ray luminosities, high ICM temperatures and large galaxy velocity dispersions (e.g., Hanisch 1982). Cluster mergers are highly energetic events ($\sim 10^{64}$ ergs) that offer an explanation for the non-relaxed cluster state (e.g., Ferrari et al. 2008). The diffuse radio emission originating from these radio clusters does not appear to be associated with AGN, but with the gas in the ICM. Halos are central, unpolarized radio sources for which the regular morphology roughly coincides with the X-ray morphology. Relics are more elongated, highly polarized radio sources at the outskirts of clusters (e.g., Röttgering et al. 1997; Brentjens & de Bruyn 2004), which are thought to be tracers of the shock waves generated by cluster mergers (Enßlin et al. 1998; Miniati et al. 2000). Clusters with

diffuse radio emission also have relatively many head-tail galaxies (e.g., Röttgering et al. 1994a; Klammer et al. 2004), which may indicate a relation between cluster mergers and the appearance of radio-loud AGN.

The radio emission from AGN and clusters is synchrotron radiation, which is recognised by the typical power-law spectral shape $S_\nu \propto \nu^{-\alpha}$ over decades in frequency (e.g., Klammer et al. 2006). Synchrotron radiation requires relativistic electrons to spiral around magnetic field lines. For both halos and relics, the exact mechanism that produces the synchrotron emission is not fully understood. For AGN, the relativistic electrons and magnetic field are likely to originate from the accretion disk near the central, supermassive black hole (Rees 1978; Blandford & Payne 1982). For clusters, the origin of both the magnetic field and relativistic electrons is uncertain. The magnetic field may be an amplification of a primordial magnetic field (e.g., Carilli & Taylor 2002). The large size of both the halo and relic require that the relativistic electrons are generated in-situ, possibly by merger-induced shocks or turbulence in the ICM (e.g., Feretti & Johnston-Hollitt 2004; Ferrari et al. 2008). Generally, synchrotron radio emission provides a unique diagnostic for studying the magnetic field, plasma distribution, and gas motion within clusters of galaxies.

For bright samples of radio sources, the median spectral index is found to be $\alpha \approx -0.8$ (e.g., De Breuck et al. 2000), which indicates that most of these radio sources become increasingly brighter towards lower frequencies. This is typically limited at lower frequencies by a spectral turnover due to synchrotron self-absorption or free-free absorption (Rybicki & Lightman 1979). Nonetheless, radio observations can benefit from the increased brightness towards low-frequencies, especially for steep-spectrum sources ($\alpha \lesssim -1$) like distant radio galaxies and diffuse cluster sources. Other sources with steep spectra are fossil radio lobes of previously radio-loud AGN, where the energy loss of radiating electrons steepens the synchrotron spectrum, which can provide a record of the cluster history (e.g., Miley 1980). Tielens et al. (1979), Blumenthal & Miley (1979) and others found that, in flux-limited surveys, radio sources with the steepest spectra (e.g., the lowest α) are systematically more distant. Selection of radio sources by their ultra-steep spectra (USS; $\alpha < -1.3$) has led to the discovery of the most distant radio galaxies to date (see Miley & De Breuck 2008).

1.3 Low-frequency radio interferometry

The study of large-scale structure formation clearly benefits from radio observations at low frequencies. An additional benefit is the relatively large field-of-view, which can be several degrees in diameter. From here on, ‘low-frequency’ (LF for short) refers to radio frequencies around 300 MHz and below. The lower limit in radio observing is set by the opacity of the Earth’s atmosphere for radio waves with a frequency below 10–30 MHz (depending on the ionospheric conditions). The fundamental relationship between angular resolution and the wavelength to telescope size ratio requires LF observations to be performed with an interferometer rather than a single dish to obtain an angular resolution that can be expressed in arcseconds rather than arcminutes. The two largest operational LF interferometer arrays are the Very Large Array (VLA) at 74 MHz (Kassim et al. 2007) and the Giant Metrewave Radio Telescope (GMRT) at 153 and 235 MHz (Swarup 1991). Both arrays have maximum baselines (antenna-antenna separations) of around 30 km.

To date, the LF capabilities of these and other radio interferometers remain poorly utilized,

which is reflected in the relatively few scientific publications using LF observations from the VLA and the GMRT. The main reason is that, towards low frequencies, the image background RMS typically rises even faster than the flux density of an USS source. This results in a relative loss of dynamic range. The increase in background RMS is typically the result of several effects (e.g., Thompson et al. 2001): (i) a high sky temperature from the Milky Way foreground, (ii) reduced telescope efficiency, (iii) wide-field imaging issues (like the w -term, bandwidth & time averaging smearing), (iv) poorly constrained and variable antenna beam patterns on the sky (including pointing errors, beam squint), (v) radio frequency interference, and (vi) ionospheric propagation effects. Several of these effects can be removed or suppressed during data reduction if suitable algorithms are available.

Given the current state of data reduction software, the effects of the ionosphere are considered to be one of the main limiting factors for high-resolution LF radio observations (e.g., Kassim et al. 1993). The dominant error on intensity measurements is due to a phase rotation that varies with antenna position and viewing direction and scales with wavelength. Lonsdale (2005) explains how the increase of the field-of-view and the increase of the array size complicates ionospheric phase calibration. Self-calibration (e.g., Pearson & Readhead 1984), which can determine one correction per antenna, breaks down in the presence of direction-dependent errors. Field-based calibration (Cotton et al. 2004) is the single existing implementation of a direction-dependent correction scheme for ionospheric phase rotations, but it is limited in applicability to compact ($\lesssim 10$ km) arrays.

1.4 This thesis

In this thesis, three studies are performed on large-scale structure formation (Chapters 4 to 6). The main tool for two of these studies is high-resolution, low-frequency radio interferometric observations. Therefore, the first part of the thesis is dedicated to improving the image quality of these observations (Chapters 2 and 3).

In **Chapter 2**, a new calibration method is presented to suppress the effects of ionospheric phase rotations on low-frequency interferometric observations. The new calibration method, named SPAM, has two important advantages over field-based calibration (Cotton et al. 2004), namely: (i) the base functions of the ionosphere model are not polynomials, but optimized base-functions derived using the Karhunen-Loève transform, and (ii) the ionospheric corrections are not limited to gradients over the array, but can contain higher-order terms as well. These items are expected to improve the calibration accuracy, in particular for larger arrays (a few tens of kilometers). Tests on simulated and real observations with the VLA at 74 MHz (up to 23 km baselines) show a significant improvement of the output image quality as compared to existing calibration methods, which reflects the relative improvement in ionospheric calibration accuracy.

In **Chapter 3**, extensions to the SPAM algorithm are presented to make the method more robust. The extensions consist of: (i) a model in which the 3-dimensional ionosphere is represented by multiple discrete layers instead of one discrete layer, and (ii) a filter to solve for slow instrumental phase drifts that were previously assumed to be constant. As the first extension is expected to yield improved results for larger arrays, the performance of the new SPAM functionality is applied to extended VLA 74 MHz observations in its largest configuration (35 km baselines). Image analysis shows a nearly equal performance of the single- and multi-layer models, except for a slight improvement in the overall astrometric accuracy of the multi-layer

model images. Detection and removal of instrumental phase drifts significantly improved the fitting accuracy of both single- and multi-layer ionospheric phase models to the observational data.

In **Chapter 4**, the SPAM algorithm is applied to a deep, high-resolution GMRT 153 MHz survey of the NOAO Boötes field (Jannuzi & Dey 1999). This 9 square degree northern field has been previously targeted by surveys spanning the entire electromagnetic spectrum, including deep Westerbork Synthesis Radio Telescope (WSRT) observations at 1.4 GHz (de Vries et al. 2002) and near-infrared K_s -band observations (Elston et al. 2006). Source extraction on the 153 MHz image yields a catalog of ~ 600 sources down to ~ 4 mJy, with very low contamination and high positional accuracy. This catalog includes 4 sources that were previously identified as possible distant radio galaxies (Croft et al. 2008). Source counts are accurately determined down to a flux level of 20 mJy (for the first time at this frequency), which are found to match well with source counts at 325 MHz. Combination with the 1.4 GHz catalog by de Vries et al. (2002) yields ~ 400 accurate spectral index measurements. The detection fraction of radio sources in the K_s -band image drops with spectral index, indirectly reproducing the known correlation between distance and spectral index. The 153 MHz catalog contains 16 compact USS sources that are candidate distant radio galaxies. Follow-up observations are needed to determine the true nature of these sources.

In **Chapter 5**, a low-frequency radio study is presented on the local rich cluster Abell 2256. This cluster is known to possess a central radio halo, a peripheral radio relic and an unusual large number of tailed radio sources (e.g., Bridle et al. 1979; Röttgering et al. 1994a; Miller et al. 2003; Clarke & Enßlin 2006; Brentjens 2008). The study comprises low-resolution, wide-band WSRT observations between 115 and 165 MHz, and high-resolution GMRT observations at 153 and 325 MHz. SPAM calibration is applied to the GMRT 153 MHz data. A full bandwidth WSRT intensity map reproduces the halo and relic detections, while a spectral index map across the WSRT band reproduces the spectral steepening across the relic and the extreme ($\alpha \approx -2$) steep spectrum over large parts of the halo (Clarke & Enßlin 2006). The spectral steepening across the relic supports the hypothesis that a large merger shock is responsible for its appearance. The complementary GMRT images are used for a detailed study of two emission regions that have been noted for their entangled and complex morphologies. Near the cluster center we find two new radio sources that have no clear origin. One region is elongated and may be a low-frequency extension of a head-tail galaxy. The other may be old AGN plasma. Overall, the presence of several head-tail galaxies and several bright emission regions with no clear origin support a recent cluster merger scenario, in which disturbances in the ICM strongly influence the appearance of (previously) radio-loud AGN.

In **Chapter 6**, the Lyman break technique (e.g., Steidel et al. 1998) is used to search for distant galaxies in the vicinity of a distant radio galaxy TN J1338-1942 (De Breuck et al. 2001). This USS radio galaxy is known to inhabit a volume overdensity of Lyman- α emitting (LAE) galaxies (Venemans et al. 2002; Venemans 2005) that is likely to be a protocluster (a forming cluster). Deep, wide-field optical and near-infrared images in B -, R_c - and i' -bands from the Subaru-telescope facilitate a search for Lyman break galaxies (LBGs) out to the boundary of the protocluster structure and beyond. Using color selection criteria by Ouchi et al. (2004a) yields ~ 900 candidate LBGs within the $0.5^\circ \times 0.5^\circ$ field, including TN J1338-1942. Although the probed volume is much deeper than the depth of the protocluster, the projected distribution of LBGs shows a prominent overdensity near the radio galaxy, similar to the overdensity found earlier using LAEs. The angular clustering signal of the overall LBG distribution is found to

be significant, which is complemented by a significant excess of empty areas (possibly voids). When the number of observed concentrations in the projected LBG distribution is translated into a volume density, this number is similar to the volume density of rich clusters in the local Universe. The observed angular distribution can be explained as the projection of the large-scale structure in the distant Universe.

1.5 Future prospects

The future of high-resolution, low-frequency radio astronomy looks bright. There are two new major LF radio telescopes in different stages of development. Most progressed is the construction of the Dutch Low Frequency Array (LOFAR; e.g., Röttgering et al. 2006), covering frequency ranges from 10 to 90 MHz and 110 to 250 MHz. This telescope will consist of 36 stations (fields of static antennas, electronically equivalent to dishes) in the Netherlands alone, with baselines up to 50 km. For E-LOFAR, several additional stations are planned for construction in various other European countries, stretching the longest baseline to above 1000 km. In full operation, the imaging resolution and sensitivity are expected to be at least 1–2 orders of magnitude better than VLA and GMRT. Construction of the Dutch LOFAR is expected to be completed in 2010. The second new LF telescope is the American Long Wavelength Array (LWA; e.g., Taylor 2007), planned to cover a frequency range of 20 to 80 MHz. This project is currently in the prototype phase. The full LWA will consist of 53 stations of static antennas, with baselines up to 400 km. Upon completion, the LWA will be a serious competitor for (E-)LOFAR.

The existing large arrays with low-frequency capabilities, VLA and GMRT, will benefit from ongoing developments. The GMRT has a new software correlator available that is currently being commissioned. There are also ongoing developments for a new LF receiver that can be used between 30 and 90 MHz. The current transition of the VLA to the extended (E-)VLA includes a planned preservation of the 74 and 330 MHz receivers at the antennas. This means the LF signals are to be correlated with the new software correlator. There is rumour that even the 74 and 330 MHz receivers may be replaced with improved, wide-band versions.

One important lesson to be learned from this thesis is that, for optimal performance of LOFAR, LWA and other large LF telescopes, it is crucial to use calibration algorithms that can properly model and remove ionospheric contributions from the observations.

Ionospheric calibration of low-frequency radio interferometric observations using the peeling scheme I. Method description and first results

Abstract. Calibration of radio interferometric observations becomes increasingly difficult towards lower frequencies. Below ~ 300 MHz, spatially variant refractions and propagation delays of radio waves traveling through the ionosphere cause phase rotations that can vary significantly with time, viewing direction and antenna location. In this chapter we present a description and first results of SPAM (Source Peeling and Atmospheric Modeling), a new calibration method that attempts to iteratively solve and correct for ionospheric phase rotations. To model the ionosphere, we construct a time-variant, 2-dimensional phase screen at fixed height above the Earth's surface. Spatial variations are described by a truncated set of discrete Karhunen-Loève base functions, optimized for an assumed power-law spectral density of free electrons density fluctuations, and a given configuration of calibrator sources and antenna locations. The model is constrained using antenna-based gain phases from individual self-calibrations on the available bright sources in the field-of-view. Application of SPAM on three test cases, a simulated visibility data set and two selected 74 MHz VLA data sets, yields significant improvements in image background noise (5 to 75 percent reduction) and source peak fluxes (up to 25 percent increase) as compared to the existing self-calibration and field-based calibration methods, which indicates a significant improvement in ionospheric phase calibration accuracy.

H. T. Intema, S. van der Tol, W. D. Cotton, A. S. Cohen,
I. M. van Bemmelen, and H. J. A. Röttgering
Accepted for publication in *Astronomy & Astrophysics*

2.1 Introduction

Radio waves of cosmic origin are influenced by the Earth's atmosphere before detection at ground level. At low frequencies (LF; $\lesssim 300$ MHz), the dominant effects are refraction, propagation delay and Faraday rotation caused by the ionosphere (e.g., Thompson et al. 2001). For a ground-based interferometer (array from here on) observing a LF cosmic source, the ionosphere is the main source of phase errors in the visibilities. Amplitude errors may also arise under severe ionospheric conditions due to diffraction or focussing (e.g., Jacobson & Erickson 1992a).

The ionosphere causes propagation delay differences between array elements, resulting in a phase rotation of the complex-valued visibilities. The delay per array element (antenna from here on) depends on the line-of-sight (LoS) through the ionosphere, and therefore on antenna position and viewing direction. The calibration of LF observations requires phase corrections that vary over the field-of-view (FoV) of each antenna. Calibration methods that determine just one phase correction for the full FoV of each antenna (like self-calibration; e.g., see Pearson & Readhead 1984) are therefore insufficient.

Ionospheric effects on LF interferometric observations have usually been ignored for several reasons: (i) the resolution and sensitivity of the existing arrays were generally too poor to be affected, (ii) existing calibration algorithms (e.g., self-calibration) appeared to give reasonable results most of the time, and (iii) a lack of computing power made the needed calculations prohibitly expensive. During the last 15 years, two large and more sensitive LF arrays have become operational: the VLA at 74 MHz (Kassim et al. 2007) and the GMRT at 153 and 235 MHz (Swarup 1991). Observations with these arrays have demonstrated that ionospheric phase rotations are one of the main limiting factors for reaching the theoretical image noise level.

For optimal performance of these and future large arrays with LF capabilities (such as LO-FAR, LWA and SKA), it is crucial to use calibration algorithms that can properly model and remove ionospheric contributions from the visibilities. Field-based calibration (Cotton et al. 2004) is the single existing ionospheric calibration & imaging method that incorporates direction-dependent phase calibration. This technique has been successfully applied to many VLA 74 MHz data sets, but is limited by design for use with relatively compact arrays.

In Section 2.2, we discuss ionospheric calibration in more detail. In Section 2.3, we give a detailed description of SPAM, a new ionospheric calibration method that is applicable to LF observations with relatively larger arrays. In Section 2.4, we present the first results of SPAM calibration on simulated and real VLA 74 MHz observations and compare these with results from self-calibration and field-based calibration. A discussion and conclusions are presented in Section 2.5.

2.2 Ionosphere and calibration

In this Section, we describe some physical properties of the ionosphere, the phase effects on radio interferometric observations and requirements for ionospheric phase calibration.

2.2.1 The ionosphere

The ionosphere is a partially ionised layer of gas between ~ 50 and 1000 km altitude over the Earth's surface (e.g., Davies 1990). It is a dynamic, inhomogeneous medium, with electron

density varying as a function of position and time. The state of ionization is mainly influenced by the Sun through photo-ionization at UV and short X-ray wavelengths and through injection of charged particles from the solar wind. Ionization during the day is balanced by recombination at night. The peak of the free electron density is located at a height around 300 km. The free electron column density along a LoS through the ionosphere is generally referred to as *total electron content*, or TEC. The TEC unit (TECU) is 10^{16} m^{-2} which is a typically observed value at zenith during nighttime.

The refraction and propagation delay are caused by a varying refractive index n of the ionospheric plasma along the wave trajectory. For a cold, collisionless plasma without magnetic field, n is a function of the free electron density n_e and is defined by (e.g., Thompson et al. 2001)

$$n^2 = 1 - \frac{\nu_p^2}{\nu^2}, \quad (2.1)$$

with ν the radio frequency and ν_p the plasma frequency, given by

$$\nu_p = \frac{e}{2\pi} \sqrt{\frac{n_e}{\epsilon_0 m}}, \quad (2.2)$$

with e the electron charge, m the electron mass, ϵ_0 the vacuum permittivity. Typically, for the ionosphere, ν_p ranges from 1 to 10 MHz, but may locally rise up to ~ 200 MHz in the presence of sporadic E-layers (clouds of unusually high free electron density). Cosmic radio waves with frequencies below the plasma frequency are reflected by the ionosphere and do not reach the Earth's surface. For higher frequencies, the spatial variations in electron density cause local refractions of the wave (Snell's Law) as it travels through the ionosphere, thereby modifying the wave's trajectory. The total propagation delay, integrated along the LoS, results in a phase rotation given by

$$\phi^{\text{ion}} = -\frac{2\pi\nu}{c} \int (n - 1) dl, \quad (2.3)$$

with c the speed of light in vacuum. For frequencies $\nu \gg \nu_p$, this can be approximated by

$$\phi^{\text{ion}} \approx \frac{\pi}{c\nu} \int \nu_p^2 dl = \frac{e^2}{4\pi\epsilon_0 m c \nu} \int n_e dl, \quad (2.4)$$

where the integral over n_e on the right is the TEC along the LoS. Note that this integral depends on the wave's trajectory, and therefore on local refraction. Because the refractive index is frequency-dependent, the wave's trajectory changes with frequency. As a consequence, the apparent scaling relation $\phi^{\text{ion}} \propto \nu^{-1}$ from Equation 2.4 is only valid to first order in frequency.

Although bulk changes in the large scale TEC (e.g., a factor of 10 increase during sunrise) have the largest amplitudes, the fluctuations on relatively small spatial scales and short temporal scales are most troublesome for LF interferometric observations. Most prominent are the traveling ionospheric disturbances (TIDs), a response to acoustic-gravity waves in the neutral atmosphere (e.g., van Velthoven 1990). Typically, medium-scale TIDs are observed at heights between 200 and 400 km, have wavelengths between 250 and 400 km, travel with near-horizontal velocities between 300 and 700 km h⁻¹ in any direction and cause 1 to 5 percent variations in TEC (Thompson et al. 2001).

The physics behind fluctuations on the shortest spatial and temporal scales is less well understood. Temporal and spatial behaviour may be coupled through quasi-frozen patterns that move over the area of interest with a certain velocity and direction (Jacobson & Erickson 1992a,b). Typical variations in TEC are on the order of 0.1 percent, observed on spatial scales of tens of kilometers down to a few km, and time scales of minutes down to a few tens of seconds. The statistical behaviour of radio waves passing through this medium suggests the presence of a turbulent layer with a power-law spectral density of free electron density fluctuations $P_{n_e}(q) \propto q^{-\alpha}$ (e.g., Thompson et al. 2001), with $q \equiv |\mathbf{q}|$ the magnitude of the 3-dimensional spatial frequency. $P_{n_e}(q)$ is defined in units of electron density squared per spatial frequency. The related 2-dimensional structure function of the phase rotation ϕ of emerging radio waves from a turbulent ionospheric layer is given by

$$D_\phi = \langle [\phi(\mathbf{x}) - \phi(\mathbf{x} + \mathbf{r})]^2 \rangle \propto r^\gamma, \quad (2.5)$$

where \mathbf{x} and $\mathbf{x} + \mathbf{r}$ are Earth positions, $r \equiv |\mathbf{r}|$ is the horizontal distance between these two points, $\langle \dots \rangle$ denotes the expected value and $\gamma = \alpha - 2$. For pure Kolmogorov turbulence, $\alpha = 11/3$, therefore $\gamma = 5/3$.

Using differential Doppler-shift measurements of satellite signals, van Velthoven (1990) found a power-law relation between spectral amplitude of small-scale ionospheric fluctuations and latitudinal wave-number with exponent $\alpha/2 = 3/2$. Combining with radio interferometric observations of apparent cosmic source shifts, van Velthoven derived a mean height for the ionospheric perturbations between 200 and 250 km. Through analysis of differential apparent movement of pairs of cosmic sources in the VLSS, Cohen & Röttgering (2009) find typical values for $\gamma/2$ of 0.50 during nighttime and 0.69 during daytime. Direct measurement of phase structure functions from different GPS satellites (van der Tol, *unpublished*) shows a wide distribution of values for γ that peaks at ~ 1.5 . On average, these results indicate the presence of a turbulent layer below the peak in the free electron density that has more power in the smaller scale fluctuations than in the case of pure Kolmogorov turbulence. Note that for individual observing times and locations, the behaviour of small-scale ionospheric fluctuations may differ significantly from this average.

2.2.2 Image plane effects

Interferometry uses the phase differences as measured on baselines to determine the angle of incident waves, and is therefore only sensitive to TEC differences. A baseline is sensitive to TEC fluctuations with linear sizes that are comparable to or smaller than the baseline length. At 74 MHz (the lowest observing frequency of the VLA), a 0.01 TECU difference on a baseline causes a ~ 1 radian visibility phase rotation (Equation 2.4). Because the observed TEC varies with time, antenna position and viewing direction, visibility phases are distorted by time-varying differential ionospheric phase rotations.

An instantaneous spatial phase gradient over the array in the direction of a source causes an apparent position shift in the image plane (e.g., Cohen & Röttgering 2009), but no source deformation. If the spatial phase behaviour deviates from a gradient, this will also distort the apparent shape of the source. Combining visibilities with different time labels while imaging causes the image plane effects to be time-averaged. A non-zero time average of the phase gradient results in a source shift in the final image. Both a zero-mean time variable phase gradient and higher order phase effects cause smearing and deformation of the source image, and consequently a

reduction of the source peak flux (e.g., see Cotton & Condon 2002). In the latter case, if the combined phase rotations behave like Gaussian random variables, a point source in the resulting image experiences an increase of the source width and reduction of the source peak flux, but the total flux density (the integral under the source shape) is conserved.

For unresolved sources, the *Strehl ratio* is defined as the ratio of observed peak flux over true peak flux. In case of Gaussian random phase rotations, the Strehl ratio R is related to the RMS phase rotation σ_ϕ by (Cotton et al. 2004)

$$R = \exp\left(-\frac{\sigma_\phi^2}{2}\right). \quad (2.6)$$

A larger peak flux is equivalent to a smaller RMS phase rotation. This statement is more generally true, because all phase rotations cause scattering of source power into sidelobes.

A change in the apparent source shape due to ionospheric phase rotations leads to an increase in residual sidelobes after deconvolution. Deconvolution subtracts a time-averaged source image model from the visibility data at all time stamps. In the presence of time-variable phase rotations, the mean source model deviates from the apparent, instantaneous sky emission and subtraction is incomplete. Residual sidelobes increase the RMS background noise level and, due to its non-Gaussian character, introduce structure into the image that mimics real sky emission. In LF observations, due to the scaling relation of the dirty beam with frequency (width $\propto \nu^{-1}$), residual sidelobes around bright sources can be visible at significant distances from the source.

2.2.3 Ionospheric phase calibration

Lonsdale (2005) discussed four different regimes for (instantaneous) ionospheric phase calibration, depending on the different linear spatial scales involved. These scales are the array size A , the scale size S of ionospheric phase fluctuations and the projected size V of the FoV at a typical ionospheric height. We use the term *compact* array when $A \ll S$ and *extended* array when $A \gtrsim S$. Note that these definitions change with ionospheric conditions, so there is no fixed linear scale that defines the difference between compact and extended. A schematic overview of the different regimes is given in Figure 2.1.

The combination AV/S^2 is a measure of the complexity of ionospheric phase calibration. Both S and V depend on the observing frequency ν . For a power-law spectral density of free electron density fluctuations (see Section 2.2.1) S scales with ν , and for a fixed circular antenna aperture V scales with ν^{-1} . Therefore, AV/S^2 scales with ν^{-3} , signalling a rapid increase in calibration problems towards low frequencies.

Under *isoplanatic* conditions ($V \ll S$), the ionospheric phase rotation per antenna does not vary with viewing direction within the FoV, for both compact and large arrays (Lonsdale regimes 1 and 2, respectively). Phase-only self-calibration on short enough time-scales is sufficient to remove the ionospheric phase rotations from the visibilities.

Under *anisoplanatic* conditions ($V \gtrsim S$), the ionospheric phase rotation varies over the FoV of each antenna. A single phase correction per antenna is no longer sufficient. Self-calibration may still converge, but the resulting phase correction per antenna is a flux-weighted average of ionospheric phases across the FoV (see Section 2.3.1). Accurate self-calibration and imaging of individual very bright and relatively compact sources is therefore possible, even with extended arrays (e.g., see Gizani et al. 2005). For a compact array (Lonsdale regime 3), the FoV of different antennas effectively overlap at ionospheric height. The LoS of different antennas towards

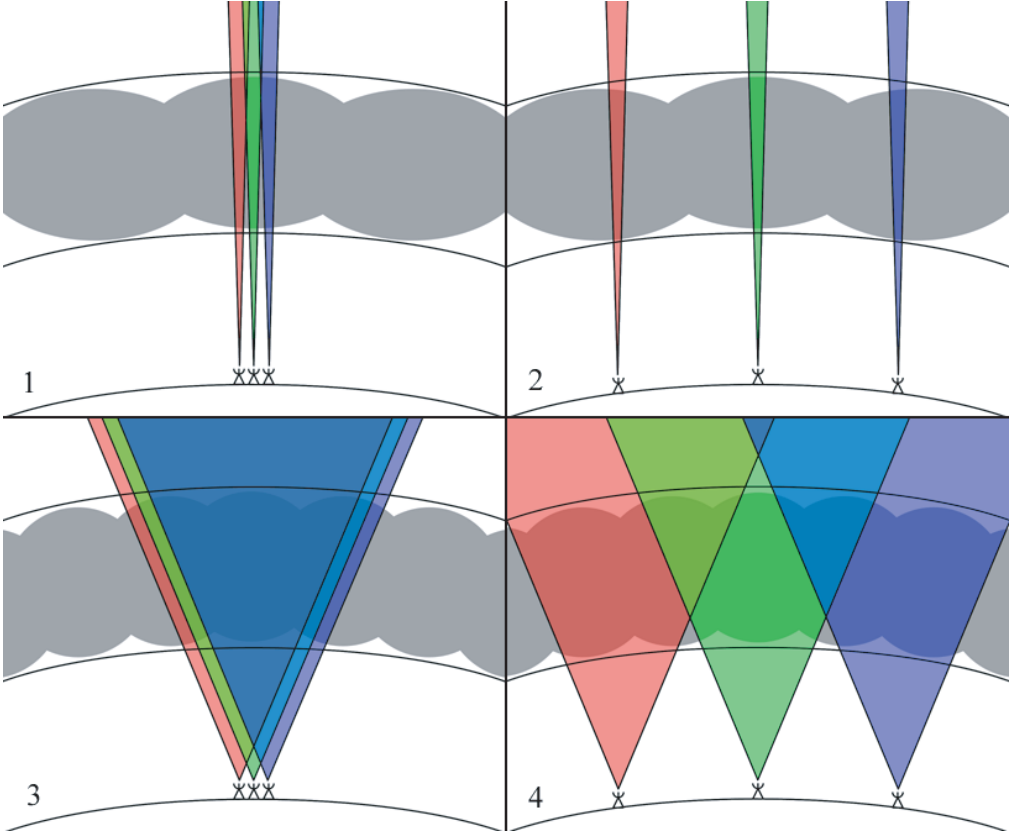


Figure 2.1: Schematic overview of the different calibration regimes as discussed by Lonsdale (2005). For clarity, only two spatial dimensions and one calibration time interval are considered. In this overview, the array is represented by three antennas at ground level, looking through the ionospheric electron density structure (grey bubbles) with individual fields-of-view (red, green and blue areas). Due to the relatively narrow primary beam patterns in regimes 1 and 2 (*top left* and *top right*, respectively), each individual antenna ‘sees’ an approximately constant TEC across the FoV. The relatively wide primary beam patterns in regimes 3 and 4 (*bottom left* and *bottom right*, respectively) causes the antennas to ‘see’ TEC variations across the FoV. For the relatively compact array configurations in regimes 1 and 3, the TEC variation across the array for a single viewing direction within the FoV is approximately a gradient. For the relatively extended array configurations in regimes 2 and 4, the TEC variation across the array for a single viewing direction differs significantly from a gradient. The consequences for calibration of the array are discussed in the text.

one source run close and parallel through the ionosphere. For an extended array (Lonsdale regime 4), the FoV of different antennas may partially overlap at ionospheric height, but not necessarily. Individual LoS from widespread antennas to one source may trace very different paths through the ionosphere

In regime 3, ionospheric phases behave as a spatial gradient over the array that varies with viewing direction. This causes the apparent position of sources to change with time and viewing direction, but no source deformation takes place. The 3-dimensional phase structure of the ionosphere can be effectively reduced to a 2-dimensional phase screen, by integrating the free electron density along the LoS (Equation 2.4). Radio waves that pass the virtual screen experience an instantaneous ionospheric phase rotation depending on the *pierce point* position (where the LoS pierces the phase screen). When assuming a fixed number of required ionospheric parameters per unit area of phase screen, calibration of a compact array requires a minimal number of parameters because each antenna illuminates the same part of the phase screen.

In regime 4, the dependence of ionospheric phase on antenna position and viewing direction is more complex. This causes source position shifts and source shape deformations that both vary with time and viewing direction. A 2-dimensional phase screen model may still be used, but only when the dominant phase fluctuations originate from a restricted height range $\Delta h \ll S$ in the ionosphere. The concept of a thin layer at a given height is attractive, because it reduces the complexity of the calibration problem drastically. When using an airmass function to incorporate a zenith angle dependence, the spatial phase function is in effect reduced to 2 spatial dimensions. Generally, a phase screen in regime 4 requires a larger number of model parameters than in regime 3, because the phase screen area illuminated by the total array is larger.

It is currently unclear under which conditions a 2-dimensional phase screen model becomes too inaccurate to model the ionosphere in regime 4. For very long baselines or very severe ionospheric conditions, a full 3-dimensional ionospheric phase model may be required, where ionospheric phase corrections need to be determined by ray-tracing. Such a model is likely to require many more parameters than can be extracted from radio observations alone. To first order, it may be sufficient to extend the phase screen model with some form of height-dependence. Examples of such extensions are the use of several phase screens at different heights (Anderson et al. 2005) or introducing smoothly varying partial derivatives of TEC or phase as a function of zenith angle (Noordam 2008).

Calibration needs to determine corrections on sufficiently short time scales to track the ionospheric phase changes. The phase rate of change depends on the intrinsic time variability of the TEC along a given LoS and on the speed of the LoS from the array antennas through the ionosphere while tracking a cosmic source. The latter may range up to $\sim 100 \text{ km h}^{-1}$ at 200 km height. The exact requirements on the time resolution of the calibration are yet to be determined. In principle, the time-variable ionospheric phase distortions need to be sampled at least at the Nyquist frequency. However, during phase variations of large amplitude ($\gg 1$ radian), 2π radian phase winding introduces periodicity on much shorter time scales. To successfully unwrap phase winds, at least two corrections per 2π radian phase change are required, but preferably more (also to suppress phase decorrelation of the visibility amplitudes).

2.2.4 Proposed and existing ionospheric calibration schemes

Schwab (1984) and Subrahmanya (1991) have proposed modifications to the self-calibration algorithm to support direction-dependent phase calibration. Both methods discuss the use of a

spatial grid of interpolation nodes (additional free parameters) to characterize the spatial variability of the ionospheric phase rotations. Schwab suggests to use a different set of nodes per antenna, while Subrahmanya suggests to combine these sets by positioning them in a quasi-physical layer at fixed height above the Earth's surface (this to reduce the number of required nodes when the FoVs from different antennas overlap at ionospheric height). Neither of these proposed methods have been implemented.

Designed to operate in Lonsdale regime 3, field-based calibration by Cotton et al. (2004) is the single existing implementation of a direction-dependent ionospheric phase calibration algorithm. Typically, for each time interval of 1 or 2 minutes of VLA 74 MHz data, the method measures and converts the apparent position shift of 5 to 10 detectable bright sources within the FoV into ionospheric phase gradients over the array. To predict phase gradients in arbitrary viewing directions for imaging of the full FoV, an independent phase screen per time interval is fitted to the measured phase gradients. The phase screen is described by a 5 term basis of Zernike polynomials (up to second order, excluding the constant zero order).

Field-based calibration has been used to calibrate 74 MHz VLA observations, mostly in B-configuration (e.g., Cohen et al. 2007) but also several in A-configuration (e.g., Cohen et al. 2003, 2004). Image plane comparison of field-based calibration against self-calibration shows an overall increase of source peak fluxes (in some cases up to a factor of two) and reduction of residual sidelobes around bright sources, a clear indication of improved phase calibration over the FoV (Cotton & Condon 2002). The improved overall calibration performance sometimes compromises the calibration towards the brightest source.

Zernike polynomials are often used to describe aberrations in optical systems, because lower order terms match well with several different types of wavefront distortions, and the functions are an orthogonal set on the circular domain of the telescope pupil. Using Zernike polynomials to describe an ionospheric phase screen may be less suitable, because they are not orthogonal on the discrete domain of pierce points, diverge when moving away from the field center and have no relation to ionospheric image aberrations (except for first order, which can model a large scale TEC gradient). Non-orthogonality leads to interdependence between model parameters, while divergence is clearly non-physical and leads to undesirable extrapolation properties.

For extended LF arrays or more severe ionospheric conditions, the ionospheric phase behaviour over the array for a given viewing direction is no longer a simple gradient. Under these conditions, performance of field-based calibration degrades. For the 74 MHz VLA Low-frequency Sky Survey (VLSS; Cohen et al. 2007), field-based calibration was unable to calibrate the VLA in B-configuration for about 10 to 20 percent of the observing time due to severe ionospheric conditions. Observing at 74 MHz with the ~ 3 times larger VLA A-configuration leads to a relative increase in the failure rate of field-based calibration. This is to be expected, as the larger array size results in an increased probability for the observations to reside in Lonsdale regime 4.

The presence of higher order phase structure over the array in the direction of a calibrator requires an antenna-based phase calibration rather than a source position shift to measure ionospheric phases. The calibration methods proposed by Schwab (1984) and Subrahmanya (1991) do allow for higher order phase corrections over the array and could, in principle, handle more severe ionospheric conditions. An alternative approach is to use the *peeling* technique (Noordam 2004), which consists of sequential self-calibrations on individual bright sources in the FoV. This yields per source a set of time-variable antenna-based phase corrections and a source model. Because the peeling corrections are applicable to a limited set of viewing directions, they

need to be interpolated in some intelligent way to arbitrary viewing directions while imaging the full FoV. Peeling is described in more detail in Section 2.3.3.

Noordam (2004) has proposed a ‘generalized’ self-calibration method for LOFAR (e.g., Röttgering et al. 2006) that includes calibration of higher order ionospheric phase distortions. Similar to ‘classical’ self-calibration, instrumental and environmental (including ionospheric) parameters are estimated by calibration against a sky brightness model. Sky model and calibration parameters are iteratively updated to converge to some final result. Uniqueness of the calibration solution is controlled by putting restrictions on the time-, space- and frequency behaviour of the fitted parameters. The effects of the ionosphere are modeled in a Minimum Ionospheric Model (MIM; Noordam 2008), which is yet to be defined in detail. The philosophy of the MIM is to use a minimal number of physical assumptions and free parameters to accurately reproduce the observed effects of the ionosphere on the visibilities for a wide-as-possible range of ionospheric conditions. The initial MIM is to be constrained using peeling corrections.

2.3 Method

SPAM, an abbreviation of ‘Source Peeling and Atmospheric Modeling’, is the implementation of a new ionospheric calibration method, combining several concepts from proposed and existing calibration methods. SPAM is designed to operate in Lonsdale regime 4 and can therefore also operate in regimes 1 to 3. It uses the calibration phases from peeling sources in the FoV to constrain an ionospheric phase screen model. The phase screen mimics a thin turbulent layer at a fixed height above the Earth’s surface, in concordance with the observations of ionospheric small-scale structure (Section 2.2.1). The main motivation for this work was to test several aspects of ionospheric calibration on existing VLA and GMRT data sets on viability and qualitative performance, and thereby support the development of more advanced calibration algorithms for future instruments such as LOFAR.

Generally, the instantaneous ionosphere can only be sparsely sampled, due to the non-uniform sky distribution of a limited number of suitable calibrators and an array layout that is optimized for UV-coverage rather than ionospheric calibration. To minimize the error while interpolating to unsampled regions, an optimal choice of base functions for the description of the phase screen is of great importance. Based on the work by van der Tol & van der Veen (2007), we use the discrete Karhunen-Loève (KL) transform to determine an optimal set of base ‘functions’ to describe our phase screen. For a given pierce point layout and an assumed power-law slope for the spatial structure function of ionospheric phase fluctuations (see Section 2.2.1), the KL transform yields a set of base vectors with several important properties: (i) the vectors are orthogonal on the pierce point domain, (ii) truncation of the set (reduction of the model order) gives a minimal loss of information, (iii) interpolation to arbitrary pierce point locations obeys the phase structure function, and (iv) spatial phase variability scales with pierce point density, i.e., most phase screen structure is present in the vicinity of pierce points, while it converges to zero at infinite distance. More details on this phase screen model are given in Section 2.3.4.

Because the required calibration time resolution is still an open issue, and the SPAM model does not incorporate any restrictions on temporal behaviour, independent phase screens are determined at the highest possible time resolution (which is the visibility integration time resolution).

SPAM calibration can be separated in a number of functional steps, each of which is dis-

cussed in detail in the sections to follow. The required input is a spectral-mode visibility data set that has flux calibration and bandpass calibration applied, and radio frequency interference (RFI) excised (e.g., see Lazio et al. 2005; Cohen et al. 2007). The SPAM recipe consists of the following steps:

1. Obtain and apply instrumental calibration corrections for phase (Section 2.3.1).
2. Obtain an initial model of the apparent sky, together with an initial ionospheric phase calibration (Section 2.3.2).
3. Subtract the sky model from the visibility data while applying the phase calibration. Peel apparently bright sources (Section 2.3.3).
4. Fit an ionospheric phase screen model to the peeling solutions (Section 2.3.4).
5. Apply the model phases on a facet-to-facet basis during re-imaging of the apparent sky (Section 2.3.5).

Steps 3 to 5 define the SPAM calibration cycle, as the image produced in step 5 can serve as an improved model of the apparent sky in step 3.

The scope of applications for SPAM is limited by a number of assumptions that were made to simplify the current implementation:

- The ionospheric inhomogeneities that cause significant phase distortions are located in a single, relatively narrow height range.
- There exists a finitely small angular patch size, which can be much smaller than the FoV of an individual antenna, over which the ionospheric phase contribution is effectively constant. Moving from one patch to neighbouring patches results in small phase transitions ($\ll 1$ radian).
- There exists a finitely small time range, larger than the integration time interval of an observation, over which the apparent ionospheric phase change for any of the array antennas along any line-of-sight is much smaller than a radian.
- The bandwidth of the observations is small enough to be effectively monochromatic, so that the ionospheric dispersion of waves within the frequency band is negligible.
- Within the given limitations on bandwidth and integration time, the array is sensitive enough to detect at least a few ($\gtrsim 5$) sources within the target FoV that may serve as phase calibrators.
- The ionospheric conditions during the observing run are such that self-calibration is able to produce a good enough initial calibration and sky model to allow for peeling of multiple sources. This might not work under very bad ionospheric conditions, but for the applications presented in this chapter it proved to be sufficient.
- After each calibration cycle (steps 3 to 5), the calibration and sky model are equally or more accurate than the previous. This implies convergence to a best achievable image.

- The instrumental amplitude and phase contributions to the visibilities, including the antenna power patterns projected onto the sky towards the target source, are constant over the duration of the observing run.

SPAM does not attempt to model the effects of ionospheric Faraday rotation on polarization products, and is therefore only applicable to intensity measurements (stokes I).

In our implementation we have focussed on functionality rather than processing speed. In its current form, SPAM is capable of processing quite large offline data sets, but is not suitable for real-time processing as is required for LOFAR calibration. SPAM relies heavily on functionality available in NRAO's Astronomical Image Processing System (AIPS; e.g., Bridle & Greisen 1994). It consists of a collection of Python scripts that accesses AIPS tasks, files and tables using the ParselTongue interface (Kettenis et al. 2006). Two main reasons to use AIPS are its familiarity and proven robustness while serving a large group of users over a 30 year lifetime, and the quite natural way by which the ionospheric calibration method is combined with polyhedron imaging (Perley 1989a; Cornwell & Perley 1992). SPAM uses a number of 3rd party Python libraries, such as *scipy*, *numpy* and *matplotlib* for math and matrix operations and plotting. For non-linear least squares fitting of ionospheric phase models, we have adopted a Levenberg-Marquardt solver (LM; e.g., Press et al. 1992) based on IDL's MPFIT package (Markwardt 2009).

2.3.1 Instrumental phase calibration

Each antenna in the array adds an instrumental phase offset to the recorded signal before correlation. At low frequencies, changes in the instrumental signal path length (e.g., due to temperature induced cable length differences) are very small compared to the wavelength, therefore instrumental phase offsets are generally stable over long time periods (hours to days). SPAM requires removal of the instrumental phase offsets from the visibilities prior to ionospheric calibration.

Instead of directly measuring the sky intensity $I(l, m)$ as a function of viewing direction cosines (l, m) , an interferometer measures an approximate Fourier transform of the sky intensity. For a baseline consisting of antennas i and j , the perfect response to all visible sky emission for a single time instance and frequency is given by the measurement equation (ME) for visibilities (e.g., Thompson et al. 2001):

$$V_{ij} = \iint I(l, m) \exp\left(-2\pi J \left[u_{ij}l + v_{ij}m + w_{ij}(n-1)\right]\right) \frac{dl dm}{n}, \quad (2.7)$$

where $J = \sqrt{-1}$, $n = \sqrt{1 - l^2 - m^2}$, u_{ij} and v_{ij} are baseline coordinates in the UV plane (expressed in wavelengths) parallel to l and m , respectively, and w_{ij} is the perpendicular baseline coordinate along the LoS towards the chosen celestial *phase tracking center* at $(l, m) = (0, 0)$. In practice, these measurements are modified with predominantly antenna-based complex gain factors a_i that may vary with time, frequency, antenna position and viewing direction. This modifies the ME into

$$\hat{V}_{ij} = \iint a_i(l, m) a_j^*(l, m) I(l, m) \exp\left(-2\pi J \left[u_{ij}l + v_{ij}m + w_{ij}(n-1)\right]\right) \frac{dl dm}{n}. \quad (2.8)$$

Determination of the gain factors is generally referred to as *calibration*. When known, only gain factors that do not depend on viewing direction can be removed from the visibility data prior to

image reconstruction by applying the calibration:

$$V_{ij} = (a_i a_j^\dagger)^{-1} \hat{V}_{ij} \quad (2.9)$$

This operation is generally not possible for gain factors that do depend on viewing direction, because these gain factors cannot be moved in front of the integral in Equation 2.8. One may still choose to apply gain corrections for a single viewing direction (e.g. to image a particular source), but the accuracy of imaging and deconvolution of other visible sources will degrade when moving away from the selected viewing direction. A solution for wide-field imaging and deconvolution in the presence of direction-dependent gain factors is discussed in Section 2.3.5.

The standard approach for instrumental phase calibration at higher frequencies is to repeatedly observe a bright (mostly unresolved) source during an observing run. Antenna-based gain phase corrections $g_i \approx a_i^{-1}$ are estimated by minimizing the weighted difference sum S between observed visibilities \hat{V}_{ij} and source model visibilities $V_{ij}^{\text{model}} \approx V_{ij}$ (e.g., Thompson et al. 2001, implemented in AIPS task CALIB):

$$S = \sum_i \sum_{j>i} W_{ij} \|V_{ij}^{\text{model}} - g_i g_j^\dagger \hat{V}_{ij}\|^p, \quad (2.10)$$

with W_{ij} the visibility weight (reciprocal of the uncertainty in the visibility measurement), $g_i = \exp(J\phi_i^{\text{cal}})$ and p the power of the norm (typically 1 or 2). The source model visibilities V_{ij}^{model} are calculated using Equation 2.7 with $I(l, m) = I^{\text{model}}(l, m)$. The phase corrections ϕ_i^{cal} consist of an instrumental and an atmospheric part. The corrections are interpolated in time and applied to the target field visibilities, under the assumptions that the instrumental and atmospheric phase offsets vary slowly in time, and that the atmospheric phase offsets in the direction of the target are equal to those in the direction of the calibrator.

At low frequencies, there are two complicating factors for the standard approach: (i) the FoV around the calibrator source is large and includes many other sources, and (ii) the ionospheric phase offset per antenna changes significantly with time and viewing direction. The former can be overcome by choosing a very bright calibrator source with a flux density that dominates over the combined flux density of all other visible sources on all baselines. For the VLSS (Cohen et al. 2007), the 17,000 Jy of Cygnus A was more than sufficient to dominate over the total apparent flux density of 400 – 500 Jy in a typical VLSS field. The latter requires filtering of the phase corrections to extract only the instrumental part, which is then applied to the target field visibilities.

For SPAM, we have adopted an instrumental phase calibration method that is very similar to the procedure used for field-based calibration (Cotton et al. 2004). Antenna-based phase corrections are obtained on the highest possible time resolution by calibration on a very bright source k using the robust L1 norm (Equation 2.10 with $p = 1$; Schwab 1981). A phase correction ϕ_{ikn}^{cal} for antenna i at time interval n consist of several contributions:

$$\phi_{ikn}^{\text{cal}} = \phi_i^{\text{instr}} + \phi_{ikn}^{\text{ion}} - \phi_{rkn} - \phi_{ikn}^{\text{ambig}}, \quad (2.11)$$

where the instrumental and ionospheric phase corrections, ϕ_i^{instr} and ϕ_{ikn}^{ion} respectively, are assumed to be constant resp. vary with time and antenna position over the observing run. The other right-hand terms are the phase offset $\phi_{rkn} = \phi_r^{\text{instr}} + \phi_{rkn}^{\text{ion}}$ of an arbitrarily chosen reference

antenna $r \in \{i\}$, and the phase ambiguity term $\phi_{ikn}^{\text{ambig}} = 2\pi N_{ikn}$ with integer N_{ikn} that maps ϕ_{ikn}^{cal} into the $[0, 2\pi)$ domain.

The antenna-based phase corrections are split into instrumental and ionospheric parts on the basis of their temporal and spatial behaviour. The phase corrections are filtered by iterative estimation of invariant instrumental phases (together with the phase ambiguities) and time- and space-variant ionospheric phases. The instrumental phases are estimated by robust averaging ($+3\sigma$ rejection) over all time intervals n :

$$\tilde{\phi}_i^{\text{instr}} = \left\langle \left(\phi_{ikn}^{\text{cal}} - \tilde{\phi}_i^{\text{ion}} \right) \bmod 2\pi \right\rangle_n. \quad (2.12)$$

The phase ambiguity estimates follow from

$$\tilde{\phi}_{ikn}^{\text{ambig}} = 2\pi \text{round} \left(\left[\tilde{\phi}_i^{\text{instr}} + \tilde{\phi}_i^{\text{ion}} - \phi_{ikn}^{\text{cal}} \right] / 2\pi \right), \quad (2.13)$$

where the round() operator rounds a number to the nearest integer value. The instrumental phase offset of the reference antenna is arbitrarily set to zero. The ionospheric phases are constrained by fitting a time-varying spatial gradient \mathbf{G}_{kn} to the phases over the array. The gradient fit consists of an initial estimate directly from the calibration phase corrections, followed by a refined fit by using the LM solver to minimize

$$\chi_{kn}^2 = \sum_i \left[\left(\phi_{ikn}^{\text{cal}} - \tilde{\phi}_i^{\text{instr}} + \tilde{\phi}_{ikn}^{\text{ambig}} \right) - \underbrace{\mathbf{G}_{kn} \cdot (\mathbf{x}_i - \mathbf{x}_r)}_{\tilde{\phi}_{ikn}^{\text{ion}}} \right]^2, \quad (2.14)$$

where \mathbf{x}_i is the position of antenna i . The ionospheric phase offset of the reference antenna is arbitrarily set to zero, which makes it a pivot point over which the phase gradient rotates. Higher order ionospheric effects are assumed to average to zero in Equation 2.12.

A new, ‘calibrated’ visibility data set is created by applying the time-constant instrumental phase corrections derived above to the initial input visibility data set of the target field. Any subsequent calibration phase corrections that are to be determined for this calibrated data set will (in the ideal case) consist of ionospheric phase rotations only. The carefully derived calibration state of the new data set is preserved during further processing by storing any subsequent (time-variable) calibration phase corrections in tables (AIPS SN table) rather than applying them directly to the visibility data.

2.3.2 Initial phase calibration and initial sky model

The instrumental phase calibration method described in Section 2.3.1 assumes that the time-averaged ionospheric phase gradient over the array in the direction of the bright phase calibrator is zero. Any non-zero average is absorbed into the instrumental phase estimates, causing a position shift of the whole target field and thereby invalidating the astrometry. Before entering the calibration cycle (Sections 2.3.3 to 2.3.5), SPAM requires restoration of the astrometry and determination of an initial sky model and initial ionospheric calibration.

To restore the astrometry, the calibrated visibility data of the target field (the output of Section 2.3.1) is phase calibrated against an apparent sky model (AIPS task CALIB). The default is a multiple point source model, using NVSS catalog positions (Condon et al. 1994, 1998), power-law interpolated flux densities from NVSS and WENSS/WISH catalogs (Rengelink et al. 1997) and a given primary beam model. The sky model calibration is followed by wide-field imaging

(AIPS task IMAGR) and several rounds of phase-only self-calibration (CALIB and IMAGR) at the highest possible time resolution, yielding the initial sky model and initial phase calibration.

For wide-field imaging with non-coplanar arrays, the standard imaging assumptions that the relevant sky area is approximately flat and the third baseline coordinate (w -term in Equation 2.7) is constant across the FoV are no longer valid. To overcome this, SPAM uses the polyhedron method (Perley 1989a; Cornwell & Perley 1992) that divides the large FoV into a hexagonal grid of small, partially overlapping *facets* that individually do satisfy the assumptions above (AIPS task SETFC). Additional facets are centered on relatively bright sources inside and outside the primary beam area to reduce image artifacts due to pixellation (Perley 1989b; Briggs & Cornwell 1992; Briggs 1995; Voronkov & Wieringa 2004; Cotton & Uson 2008).

The Cotton-Schwab algorithm (Schwab 1984; Cotton 1989, 1999; Cornwell et al. 1999) is a variant of CLEAN deconvolution (Hogbom 1974; Clark 1980) that allows for simultaneous deconvolution of multiple facets, using a different dirty beam for each facet. *Boxes* are used to restrict CLEANing to real sky emission, making sure that sources are deconvolved in the nearest facet only (CLEAN model components are stored in facet-based AIPS CC tables). After deconvolution, the CLEAN model is restored to the relevant residual facets (AIPS task CCRES) using a CLEAN beam, and the facets are combined to form a single image of the full FoV (AIPS task FLATN).

2.3.3 Peeling

To construct a model of ionospheric phase rotations in arbitrary viewing directions within the FoV, SPAM requires measurements in as many directions as possible. When no external sources of ionospheric information are available, the target field visibilities themselves need to be utilized. Calibration on individual bright sources in the FoV can supply the required information, even in the presence of higher order phase structure over the array. After instrumental phase offsets are removed, phase calibration corrections are an relative measure of ionospheric phase:

$$\phi_{ikn}^{\text{cal}} = \phi_{ikn}^{\text{ion}} - \phi_{rkn}^{\text{ion}} - \phi_{ikn}^{\text{ambig}}, \quad (2.15)$$

where we used Equation 2.11 with $\phi_i^{\text{instr}} = \phi_r^{\text{instr}} = 0$.

SPAM uses the peeling technique (Noordam 2004) to obtain phase corrections in different viewing directions. Peeling consists of self-calibration on individual sources, yielding per source a set of time-variable antenna-based phase corrections and a source model, after which the source model is subtracted from the visibility data set while temporarily applying the phase corrections (AIPS tasks SPLIT, UVSUB and CLINV/SPLIT).

For peeling to converge, the source needs to be the dominant contributor to the visibility amplitude on all baselines. Especially at low frequencies, the presence of many other sources in the large FoV adds considerable noise to the peeling phase corrections. To suppress this effect, the following steps are performed: (i) The best available model of the apparent sky is subtracted from the visibility data while temporarily applying the associated phase calibration(s). The initial best available model and associated phase calibration is the self-calibration output of Section 2.3.2. Individual source models are added back before peeling. (ii) Sources are peeled in decreasing flux density order to suppress the effect of brighter sources on the peeling of fainter sources. (iii) Calibration only uses visibilities with projected baseline lengths longer than a certain threshold. This excludes the high ‘noise’ in the visibilities near zero-length baselines from the coherent flux contribution of imperfectly subtracted sources.

The radio sky can be approximated by a discrete number of isolated, invariant sources of finite angular extend. Visibilities in the ME (Equation 2.7) for a single integration time n can therefore be split into a linear combination of contributions from individual sources k :

$$V_{ijn} = \sum_k V_{ijkn} = \sum_k \int \int I_k(l, m) \exp(-2\pi J [u_{ijn}l + v_{ijn}m + w_{ijn}(n-1)]) \frac{dl dm}{n}. \quad (2.16)$$

The subtraction of all but the peeling source k' from the measured visibilities in step (i) above can be described as

$$\hat{V}_{ijk'n} \approx \hat{V}_{ijn} - \sum_{k \neq k'} (g_{ikn} g_{jkn}^\dagger)^{-1} V_{ijkn}^{\text{model}}, \quad (2.17)$$

with $g_{ikn} = g_i(l_k, m_k, t_n) = \exp(J\phi_{ikn}^{\text{cal}})$ the best available calibration in the viewing direction of source k , and V_{ijkn}^{model} the visibilities that are derived from the best available model I_{ijk}^{model} of source k . The peeling itself consists of iterative calibration and imaging steps of the peeling source k' . The calibration (Equation 2.10 with $p = 1$) updates the antenna gain corrections g_{ikn} by minimizing

$$S_n = \sum_i \sum_{j>i} w_{ijn} \|V_{ijk'n}^{\text{model}} - g_{in} g_{jn}^\dagger \hat{V}_{ijk'n}\|, \quad (2.18)$$

while the imaging step updates $I_{ijk'}^{\text{model}}$ and therefore $V_{ijk'n}^{\text{model}}$.

In practice, due to incompleteness of the sky model and inaccuracies in the phase calibration, there will always remain some contaminating source flux in the visibilities while peeling. Complemented with system noise, sky noise, residual RFI and other possible sources of noise, the noise in the visibilities propagates into the phase corrections from the peeling process.

Absolute astrometry is not conserved during peeling, because self-calibration allows antenna-based phase corrections to vary without constraint. In subsequent peeling cycles, small non-zero phase gradients in the phase residuals after calibration can cause the source model to wander away from its true position. In SPAM, astrometry errors are minimized by re-centering the source model to its true (catalog) position before calibration in each self-calibration loop. By default, SPAM re-centers the peak of the flux model to the nearest bright point source position in the NVSS catalog (Condon et al. 1994, 1998). It is recommended to visually check the final peeling source images for possible mismatches with the catalog (e.g., in case of double sources or sources with a spatially varying spectral index).

While peeling, SPAM attempts to calibrate sources on the highest possible time resolution, which is the visibility time grid. The noise in the resulting phase corrections depends on the signal-to-noise ratio (SNR) of the source flux in the visibilities. To increase the number of peeling sources and limit the phase noise in case of insufficient SNR, SPAM is allowed to increase the calibration time interval beyond the visibility integration time up to an arbitrary limit. Through image plane analysis, SPAM estimates the required calibration time-interval per source:

$$n_t = \left(\frac{\sigma_L}{\alpha S_p} \right)^2 N_t, \quad (2.19)$$

where n_t is the required number of integration times in a calibration interval, N_t is the total number of integration times within the observation, α is the minimum required SNR per integration time (a tweakable parameter that sets the balance between the SNR and the time resolution of the peeling phase corrections), and S_p and σ_L are the measured source peak flux and local

background noise level in the image. For a fixed upper limit on the calibration time interval, an increase in α results in a decrease in the number of peeling sources. For $n_t < 1$, phase corrections are determined on the visibility time grid. For $n_t > 1$, a spline is used to resample the phase corrections per antenna in time onto the visibility time grid.

Apart from SNR issues, the number of sources that can be peeled is fundamentally limited by the available number of independent visibility measurements. When peeling N_s sources, self-calibration fits $N_s(N_a - 1)$ phase solutions per calibration time interval to the visibility data, where N_a is the number of antennas. For self-calibration to converge to a unique combination of phase solutions and source model, this number needs to be much smaller than the number of independent visibility measurements. The maximum of visibilities measurements that is available in one calibration time interval is given by $N_c \langle n_t \rangle N_a (N_a - 1)/2$, with N_c the number of frequency channels and $\langle n_t \rangle$ the average number of visibility integration times in a calibration interval. In the ideal case, when we assume that each visibility is an independent measurement, the determination of antenna-based phase corrections for all peeling sources is well constrained if

$$N_s \ll \frac{N_a N_c \langle n_t \rangle}{2}. \quad (2.20)$$

The applications presented in this chapter do satisfy this minimal condition (see Section 2.4).

Equation 2.20 is equivalent to stating that the number of degrees-of-freedom (DoF; the difference between the number of independent measurements and the number of model parameters) should remain a large positive number. Correlation between visibilities over frequency and time may reduce the number of independent measurements drastically, thereby also reducing the number of DoFs. The exact number of DoFs for any data set is hard to quantify. When this number becomes too low, the data is ‘over-fitted’ (e.g., Bhatnagar et al. 2008), which could result in an artificial reduction of both the image background noise level and source flux that is not represented in the self-calibration model (Wieringa 1992). Although we have found no evidence of this effect occurring in the applications presented in this chapter, the SPAM user should be cautious not to peel too many sources. In case of a high number of available peeling sources, one can choose a subset with a sufficiently dense spatial distribution over the FoV (e.g., one source per isoplanatic patch; see Section 2.3.5).

2.3.4 Ionospheric phase screen model

The phase corrections that are obtained by peeling several bright sources in the FoV (Section 2.3.3) are only valid for ionospheric calibration in a limited patch of sky around each source. To correct for ionospheric phase rotations over the full FoV during wide-field imaging and deconvolution, SPAM requires a model that predicts the phase correction per antenna for arbitrary viewing directions.

SPAM constructs a quasi-physical phase screen model that attempts to accurately reproduce and interpolate the measured ionospheric phase rotations (or more accurately: the peeling phase corrections). The phase screen is determined independently for each visibility time stamp, therefore we drop the n -subscript in the description below. Figure 2.2 is a schematic overview of the geometry of ionospheric phase modeling in SPAM. The ionosphere is represented by a curved phase screen at a fixed height h above the Earth’s surface, compliant to the WGS84 standard (NIMA 1984). The total phase rotation experienced by a ray of radio emission traveling along a LoS through the ionosphere is represented by an instantaneous phase rotation $\phi^{\text{ion}}(\mathbf{p}, \zeta)$ on

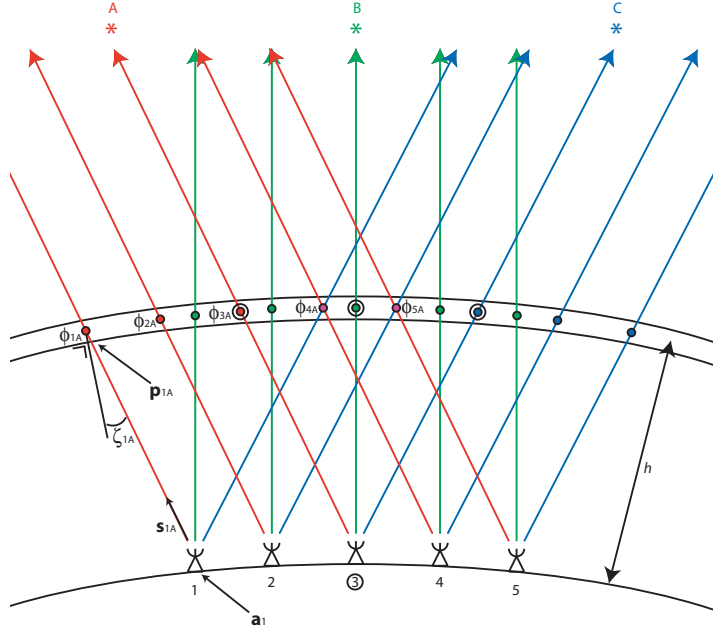


Figure 2.2: Schematic overview of the SPAM thin ionospheric phase screen model geometry. For clarity, only two spatial dimensions and one calibration time interval are considered. In this overview, five ground-based array antennas (labelled 1 to 5) observe three calibrator sources (colored red/green/blue and labelled A to C) within the FoV. The (colored) LoSs from the array towards the sources run parallel for each source and pierce the phase screen at fixed height h (colored circles). The LoS from antenna i at Earth location \mathbf{a}_i towards a peeling source k at local sky position $\hat{\mathbf{s}}_{ik}$ intersects the phase screen at a single *pierce point* \mathbf{p}_{ik} under a zenith angle ζ_{ik} . For a single LoS from antenna 1 towards source A, we have indicated how the pierce point position $\mathbf{p}_{ik} = \mathbf{p}_{1A}$ and zenith angle $\zeta_{ik} = \zeta_{1A}$ relate to the antenna position $\mathbf{a}_i = \mathbf{a}_1$ and the local sky position $\hat{\mathbf{s}}_{ik} = \mathbf{s}_{1A}$ of the source. For some LoSs the pierce points may overlap (or nearly overlap), as is the case for 1C & 4A and 2C & 5A in our example. The total (integrated) phase rotation along any LoS through the ionosphere is modeled by an instantaneous phase rotation ϕ_{ik}^{ion} at the phase screen height. For example, radio waves traveling along LoSs from source A towards antennas 1 to 5 experience an instantaneous phase rotation $\phi_{ik}^{\text{ion}} = \phi_{1A}$ to ϕ_{5A} , respectively, while passing the screen at their related pierce points $\mathbf{p}_{ik} = \mathbf{p}_{1A}$ to \mathbf{p}_{5A} , respectively. Peeling the three calibrator sources yields measurements of the ionospheric phases ϕ_{ik}^{ion} , relative to a common reference antenna (in this example antenna 3; encircled).

passage through the phase screen that is a function of pierce point position \mathbf{p} and zenith angle ζ . For a thin layer ($\Delta h \ll S$; see Section 2.2.3), the dependence of ϕ^{ion} on ζ can be represented by a simple airmass function, so that

$$\phi^{\text{ion}}(\mathbf{p}, \zeta) = \frac{\phi^{\text{ion}}(\mathbf{p})}{\cos(\zeta)}. \quad (2.21)$$

SPAM uses an angular local longitude/latitude coordinate system to specify \mathbf{p} , relative to the central pierce point from array center to field center. For the applications presented in this chapter, the angular distances between pierce points over the relevant ionospheric domain are all

< 5 degrees, which effectively makes the pierce point vector \mathbf{p} a 2-dimensional cartesian vector.

The 2-dimensional phase screen $\phi^{\text{ion}}(\mathbf{p})$ is defined on a set of KL base vectors, generated from the instantaneous pierce point configuration $\{\mathbf{p}_{ik}\}$ and an assumed power-law shape for the phase structure function (Section 2.2.1). The KL base vector generation and interpolation is based on the work by van der Tol & van der Veen (2007) and is described in detail in Appendix 2.7. The phase screen model requires one free parameter per KL base vector. The initial complete set of KL base vectors is arbitrarily reduced in order by selecting a subset based on statistical relevance (principle component analysis). This reduces the effect of noise in the peeling solutions on the model accuracy and simultaneously limits the number of model parameters. However, the subset should still be large enough to accurately reproduce the peeling phase corrections. Per visibility time stamp, the KL base vectors are stored for later use during imaging (for this purpose, we mis-use the AIPS OB table). As an example, the first six interpolated KL base vectors for a single configuration of ionospheric pierce points are plotted in Figure 2.3.

The peeling phase corrections ϕ_{ik}^{cal} are interpreted to be relative measurements of the absolute ionospheric phase screen model $\phi^{\text{ion}}(\mathbf{p}, \zeta)$ which may be determined up to a constant. The model parameters are determined by minimizing the differences between the observed and the model phases using the LM non-linear least-squares solver, for which a χ^2 sum needs to be defined. From Equation 2.15 it follows that

$$\phi_{ik}^{\text{cal}} = \phi^{\text{ion}}(\mathbf{p}_{ik}, \zeta_{ik}) - \phi^{\text{ion}}(\mathbf{p}_{rk}, \zeta_{rk}) - \phi_{ik}^{\text{ambig}}. \quad (2.22)$$

Consequently, the phase correction in the direction of source k for a baseline consisting of antennas i and j is

$$\phi_{ik}^{\text{cal}} - \phi_{jk}^{\text{cal}} = [\phi^{\text{ion}}(\mathbf{p}_{ik}, \zeta_{ik}) - \phi^{\text{ion}}(\mathbf{p}_{jk}, \zeta_{jk})] - [\phi_{ik}^{\text{ambig}} - \phi_{jk}^{\text{ambig}}]. \quad (2.23)$$

The χ^2 sum is defined as:

$$\chi^2 = \sum_k \sum_i \sum_{j>i} \left[([\phi_{ik}^{\text{cal}} - \phi_{jk}^{\text{cal}}] - [\phi^{\text{ion}}(\mathbf{p}_{ik}, \zeta_{ik}) - \phi^{\text{ion}}(\mathbf{p}_{jk}, \zeta_{jk})]) \bmod 2\pi \right]^2. \quad (2.24)$$

This definition has several properties: (i) By remapping the χ^2 terms into the $[0, 2\pi)$ domain, the phase ambiguity terms do not have to be fitted explicitly, (ii) the χ^2 terms of all calibrator sources are weighted equally, so the model is not biased towards the brightest source (as is the case for self-calibration), and (iii) using χ^2 terms from all possible antenna pairs prevents a bias towards the reference antenna.

Using Equation 2.24, the LM solver yields a set of model parameters per visibility time stamp. These are stored for later use during imaging (AIPS NI table). The square root of the average of the χ^2 terms equals the average RMS phase residual between peeling and model phases. Time intervals that have a bad fit are identified and removed by means of an upper limit ($+2.5\sigma$ rejection) on the distribution of RMS phase residuals over time.

Convergence of the LM solver is troubled by 2π phase ambiguities, because these introduce local minima in χ^2 space. A good initial guess of the model parameters greatly helps to overcome this problem. To this purpose, SPAM estimates the global phase gradient over all the pierce points directly from the phase corrections ϕ_{ik}^{cal} and projects it onto the KL base vectors before invoking the LM solver.

Figure 2.4 shows an example of an ionospheric phase screen that was constructed as described above. The pierce point layout consists of multiple projections of the array onto the

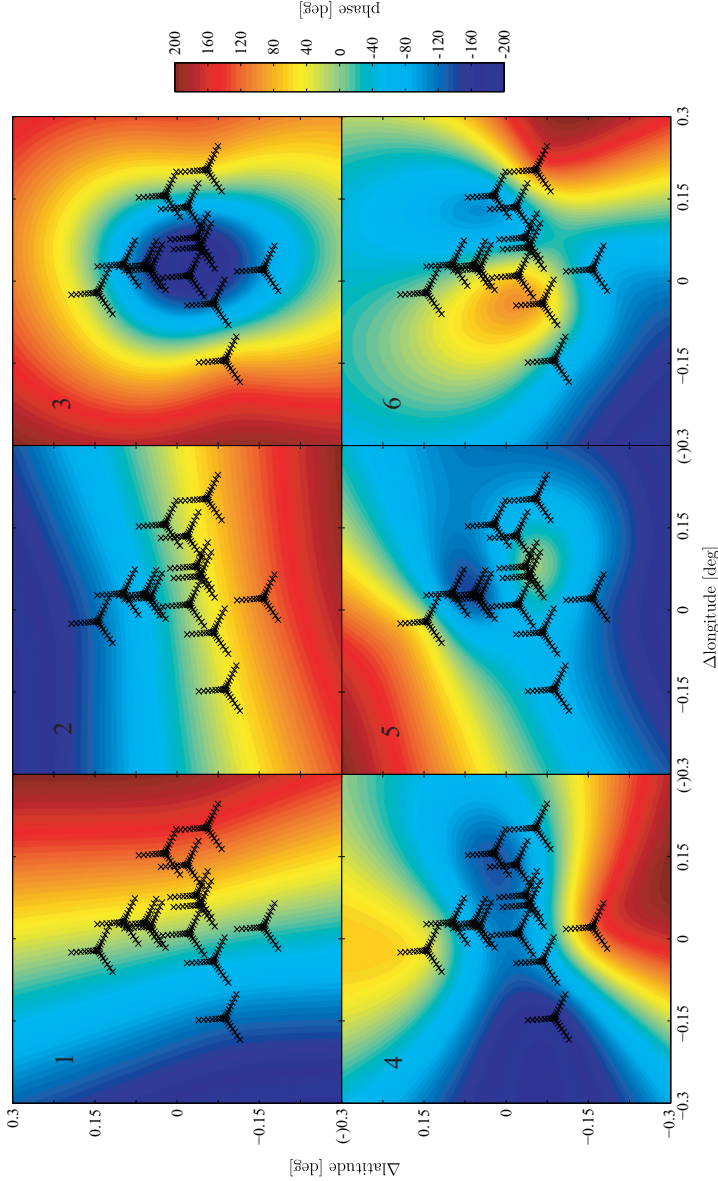


Figure 2.3: Plots of the interpolations of the first six KL base vectors, derived for an artificial but realistic configuration of ionospheric pierce points. In this example, the pierce points (black crosses) are calculated for a single time instance during a 74 MHz VLA-B observation with 13 available calibrator sources in the ~ 10 degree FoV, adopting a phase screen height $h = 200$ km and a structure function power-law slope $\gamma = 5/3$. The horizontal and vertical axes represent angular distances in East-West and North-South directions, respectively, as seen from the center of the Earth, relative to the phase screen's pierce point along the line-of-sight from array center to pointing center, with East- and Northward offsets being positive. At this height, a 0.1 degree angular offset represents a physical horizontal offset of ~ 11.5 km. The direction-dependent phase for each interpolated KL base vector is color-coded and scaled to an arbitrary amplitude range.

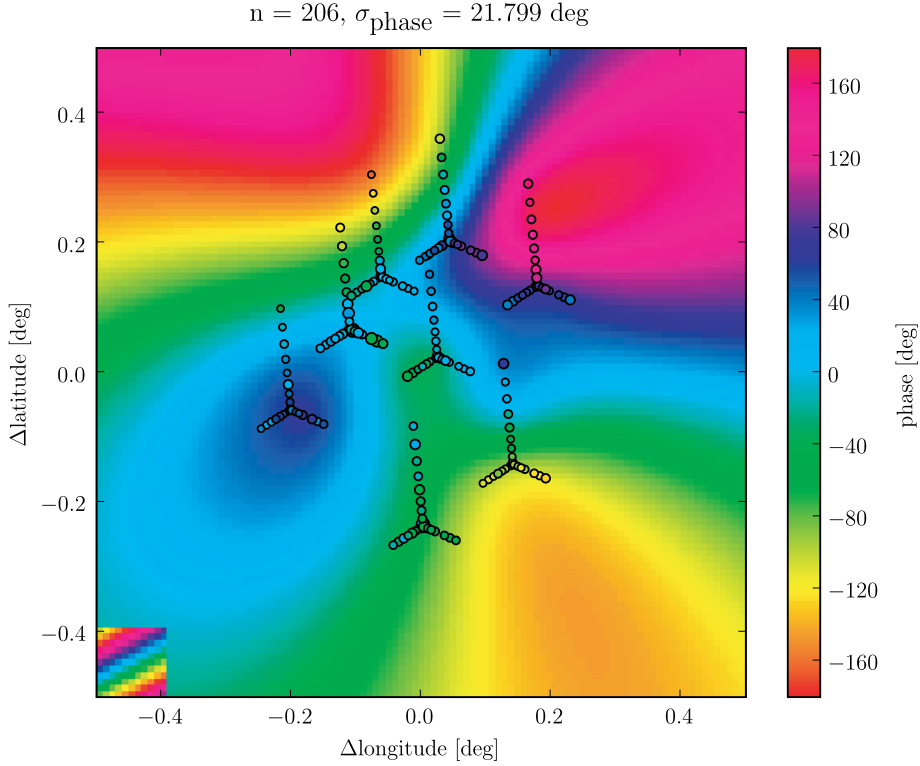


Figure 2.4: Example of an ionospheric phase screen model fit. The color map represents an ionospheric phase screen at 200 km height that was fitted to the peeling phase solutions of 8 calibrator sources at time-interval $n = 206$ of 10 seconds during a VLSS observing run of the 74 MHz VLA in BnA-configuration (see Section 2.4, the J1300-208 data set). The plot layout is similar to Figure 2.3. The overall phase gradient (depicted in the bottom-left corner) was removed to make the higher order terms more clearly visible. The collection of pierce points from all array antennas to all peeling sources are depicted as small circles. The color in the circle represents the measured peeling phase (the reference antenna VLA N36 was set to match the phase screen value). The size of the circle scales with the magnitude of the estimated phase residual after model correction. The overall RMS phase residual $\sigma_{\text{phase}} = 21.799$ degrees (averaged over all pierce points) was one of the better fitting results during this particular observing run.

phase screen. The low density of calibrators causes a minimal overlap between array projections. Figure 2.5 shows a comparison between time-sequences of phase corrections from self-calibration, peeling and model fitting. Because the self-calibration corrections are a flux-weighted average for the full FoV, they are biased towards the brightest source. They look somewhat similar to the peeling solutions of the brightest source, but the latter contains additional fluctuations that vary on a relatively short timescale. The model phases appear similar to the peeling phases, but vary more smoothly. Their values fall somewhere in between the self-calibration phases and the peeling phases. The difference between the peeling phases and model phases are mainly caused by the constraints on the spatial variability of the phase screen model.

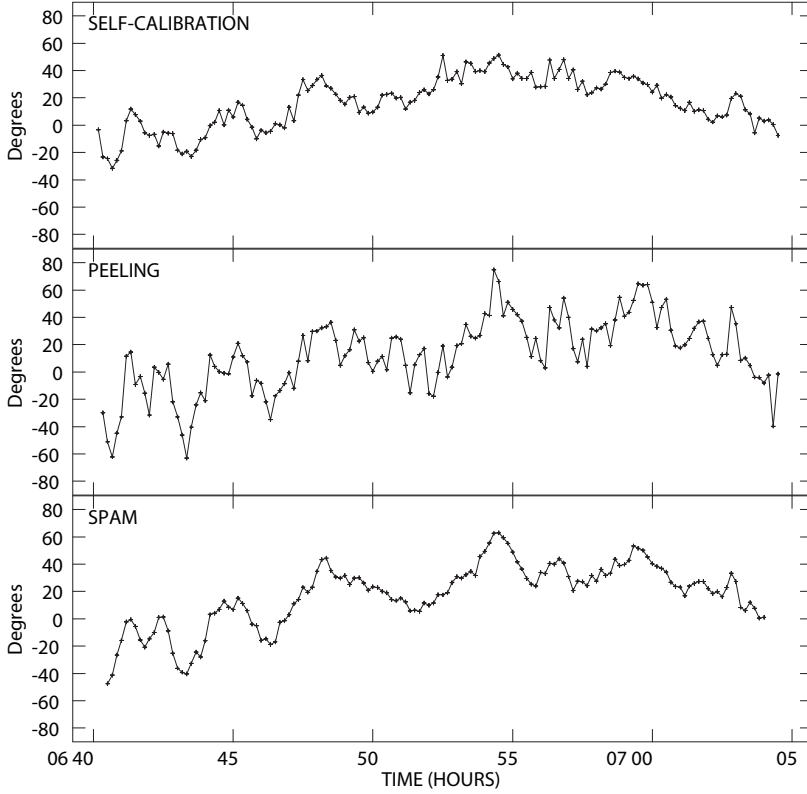


Figure 2.5: Example of phase corrections from different steps in the ionospheric calibration process, resulting from processing a VLSS data set with SPAM (see Section 2.4, the real J0900+398 data set). The antenna under consideration is VLA E28, with W20 being the reference antenna (an 5.7 km east-west baseline). The plots represent 25 minutes of observing time, using a 10 second time resolution. *Top:* Antenna-based phase corrections resulting from self-calibration on the whole FoV. *Middle:* Phase corrections resulting from peeling the brightest (30 Jy) source. *Bottom:* Corrections resulting from ionospheric phase modeling in the direction of the (same) brightest source.

2.3.5 Imaging

With an ionospheric phase screen model available for a given visibility data set, antenna-based phase corrections for any direction in the wide FoV can be calculated (Equation 2.22). Because each visibility consist of contributions from visible sources in different viewing directions, there is no simple operation that removes the ionospheric phase rotations from a visibility data set prior to imaging. Instead, SPAM requires an algorithm that calculates and applies the appropriate model phase corrections during imaging and deconvolving for different parts of the FoV.

SPAM works under the assumption that there exists a fixed angular *isoplanatic patch* size on the sky, with a projected size at ionospheric height smaller than the scale size of ionospheric phase fluctuations, over which variations in ionospheric phase rotation are negligible. Each isoplanatic patch requires at least one phase correction per antenna per visibility time interval.

For the VLA at 74 MHz, the isoplanatic patch size is estimated to be 2 to 4 degrees (Cotton & Condon 2002).

The facet-based polyhedron method for wide-field imaging (see Section 2.3.2) allows for a relatively simple implementation of ionospheric phase correction (Schwab 1984). By choosing a facet size smaller than the isoplanatic patch size, a set of model phase corrections calculated for the center of a facet are assumed to be accurate for the whole facet area. Ionospheric phase model corrections are calculated and stored (AIPS SN tables) for each facet center in the FoV prior to imaging and deconvolution. For the additional facets centered on bright sources (see Section 2.3.2), model phase corrections are optionally replaced by peeling phase corrections to allow for optimized calibration towards these sources.

The SPAM imaging and deconvolution procedure is similar to the procedure used for the field-based calibration method by Cotton et al. (2004), which differs from the standard Cotton-Schwab algorithm by the temporary application of the facet-based phase corrections (AIPS tasks SPLIT and CLINV/SPLIT) to the visibility data for the duration of major CLEAN cycles on individual facets (AIPS tasks IMAGR and UVSUB). After deconvolution, facets are combined to form a single image of the full FoV (AIPS task FLATN). Because antenna-based phase corrections change very little between adjacent facets, the complete set of partly overlapping facet images combine into a continuous image of the FoV.

2.4 Applications

To demonstrate the capabilities of SPAM, we have defined three test cases based on observations with the VLA at 74 MHz (Kassim et al. 2007). In each test case, SPAM is used for ionospheric phase calibration and imaging of a VLSS visibility data set (Cohen et al. 2007), following the steps described in Section 2.3. In the first test case, SPAM was applied to simulated data to validate basic functionality in a controlled environment. In the next two test cases, SPAM was applied to visibility data from real observations under varying ionospheric conditions. We compare SPAM performance against self-calibration (SC) and field-based calibration (FBC) by analyzing the resulting images. The setup and results of these test cases are described in detail in the following sections.

2.4.1 Data selection, preparation and processing

In this Section, we describe how the visibility data sets for the three test cases were selected / constructed. Furthermore, we present details on how these data sets were processed by SPAM into calibrated images of the FoV.

Two VLSS observations, at pointing centers J0900+398 and J1300-208, respectively, have been picked from more than 500 available VLSS observations on the following criteria: (i) both fields contain a relatively large number of bright sources that can serve as calibrators, and (ii) the ionospheric conditions during the observations appear to be relatively good (J0900+398) and relatively bad (J1300-208). The presence of more than 5 bright sources of at least 5 Jy compensates for the relatively poor efficiency of the VLA 74 MHz receiving system (Kassim et al. 2007). The ionospheric conditions were derived from the apparent smearing of point sources in the images, due to residual phase errors after applying FBC. From experience, we adopted the qualification ‘good’ when the mean width of apparent point sources was at most 5''

larger than the intrinsic 80'' resolution, while for 'bad' conditions the mean point source width was larger by at least 15''. In terms of Strehl ratio R (Equation 2.6), 'good' and 'bad' conditions correspond with $R > 0.996$ and $R < 0.966$, respectively. Additionally, candidate fields were visually inspected for evidence of residual phase errors by the presence or absence of image artifacts near bright sources, which lead to the final selection of the two fields mentioned above.

The difference in observed ionospheric conditions between the two real data sets may be the result of the difference in array size and elevation of the target field. From the VLA site at +34 degrees declination, the J0900+398 field was observed in B-configuration (up to 11 km baselines) at relatively high elevation, while the J1300-208 field was observed in BnA-configuration (up to 23 km baselines) at relatively low elevation. For the J1300-208 observation, the array observed through the ionosphere at larger separations and along longer path lengths than for the J0900+398 observation, which is expected to result in both larger and less coherent phase rotations over the array.

Because both real data sets have been previously calibrated and imaged with FBC, the data sets were already partly reduced at the start of SPAM processing. Instrumental calibration was applied (including instrumental phase calibration, similar to Section 2.3.1), most RFI-contaminated data was flagged and the spectral resolution was reduced (see Cohen et al. 2007, for details), but no FBC has been applied yet. For the simulated data set, which is based on the real J0900+398 observations, the measured visibilities were replaced by noiseless model visibilities of an idealized sky, consisting of 91 bright point sources with peak fluxes (larger than 1 Jy) and positions as measured in the J0900+398 FBC image. For each point source, the corresponding model visibility phases were corrupted using the direction-dependent ionospheric phase model that was obtained with FBC to correct the real J0900+398 data.

FBC images of the two real data sets were available in the VLSS archive. For the simulated J0900+398 data set, an 'undisturbed' image was made before applying the ionospheric phase corruptions. All three VLSS data sets have been processed with SPAM, yielding both an SC image and an ionosphere-corrected SPAM image. Relevant details on the processing can be found in Table 2.1. For SC and SPAM imaging, we adopted most of the imaging-specific settings from FBC (like uniform weighting). Noticeable differences are the use of CLEAN boxes, a smaller pixel size and a different facet configuration.

By choosing a minimum SNR per time interval of 15 and a maximum peeling time interval of 4 minutes (see Equation 2.19), SPAM was able to peel ~ 10 sources in each of the real data sets. Lowering the SNR resulted in a much larger scatter in the peeling phases over time, or prevented peeling from converging at all. The peeling time upper limit was chosen to roughly match the spatial density of calibrator sources used in FBC. Determining phase corrections on a 4 minute time scale could result in undersampling the time evolution of ionospheric phase rotations. Note that this only applies to the faintest of the calibrator sources. The limitations on spatial and temporal sampling of the ionosphere are dictated by the given sensitivity of the VLA.

Because of the high SNR, all 91 sources in the simulated J0900+398 data set qualified for peeling at the highest time resolution of 10 seconds. To mimic a more realistic scenario for further SPAM processing, the number of calibrators was arbitrarily limited to 10. Generally, for all data sets, the images of peeling sources showed larger peak fluxes and less background structure than their counterparts in the SC image, although the contrast became less apparent for weaker and extended (mostly doubles) peeling sources.

As stated in Section 2.3.3, the number of peeling sources is fundamentally limited by the

Field name	VLSS J0900+398 (simulated)	VLSS J0900+398 (real)	VLSS J1300-208 (real)
Pixel size ^a	18.9''	18.9''	11.1''
Number of facets	347	243	576
Facet separation	1.18°	1.18°	0.62°
SPAM calibration cycles ^b	1	1	3
Peeling sources	10 ^c	11	9
KL model height	1000 km ^d	200 km	200 km
Fitted KL model terms	15	15	20 ^e
Rejected time intervals	0 / 464	25 / 464	86 / 484
Model fit phase RMS	3.0° ± 0.8°	21.3° ± 2.4°	23.2° ± 3.2°
Peeling corrections applied directly	no	yes	yes

^a The pixel size for all field-based calibration images is 20'.
^b Adding more cycles did not significantly improve the image quality.
^c Arbitrarily limited to mimic a more realistic scenario.
^d Increased to improve match with FBC phase screen.
^e In this case, 15 terms proved to be insufficient.

Table 2.1: Overview of processing parameters for the three data sets that are handled with SPAM as defined in the test cases.

requirement for a large positive number of degrees-of-freedom in the available visibility data. The minimal requirement is given in Equation 2.20. Typically, for the VLSS data sets, there were 25 active antennas, 12 frequency channels and 6 visibility intervals (of 10 seconds) in an average peeling interval of 1 minute. In our test cases, we typically peel 10 sources, which is much less than $25 \times 12 \times 6/2 = 900$, thereby satisfying the minimal requirement.

Due to the uncertainty in their optimal values, it is left to the SPAM user to specify the phase screen model order (the number of KL base vectors), the height h of the phase screen and the power-law exponent γ of the phase structure function. For the applications presented here, we used $h = 200$ km and $\gamma = 5/3$, which is compliant to the measured values given in Section 2.2.1 given the uncertainty in these values. For the simulated data set, we chose instead $h = 1000$ km to better match the corrupting FBC ionospheric phase model that is attached to the sky plane at infinite height. These values gave satisfactory results for the test applications presented here, but can be further optimized. The optimal model order was found to lie in the range of 15 to 20 terms, which is 1.5 to 2 times the number of available peeling sources. Increasing or decreasing the model order caused the model fit to be less accurate or more problematic in terms of convergence.

For both the simulated and real J0900+398 data sets, no improvement in background noise was observed by adding a second calibration cycle after the first. This indicates fast convergence of the SPAM calibration method for quiet ionospheric conditions, where the initial self-calibration is already close to the best achievable calibration of SPAM. For the real J1300-208 data set, adding up to a third calibration cycle did improve over the previous cycles.

2.4.2 Phase calibration accuracy

For the simulated J0900+398 data set, the absolute accuracy of ionospheric calibration can be determined by a direct comparison between the corrupting FBC phase screen and the correcting SPAM phase screen. For this purpose, phase corruptions and corrections were calculated from the models for a hexagonal grid of 342 viewing directions within the FoV. Per viewing direction, the RMS phase error was calculated by differencing of the phases from both models and averaging over all time stamps and baselines. The result is depicted in Figure 2.6.

For areas near the calibrators and in the center of the field in general, there is a relatively good match between the input and output model, with typical RMS phase errors $\lesssim 5$ degrees. The absence of calibrator sources south-west of the field center still results in relatively accurate predictions by the SPAM model. In the direction of peeling sources, the measured RMS phase error can be split into a contribution from inaccuracies in the peeling process and a contribution from imperfect model fitting. The latter is approximately 3 degrees (Table 2.1), therefore the RMS phase error introduced by peeling is $\lesssim 4$ degrees. Considering the model setup, the only possible source of error is contamination from other sources while peeling (which appears to happen despite the initial subtraction of the SC model).

Overall, the change in model base from the corrupting FBC model (5 Zernike polynomials) to the correcting SPAM model (15 KL vectors) has a constant accuracy over large parts of the FoV. Towards some parts of the edge of the field the phase errors are substantially larger, up to 20–25 degrees at worst. This agrees with the different asymptotic behaviour towards large radii of the Zernike model (diverge to infinity) and the KL model (converge to zero) in the absence of calibrators. The presence of calibrator sources near the edge (such as the source on the North-East edge of the field) leads to a better local match between corrupting ionosphere and correcting

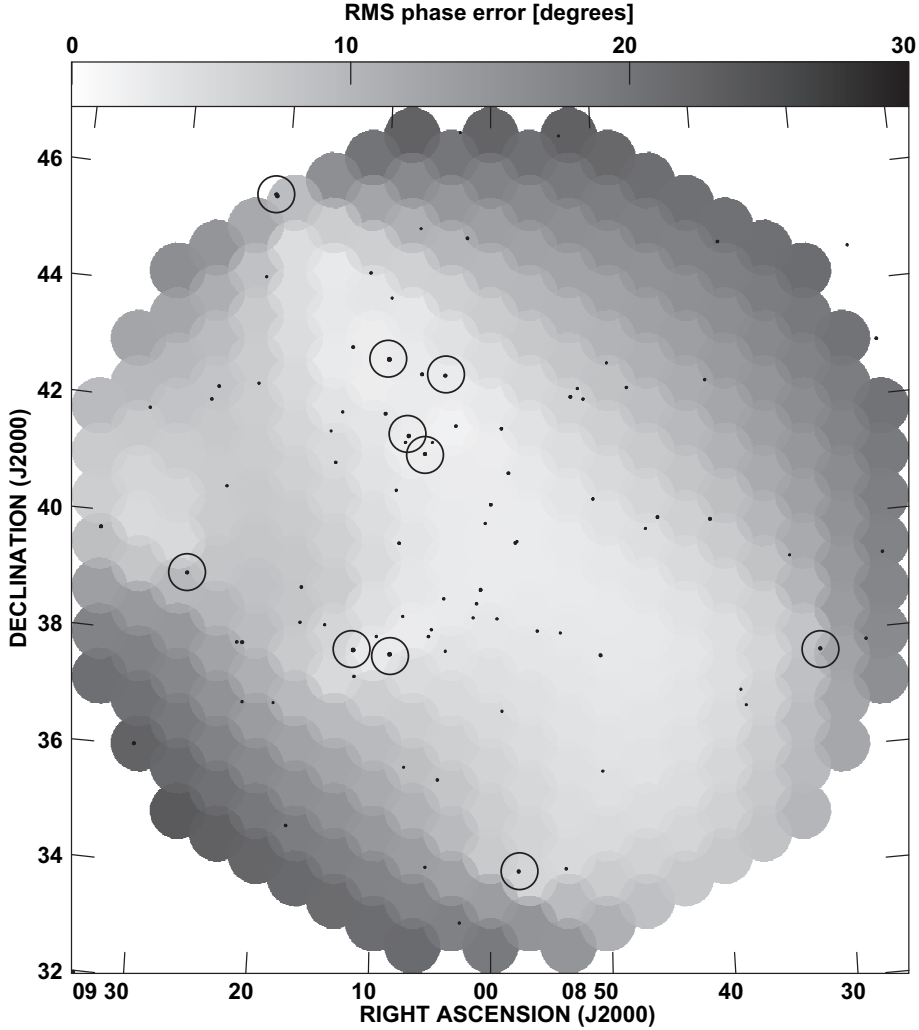


Figure 2.6: The grayscale map represents the residual phase RMS between the distorting and correcting ionospheric phase models across the primary beam area of a simulated observation, averaged over baselines and time. The phase RMS was calculated for a hexagonal grid of viewing directions across the FoV. Each viewing direction is depicted by a small circular area. Overplotted is a contour map of the point sources as seen in the SPAM image (which extends slightly beyond the grid of circles). The 10 peeling sources are marked by circles. The correspondence between the models is largest near the calibrator sources and over a large part of the inner primary beam. The discrepancy is largest near the South-East and North-West borders, away from the calibrators.

model.

For the real observations, in the absence of external sources of information (e.g., GPS measurements), it is not possible to derive the absolute accuracy of ionospheric calibration from the observations themselves. Instead, the residual RMS phase error of the model fit to the peeling phases is used as an relative indicator for calibration accuracy over time. For both the real J0900+398 and J1300-208 data sets, the residual RMS phase error of ~ 22 degrees is much larger than for the simulated data. This already excludes rejected time stamps with exceptionally large RMS values. By inspecting model fits on individual time stamps, we found that there are often a few pierce point phases that deviate significantly more from the fitted model than most neighbouring points. These errors do not appear to be antenna-based instrumental errors, because peeling solutions for the same antenna towards other calibrator sources do not deviate in the same manner. Typically, these deviating points persist for a few time stamps before disappearing. The ionosphere may be responsible for these very small scale deviations. Another possibility is that the peeling solutions are (sometimes) noisy due to limitations in source SNR.

2.4.3 Background noise

In this and the next sections, we revert to analyzing image properties for an indirect, relative comparison between the different calibration techniques. In the presence of residual phase errors, part of the image background noise level consists of residual sidelobes after CLEANing. The local sidelobe noise increases with both the RMS phase error and the local source flux density. When measured over a large image area, the mean sidelobe noise depends mainly on RMS phase error. For all relevant output images, the mean image noise σ was determined by fitting a Gaussian to the histogram of image pixel values from the inner quarter radius of the FoV (AIPS task IMEAN). Note that these images have not been corrected for primary beam attenuation. The results are given in Table 2.2.

Because no noise was added to the simulated J0900+398 data set, the resulting image noise of $3.0 \text{ mJy beam}^{-1}$ in the undisturbed image is caused by incomplete UV coverage and inaccuracies in the imaging process (see Section 2.3.2), limiting the dynamic range to $\sim 10^4$. The local noise is highest near the sources, but significantly less near the brightest 10 sources with dedicated facets centered on their peak position. The SC and SPAM images from this data set were created using the same facet configuration. The SC image noise of $10.2 \text{ mJy beam}^{-1}$ is 3.4 times as high as the undisturbed image noise, therefore dominated by phase error induced sidelobe noise. The SPAM image noise of $6.7 \text{ mJy beam}^{-1}$ is a significant improvement over the SC image, but still 2.2 times as high as in the undisturbed image. The local noise in the SC and SPAM images has increased most apparently near bright sources as compared to the undisturbed image, which confirms the presence of residual phase errors after calibration.

For the real J0900+398 data set, both the SC and SPAM images have an image noise of $\sim 70 \text{ mJy beam}^{-1}$. The SPAM image noise is slightly lower than SC. The local noise in the SC image is higher near bright sources. This is not the case in the SPAM image, which must be a direct result of an improved calibration accuracy near these sources. The FBC image noise for this data set is ~ 20 percent higher, a combination of a higher average noise over the FoV and higher local noise near bright sources.

For the real J1300-208 data set, the SPAM image has the same image noise as for the real J0900+398 data set, with no apparent increase near bright sources. At the same time, the noise levels in the SC and FBC images have increased with 30 and 35 percent, respectively. The noise

Field name	VLSS J0900+398 (simulated)	VLSS J0900+398 (real)	VLSS J1300-208 (real)
Mean background noise σ [mJy beam ⁻¹]:			
Undisturbed	3.0	–	–
SC	10.2	71	92
FBC	–	87	118
SPAM	6.7	67	68
Number of sources with a peak flux larger than 5σ :			
Undisturbed	91	–	–
SC	91	393	374
FBC	–	310	285
SPAM	91	372	392
5σ source fraction with an NVSS counterpart within $80''$:			
Undisturbed	1.	–	–
SC	1.	0.83	0.60
FBC	–	0.86	0.74
SPAM	1.	0.97	0.97

Table 2.2: Overview of results from calibrating and imaging three test case data sets with no ionosphere (Undisturbed), self-calibration (SC), field-based calibration (FBC) and SPAM.

in the SC image is highest near the bright sources (see Figure 2.7). The FBC noise is highest near the brightest source and remains high in the rest of the image. The significant increase of the average FBC noise level indicates a dependence on ionospheric conditions, and therefore on calibration accuracy. The SPAM image noise appears to have little or no dependence on varying ionospheric conditions.

2.4.4 Source properties

The presence of residual phase errors changes the apparent distribution of flux of a source (see Section 2.2.2). In the time-averaged image, sources may appear offset from their intrinsic position, may suffer from smearing or deformation, and sidelobes may be misidentified as sources. Comparing the properties of the same sources in differently calibrated images allows for a relative comparison of the performance of the different calibration techniques.

To allow for comparison of source properties, we applied the source extraction tool BDSM (Mohan 2008) on all relevant images. BDSM performed a multiple 2-dimensional Gaussian fit on islands of adjacent pixels with amplitudes above a specified threshold based on the *local* image noise σ_L in the image. Multiple overlapping Gaussians were grouped together into single sources. We applied BDSM to all images, using the default extraction criteria, except for the following: a source detection requires at least 4 adjacent pixel values above $2.5\sigma_L$, with at least one pixel value above $4\sigma_L$.

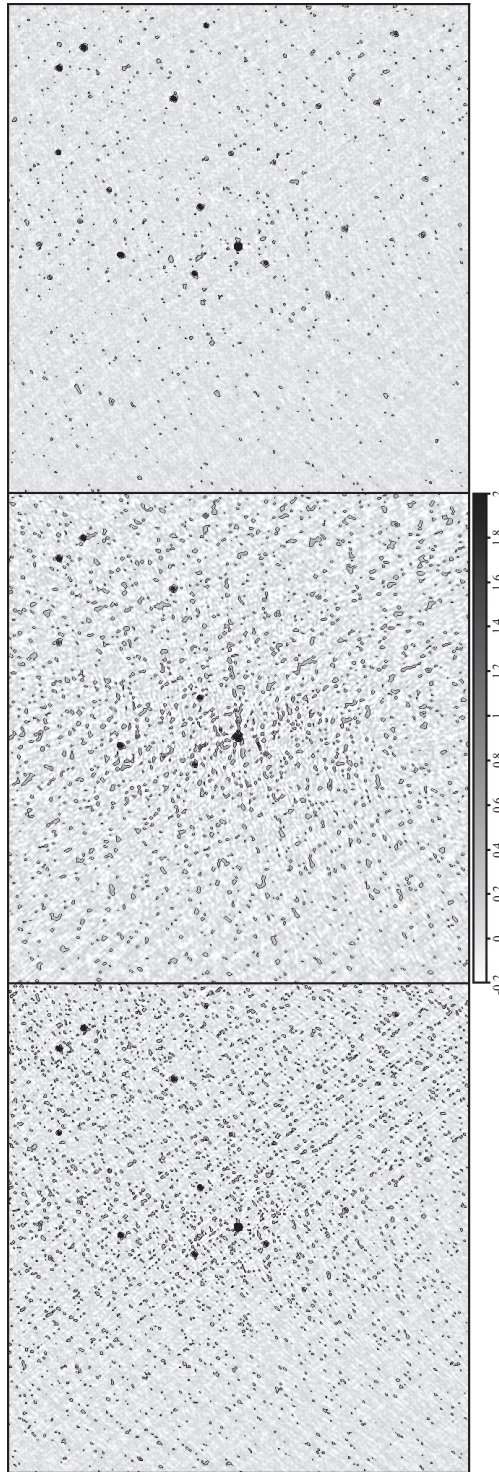


Figure 2.7: Greyscale plots of a 3.5×3.5 square degree area in the VLSS J1300-208 field centered on the bright (40 Jy) point source 3C 283. All three images have contours (black lines) overplotted at [0.15, 0.48, 0.83, 1.16, 1.50] Jy. *Left:* Image after self-calibration, *middle:* image after field-based calibration, and *right:* image after SPAM calibration.

Source counts

Due to the non-Gaussian character of the phase-induced sidelobe noise, the source catalogs will contain spurious detections. To suppress these, we removed sources with a peak flux smaller than 5σ from the catalogs. The remaining number of catalog entries are listed in Table 2.2. Additionally, each catalog was cross-associated against the NVSS catalog, which has a slightly higher resolution ($45''$). For an average spectral index of -0.8 , the NVSS detection limit is at least 10 times lower than for the VLSS. At the risk of missing an incidental ultra-steep spectrum source, we determined the source fraction that has an NVSS counterpart within an $80''$ radius (one VLSS beamsize), which are also listed in Table 2.2.

For the simulated J0900+398 data set, all 91 input sources are detected and matched against NVSS counterparts, regardless of the calibration method. Due to the low noise levels and the lower limit of 1 Jy on the input source catalog, all sources are effectively $\gtrsim 100\sigma$ detections. None of the sources had more than one Gaussian fitted to it, despite the freedom to do so.

For the real J0900+398 data set, the higher σ in the FBC image is reflected in a smaller number of source detections as compared to SC and SPAM. SC detects slightly more sources than SPAM, despite the slightly higher σ . However, there is a very large fraction of sources in the SPAM catalog that has an NVSS counterpart, significantly larger than for both the SC and FBC catalogs. This suggests that the SPAM catalog is much less contaminated by false detections than the SC and FBC catalogs, resulting in a larger absolute number of true detections.

This is further strengthened by the results from the real J1300-208 data set. For this test case, the SPAM image has the largest number of source detections. Again, the SPAM catalog has the largest fraction of associations with the NVSS catalog, the same fraction as with the J0900+398 data set. In contrast, the fraction of NVSS counterparts for SC and VLSS have both gone down. This is best explained by an increase in (non-Gaussian) sidelobe noise in the image background due to calibration errors, which corresponds with the observed increase in σ .

Source peak fluxes

The presence of residual phase errors after calibration can cause an unresolved source shape to deviate from a point source shape. The source flux is redistributed over a larger area and the peak flux of the source drops. At $80''$ resolution, most sources in a VLSS field are unresolved. Therefore, a mean increase of source widths over the point source width is a direct measure of ionospheric conditions. This argument was used in the pre-selection of data sets for our test cases.

For significant source deformations or low SNR sources, determination of the shape of individual sources is subject to large uncertainties (e.g., Condon 1997). Because determination of peak fluxes is much more robust, we use these for a relative comparison of calibration accuracy. Starting with the original catalogs as produced by BDSM, we associate sources between the undisturbed, FBC, SC and SPAM catalogs that lie within $80''$ of the same NVSS source and has a peak flux larger than 5σ in at least one of the two catalogs.

For the simulated J0900+398 data set, the true peak fluxes of all 91 sources are known. A comparison between peak fluxes from the undisturbed image and the input catalog identifies a small (< 1 percent) CLEAN bias of $3.6 \text{ mJy beam}^{-1}$ (e.g., Condon et al. 1994, 1998; Becker et al. 1995). Ignoring the image noise dependency of CLEAN bias, we applied this small correction to the peak fluxes in the undisturbed, SC and SPAM source catalogs before proceeding. Figure 2.8 shows a comparison of the measured-to-input peak flux ratios for sources in the SC

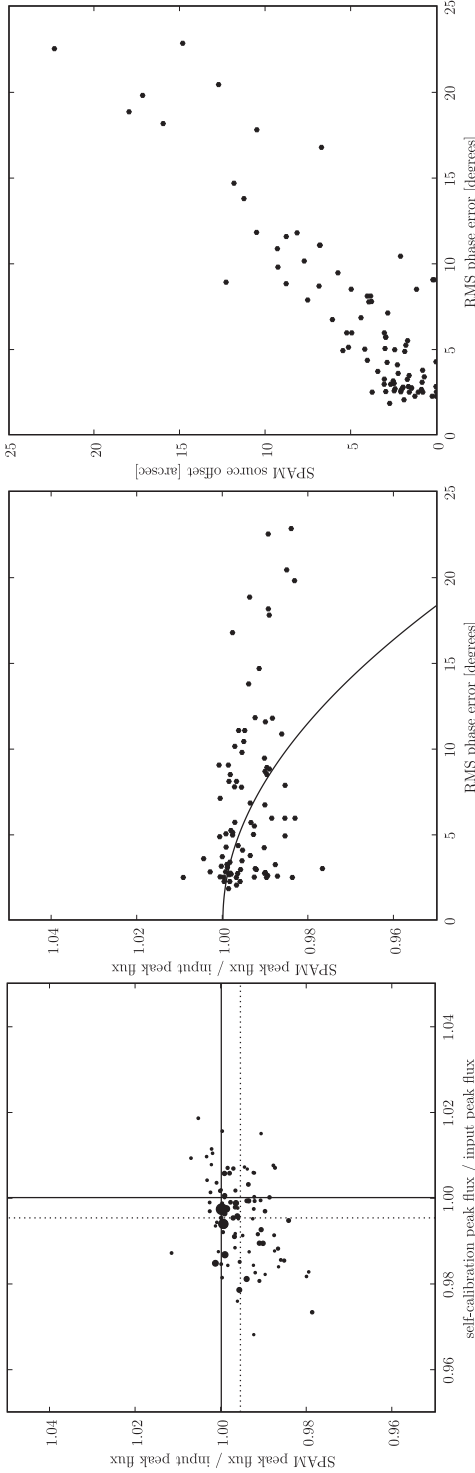


Figure 2.8: Peak flux ratios in the simulated J0900+398 field. *Left:* Peak fluxes of 91 extracted sources were measured in the self-calibration image and the SPAM image, corrected for a small CLEAN bias and divided by the input model peak fluxes. The size of each dot scales with the input model peak flux, ranging from 1.02 to 26.7 Jy. Ideally (without phase errors), the peak flux ratios would be scattered around *one* (solid lines) due to image noise dependent errors in the peak flux determination. Instead, the peak flux ratio distributions along the x- and y-axis are centered around 0.995 and 0.996, respectively (dotted lines), which is a direct result of the residual phase errors. The smaller and larger scatter in distribution of SPAM- and self-calibration peak flux ratios is consistent with peak flux determination inaccuracies due to image background noise levels. *Middle:* Peak flux ratios from the SPAM image as compared to the input model sources, plotted as a function of the residual RMS phase error after SPAM calibration. Overplotted is the theoretical Strehl ratio (solid line) as given in Equation 2.6. For larger RMS phase errors, the measured peak flux ratios do not follow the theoretical Strehl ratio curve. This indicates that systematic phase errors dominate the larger RMS phase errors. *Right:* Same peak flux ratios as middle plot, now as a function of absolute position offset between extracted sources in the SPAM image and the input model (see Figure 2.11). The presence of a strong correlation indicates that residual phase gradients dominate the larger RMS phase errors.

and SPAM images. The mean peak flux ratio for both images is approximately equal and just slightly smaller than one. The larger scatter in the SC peak fluxes is consistent with a higher σ . Using Equation 2.6, the random part of the mean RMS phase error for both SC and SPAM is estimated at 5 to 6 degrees. This value is comparable to the observed RMS phase error over large parts of the SPAM image (Section 2.4.2).

To study the nature of residual RMS phase errors after application of SPAM, we plot the RMS phase errors at the source positions from Figure 2.6 against SPAM-to-input peak flux ratios (Figure 2.8). For Gaussian random phase errors, the peak flux ratio is expected to decrease with increased RMS phase error as described in Equation 2.6. However, the discrepancy between the data points and Equation 2.6 indicates that for larger RMS values the phase errors are predominantly systematic rather than random.

For the real J0900+398 data set, Figure 2.9 shows a comparison of peak fluxes for associated sources in the SC, FBC and SPAM catalogs. There is a good match between peak fluxes measured in the SC and SPAM catalogs. For high SNR sources with a peak flux above 1 Jy, the SPAM peak fluxes match on average within 1 percent with the SC peak fluxes. Similarly, SC and SPAM peak fluxes are on average 10 percent higher than FBC peak fluxes. The systematic increase of peak fluxes for SC and SPAM as compared to FBC for many more than the calibrator sources denotes a more accurate calibration over large parts of the FoV. Towards the low flux end, source detections are slightly biased towards the image with the highest noise level, which is the FBC image.

Figure 2.10 shows the same comparison of peak fluxes for the real J1300-208 data set. For high SNR sources with a peak flux above 1 Jy, the SC peak fluxes are by far the smallest, while FBC and SPAM peak fluxes are on average higher by 15 and 24 percent, respectively. The relative loss of peak flux in the SC image is a clear indication of the break-down of the assumption of isoplanaticity across the FoV. Under the conditions that clearly need direction-dependent corrections, the SPAM peak fluxes are on average 7 percent higher than the FBC peak fluxes.

Astrometry

When the time-average of residual phase errors towards a source contains a non-zero spatial gradient, the source will appear to have shifted its position in the final image (see Section 2.2.2). This gradient may indicate a limitation of the calibration model to reproduce the ionospheric phase corruptions (e.g., in the absence of nearby calibrators), but may also be introduced by the peeling process. The latter occurs when a peeling source is re-centered to the wrong catalog position (see Section 2.3.3). Because such an error propagates into the calibration model, many sources in the vicinity of the peeling source may also suffer from a systematic astrometric error.

For the simulated data set, the peak positions of sources as determined by BDSM were compared against the positions of counterparts in the input model. For the real data sets, we compared against the NVSS catalog instead. When comparing against NVSS positions, apparently large position offsets may occur due to resolution differences and spectral variation across the source. Averaged over a large number of sources, these offsets should have no preferential orientation. In contrast, a residual phase gradient in a certain viewing direction is expected to cause systematic offsets for groups of sources in a certain preferential direction.

For the simulated J0900+398 data set, Figure 2.11 shows that the positions for both SC and SPAM are accurate to within $\sim 10''$, except for a small tail of ~ 15 SPAM sources that have

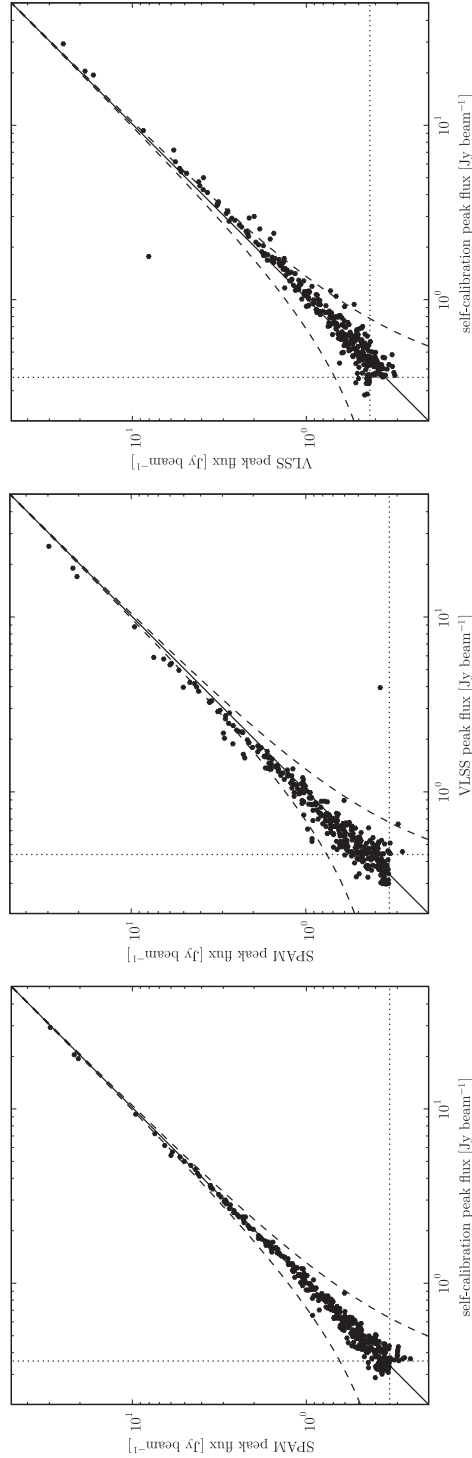


Figure 2.9: Peak fluxes in the real J0900+398 field *Left:* Peak flux comparison for 367 sources detected in both the self-calibration and SPAM images. The straight diagonal line represents equality, the dashed lines represent $3\sigma_C$ deviations (where σ_C is the combined noise level from both images), and the dotted lines indicate the 5σ detection limit. For bright sources (peak fluxes $\gtrsim 1 \text{ Jy beam}^{-1}$), the average peak flux ratio is 1.00. *Middle:* Same for 329 sources in the field-based calibration (VLSS) and SPAM images. The average bright peak flux ratio of SPAM over field-based calibration is 1.10. *Right:* Same for 313 sources in the self-calibration and field-based calibration (VLSS) images. The average bright peak flux ratio of self-calibration over field-based calibration is 1.10. In all plots, the image noise causes a larger scatter in the peak flux determinations of faint sources ($\lesssim 1 \text{ Jy beam}^{-1}$) and consequently, a selection bias towards positively enhanced peak fluxes that increases with image noise.

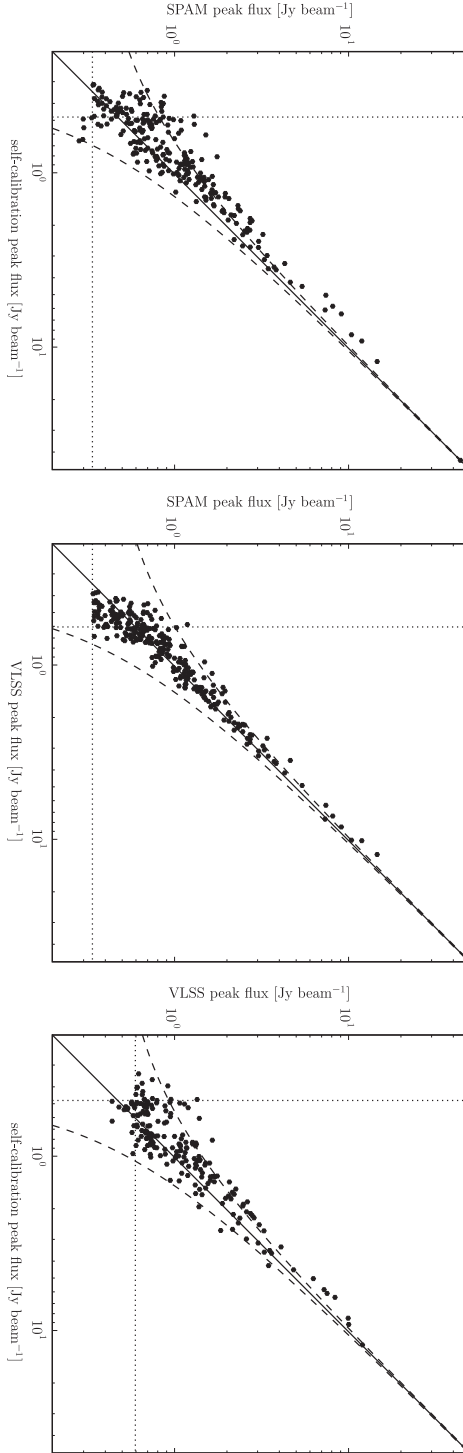


Figure 2.10: Peak fluxes in the (real) J1300-208 field. *Left:* Peak flux comparison for 247 sources detected in both the self-calibration and SPAM images. For bright sources (peak fluxes $\gtrsim 1$ Jy beam $^{-1}$), the average peak flux ratio of SPAM over SC is 1.24. *Middle:* Same for 278 sources in the field-based calibration (VLSS) and SPAM images. The average bright peak flux ratio of SPAM over field-based calibration is 1.07. *Right:* Same for 202 sources in the self-calibration and field-based calibration (VLSS) images. The average bright peak flux ratio of field-based calibration over self-calibration is 1.15.

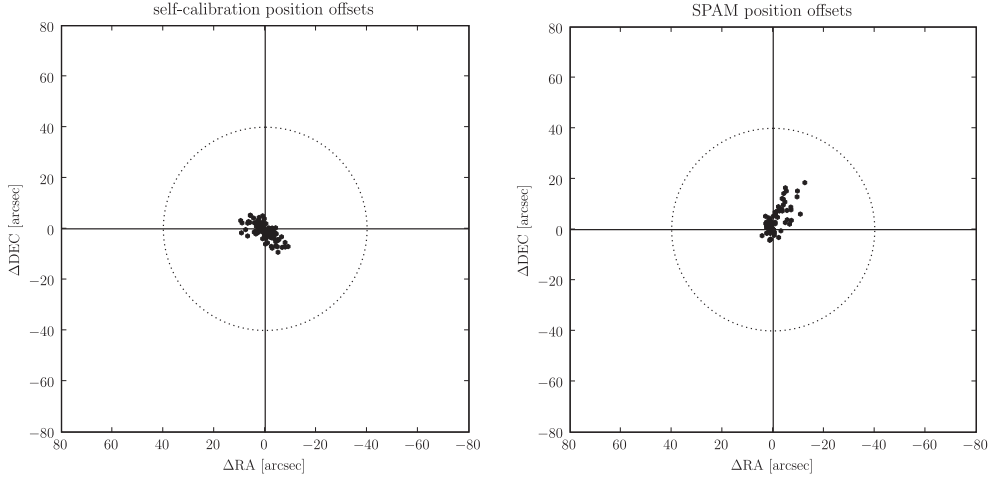


Figure 2.11: Position offsets in the simulated J0900+398 field: *Left:* Offsets between the measured source positions in the self-calibration image as compared to the input model. *Right:* Same for the SPAM image. In both cases, the distribution around the origin is non-Gaussian. For the SPAM image, the tail of points extending roughly northwards indicates the presence of persistent phase gradients in local parts of the SPAM image. All source position offsets fall well within the size of the 80'' restoring beam (dotted line).

somewhat larger offsets. These sources are all positioned near the edge of the FoV, where the RMS phase error is large (Figure 2.6). Figure 2.8 also confirms this by the clear correlation between RMS phase error and absolute position offsets.

For the real J0900+398 data set, the source position offsets for SC, FBC and SPAM relative to NVSS catalog positions are plotted in Figure 2.12. The larger scatter as compared to the simulated J0900+398 data set can be the (combined) result of less accurate position measurements due to higher image noise, resolution and spectral differences between the observations and the NVSS catalog or larger residual RMS phase errors after calibration. The observed scatter for SC is centered around a point that is offset from the origin by $\sim 5''$, which is either caused by inaccuracies in the initial sky model or during the self-calibration process (Section 2.3.2). The scatter of both FBC and SPAM offsets is centered close to the origin. The RMS of the scatter around the mean position offset is $10.5''$ for both FBC and SPAM (despite the apparently larger scatter for SPAM, which is due to a larger number of data points), both smaller than the $11.9''$ for SC.

For the real J1300-208 data set, the source position offsets for SC, FBC and SPAM relative to NVSS catalog positions are plotted in Figure 2.13. The position scatter for all three methods is significantly larger than for the real J0900+398 data set, and all suffer from systematic position offsets in varying degrees of severity. The position offsets in the SC image have a seriously distorted distribution, which includes a large tail of points that extends roughly southwards. This indicates the presence of varying systematic source offsets over the whole FoV. The distribution of position offsets in the FBC image is more compact but also asymmetric, and is approximately centered around a point that is $\sim 10''$ offset in northward direction from the origin. A large number of the SPAM position offsets are clustered near the origin, similar to the real J0900+398

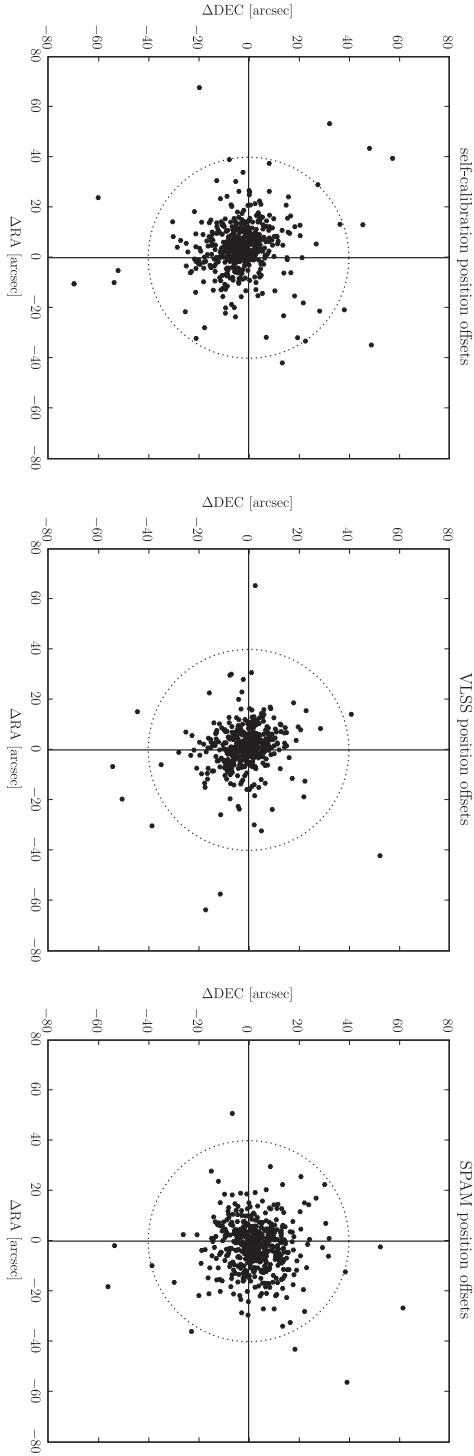


Figure 2.12: Position offsets in the real J0900+398 field *Left*: Offsets between the measured source positions in the self-calibration image as compared to the NVSS catalog. *Middle*: Same for the field-based calibration (VLSS) image. *Right*: Same for the SPAM image.

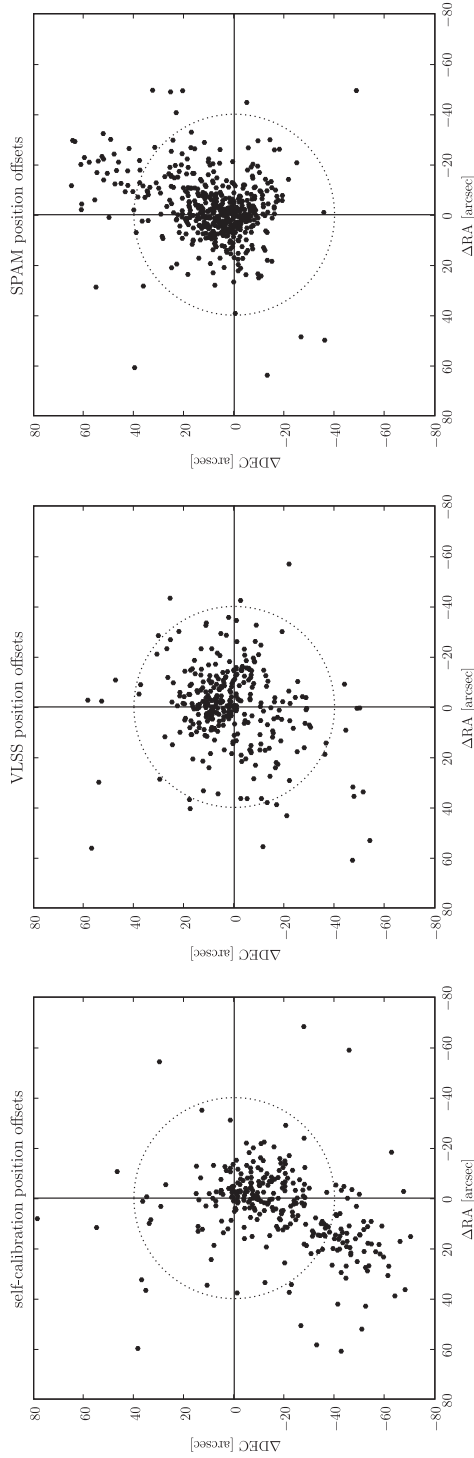


Figure 2.13: Position offsets in the real J1300-208 field: *Left:* Offsets between the measured source positions in the self-calibration image as compared to the NVSS catalog. *Middle:* Same for the field-based calibration (VLSS) image. *Right:* Same for the SPAM image.

data set, but there is an additional tail of points that runs roughly northwards. The RMS of the scatter around the mean position offset is $20.7''$, $16.5''$ and $14.8''$ for SC, FBC and SPAM, respectively, which confirms the apparently strongest clustering of points in the SPAM position offset plot.

Systematic position offsets in the images can be reduced by distortion and regridding of the images. To this purpose, Cohen et al. (2007) fit a fourth order Zernike polynomial to the (time constant) position offsets of typically more than 100 sources in the FBC images of the VLSS. They estimate that, after correction, the final residual position error in the full VLSS catalog due to the ionosphere is $\lesssim 3''$ in both RA and DEC.

2.5 Discussion and conclusions

The SPAM method for ionospheric calibration has been successfully tested on one simulated and two carefully selected visibility data sets of 74 MHz observations with the VLA (taken from the VLSS; Cohen et al. 2007). From the results of these test cases, we draw the following conclusions:

(i) A proof-of-concept is given for several different techniques that were incorporated in SPAM calibration. The peeling technique (Noordam 2004) was successful in providing relative measurements of ionospheric phase rotations in the direction of several bright sources in the FoV. The Karhunen-Loève phase screen (van der Tol & van der Veen 2007) at fixed height was able to combine these measurements into a consistent model per time stamp. For relatively bad ionospheric conditions, it was demonstrated that the ionospheric calibration cycle (repeated ionospheric calibration and subsequent imaging; Noordam 2004) converges within a few iterations to a calibration of similar accuracy as under relatively good ionospheric conditions (for which one iteration was sufficient).

(ii) Ionospheric calibration with SPAM is more accurate than the existing self-calibration (e.g., Pearson & Readhead 1984) and field-based calibration (Cotton et al. 2004) techniques. Even for relatively compact array configuration like VLA-B and BnA, significant improvements in image quality are obtained by allowing for higher-order (i.e., more than a gradient) spatial phase corrections over the array in any viewing direction. In the resulting images, we obtained dynamic range improvements of 5 to 45 percent and 70 to 80 percent under relatively good and bad ionospheric conditions, respectively.

(iii) Although the mean astrometric accuracy of source positions in SPAM images is similar to or better than for self-calibration and field-based calibration, systematically larger astrometric errors are present in regions of the output images of all calibration methods. This is caused by a shortage of available calibrators in these regions and positional inaccuracies in the reference source catalog used for calibration.

The 65 mJy beam^{-1} noise levels in the SPAM images match the lowest noise levels of the more than 500 images that define the VLSS survey. A potential reduction of the average noise level from $100 \text{ mJy beam}^{-1}$ to 65 mJy beam^{-1} for the full VLSS survey would significantly increase the number of source detections from $\sim 70,000$ to about 120,000 (an increase of ~ 75 percent), but also it would greatly enhance virtually every science goal. For example, using the radio luminosity function for high-luminosity radio galaxies from Jarvis et al. (2001), the estimated number of detectable HzRGs in the VLSS would increase by 65 percent, but also the maximum redshift would increase. For a luminous radio galaxy with a luminosity of $2 \times$

$10^{28} \text{ W Hz}^{-1} \text{ sr}^{-1}$ at 74 MHz, the redshift limit would rise from $z = 5.7$ to $z = 6.8$. Another example is the detection and study of cluster radio halos. Using available halo population models (Enßlin & Röttgering 2002; Cassano et al. 2006), the anticipated noise reduction would roughly double the number of detectable halo systems.

For the VLSS, the estimated theoretical thermal noise level of 35 mJy beam^{-1} is still a factor of two lower than the average background noise level of $\sim 65 \text{ mJy beam}^{-1}$ in the SPAM images. From inspection of the SPAM images we cannot identify an obvious single cause for this. Therefore, similar to Cohen et al. (2007), we expect the remaining excess noise to be the combined result of several different causes, including residual ionospheric phase errors after SPAM calibration, but also residual RFI, collective sidelobe noise from many non-deconvolved sources (too faint or outside the FoV) and variable source amplitude errors (e.g., due to pointing errors and non-circular antenna beam patterns; see Bhatnagar et al. 2008).

The SPAM test results indicate that the ionospheric calibration accuracy may be further improved. The typical model fit RMS phase error per antenna of 20 to 30 degrees for real data sets is much larger than the 3 degrees for the noiseless simulated data set. There are several possible sources of error, either in the peeling phase corrections or the ionospheric phase model. Noise in the visibilities (either thermal or non-thermal), contamination from other sources, inaccuracies in the peeling source model and undersampling of the fastest phase fluctuations are factors that degrade the accuracy of peeling. Also, the ionospheric phase screen model may be a poor representation of reality, either because it is incomplete (e.g., absence of vertical structure) or the fixed model parameters are chosen poorly (e.g., screen height, spectral index of phase fluctuations). Several of these issues will be addressed in future work (Section 2.6).

The potential problems with the peeling technique raises the question whether one should use alternative methods. Apart from the precautions described in Section 2.3.3, we have found little means to improve the accuracy of the peeling process for single sources any further. One unexplored option is to peel sources in groups, e.g. identify isoplanatic patches of sky with a large enough total flux density from multiple sources. Two possible alternative approaches to peeling are: (i) simultaneous self-calibration towards multiple sources in the FoV, or (ii) fitting the ionosphere model directly to the visibilities rather than using peeling as an intermediate step. Although these alternative approaches have not been tested by us in practice, we anticipate little improvement over our current accuracy. Theoretically, iterative peeling converges to the same solution as simultaneous self-calibration (van der Tol et al. 2007). A direct fit of the ionosphere model to the visibilities is, similar to self-calibration, biased towards accurate solutions in the direction of the apparently strongest source in the FoV. Although not conclusive for this approach, tests with SPAM show that using even a moderate flux-based weighting into the ionospheric phase model fitting of peeling phase corrections introduces a strong bias towards the brightest source, while calibration accuracy towards other peeled sources degrades severely.

For the existing and future large low-frequency radio interferometer arrays such as VLA-A, GMRT, LOFAR, LWA and SKA, the need for a direction-dependent ionospheric calibration method is evident. Based on the results presented in this chapter, it is difficult to draw quantitative conclusions on the achievable calibration accuracy for these arrays. If a SPAM-like calibration algorithm is to be used in a very high signal-to-noise observing regime under quiet to moderate ionospheric conditions, it seems likely that residual RMS phase errors in the order of a few degrees could be achieved, comparable to the SPAM results on the simulated VLSS data set.

When relying on the array itself to provide the necessary measurements to constrain iono-

spheric correction models, ionospheric calibration requires an array layout and sensitivity that allows for sampling the ionosphere over the array at the relevant spatial scales and time resolution. The spatial sampling is determined by the instantaneous pierce point distribution (or more general, the distribution of lines-of-sight through the ionosphere), which depends on the array layout and the detectable calibrator constellation. For future design of low-frequency arrays, it is recommended to optimize the array layout not just for scientific arguments (in general, centrally dense and sparse outside for good UV coverage), but also for ionospheric calibrability (in general, both uniform and randomized).

2.6 Future work

To test the robustness and limitations of the method, it is necessary to apply SPAM calibration on a wide variety of data sets at different (low) frequencies, obtained with different arrays under different ionospheric conditions. Our highest priority is to test SPAM on observations from the largest existing LF arrays; the VLA in A-configuration and the GMRT. Data for these tests have been obtained and tests are currently in progress. One important possible limitation is the use of a 2-dimensional phase screen to represent the ionosphere. We plan to expand the SPAM model by including multiple screens at different heights and compare the resulting image properties against the current single screen model.

Another limitation of the current implementation is the absence of restrictions on the time behaviour of the model. Antenna-based peeling phases clearly show a coherent temporal behaviour, which is likely to exist for physical reasons. This could be used to reduce the number of required model parameters and suppress the noise propagation from the peeling solutions. We are currently investigating the possibilities of forcing the SPAM model to be continuous in time.

Several of us are currently involved in setting up a simulation framework in which one has full control over the sky emission, ionospheric behaviour and array characteristics when generating artificial low-frequency observations. Like in the test case on simulated data presented in Section 2.4, this allows for direct and quantitative comparison between the distorting ionosphere model and the recovered ionospheric phase model by SPAM. We plan to use this setup to further test optimize SPAM calibration for a broad range of ionospheric conditions.

Acknowledgements. The authors would like to thank Rudolf Le Poole, Reinout van Weeren, Sridharan Rengaswamy, Amitesh Omar, Mamta Pandey, Oleksandr Usov, James Anderson, Ger de Bruyn, Jan Noordam, Maaijke Mevius, Dharam Vir Lal, C.H. Ishwara-Chandra, A. Pramesh Rao, Jim Condon and Juan Uson for useful discussions. Special thanks to Mark Kettenis for fast bug fixing and implementation of new functionality in ParseITongue, and Niruj Ramanujam Mohan for similar performance on BDSM. The authors also thank the anonymous referee for useful comments and suggestions. HTI acknowledges a grant from the Netherlands Research School for Astronomy (NOVA). SvdT acknowledges NWO-STW grant number DTC.5893. This publication made use of data from the Very Large Array, operated by the National Radio astronomy Observatory. The National Radio Astronomy Observatory is a facility of the National Science Foundation operated under cooperative agreement by Associated Universities, Inc.

2.7 Appendix: Derivation and interpolation of the KL base vectors

This Section contains an outline of the derivation and interpolation of the Karhunen-Loève (KL) base vectors that are used to describe the ionospheric phase screen in SPAM. The KL technique is adopted from the work by van der Tol & van der Veen (2007). For a given stochastic model of spatial electron density fluctuations in the ionosphere, the differential phase rotation on rays of passing radio waves can be described by a (zero mean) isotropic phase screen $\phi(\mathbf{p})$ with a given spatial covariance function

$$C_{\phi\phi}(r) = \langle \phi(\mathbf{p})\phi(\mathbf{p} + \mathbf{r}) \rangle, \quad (2.25)$$

where $\langle \dots \rangle$ denotes the expected value and $r = |\mathbf{r}|$ is the length of vector \mathbf{r} . In Kolmogorov turbulence theory, a phase structure function is defined as (Equation 2.5)

$$D_{\phi\phi}(\mathbf{r}) = \langle [\phi(\mathbf{p}) - \phi(\mathbf{p} + \mathbf{r})]^2 \rangle. \quad (2.26)$$

The structure function and the covariance function are related through

$$D_{\phi\phi}(r) = 2 [C_{\phi\phi}(0) - C_{\phi\phi}(r)] \Leftrightarrow C_{\phi\phi}(r) = C_{\phi\phi}(0) - \frac{1}{2} D_{\phi\phi}(r), \quad (2.27)$$

where $C_{\phi\phi}(0) \equiv \sigma_\phi^2$ is the phase variance. The phase structure function of a plane wave that passed through a turbulent layer is found to behave as a power-law over a large range of spatial scales (see Section 2.2.1)

$$D_{\phi\phi}(r) = (r/r_0)^\gamma, \quad (2.28)$$

where r_0 is a measure of the scale size of phase fluctuations and γ is the power-law slope.

Because the domain of \mathbf{p} is a limited set of P discrete ionospheric pierce points \mathbf{p} , we switch to matrix notation. The elements of the $(P \times P)$ phase covariance matrix are given by

$$\mathbf{C}_{\phi\phi}[i, j] = C_{\phi\phi}(r_{ij}), \quad (2.29)$$

with $\mathbf{p}_i, \mathbf{p}_j \in \{\mathbf{p}\}$ and $r_{ij} = |\mathbf{p}_i - \mathbf{p}_j|$. The symmetric covariance matrix can be decomposed into

$$\mathbf{C}_{\phi\phi} = \mathbf{U} \mathbf{\Lambda} \mathbf{U}^T, \quad (2.30)$$

where the columns of $(P \times P)$ matrix \mathbf{U} contain the orthonormal eigenvectors of $\mathbf{C}_{\phi\phi}$, \mathbf{U}^T is the transpose of \mathbf{U} and the $(P \times P)$ diagonal matrix $\mathbf{\Lambda}$ contains the eigenvalues. The eigenvectors in the columns of \mathbf{U} are a suitable set of base vectors to describe the phase screen at the pierce points $\{\mathbf{p}\}$. The eigenvalues on the diagonal of $\mathbf{\Lambda}$ are a measure of the variance of the eigenvector coefficients. Reducing the fitting order is an arbitrary, but necessary step. An optimal subset of eigenvectors is determined by selecting only those with the largest eigenvalues, as the coefficients with the highest variances are the most significant in the modeling problem.

When the fitting order is reduced from P to $\tilde{P} < P$, we are left with a subset of eigenvectors in the columns of $(P \times \tilde{P})$ matrix $\tilde{\mathbf{U}}$, and eigenvalues on the diagonal of $(\tilde{P} \times \tilde{P})$ matrix $\tilde{\mathbf{\Lambda}}$, for which

$$\mathbf{C}_{\phi\phi} \approx \tilde{\mathbf{U}} \tilde{\mathbf{\Lambda}} \tilde{\mathbf{U}}^T. \quad (2.31)$$

The phase screen at the pierce point locations can be approximated by

$$\Phi \approx \tilde{\mathbf{U}} \mathbf{q}, \quad (2.32)$$

where we have denoted the phases and eigenvector coefficients in matrix notation as Φ ($P \times 1$) and \mathbf{q} ($\hat{P} \times 1$), respectively. \mathbf{q} is unknown and needs to be solved for by use of a non-linear least squares method using Equation 2.24. When \mathbf{q} is determined, the phase screen can be evaluated at arbitrary pierce point locations $\{\hat{\mathbf{p}}\}$ through Kriging interpolation (Matheron 1973):

$$\hat{\Phi} = \mathbf{C}_{\hat{\phi}\phi} \mathbf{C}_{\phi\phi}^{-1} \tilde{\mathbf{U}} \mathbf{q} \quad (2.33)$$

where $\mathbf{C}_{\hat{\phi}\phi}$ is the ($\hat{P} \times P$) covariance matrix between $\{\hat{\mathbf{p}}\}$ and $\{\mathbf{p}\}$. Inversion of the full $\mathbf{C}_{\phi\phi}$ can be approximated using

$$\mathbf{C}_{\phi\phi}^{-1} \approx \tilde{\mathbf{U}} \tilde{\Lambda}^{-1} \tilde{\mathbf{U}}^T. \quad (2.34)$$

The elements of the covariance matrix can be calculated using Equations 2.27 and 2.28. For our application, the absolute value of r_0 is not relevant because we only require the relative eigenvalues for the order reduction. The elements of the ($P \times P$) structure matrix are given by

$$\mathbf{D}_{\phi\phi}[i, j] = D_{\phi\phi}(r_{ij}). \quad (2.35)$$

The relation between the structure matrix and the covariance matrix is given by

$$\mathbf{C}_{\phi\phi} = \sigma_{\phi}^2 \mathbf{1} \mathbf{1}^T - \frac{1}{2} \mathbf{D}_{\phi\phi}, \quad (2.36)$$

with $\mathbf{1}$ a ($P \times 1$) vector containing ones. The phase variance terms σ_{ϕ}^2 are removed from the equations by explicitly removing the mean phase from the individual phases through the substitution

$$\phi \rightarrow \phi' = \phi - \langle \phi \rangle \quad \Rightarrow \quad \Phi \rightarrow \Phi' = \left(\mathbb{I} - \frac{1}{P} \mathbf{1} \mathbf{1}^T \right) \Phi, \quad (2.37)$$

where \mathbb{I} is the ($P \times P$) identity matrix. Applying this substitution to the covariance matrix yields

$$\mathbf{C}_{\phi'\phi'} = \left(\mathbb{I} - \frac{1}{P} \mathbf{1} \mathbf{1}^T \right) \mathbf{C}_{\phi\phi} \left(\mathbb{I} - \frac{1}{P} \mathbf{1} \mathbf{1}^T \right) = \left(\mathbb{I} - \frac{1}{P} \mathbf{1} \mathbf{1}^T \right) \left[-\frac{1}{2} \mathbf{D}_{\phi\phi} \right] \left(\mathbb{I} - \frac{1}{P} \mathbf{1} \mathbf{1}^T \right), \quad (2.38)$$

The σ_{ϕ}^2 terms have dropped because of the properties

$$\left(\mathbb{I} - \frac{1}{P} \mathbf{1} \mathbf{1}^T \right) \mathbf{1} = \mathbf{0}, \quad \mathbf{1}^T \left(\mathbb{I} - \frac{1}{P} \mathbf{1} \mathbf{1}^T \right) = \mathbf{0} \quad (2.39)$$

For Kriging interpolation, a similar substitution is performed as in Equation 2.37:

$$\hat{\Phi} \rightarrow \hat{\Phi}' = \hat{\Phi} - \left(\frac{1}{\hat{P}} \hat{\mathbf{1}} \hat{\mathbf{1}}^T \right) \hat{\Phi}, \quad (2.40)$$

with $\hat{\mathbf{1}}$ a ($\hat{P} \times 1$) vector containing ones. The covariance matrix between $\{\hat{\mathbf{p}}\}$ and $\{\mathbf{p}\}$ (Equation 2.33) now becomes

$$\mathbf{C}_{\hat{\phi}'\phi'} = \left(\left[-\frac{1}{2} \mathbf{D}_{\hat{\phi}\phi} \right] - \left(\frac{1}{\hat{P}} \hat{\mathbf{1}} \hat{\mathbf{1}}^T \right) \left[-\frac{1}{2} \mathbf{D}_{\hat{\phi}\phi} \right] \right) \left(\mathbb{I} - \frac{1}{P} \mathbf{1} \mathbf{1}^T \right) \quad (2.41)$$

where $\mathbf{D}_{\hat{\phi}\phi}$ is the ($\hat{P} \times P$) structure matrix between $\{\hat{\mathbf{p}}\}$ and $\{\mathbf{p}\}$, calculated using Equations 2.28 and 2.35.

Ionospheric calibration of low-frequency radio
interferometric observations using the peeling scheme
II. Method extensions & application to a larger array

Abstract. In the previous chapter, we presented a description and first results of SPAM (Source Peeling and Atmospheric Modeling), a method for calibration of direction-dependent ionospheric phase rotations in low-frequency radio interferometric observations. By assuming a time-constant instrumental phase offset per antenna, and by representing the ionosphere with a single phase screen model at fixed height, SPAM was able to significantly improve the calibration accuracy of 74 MHz observations from the VLA in relatively compact configurations ($\lesssim 20$ km baselines) as compared to other existing calibration methods. In this chapter, we present two extensions of the SPAM method: a multi-layer ionosphere model to represent the vertical ionospheric structure, and an estimator for slow instrumental phase drifts in the presence of ionospheric phase fluctuations. We describe the data reduction steps while applying SPAM on archival 74 MHz observational data from the VLA in its most extended A-configuration (up to 35 km baselines) during quiet ionospheric conditions. Detection and removal of phase drifts significantly reduces the RMS residual phase when fitting ionospheric phase models. The data sets of two target fields are calibrated and imaged, using both the single-layer and multi-layer ionosphere model. Image analysis shows an equal performance of the single- and multi-layer models in terms of background noise (~ 30 mJy beam $^{-1}$) and source peak fluxes, but a slight (5–10 percent) improvement in the overall astrometric accuracy of the multi-layer model images as compared to the single-layer model images. This outcome is consistent with the concept of a smooth 3-dimensional ionosphere that is poorly represented by a single-layer model.

H. T. Intema, S. van der Tol, W. D. Cotton, A. S. Cohen,
I. M. van Bemmelen, and H. J. A. Röttgering
To be submitted

3.1 Introduction

For ground-based radio interferometry at low frequencies ($\lesssim 300$ MHz), the Earth's ionosphere is one of the main sources of systematic error in the measurement of phases (e.g., Thompson et al. 2001). The partially ionized gas (mainly the free electrons), permeated with the Earth's magnetic field, causes refraction and propagation delay to passing radio waves (Davies 1990). Because the ionosphere is dynamic and inhomogeneous, the refractive index for radio waves changes with position and time. This influences the ray path of the radio wave and the amount of ionospheric phase rotation accumulated along the ray path. The phase rotation scales (approximately) linearly with wavelength and with free electron column density (total electron content, or TEC) along the ray path. The presence of the magnetic field adds complexity by introducing Faraday rotation, a differential phase rotation between left- and right-polarized waves, which is not considered further in this chapter.

An interferometer array measures phase differences to determine the direction of incident radio waves (e.g., Thompson et al. 2001). The ionosphere adds a differential phase rotation to the complex-valued visibility measurement on each baseline, which is the difference of the phase rotation along two lines-of-sight (LoSs) from the two baseline antennas towards the cosmic radio source. Under *non-isoplanatic* conditions, the differential phase rotation on a single baseline varies over the field-of-view (FoV). This is typically the case for wide-field, low-frequency observations. Calibration of the visibility measurements requires direction-dependent, antenna-based phase corrections. Calibration methods that yield direction-*independent* phase corrections (like self-calibration; e.g., see Pearson & Readhead 1984) will therefore not work. For optimal performance of existing and future low-frequency radio interferometer arrays (e.g., VLA, GMRT, LOFAR, LWA and SKA), it is crucial to have calibration algorithms available that can properly model and remove direction-dependent ionospheric phase rotations from the visibilities.

There are currently two implemented calibration methods for radio interferometers that incorporate direction-dependent ionospheric phase corrections, namely *field-based calibration* (FBC) by Cotton et al. (2004) and *source peeling & atmospheric modeling* (SPAM; see Chapter 2). Both methods attempt to measure, model and remove the ionosphere-induced phase rotations in the visibilities. The direction-dependent ionospheric phase rotation is modeled with a phase screen over the array. Both methods assume that the instrumental phase contribution to the visibility phase is constant over time (up to a few hours) and viewing direction. This seems reasonable, as the changes in the instrumental signal path length (e.g., due to temperature induced cable length differences) are very small compared to metre wavelengths.

FBC has been designed and used extensively for calibration of relatively compact arrays, mainly the 74 MHz VLA (Kassim et al. 2007) in B-configuration ($\lesssim 11$ km; e.g., Cohen et al. 2007). FBC assumes that the instantaneous differential ionospheric phase structure over the array in any viewing direction can be accurately described by a gradient, and that this gradient varies smoothly with viewing direction. Effectively, the 3-dimensional structure of the ionosphere is integrated along an average LoS from the array into a 2-dimensional phase gradient screen at infinite height. The performance of FBC degrades in the presence of higher-order phase structure over the array.

The SPAM method attempts to correct for higher order phase structure over the array. Assuming that the dominant phase rotations originate from a limited height range in the ionosphere, SPAM combines the observed instantaneous direction-dependent, higher order iono-

spheric phase structure over the array into a thin-layer phase model at a fixed height. By using an airmass function to incorporate a zenith angle dependence, the thin-layer phase model is in effect again reduced to two spatial dimensions.

In this chapter, we attempt to relax two potentially limiting assumptions of the current SPAM algorithm: the thin ionospheric layer and the stable instrumental phase. In Section 3.2, we discuss the limitations of a single-layer ionosphere model. In Section 3.3, we present a detailed description of a 3-dimensional, multi-layer extension of the ionospheric model in SPAM. Section 3.4 contains a description for estimating slow instrumental phase drifts. In Section 3.5, we present the results of SPAM calibration on VLA 74 MHz observations in the largest A-configuration using the extensions presented in Sections 3.3 and 3.4. We compare the images resulting from application of both the single- and multi-layer ionosphere models. A discussion and conclusions are presented in Section 3.6.

3.2 Limitations of the single-layer ionosphere model

In this section, we provide a rationale for using a 3-dimensional rather than a 2-dimensional model to remove ionospheric phase rotations from radio interferometric observations. We give a basic description of the relevant ionospheric physics. Using a simple model, we perform an order of magnitude estimation of the error induced by representing the 3-dimensional ionosphere by a 2-dimensional model.

3.2.1 Ionospheric phase rotation

The ionosphere (e.g., Davies 1990) is a thick shell of partially ionized gas, extending roughly from ~ 50 km height into outer space (> 1000 km). The free electron density, most relevant for our problem, varies with time and location, influenced mainly by the Sun (direct photo-ionization through radiation, particle injection through the solar wind). On average, the electron density peaks at 300–400 km height.

A radio wave with frequency ν that travels from an extra-terrestrial source k towards a ground-based antenna i experiences a propagation delay, and therefore a phase rotation ϕ_{ik} , due to free electrons with density n_e along its path through the ionosphere. By assuming that the ionosphere is an unmagnetized, cold, collisionless plasma and the observing frequency ν is much larger than the plasma frequency (typically 1–10 MHz), the ionospheric phase rotation is given by (Section 2.2.1)

$$\phi_{ik} = \frac{e^2}{4\pi\epsilon_0 m c \nu} \int n_e dl, \quad (3.1)$$

where the integral runs along the ray path through the ionosphere from source k to antenna i , and where e is the electron charge, ϵ_0 the vacuum permittivity, m the electron mass, and c the speed of light in vacuum. The integral on the right is the column density of free electrons along the line-of-sight (LoS), or TEC. Measuring phase rotations on radio signals is a powerful tool to study the ionosphere. Ionospheric researchers distinguish between vertical TEC (VTEC) along a vertical (zero zenith angle) LoS, and slant TEC (STEC) along a LoS at a non-zero zenith angle (e.g., Smith et al. 2008). The related TEC unit (TECU) is 10^{16} m^{-2} , a typical value for the VTEC during nighttime. In daytime, the VTEC may locally increase by 1–2 orders of magnitude (e.g., Davies 1990).

On smaller scales, the coupling with acoustic-gravity waves in the troposphere is known to generate wave-like travelling ionospheric disturbances (TIDs) at 200–400 km height, with wavelengths between 200–500 km, traveling horizontally at speeds of 300–700 km h⁻¹ in any direction, giving rise to 1–5 percent changes in VTEC. Fluctuations on even smaller scales (e.g., Cohen & Röttgering 2009) are less well understood, but are known to give rise to scintillations in astronomical radio observations (e.g., Spoelstra & Yang Yi-pei 1995). These ~ 0.1 percent fluctuations in TEC appear to originate from a turbulent layer roughly 100 km below the peak in the electron density (van Velthoven 1990).

A radio interferometer (or array) correlates the radio signals received from cosmic sources on pairs of antennas (baselines) into complex visibility measurements. Visibilities are approximate spatial Fourier components of the apparent sky brightness distribution (e.g., Thompson et al. 2001). The ionospheric phase rotation in the visibility contribution of a source k , measured on a baseline consisting of antennas i and j , is the differential phase rotation along the LoS from k to i and the LoS from k to j :

$$\phi_{ijk} = \phi_{ik} - \phi_{jk} \quad (3.2)$$

For a given viewing direction, the array is most sensitive to differential ionospheric phase structure on horizontal spatial scales comparable or smaller than the array. Large-scale changes in the ionospheric free electron density (e.g., during sunrise or sunset) can cause steep phase gradients to appear over the array in all directions, but these gradual changes are generally easy to track.

3.2.2 Single-layer ionosphere models

Despite the true 3-dimensional structure of the ionosphere, 2-dimensional models with a screen at a fixed, representative height above the earth's surface have been used extensively to characterize the ionosphere. Typically, these screens define the VTEC as a function of horizontal ionospheric pierce point (IPP) \mathbf{p} . The IPP is the position at which a straight LoS from a ground-based observer towards an extraterrestrial source pierces the screen. The mapping factor from VTEC to STEC depends on the local zenith angle ζ under which the LoS pierces the screen, and is typically taken to be an airmass function:

$$\text{STEC}(\mathbf{p}, \zeta) = \frac{\text{VTEC}(\mathbf{p})}{\cos(\zeta)}. \quad (3.3)$$

VTEC screen models are used for ionospheric research and for radio navigation applications (e.g., see Smith et al. 2008). The VTEC is most often derived from ground-based STEC measurements with the ionosphere being back-lighted by some radio source, e.g. a satellite. Two-dimensional screens are mathematically simple, computationally cheap and can be constructed with relatively few measurements. Smith et al. (2008) estimate that under normal ionospheric conditions (i.e. no solar activity and away from the Sun-induced ionized bubble over the geomagnetic equator) the RMS VTEC accuracy of 2-dimensional screens is at best 1 TECU.

Reconstruction of the 3-dimensional electron density structure from TEC measurements is more difficult but possible (e.g., see Bust & Mitchell 2008) if sufficient STEC measurements through the volume of interest are available for a variety of viewing angles. This yields more accurate VTEC estimates ($\lesssim 1$ TECU) at the cost of adding complexity to the model. Global 3-dimensional models for the ionosphere are publicly available (e.g., the International Reference Ionosphere or the US-TEC ionosphere model; Bilitza & Reinisch 2008; Fuller-Rowell et al.

2006). Typically, in the absence of a dense constellation of satellites and ground-based receivers, the spatial resolution of 3-dimensional ionosphere models is in the order of 50–100 km at best.

Current low-frequency radio arrays (e.g., VLA and GMRT) are not equipped with dedicated (GPS) systems to measure the local ionosphere over the array. Also, the currently best achievable accuracy and spatial resolution would not be sufficient to directly calibrate the instrument, but could provide a starting point for further calibration actions (Noordam 2008). For a VLA observation at 74 MHz, a differential TEC accuracy of 0.01 TECU is equivalent to an ionospheric phase rotation of ~ 1 radian (Equation 3.1). For an extremely smooth ionosphere, a global model with a 1 TECU error over 100 km could calibrate a 1 km baseline to ~ 1 radian accuracy at 74 MHz. The presence of smaller scale (< 100 km) structure (e.g., Cohen & Röttgering 2009) will cause the this calibration accuracy to deteriorate.

For high accuracy calibration on small spatial scales, a radio array relies on direct calibration against cosmic radio sources to derive an accurate model for ionospheric phase rotations. Under the assumption that the small-scale phase fluctuations originate from a thin layer below the electron density peak, SPAM calibration contains a 2-dimensional phase screen model that has been placed at 200 km height during successful initial testing (see Chapter 2). The RMS residual phase error after model fitting is 20 to 25 degrees at 74 MHz, which includes the propagated error from the ionospheric phase measurement. This corresponds to a differential TEC accuracy of 3.5×10^{-3} TECU over an 11 km array. The SPAM model yields no information on absolute TEC. When assuming the RMS error is dominated by residual gradients, the RMS gradient error is 10^{-3} TECU km^{-1} for a typical baseline length of 3.5 km.

The 2-dimensional SPAM model (SPAM2D from here on) mimicks the integrated phase effect for a thin, turbulent layer of free electrons, much thinner than the scale size of dominant electron density fluctuations in the ionosphere. An extensive description of this model is given in Chapter 2. For the discussion here, it is sufficient to note that the phase model $\phi(\mathbf{p}, \zeta)$ is constructed in a similar way as the VTEC screens (Equation 3.3):

$$\phi(\mathbf{p}, \zeta) = \frac{\phi(\mathbf{p})}{\cos(\zeta)}. \quad (3.4)$$

For a given antenna position, source position and layer height, \mathbf{p} and ζ are fully determined (see Figure 2.2). The phase screen $\phi(\mathbf{p})$ describes the horizontal phase structure. The airmass term $1/\cos(\zeta)$ extends the horizontal phase structure over some limited vertical range. Equation 3.4 is combined with Equation 3.2 to produce model phase differences. The free model parameters contained within $\phi(\mathbf{p})$ are determined per integration interval by non-linear least squares (NLLS) fitting of the model phase differences against measurements of the differential ionospheric phase rotations in several viewing directions. The latter estimates are derived from individual phase calibrations on available calibrator sources in the FoV, a technique known as *peeling* (Noordam 2004).

3.2.3 Phase errors induced by a single-layer ionosphere model

In SPAM2D, we have approximated the phase effects of the 3-dimensional ionosphere by a 2-dimensional phase screen at one height. In this section we estimate the order of magnitude of the phase errors that may arise from this incomplete representation. The state of the ionosphere is highly variable over space and time, therefore we attempt to obtaining an *average* error estimate. To this purpose, we use an empirical error function by Smith et al. (2008) that

x	0	1	2	3
a_x	-64.4297	0.0942437	1.39436	-0.196357
b_x	-64.3659	0.104974	1.41152	0.000463341

Table 3.1: Fitted values for the empirical function in Equation 3.6, with h in km and ζ in degrees (from Smith et al. 2008).

describes the average error in 2-dimensional screen models when converting (mapping) from VTEC to STEC. This function is derived by fitting against average mapping errors, obtained by ray-tracing through the 3-dimensional US-TEC ionosphere model (Fuller-Rowell et al. 2006). The error function can also be used for more accurate mapping of VTEC to STEC than the simple airmass relation in Equation 3.3. The accuracy for individual cases is given to be 30 to 50 percent better than $1/\cos(\zeta)$.

The empirical error function f is defined as the relative error of the mapped STEC (Equation 3.3) as compared to the true STEC (Smith et al. 2008):

$$f = \left[\frac{\text{VTEC}}{\cos(\zeta)} - \text{STEC} \right] / \text{STEC} \quad (3.5)$$

The function f depends on both the chosen screen height h and the zenith angle ζ at the IPP:

$$\begin{aligned} f &= (a + b h) \\ a &= a_3(a_2 + \tan^{-1}(a_1(\zeta + a_0))) \\ b &= b_3(b_2 + \tan^{-1}(b_1(\zeta + b_0))), \end{aligned} \quad (3.6)$$

with the fitted values for the parameters a_x and b_x given in Table 3.1. The valid zenith angle domain runs approximately from 0 to 65 degrees.

Our application differs in that we aim to solve for *differential* ionospheric phase rotation along the two LoSs for each baseline rather than solving for absolute TEC along a single LoS. For the estimation of the phase error induced by the SPAM2D model, we use the scenario as depicted in Figure 3.1. A baseline consisting of two antennas i and j observes a bright source k . We assume that the differential ionospheric phase contribution to visibility measurements on this baseline in the direction of source k can be accurately determined through calibration on the source. A second baseline consisting of antennas i' and j' observes a faint source k' on which calibration is not possible. A phase screen model is positioned at height h to extrapolate the ionospheric phase from (baseline-source pair) ijk to $i'j'k'$. The special configuration under consideration causes the IPPs \mathbf{p}_{ik} and \mathbf{p}_{jk} to coincide with $\mathbf{p}_{i'k'}$ and $\mathbf{p}_{j'k'}$, respectively. With this configuration we can evaluate the effect of extrapolating the zenith angles while keeping the positions in the phase screen the same.

We derive an expression for the phase error that is introduced by extrapolating the model from ijk to $i'j'k'$, which only varies the zenith angles. In this derivation, the total ionospheric electron content is assumed to consist of a bulk component with a smooth spatial electron density distribution on large scales (several 100 km), and a thin turbulent layer containing smaller-scale fluctuations. Because ionospheric phase rotation is linear in TEC, and the SPAM2D model is linear in its free parameters, the modeling of the total ionosphere can be separated into a bulk

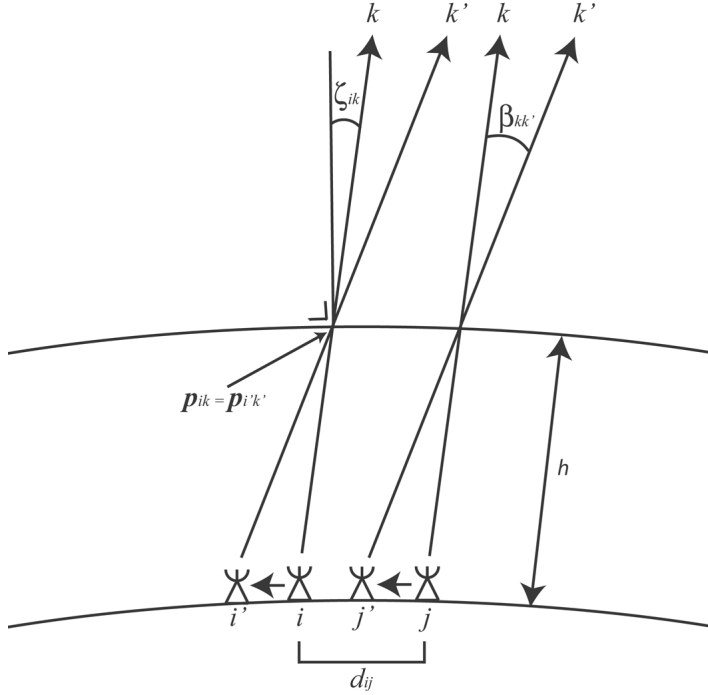


Figure 3.1: Schematic overview of the calibration geometry used for estimating the phase error from representing a smooth 3-dimensional ionosphere with the SPAM2D single-layer model. Two antennas i and j , at distance d_{ij} from each other, form a baseline ij that observes calibrator source k . The SPAM2D model, consisting of a single-layer model at height h , is fitted to the measurable differential (bulk) ionospheric phase rotations at the IPPs $\{p\}$, assuming a $1/\cos(\zeta)$ airmass dependence. For a second baseline $i'j'$ observing a source k' at angular distance $\beta_{kk'}$ from source k , sharing the same IPPs, the SPAM2D model is used to predict the differential phase rotation for this baseline. For a bulk ionosphere with constant VTEC, the prediction will differ from the real differential phase rotation, because the true airmass dependence is more complex than $1/\cos(\zeta)$.

part and a turbulent layer part. We assume that the SPAM2D model is accurate in reproducing and interpolating the phase contribution originating from the turbulent layer, therefore we only consider the bulk contribution.

The (differential) ionospheric phase rotation ϕ_{ijk}^b due to the bulk on a baseline consisting of antennas i and j , looking towards source k (see Figure 3.1) is given by (Equation 3.2)

$$\phi_{ijk}^b = \phi_{ik}^b - \phi_{jk}^b. \quad (3.7)$$

The expression for $\phi_{i'j'k'}^b$ on baseline $i'j'$ looking towards source k' is similar. For the ionospheric volume of interest, we assume that the VTEC is approximately constant. Due to the linear relation between TEC and phase rotation (Equation 3.1), we can rewrite Equation 3.5 in terms of phase:

$$\phi_{ik}^b = \frac{\phi_v^b}{[1 - f(h, \zeta_{ik})] \cos(\zeta_{ik})}, \quad (3.8)$$

with ϕ_v^b the constant bulk phase rotation along a vertical LoS. For this derivation, we combine Equations 3.7 and 3.8 to estimate the ‘true’ ionospheric phase rotation that is measured on baseline ij towards source k . Again, this is similar for baseline $i'j'$ looking towards source k' .

Accurately fitting the SPAM2D model (Equation 3.4) to the measured ionospheric phase rotation ϕ_{ijk}^b yields

$$\phi_{ijk}^b = \frac{\phi^b(\mathbf{p}_{ik})}{\cos(\zeta_{ik})} - \frac{\phi^b(\mathbf{p}_{jk})}{\cos(\zeta_{jk})}. \quad (3.9)$$

Based on this fit, the predicted phase rotation for this baseline is

$$\hat{\phi}_{i'j'k'}^b = \frac{\phi^b(\mathbf{p}_{ik})}{\cos(\zeta_{i'k'})} - \frac{\phi^b(\mathbf{p}_{jk})}{\cos(\zeta_{j'k'})}, \quad (3.10)$$

where we have used $\mathbf{p}_{i'k'} = \mathbf{p}_{ik}$ and $\mathbf{p}_{j'k'} = \mathbf{p}_{jk}$. The absolute error in this prediction is defined by

$$\Delta\phi_{i'j'k'}^b = |\hat{\phi}_{i'j'k'}^b - \phi_{i'j'k'}^b| \quad (3.11)$$

With the expressions above we can evaluate the *average* error induced by the use of a 2-dimensional screen. For individual situations, the error may increase by a factor of a few. Because fitting to differential phase (Equation 3.9) allows for an arbitrary offset to be added to the model, we assume a zero mean phase for the model near the pierce points. By positioning antennas i, j, i', j' on a plane through sources k, k' and the center of the Earth, the change in zenith angles (or shift in baseline; see Figure 3.1) can be easily linked to the angular separation $\beta_{kk'}$ between sources k and k' . The maximum possible value of $\beta_{kk'}$ is either determined by the size of the FoV or the size of the array.

For the 74 MHz VLA in A-configuration, we have calculated the error for a single-layer model at 300 km height for different values of zenith angle, VTEC, baseline length and angular separation. For the default SPAM2D height of 200 km, the mapping function in Equation 3.8 appears to be less accurate for large ($\gtrsim 55$ degrees) zenith angles. We found that our error estimates change very little with screen height, therefore we use 300 km instead. Both the FoV and the angular extend of the array as seen from a screen height of 300 km are both ~ 10 degrees. The maximum $\beta_{kk'}$ will be smaller than this, because a typical FoV contains multiple calibrator sources $\{k\}$ and because *both* antennas of a shifted baseline are bound to the array dimensions.

The estimated phase errors for a 2-dimensional phase screen model are plotted in Figure 3.2. Except for the zenith angle, the default parameter values (see caption) are chosen to be at the high end of a range of typical values. Most apparent is the steep rise of the error for zenith angles above ~ 50 degrees. Furthermore, a significant increase of the error is to be expected for extremely large VTEC values (~ 100 TECU) during an ionospheric storm. Under more typical situations (the default values), the error estimate is found to be in the order of 10 degrees or less. Apart from the anticipated linear relation between error and VTEC, there also exists a (approximate) linear relation between the error and both baseline length and angular separation over the parameter domains investigated here. The linear relation between error and baseline length causes a phase gradient over the array, which results in an apparent position shift of source k' . This offers an explanation for the systematic source position offsets that were observed in Chapter 2 for image regions without calibrators.

In general, the error estimates for 74 MHz observations show that even under the most ideal ionospheric conditions, the use of a 2-dimensional phase screen can lead to significant prediction errors when observing towards higher zenith angles or under ionospheric conditions with increased VTEC values. In the additional presence of irregular vertical electron density variations, the 2-dimensional representation will degrade further. This provides a strong argument for using a 3-dimensional representation of the ionosphere. This argument holds for observing frequencies up to a few times 74 MHz, because even though the error scales linearly with wavelength (which follows directly from Equation 3.1), it can still be significant for high zenith angles and larger VTEC values.

3.3 The multi-layer ionosphere model

In this Section, we describe the multi-layer ionospheric model extension of the SPAM ionospheric calibration method (SPAM3D from here on).

3.3.1 Towards a multi-layer model

The problem of astronomical imaging in the presence of atmospheric turbulence has been addressed for many years in optical and near-infrared astronomy. To overcome the typical optical *seeing* resolution limit of $\sim 1''$ due to tropospheric turbulence, large ground-based telescopes have been equipped with adaptive optics systems (AO; e.g., Hardy 1998) that track the atmospheric distortion of a (possibly artificial laser) guide star in the target field, and change the shape of a deformable mirror in real-time to correct the distorted wavefronts. This generally leads to significant improvements in image resolution near the guide star, but performance decreases at larger distance. The development of telescopes with increasing fields-of-view ($\gtrsim 10'$) also triggered the development of multi-conjugate adaptive optics (MCAO; e.g., Esposito 2005). This technique uses multiple guide stars to allow for significant wavefront corrections over a larger sky area, using multiple deformable mirrors to represent turbulent layers at different (conjugate) heights in the troposphere. This technique has been successfully tested on several selected fields (Marchetti et al. 2007).

The concept of dividing the vertical dimension of a distorting atmospheric volume into a number of representative layers has also been proposed for ionospheric modeling. Airplane navigation in the United States is aided by the Wide Area Augmentation System (WAAS),

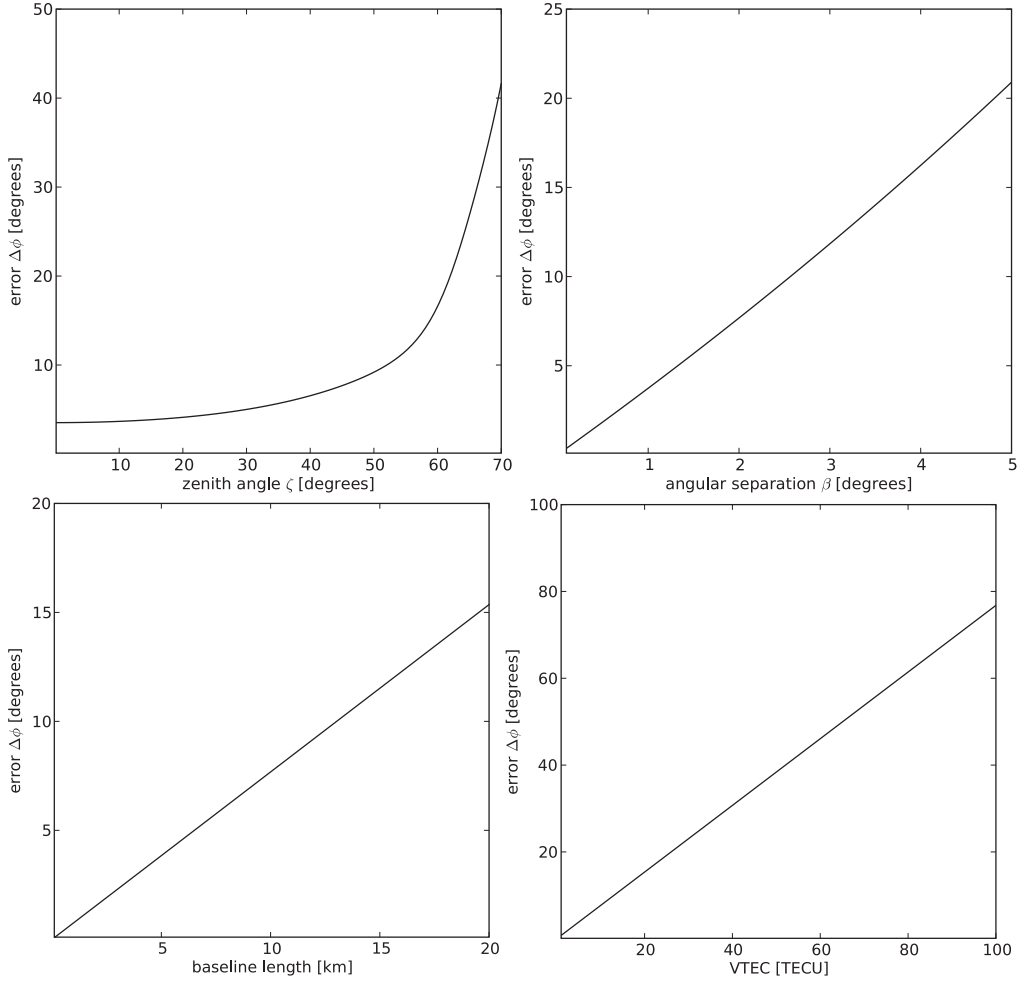


Figure 3.2: Plots of the estimated differential phase error $\Delta\phi$ (Equation 3.11) for an ideal single-layer ionosphere model in the presence of a bulk ionosphere, assuming a constant VTEC over the relevant domain. These plots are based on the 74 MHz VLA in A-configuration for a layer height of 300 km. The default parameter setup (see text) is a baseline length of 10 km, an angular separation β of 2 degrees, a VTEC of 10 TECU and a zenith angle of 45 degrees. Note that the zenith angle used here is the (mean) zenith angle at the antennas, from which the zenith angles at the IPPs is derived. For each plot, one of the parameter was varied, while the others were kept constant. *Top left:* Phase error as a function of zenith angle. *Top right:* Phase error as a function of angular separation β . *Bottom left:* Phase error as a function of baseline length. *Bottom right:* Phase error as a function of VTEC. Note that the vertical scale changes between plots.

which includes a thin-layer ionosphere model for correcting propagation delays in GPS-signals. Blanch et al. (2004) propose a generalization of the ionosphere model by introducing multiple (statistically independent) thin layers at representative heights. The total propagation delay for any (straight) LoS from GPS satellite to receiver is assumed to be the sum of the contributions of the individual layers. In effect, the TEC integral (Equation 3.1) along the LoS through the ionosphere is replaced by a simpler sum. For two test cases on real data, the multi-layer ionosphere model reduces the VTEC estimation error by 30–50 percent as compared to the single-layer model (Blanch et al. 2004).

3.3.2 Ionospheric multi-layer phase screen model

In this section we present a mathematical description of the multi-layer model as implemented in SPAM3D. An individual layer in SPAM3D is similar to the single-layer model in SPAM2D. In this section we describe only those elements that are needed to expand from a single- to a multi-layer configuration. Chapter 2 contains an extensive description of the single-layer model, therefore we refer to this chapter for background information.

The original SPAM2D single-layer model was designed to have certain properties to aid model fit convergence and interpolation: (i) the model base vectors are orthogonal on the discrete IPP domain, (ii) model order reduction leads to minimal deviation from the assumed statistical behaviour, (iii) interpolation retains the assumed statistical behaviour, (iv) the model has most spatial structure near the IPPs and converges to zero at large distance. For the construction of a 3-dimensional model, it is highly desirable to maintain these characteristics while adding more freedom to the model to represent the vertical structure. Due to the similarities in model setup, we can apply the multi-layer approach of Blanch et al. (2004) to the SPAM model. This approach sustains the important properties of the SPAM2D model mentioned above into the SPAM3D model. This approach has two additional important properties: (i) each free model parameter applies to all layers simultaneously and does not have to be arbitrarily assigned to a single layer, and (ii) the model base functions are orthogonal over the integrated vertical model structure, therefore there is intrinsically no redundancy between model layers.

SPAM has been extended with a multi-layer ionospheric phase model that allows for multiple independent phase screens $\{\phi^h\}$ to be positioned at representative heights $\{h\}$, compliant to the WGS84 standard (NIMA 1984). For a single visibility time interval (we omit the time subscript n here), the total (integrated) ionospheric phase rotation ϕ_{ik} for a radio wave traveling along a given line-of-sight (LoS) from antenna i to source k is modeled by a weighted sum of phase rotations induced by piercing through the individual phase screens:

$$\phi_{ik} = \sum_h w_h \phi_{ik}^h = \sum_h w_h \frac{\phi^h(\mathbf{p}_{ik}^h)}{\cos(\zeta_{ik}^h)}, \quad (3.12)$$

where w_h is an arbitrary weight assigned to each layer (with $\sum_h w_h = 1$), \mathbf{p}_{ik}^h the coordinates of the IPP at height h , and ζ_{ik}^h the zenith angle of the LoS at the IPP.

In this model we assume that the LoSs are straight, while in reality they are bent due to variations in the refractive index along the ray paths. To first order, moderately large refractions (say, ≤ 10 degrees) that are common for all antennas and constant across the FoV can be represented by the multi-layer model by horizontally shifting the layers and scaling the amplitude of the horizontal phase structure per layer to incorporate the change in airmass. To some extend,

variations across the array and across the FoV can be incorporated into the horizontal phase structure of the layers, but may result in inconsistencies between (nearly) crossing LoSs and less accurate interpolation.

Using the Karhunen-Loève (KL) transform, an optimal set of base ‘functions’ can be derived to define the (total) ionospheric phase model ϕ . For this, we calculate the phase covariance of the multi-layer model. A first step in this calculation is to define the statistical behaviour of individual layers. Each phase screen ϕ^h represents a thin layer of (zero mean) turbulent electron density fluctuations. Following van der Tol & van der Veen (2007), the stochastic model for each layer is defined in terms of a power-law phase structure function

$$D_{\phi\phi}^h(r) = \langle [\phi^h(\mathbf{p}^h) - \phi^h(\mathbf{p}^h + \mathbf{r})]^2 \rangle = (r/r_0^h)^{\gamma_h}, \quad (3.13)$$

where $\langle \dots \rangle$ denotes the expected value, $r = |\mathbf{r}|$ is the length of a horizontal offset vector \mathbf{r} in the screen, r_0^h is a measure of the scale size of phase fluctuations and γ_h is a power-law slope. Both r_0^h and γ_h are layer parameters that need to be specified by the user. It is convenient to use the same values for r_0^h and γ_h for all layers. This causes the phase structure function of the full model to have the same shape as the structure function of individual layers (Roddier 1981), which can be made to match observations. Similar to SPAM2D, we use $\gamma_h = 5/3$ (pure Kolmogorov turbulence) and $r_0^h = 1$ (although the actual value is irrelevant in our model).

The phase covariance function $C_{\phi\phi}^h(r)$ for each layer is given by

$$C_{\phi\phi}^h(r) = \langle \phi^h(\mathbf{p}^h) \phi^h(\mathbf{p}^h + \mathbf{r}) \rangle. \quad (3.14)$$

The structure function and the covariance function are related through

$$C_{\phi\phi}^h(r) = C_{\phi\phi}^h(0) - \frac{1}{2} D_{\phi\phi}^h(r), \quad (3.15)$$

where $C_{\phi\phi}^h(0)$ is the phase variance.

For a finite set of LoSs of different antenna-source pairs $\{(i, k)\}$, the data domain of ϕ is discrete, therefore we switch to matrix notation. The phase contributions of one layer can be described by a phase vector $\Phi^h = [\dots \phi^h(\mathbf{p}_{ik}^h) \dots]^T$, where T denotes the transpose. Equation 3.12 translates into

$$\Phi = \sum_h w_h \mathbf{A}^h \Phi^h, \quad (3.16)$$

with \mathbf{A}^h a diagonal matrix with the $1/\cos(\zeta_{ik}^h)$ airmass terms on the diagonal. We can construct a structure matrix $\mathbf{D}_{\phi\phi}^h$ with elements

$$\mathbf{D}_{\phi\phi}^h[a, b] = D_{\phi\phi}^h(|\mathbf{p}_a^h - \mathbf{p}_b^h|), \quad (3.17)$$

where $a, b \in \{(i, k)\}$ are antenna-source pair indices. Appendix 2.7 contains a recipe to translate the phase structure matrix $\mathbf{D}_{\phi\phi}^h$ into a phase covariance matrix $\mathbf{C}_{\phi\phi}^h$ with elements

$$\mathbf{C}_{\phi\phi}^h[a, b] = C_{\phi\phi}^h(|\mathbf{p}_a^h - \mathbf{p}_b^h|), \quad (3.18)$$

Under the assumption of independence between layers, the total phase covariance matrix $\mathbf{C}_{\phi\phi}$ of radio waves that travel through the multiple layers at nonzero zenith angles is a combination of the covariance matrices $\mathbf{C}_{\phi\phi}^h$ of the independent layers (Blanch et al. 2004):

$$\mathbf{C}_{\phi\phi} = \sum_h w_h^2 \mathbf{A}^h \mathbf{C}_{\phi\phi}^h \mathbf{A}^h. \quad (3.19)$$

An optimal set of model base vectors are derived by performing a discrete KL transform (singular value decomposition) on the total phase covariance matrix defined in Equation 3.19

$$\mathbf{C}_{\phi\phi} = \mathbf{U}\mathbf{\Lambda}\mathbf{U}^T, \quad (3.20)$$

where the columns of \mathbf{U} contain a complete set of orthonormal base vectors, \mathbf{U}^T is the transpose of \mathbf{U} and the diagonal matrix $\mathbf{\Lambda}$ contains measures of the variance of the base vector coefficients.

The initial complete set of KL base vectors in \mathbf{U} is arbitrarily reduced in order by selecting a subset $\tilde{\mathbf{U}}$ based on the magnitude of the variances (principal component analysis). The subset should be large enough to accurately reproduce the phase measurements obtained by peeling bright sources in the target FoV. The discrete phase vector $\mathbf{\Phi}$ along individual LoSs is represented by a linear combination of the dominant base vectors

$$\mathbf{\Phi} = \tilde{\mathbf{U}}\mathbf{q}. \quad (3.21)$$

The elements of vector \mathbf{q} are the free model parameters, containing one coefficient per base vector. Similar to SPAM2D, the coefficients in \mathbf{q} are determined by fitting Equation 3.21 against the peeling phase measurements. This is described in detail in Section 2.3.4.

If \mathbf{q} can be determined accurately, then the ionospheric phase model (Equation 3.21) reproduces the phase rotations in the direction of the peeled sources. Interpolation of the phase model to arbitrary viewing directions is done by Kriging interpolation (Matheron 1973). Using Equations 3.13 and 3.17, we calculate the structure matrix $\mathbf{D}_{\hat{\phi}\phi}$ between the LoSs towards the peeling sources $\{k\}$ and the LoSs towards the sources $\{\hat{k}\}$ of interest. Following the method described in Appendix 2.7, we derive the covariance matrix $\mathbf{C}_{\hat{\phi}\phi}$ from the structure matrix. The interpolated phase corrections for the arbitrary viewing directions are then given by

$$\hat{\mathbf{\Phi}} = \mathbf{C}_{\hat{\phi}\phi} \mathbf{C}_{\phi\phi}^{-1} \mathbf{\Phi}. \quad (3.22)$$

3.3.3 Reconstruction of individual ionospheric model layers

The base vectors of the multi-layer ionosphere model as described in Section 3.3.2 represent the *integrated* phase behaviour of the model. They are somewhat similar to 3-dimensional base functions that are integrated along LoSs through the relevant volume. The use of multiple layers is mainly a mathematical tool to derive the ‘integrated’ base vectors. The fitted model parameters \mathbf{q} relate to these integrated base vectors, therefore are not assigned to individual layers. The qualitative effect of assigning a higher weight to a particular layer is that relatively more structure is allowed in this layer, which propagates into the integrated base vectors.

This section contains a recipe for reconstructing the phase structure of individual layers in the multi-layer ionosphere model (which is a form of ionospheric tomography). This may prove to be a useful tool for studying the ionosphere. However, one must be cautious with the interpretation of the fitted semi-empirical multi-layer model, which doesn’t necessarily correspond to reality.

The inversion of a 2-dimensional phase measurement into a 3-dimensional phase structure is generally non-trivial (e.g., Bust & Mitchell 2008). The contents of individual layers can be estimated by Kriging interpolation, for which we require a phase covariance matrix per layer. Equation 3.19 defines the total phase covariance matrix $\mathbf{C}_{\phi\phi}$ as a combination of the phase

covariance matrices $\mathbf{C}_{\phi\phi}^h$ per layer (Equation 3.18). Kriging interpolation to an individual layer yields

$$\hat{\Phi}^h = w_h \mathbf{C}_{\phi\phi}^h \mathbf{A}^h \mathbf{C}_{\phi\phi}^{-1} \Phi. \quad (3.23)$$

This approximation obeys Equation 3.16:

$$\sum_h w_h \mathbf{A}^h \hat{\Phi}^h = \sum_h w_h^2 \mathbf{A}^h \mathbf{C}_{\phi\phi}^h \mathbf{A}^h \mathbf{C}_{\phi\phi}^{-1} \Phi = \mathbf{C}_{\phi\phi} \mathbf{C}_{\phi\phi}^{-1} \Phi = \Phi, \quad (3.24)$$

where we used Equation 3.19.

3.4 Instrumental phase drift estimation

One of the main assumptions in the SPAM calibration scheme is that instrumental and ionospheric phase rotations are separable on their spatial and temporal behaviour. Antenna-based instrumental phase rotations are assumed to be constant with time and viewing direction, while ionospheric phase rotations are assumed to vary with both. For extended (5–10 hour) low-frequency radio observations with both VLA and GMRT, we have noticed significant (> 20 degrees) phase drifts of one or more antennas over the observing run that appear to originate from the instrument rather than ionosphere. We have also identified distinct phase offsets for some antennas, which are probably the result of inaccuracies in the initial estimation of the instrumental phase offsets (Section 2.3.1). To improve the modeling accuracy of ionospheric phase rotations, these drifts and offsets need to be removed.

In SPAM we have used the direction-independence as an additional constraint to estimate residual instrumental phase offsets $\Delta\phi^{\text{instr}}$ per visibility time interval n . Under the assumptions that (i) the residual instrumental phase offsets for the majority of antennas are relatively small, and (ii) SPAM fits reasonably accurate phase models ϕ^{ion} to the peeling phase corrections ϕ^{cal} , the residual instrumental phase offset on a particular antenna can be estimated by calculating the mean offset between the phase model and the peeling phase solutions of the antenna towards multiple calibrator sources:

$$\Delta\phi_{in}^{\text{instr}} \approx \langle (\phi_{ikn}^{\text{cal}} - \phi_{ikn}^{\text{ion}}) \bmod 2\pi - \langle (\phi_{jkn}^{\text{cal}} - \phi_{jkn}^{\text{ion}}) \bmod 2\pi \rangle_{j \neq i} \rangle_k. \quad (3.25)$$

The average $\langle \dots \rangle_{j \neq i}$ estimates and removes the offset between the model and the peeling phase correction towards each calibrator source.

The estimated residual instrumental phase offset for single antennas as a function of time (Figure 3.3) generally shows a scatter of points centered around a slowly changing phase component. Interpreting these as noise and instrumental residual phase, respectively, we apply a median window filter with a width of 1 or 2 hours to extract the slowly changing component. If at least one antenna shows a significant (say $\gtrsim 10$ degrees) residual instrumental phase offset during the observing run, the slowly varying instrumental phases are corrected for in both the visibility data set and the previously obtained phase measurements to which the phase model was fitted. Repeating the model fitting to the corrected phase measurements can lead to significant reductions in the RMS phase residuals (see Section 3.5.2).

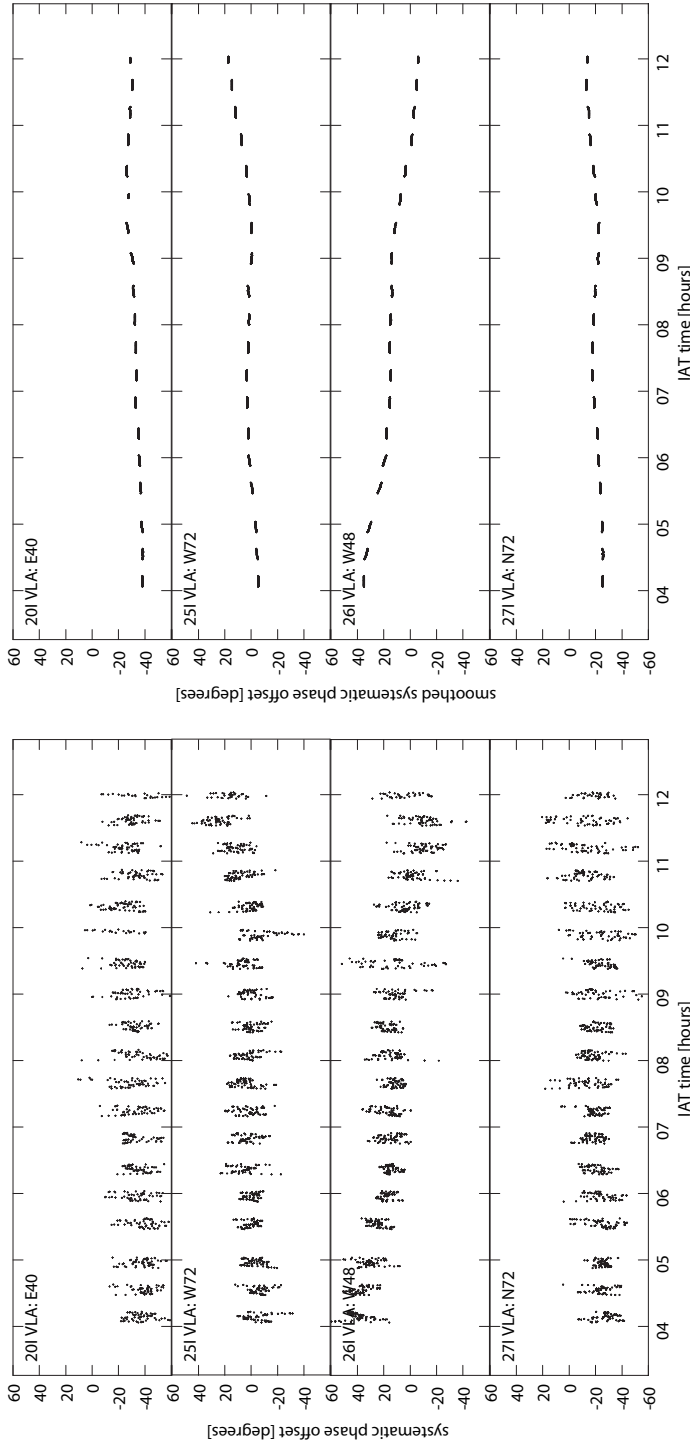


Figure 3.3: Plots of the systematic phase offsets after model fitting of four selected antennas as a function of time, using the method described in Section 3.4. These estimates were derived from the observation on NGC 4565 as presented in Section 3.5. *Left:* The phase offsets for individual visibility time stamps are noisy, but the underlying trends are clearly visible. *Right:* Median window filtering over sufficient long time scales isolates the trend from the noise. VLA antennas E40 and N72 have distinct constant offsets that probably resulted from a poor initial instrumental phase calibration. The systematic phase offsets for antennas W72 and W48 appear to be phase drifts that originate from the instrument itself. These observed trends are independently derived and confirmed from the alternated observation on NGC 4631.

VLA project code	AE119
Date	March 7, 1998
Time range	03:46–12:11 IAT ^a
Target field coordinates:	
- NGC 4565	12 ^h 36 ^m 23.705 ^s + 26°13′29.81″
- NGC 4631	12 ^h 40 ^m 56.379 ^s + 32°31′33.09″
Time per target	159 minutes
Integration time	10 seconds
Frequency	73.8 MHz
Bandwidth	1.54 KHz
Channels	63
Polarizations	RR+LL
Calibrator	Cyg A
Time on calibrator	3.5 minutes

^a The local time at the VLA is Mountain Standard Time (MST = IAT - 7).

Table 3.2: Overview of the test case observations.

3.5 Applications

To test the performance of the multi-layer model and phase drift estimation in SPAM, we apply SPAM calibration to archival VLA 74 MHz observations in the A-configuration, which is the largest low-frequency array presently available. We compare performance of SPAM3D against SPAM2D calibration by analyzing the resulting images. The data reduction and results of these test cases are described in detail. Because data reduction with SPAM differs from other approaches (e.g., Lazio et al. 2005), this description may serve as a template.

3.5.1 Data selection

For our tests we chose to re-process the visibility data sets on two target fields, NGC 4565 and NGC 4631, that were used by Cohen et al. (2004) to produce the deepest high-resolution 74 MHz maps to date. Details for this observation are given in Table 3.2. The original data processing included a phase calibration of each target field against a model derived from the NVSS source catalog (Condon et al. 1994, 1998) before applying field-based calibration (Cotton et al. 2004). Adding this initial phase calibration step is known to yield better quality images in some cases, even when it undermines the assumption of a constant instrumental phase in field-based calibration. The two resulting images of the partially overlapping fields yielded a total of ~ 1000 source detections at 5σ . Cohen et al. (2004) qualify the ionospheric conditions as ‘favourable’. The background noise level in the center of each image is ~ 35 mJy beam⁻¹. The resulting images show signs of residual calibration errors, because there are ring-like and radial patterns present in the image background near bright sources.

3.5.2 Data reduction

For the data reduction, we adopted the same imaging parameters as used by Cohen et al. (2004). After extracting the publicly available visibility data set from the VLA archive¹, it was loaded into NRAO's Astronomical Image Processing Software (AIPS; Bridle & Greisen 1994) package. For convenience, we discuss the further data reduction in terms of one target field, although this actually applies to both target fields.

Instrumental calibration

The Cyg A data was manually flagged for radio frequency interference (RFI) and bad baselines based on excessive visibility amplitudes. To remove ionospheric phase rotations towards the calibrator, a small subset of central frequency channels was used to calibrate the antenna-based gain phases against a Cyg A model² on the visibility time resolution. Normalized bandpass corrections were determined using the same data and model while temporarily applying the phase calibration. Both the phase corrections and bandpass corrections were applied while calibrating the antenna-based gain amplitudes against the model, using all frequency channels. The time-constant amplitude and bandpass corrections were applied to Cyg A and the target field. Next, the target field data was manually inspected per baseline to identify and flag excessive visibility amplitudes (mostly RFI).

To remove the constant phase offset between RR and LL polarization, a second phase calibration of Cyg A against the model was done at the visibility time resolution using the full band. The phase corrections for both polarizations were subtracted (RR-LL) and time-averaged per antenna. These averages were applied to the LL polarization of Cyg A and the target field, after which the RR and LL visibilities were combined into stokes I. To reduce storage and processing, each three frequency channels were averaged together, resulting in 21 frequency channels of 73.2 KHz each.

To remove the antenna-based instrumental phase offsets, a third phase calibration of Cyg A against the model was done at the visibility time resolution. The phase corrections were filtered to separate instrumental from ionospheric phase contributions, by fitting simultaneously for time-constant offsets and time-variant spatial gradients over the array (Section 2.3.1). The time-constant instrumental phase offsets were applied to the target field. At this point, the target field data is assumed to be instrumentally calibrated, except for an unknown spatial phase gradient over the array.

Initial target field calibration and imaging

After instrumental calibration, the astrometry for the target field was restored by phase calibrating on a 30 second time scale against a source model consisting of point source representations of 30 bright sources. The source flux densities and positions were taken from the VLSS catalog, selecting only sources within one primary beam radius from the pointing center, and scaling their absolute flux densities to apparent flux densities by multiplication with an axisymmetric primary beam pattern (e.g., Lazio et al. 2005). The calibration phase corrections were applied during the first imaging of the primary beam area (Table 3.3), followed by several rounds of phase-only self-calibration. Because it is crucial to keep the instrumental calibration intact, the calibration

¹<https://archive.nrao.edu/archive/archiveproject.jsp>

²Obtained from <http://lwa.nrl.navy.mil/tutorial>

Target field diameter	14.9°
Pixel size	5.7''
Weighting	robust ^a
Wide-field imaging	polyhedron (facet-based) ^b
Deconvolution	Cotton-Schwab CLEAN ^c
Number of initial facets	475
Facet diameter	0.81°
Facet separation	0.67°
Restoring beam	circular 25''

^a Briggs (1995)

^b Perley (1989a); Cornwell & Perley (1992)

^c Schwab (1984); Cotton (1999); Cornwell et al. (1999)

Table 3.3: Overview of imaging parameters for both target fields (NGC 4565 and NGC 4631).

phase corrections were stored in tables and temporarily applied while imaging (instead of being applied directly). Per antenna, time ranges that showed incoherent phase calibration corrections (i.e., without any notion of time continuity) were flagged.

The VLA antennas are sensitive to flux coming from directions far outside the primary beam, mainly because of large sidelobes due to a relatively small antenna diameter (25 meter is just over 6 wavelengths at 74 MHz), and because scattering of waves of the primary focus support legs (Kassim et al. 2007). Because the dirty beam sidelobe pattern scales radially with wavelength, bright outlier sources can induce noticeable sidelobe patterns in the target field image at this frequency. This potential problem is addressed in two steps: (i) subtraction of bright sources within a few primary beam radii of the pointing center, and (ii) subtraction of extremely bright sources at (possibly) very large angular distances from the pointing center.

For the first step, the final imaging round in the phase self-calibration loop on the target field included ~ 30 additional facets centered at the positions of very bright VLSS sources outside the primary beam area, up to four times the primary beam radius (except for Vir A, which is processed in the second step). If detected (typically 5–10 sources), the CLEAN models of these outlier sources were subtracted from the visibility data while temporarily applying the self-calibration phase corrections. None of the apparent source fluxes was large enough to require peeling.

For the second step of outlier removal, the updated source models were subtracted from the flagged target field data. The residual data was used to image 9 additional facets at large angular distance from the target field, centered on the Sun and 8 extremely bright sources, namely Cyg A, Cas A, Tau A, Vir A, Ori A, Sgr A, 3C 123 and 3C 10. For imaging and deconvolution of each source, we used the visibility time ranges during the observing run for which the source was above the local VLA horizon (assuming a locally flat Earth and ignoring source refraction). For both target fields, only Cyg A and Vir A were detected, at 87 and 14 degrees distance from NGC 4565, and 82 and 20 degrees from NGC 4631, respectively. Especially Vir A generated significant sidelobe noise in the NGC 4565 image (Figure 3.4). Both Cyg A and Vir A were peeled and subtracted from the target field visibility data, again taking into account the time

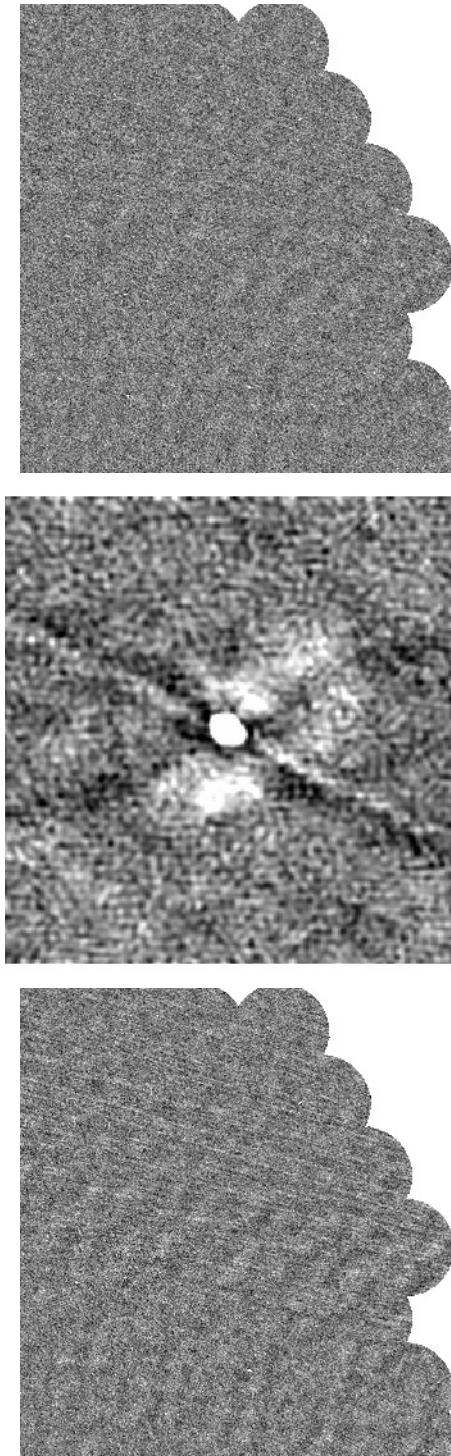


Figure 3.4: Example of the effect of bright outlier removal. *Left:* South-west boundary of the NGC 4565 field before outlier removal. This image contains considerable background structure (near-vertical striping) due to the presence of Vir A. *Middle:* Image of Vir A as derived from peeling, imaged at 14 degrees from the field center. *Right:* Same as left but with Vir A subtracted, which significantly reduces the background structure.

ranges for which these sources were above the horizon.

The resulting target field data, with the outlier sources subtracted, was phase (self-)calibrated and imaged, after which the source model was subtracted from the visibility data. This residual data was inspected per baseline to flag visibilities with excessive amplitudes. Time-frequency blocks that had a large fraction of visibilities flagged were flagged completely. The resulting flagging tables were transferred and applied to the (non-subtracted) target field data, followed by re-imaging.

Ionospheric calibration and imaging

To suppress the direction-dependent calibration errors due to ionospheric phase rotations, we applied SPAM calibration to the target field data, following the recipe in Section 2.3. Each target field data set was processed for two calibration cycles using the single-layer model (SPAM2D). The second cycle was then repeated using the multi-layer model (SPAM3D) on the same peeling phase corrections. For SPAM2D we used the same model settings as in the previous test cases described in Section 2.4, using a screen height $h = 200$ km and a phase structure function power-law exponent $\gamma = 5/3$. For SPAM3D, we used a multi-layer model with the dominant layer (with the largest weight) at $h = 200$ km and two additional layers (with smaller weights) to add a simple vertical structure (see Table 3.4), using $\gamma = 5/3$ for all layers. This multi-layer setup is a very crude representation of a typical vertical electron density profile (e.g., Smith et al. 2008).

The data processing steps in Section 3.5.2 yielded per target field (i) an instrumentally calibrated, flagged visibility data set with outlier sources suppressed, (ii) a table with self-calibration phase corrections, (iii) a deconvolved target field image and (iv) a target field source model. This data was used as an initial estimate to start the SPAM calibration cycle, consisting of the following steps:

1. Subtract the source model from the visibility data while applying the phase calibration. Peel apparently bright sources.
2. Fit an ionospheric phase model to the peeling solutions. Remove systematic (instrumental) phase drifts.
3. Apply the model phases during re-imaging of the target field.

Compared to Chapter 2, the cycle is changed by adding to step 2 an instrumental phase drift estimation as described in Section 3.4.

The peeling step typically yielded ~ 15 sources for which direction-dependent phase calibration corrections could be obtained. The SPAM model was fitted to the peeling phase corrections using the arbitrary number of 20 free parameters for all rounds of processing. The instrumental phase drift correction was mainly effective in the first SPAM cycle (see Figure 3.3 for an example), reducing the typical RMS residual phase from ~ 40 to ~ 30 degrees. The systematic phase drifts in the second cycle were negligible for both SPAM2D and SPAM3D.

Figure 3.5 shows the RMS phase residuals after fitting the SPAM3D model to the peeling phase corrections in the second calibration round of the NGC 4631 field. The RMS increases significantly at the edges of each 10 minute time block, which is caused by an increase of the peeling phase interval for weaker sources. For many peeled sources the phase corrections are initially determined each 1 to 2 minutes, followed by a time resampling to the visibility time grid

Field name	NGC 4565	NGC 4631
Peeling sources	17	13
Model layer heights (weights):		
SPAM2D:	200 km (1.00)	200 km (1.00)
SPAM3D:	100 km (0.25)	100 km (0.25)
	200 km (0.50)	200 km (0.50)
	400 km (0.25)	400 km (0.25)
RMS residual phase [degrees]:		
SPAM2D	30.8 ± 3.6	27.66 ± 4.79
SPAM3D	30.1 ± 3.6	27.03 ± 4.71
Total flagged data fraction:		
SPAM2D	0.33	0.25
SPAM3D	0.32	0.25

Table 3.4: Overview of the SPAM processing parameters for both target fields (NGC 4565 and NGC 4631).

of 10 seconds. At the edges of each time block, the accuracy of the resampled phase corrections diminishes because the resampling includes a phase extrapolation towards the edges beyond the outer initial phase corrections.

Visibility time stamps that had a RMS residual phase higher than 40 degrees were discarded (see Figure 3.5). In two calibration cycles, this removed a substantial (~ 30 percent) fraction of the data, mainly during the final 3 hours of the observing run. For both fields, the mean RMS residual phase for SPAM3D is slightly lower than for SPAM2D (see Table 3.4).

3.5.3 Output image comparison

Because there is no information available on the true ionosphere-induced phase rotations, we analyze the output images from the SPAM2D and SPAM3D calibration methods to determine the relative performance. It is not our goal to repeat the in-depth comparison against field-based calibration (for this, see Chapter 2). However, we do perform some basic sanity checks against one of the two target field images from Cohen et al. (2004), namely NGC 4565. We label this as field-based calibration (FBC), but in reality it is a (possibly suboptimal) combination of field-based calibration after applying a time-variable phase-calibration.

Residual ionospheric phase errors can generate several direction-dependent types of image artifacts. Because the images are generated from visibilities measured over an extended observing session, all time-varying residual phase errors are accumulated into time-averaged artifacts. Both image background and source properties are inspected for evidence of these artifacts. For convenience, none of the analyzed images have been corrected for primary beam attenuation, so the background noise is approximately flat.

A non-zero mean phase gradient over the array towards a source causes an apparent position shift of the source. Any non-zero mean higher order phase structure causes a deformation of the source. Both a zero-mean time variable phase gradient and higher order phase effects cause smearing and deformation of the source image, and consequently a reduction of the source

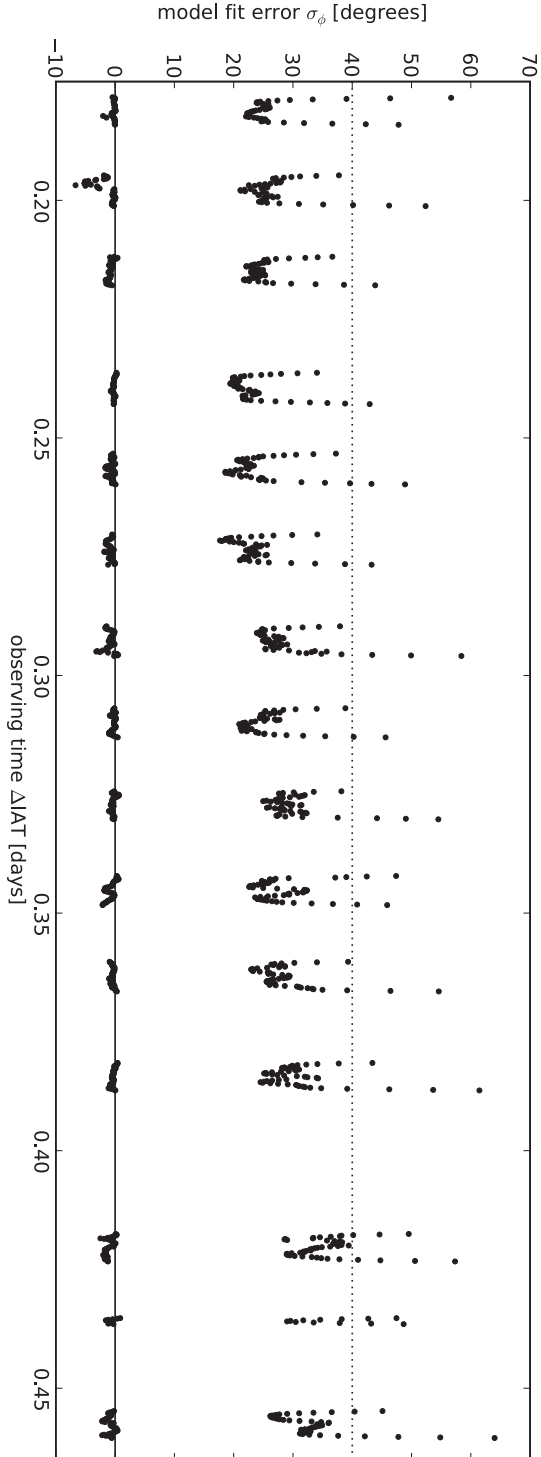


Figure 3.5: Example plot of the RMS residual phase as a function of visibility time stamp for the SPAM3D model fit on the peeling solutions of the NGC 4631 field. All time stamps with phase residuals larger than 40 degrees (dotted line) were discarded. The points near zero degrees (solid line) are the difference between the SPAM3D and SPAM2D RMS phase residuals (SPAM3D-SPAM2D).

Field name	NGC 4565	NGC 4631
Mean background noise σ [mJy beam ⁻¹]:		
FBC	33.1	—
SPAM2D	29.6	32.6
SPAM3D	30.3	32.5
Number of sources within a 6 degree radius with a peak fluxes $> 5\sigma$:		
FBC	559	—
SPAM2D	605	572
SPAM3D	584	582
5σ source count (and fraction) with an NVSS counterpart within $60''$:		
FBC	511 (0.916)	—
SPAM2D	568 (0.939)	549 (0.961)
SPAM3D	550 (0.942)	556 (0.957)

Table 3.5: Overview of results from calibrating and imaging two test fields with field-based calibration (FBC) applied, single-layer SPAM (SPAM2D) calibration applied and multi-layer SPAM (SPAM3D) applied.

peak flux (e.g., see Cotton & Condon 2002). In the presence of time-varying residual phase errors, the source model subtraction during CLEAN deconvolution is incomplete because the average, apparent source model from the output image is distorted, and because the visibilities on individual time stamps deviate from the model visibilities due to the phase errors. Therefore, part of the image background noise level consists of residual sidelobes. The local sidelobe noise increases with both the RMS phase error and the local source flux density. We use both the source peak fluxes, source peak positions and the background noise for our analysis.

To allow for comparison of source properties, we applied the source extraction tool BDSM (Mohan 2008) on all relevant images. BDSM performs a multiple 2-dimensional Gaussian fit on islands of adjacent pixels with amplitudes above a specified threshold based on the *local* image noise σ_L in the image. Multiple overlapping Gaussians are grouped together into single sources. We applied BDSM to all images, using the default extraction criteria (which includes that a source detection requires at least 4 adjacent pixel values above $3\sigma_L$, with at least one pixel value above $5\sigma_L$).

Image noise

For all relevant output images, the mean image background RMS (or simply noise) σ was determined by fitting a Gaussian to the histogram of image pixel values from the inner quarter radius of the FoV where most apparent flux is (see Table 3.5). For both fields, the noise levels for SPAM2D and SPAM3D are approximately equal. The SPAM noise levels are ~ 10 percent lower than for FBC. Visual inspection of the images per field shows that there is very little difference in background structure between SPAM2D and SPAM3D. The FBC image has relatively more traces of deconvolution errors near the brighter sources than the SPAM images.

Counterparts at 1.4 GHz

Table 3.5 contains the number of sources cataloged by BDSM within a 6 degree radius from the field center, with the additional constraint that the peak flux is at least 5 times the mean background noise. Additionally, each catalog was cross-identified against the NVSS catalog (Condon et al. 1994, 1998), which has a lower resolution ($45''$) but also a much lower detection limit (at least 5 times lower for an average spectral index of -0.8). Table 3.5 lists the number of sources (and fractions) that have an NVSS counterpart within $60''$. This limit gives sufficient room to accomodate resolution issues (e.g. single source in NVSS might be double in 74 MHz images) while introducing very few false associations (Cohen et al. 2007). For the SPAM methods, the association fractions are slightly higher for the NGC 4631 field, which makes the total number of associations for both fields roughly equal. FBC has a slightly lower association fraction, which results in ~ 8 percent fewer associated sources as compared to SPAM2D and SPAM3D. To minimize contamination with fake detections, we continue our analysis with sources that have an NVSS counterpart, thereby risking the loss of an incidental ultra-steep spectrum source.

Peak fluxes

To compare source properties from the different calibration techniques, the available catalogs for each field are individually cross-identified with a $60''$ search radius. The peak fluxes of associated sources are plotted in Figure 3.6. We use peak fluxes rather than integrated flux densities because of the larger uncertainties in the determination of the latter, and because most sources are unresolved at $25''$ resolution (Cohen et al. 2004). For each field, there is a tight match between source peak fluxes from the different calibration methods. For sources that have peak fluxes $> 10\sigma$ in both catalogs, the mean peak flux ratio lies within 2 percent of unity. The relatively high association fraction and relatively tight peak flux correlation between SPAM2D and SPAM3D is expected to be strongly influenced by the common SPAM data reduction steps.

Astrometric accuracy

Despite the $45''$ resolution of the NVSS, the RMS position error for NVSS sources brighter than 15 mJy is better than $1''$. The astrometric accuracy of extracted sources in the two 74 MHz target field images is expected to be worse, as they are likely to be dominated by systematic residual phase gradients after ionospheric calibration (see Chapter 2). We estimate the astrometric errors in the target fields by comparing the peak positions of a subset of > 300 compact sources (gaussian width $< 32.5''$) against the peak positions of close NVSS sources (within $10''$ to minimize resolution mismatches). Note that a changing spectral index across a source may add to the observed position difference, but this effect is equal for both the calibration methods (SPAM2D and SPAM3D) under examination. The position differences for both fields and both calibration methods are plotted in Figure 3.7.

For both target fields and both SPAM versions, the position offsets are scattered around a mean that is systematically offset from zero by $\lesssim 1''$ in roughly the same direction. Because the astrometry for the whole field depends on the accuracy of the assumed (NVSS) positions of the ~ 15 peeled calibrators, it is most likely that a non-zero mean position error in the assumed calibrator positions causes the observed systematic offset, which is (by coincidence) similar in amplitude and direction for both fields. We continue by removing the systematic offset from all catalog positions.

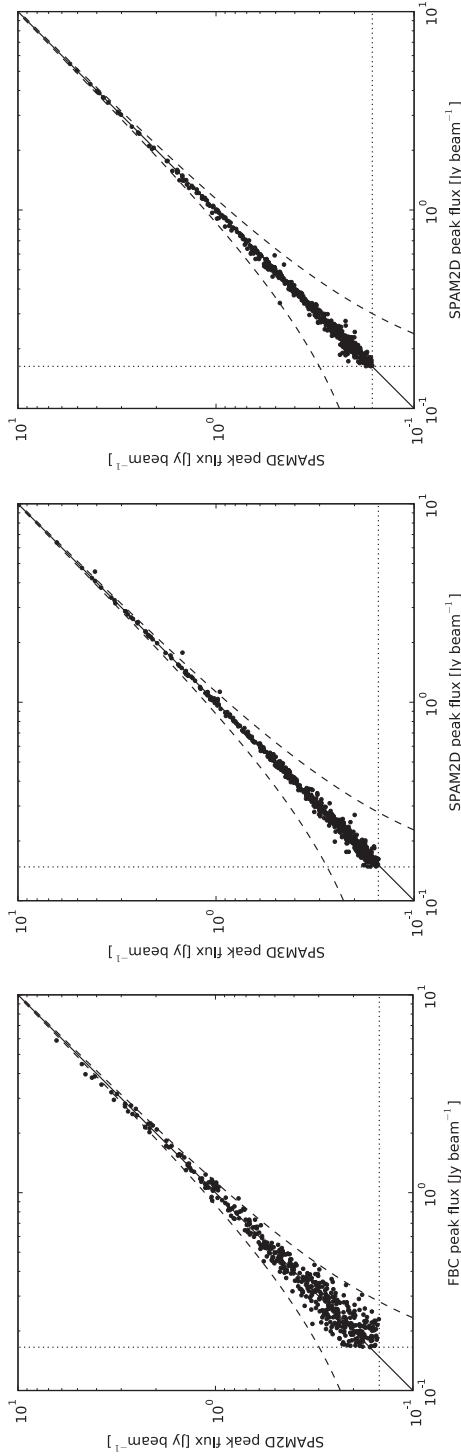


Figure 3.6: Peak flux comparisons in the NGC 4565 and NGC4631 fields *Left:* Peak flux comparison for 474 sources detected in both the FBC and SPAM2D images of the NGC 4565 field. The straight diagonal line represents equality, the dashed lines represent $3\sigma_C$ deviations (where σ_C is the combined (quadratically added) noise level from both images), and the dotted lines indicate the 5σ detection limit. The peak flux comparison of 472 sources between FBC and SPAM3D for the same field (not plotted here) is very similar. *Middle:* Same for 537 sources in the SPAM2D and SPAM3D images of the NGC 4565 field. *Right:* Same for 539 sources in the SPAM2D and SPAM3D images of the NGC 4631 field.

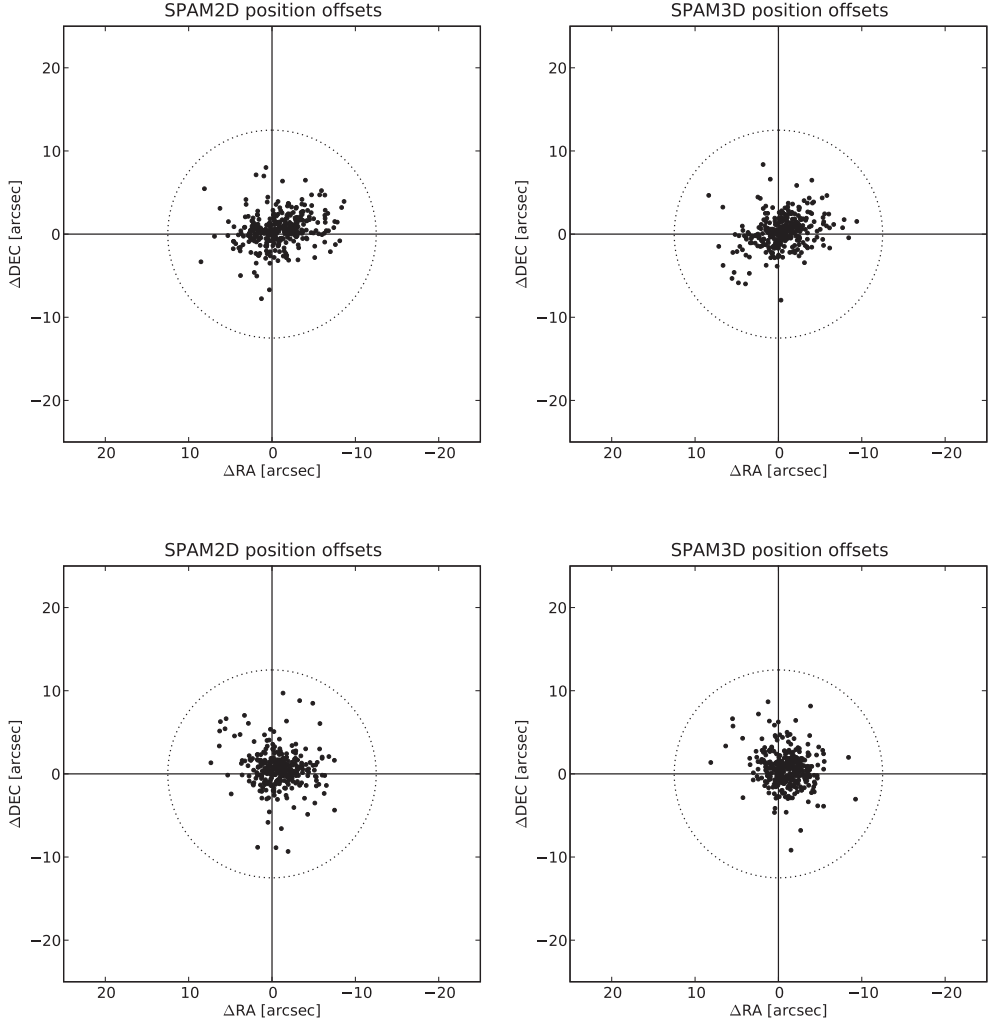


Figure 3.7: Position offsets of a subset of compact sources in the NGC 4565 field (*top row*) and NGC 4631 field (*bottom row*) as measured in the SPAM2D images (*left column*) and SPAM3D images (*right column*), using the NVSS catalog as a reference. The dotted line marks the size of the 25'' restoring beam.

For the NGC 4565 field the measured RMS position offsets around the zero mean are $3.44''$ and $3.27''$ for SPAM2D and SPAM3D, respectively, and for the NGC 4631 field the measured RMS position offsets are $3.24''$ and $2.96''$, respectively. Removing the intrinsic $< 1''$ RMS position error in NVSS would lower these values by $0.17''$ at most, but this correction has little consequence for our performance comparison. By differencing the RMS position offsets in quadrature, we estimate that using SPAM3D instead of SPAM2D improved the overall RMS astrometric accuracy by $1.31''$ and $1.07''$ for the NGC 4565 and NGC 4631 fields, respectively.

3.6 Discussion and conclusions

We have extended the ionospheric phase calibration method SPAM (Chapter 2) with a multi-layer ionosphere model and an instrumental phase drift estimator, in an attempt to improve the calibration accuracy of wide-field low-frequency radio interferometric observations. The SPAM method has been successfully tested on simultaneous, extended 74 MHz VLA observations of two fields in the largest A-configuration under quiet ionospheric conditions. From this test case we draw the following conclusions:

(i) The performance of the multi-layer ionosphere model is similar to that of a single-layer model. Application of the multi-layer model resulted in a small (~ 10 percent), but still significant improvement in the overall astrometric accuracy as compared to the single-layer model, while no noticeable changes are observed in the background noise or source peak fluxes. Global distortions in the astrometry are induced by residual phase gradients that vary across the FoV. For a single-layer model, we estimated that the presence of a 3-dimensional smooth ionosphere can cause systematic phase gradient errors, which affects the astrometric accuracy. Although not conclusive, an improved representation of the large-scale 3-dimensional ionosphere by the multi-layer model can explain the improvement in astrometry, while the other image characteristics should remain the same. This improved representation may also be reflected in the small reduction of the RMS phase residual after model fitting, which can indicate a better consistency between the astrometry of the calibrators and the multi-layer model as compared to the single-layer model.

(ii) The phase drift estimator was successful in detecting and removing several large antenna-based phase offsets and drifts from the visibility data. This significantly reduced the RMS residual phase after SPAM model fitting by ~ 25 percent on average. The phase offsets are probably the result of an inaccurate instrumental phase estimation from a relatively short calibrator observation. The phase drifts (up to 40 degrees over 8 hours for one antenna) are not known to have a clear cause. Because the data reduction does not apply time-variable phase corrections before this estimator, and because the same phase drifts are observed in both target field data sets, we exclude the data reduction as a possible cause for the phase drifts. The ionosphere itself is an unlikely candidate, because of the persistent nature of the phase deviations and the absence of the same phase structure on neighbouring antennas. Mechanical deformation or communication delay changes are unlikely, because the VLA is known to be phase stable on much higher observing frequencies (also, a 40 degree phase change at 74 MHz corresponds to a significant path length difference of ~ 45 cm). Possibly, the phase drifts are induced in 74 MHz-specific receiver hardware at some antennas.

(iii) Our full data reduction, including SPAM ionospheric calibration, generated images in which the flux density scale is well matched to an earlier, independent data reduction by Cohen et al.

(2004). There is no noticeable improvement in the peak fluxes, but the mean background noise level in the central beam area has lowered by ~ 10 percent to $\sim 30 \text{ mJy beam}^{-1}$. The improved suppression of sidelobes appears to be the main reason, which indicates a modest improvement in phase calibration accuracy.

For our test case, replacing the SPAM single-layer model with a multi-layer model did not lead to significant improvements in image quality like in Chapter 2. It was noted by Cohen et al. (2004) that the ionospheric conditions during the observations of the test case data were ‘favourable’. The observations were performed mostly during nighttime, which on average leads to more quiet ionospheric activity (e.g., Cohen & Röttgering 2009). Also, VTEC values are generally low during nighttime ($\sim 1 \text{ TECU}$). Calibrating observations that were recorded during increased ionospheric activity may unambiguously show whether the multi-layer ionosphere model indeed performs better than the single-layer model. The multi-layer model accuracy may also be improved by optimizing the set of parameters that define the model, like the number of layers, the layer heights and weights, the phase structure function power-law exponent, the number of free model parameters, etc.

To further explore the performance, robustness and limitations of the SPAM method, we will continue to process data sets obtained with different existing low-frequency arrays under different ionospheric conditions. Developments for testing SPAM in a simulated environment are currently in progress. These test cases will be used to optimize the choice of model parameters for different observing conditions. We also investigate possibilities to further extend the SPAM calibration method, like including time evolution in the ionosphere model.

Acknowledgements. The authors would like to thank Rudolf Le Poole, Reinout van Weeren, Niruj Mohan, Sridharan Rengaswamy, James Anderson, Ger de Bruyn, Jan Noordam, Maaijke Mevius, Juan Uson, Cathyn Mitchell, Paul Spencer, Ian McCrea and Hans van der Marel for useful discussions. HTI acknowledges a grant from the Netherlands Research School for Astronomy (NOVA). SvdT acknowledges NWO-STW grant number DTC.5893.

Deep low-frequency radio observations of the NOAO Boötes field I. Data reduction and catalog construction

Abstract. In this chapter we present deep, high-resolution radio interferometric observations at 153 MHz to complement the extensively studied NOAO Boötes field. We provide a description of the observations, data reduction and source catalog construction. From our single pointing GMRT observation of ~ 12 hours we obtain a high-resolution ($26'' \times 22''$) image of ~ 11.3 square degrees, fully covering the Boötes field region and beyond. The image has a central noise level below $1.0 \text{ mJy beam}^{-1}$, which rises to $2.0\text{--}2.5 \text{ mJy beam}^{-1}$ at the field edge, making it one of the deepest ~ 150 MHz surveys to date. The catalog of 598 extracted sources is estimated to be > 95 percent complete at the 20 mJy level, while the estimated contamination with false detections is < 1 percent. The low systematic RMS position error of $1.24''$ facilitates accurate matching against catalogs at optical, infrared and other wavelengths. The differential source counts, accurately measured down to ~ 20 mJy, are consistent with interpolated source counts at 325 MHz for a mean spectral index of -0.8 , indicating that the dominant population in this survey consists of AGN. Combination with available deep 1.4 GHz observations yields an accurate determination of spectral indices for 417 sources down to the lowest 153 MHz flux densities, of which 16 have ultra-steep spectra with spectral indices below -1.3 . The detection fraction of the radio sources in K -band is found to drop with radio spectral index, which is in agreement with the known correlation between spectral index and redshift for brighter radio sources.

H. T. Intema, R. J. van Weeren, H. J. A. Röttgering, D. V. Lal, and N. R. Mohan
Submitted to Astronomy & Astrophysics

4.1 Introduction

Surveying the radio sky at low frequencies ($\lesssim 300$ MHz) is a unique tool for investigating many questions related to the formation and evolution of massive galaxies, quasars and clusters of galaxies (e.g., Miley & De Breuck 2008). Low-frequency radio observations benefit from the steepness of radio spectra of various types of cosmic radio sources, such as massive high redshift radio galaxies (HzRGs; $z \gtrsim 2$) and diffuse halo & relic emission in nearby galaxy clusters ($z \lesssim 0.1$).

HzRGs are amongst the most massive galaxies in the early Universe (e.g., Miley & De Breuck 2008), usually located in forming galaxy clusters with total masses of more than $10^{14} M_{\odot}$ (e.g., Venemans et al. 2007). The most efficient way of finding HzRGs is to focus on radio sources having ultra-steep spectra (USS; Roettgering et al. 1997; De Breuck et al. 2002). This was recently reinforced by Klammer et al. (2006) who showed that the radio spectra of HzRGs in general do not show spectral curvature, but are straight. Concentrating on the faintest sources from surveys made at the lowest frequencies is therefore an obvious way of pushing the distance limit for HzRGs beyond the present highest redshift of TN J0924-2201 at $z = 5.1$ (van Breugel et al. 1999) and probing massive galaxy formation into the epoch of reionization.

Galaxy clusters containing diffuse radio sources appear to have large X-ray luminosities and galaxy velocity dispersions (e.g., Hanisch 1982), which are thought to be characteristics of cluster merger activity (e.g., Giovannini & Feretti 2000; Kempner & Sarazin 2001). Synchrotron halos and relics provide unique diagnostics for studying the magnetic field, plasma distribution and gas motions within clusters, important inputs to models of cluster evolution (e.g., Feretti & Johnston-Hollitt 2004). Cluster synchrotron emission is known to be related to the X-ray gas and pinpoints shocks in the gas. Further, cluster radio emission usually has steep radio spectra ($\alpha < -1$), the radiating electrons are old and can provide fossil records of the cluster history (e.g., Miley 1980).

Several low-frequency surveys have been performed in the past, such as the Cambridge surveys 3C, 4C, 6C and 7C at 159, 178, 151 and again 151 MHz, respectively (Edge et al. 1959; Bennett 1962; Pilkington & Scott 1965; Gower et al. 1967; Hales et al. 1988, 2007), the UTR-2 sky survey between 10-25 MHz (Braude et al. 2002), the more recent VLSS at 74 MHz (Cohen et al. 2007) and the ongoing MRT sky survey at 151.5 MHz (e.g., Pandey & Shankar 2007). All these surveys are limited in sensitivity and angular resolution, mainly due to man-made radio frequency interference (RFI), ionospheric phase distortions and wide-field imaging problems. Recent developments in data reduction techniques make it possible to perform deeper surveys ($\lesssim 50$ mJy beam $^{-1}$) of the low-frequency sky at higher resolution ($\lesssim 30''$).

In this chapter we present deep, high-resolution GMRT¹ observations at 153 MHz of the NOAO² Boötes field. The Boötes field is a large (~ 9 square degree) northern field that has been targeted by surveys spanning the entire electromagnetic spectrum. This field has been extensively surveyed with radio telescopes including the WSRT³ at 1.4 GHz (de Vries et al. 2002) and the VLA⁴ at 74 and 325 MHz (Intema et al. *in preparation*; Croft et al. 2008). The large northern NOAO Deep Wide Field Survey (NDWFS; Jannuzi & Dey 1999) provided 6 colour images ($B_w R I J H K$) to very faint optical and near-infrared (NIR) flux limits. Additional, deeper

¹Giant Metrewave Radio Telescope.

²National Optical Astronomy Observatory.

³Westerbork Synthesis Radio Telescope.

⁴Very Large Array.

NIR images in $J K_s$ are available from the FLAMINGOS Extragalactic Survey (FLAMEX; Elston et al. 2006), while additional z -band images are available from the z Bootes campaign (Cool 2007). The entire area has also been surveyed by Spitzer in seven IR bands ranging from 3.6 to $160\ \mu\text{m}$ (Eisenhardt et al. 2004; Houck et al. 2005). Chandra has covered this area in the energy range of 0.5–7 keV to a depth of $\sim 10^{-14}\ \text{ergs s}^{-1}\ \text{cm}^{-2}$, yielding 3200 quasars and 30 luminous X-ray clusters up to redshift $z \sim 1$ (Murray et al. 2005; Kenter et al. 2005). The UV space telescope GALEX has covered the Boötes field. All the 10,000 galaxies brighter than $R < 19.2$ and X-ray / IRAC / MIPS QSOs brighter than $R < 21.5$ have redshifts through the AGES project (Kochanek et al. *in preparation*). Based on the shallow Spitzer data, 3 HzRGs with photometric redshifts of $z > 4$ have been identified in the Boötes field (Croft et al. 2008). Also, Cool et al. (2006) report the discovery of 3 quasars with spectroscopic redshifts $z > 5$, while McGreer et al. (2006) found a quasar at $z = 6.1$.

Given the size of the GMRT field-of-view (FoV; ~ 3.5 degrees) and angular resolution ($\sim 25''$) at 153 MHz, the Boötes field is a well-matched region for conducting a deep survey. Combined with the existing multi-wavelength surveys, our deep 153 MHz Boötes field observations allow for a complete population study of faint ($\gtrsim 10\ \text{mJy}$) low-frequency radio sources. For the data reduction, we used the recently developed SPAM calibration software that solves for spatially variant ionospheric phase rotations (see Chapters 2 and 3). This has yielded significant improvements in the dynamic range and image reliability of several VLA 74 MHz fields as compared to previously existing calibration methods. In our initial analysis of the 153 MHz source catalog we focus on determining source counts down to the detection limit, and identifying steep-spectrum radio sources that are candidate HzRGs.

In Section 4.2, we describe the GMRT 153 MHz observations and data reduction. In Section 4.3, we present details on the source extraction and catalog construction. Section 4.4 contains an initial analysis of the source population. A discussion and conclusions are presented in Section 4.5. Throughout this chapter, source positions are given in epoch J2000 coordinates.

4.2 Observations and data reduction

In this section, we describe the observations and data reduction steps that led to the production of the 153 MHz image that is the basis of the survey.

4.2.1 Observations

The GMRT (e.g., Nityananda 2003) is an interferometer consisting of 30 antennas, with almost half the antennas located at random positions within a central square kilometer, and the remaining antennas distributed in an approximate Y-shape. The non-coplanar configuration provides baseline lengths ranging from $\sim 50\ \text{m}$ up to 30 km, covering almost three orders of magnitude in spatial scales on the sky. The 45 meter dish diameter makes the GMRT suitable for efficient observing down to the lowest frequency (currently 153 MHz). The diameter of the FoV at 153 MHz, defined by the half-power beam width (HPBW) of individual antennas, is 3.1 degrees, and the full width at half maximum (FWHM) of the synthesized beam is typically $20''$ to $25''$. At 153 MHz, the effectiveness of the shortest baselines (mostly within the central square) is compromised due to the presence of strong RFI within the full observing bandwidth. Also, the low observing frequency, in combination with the low-latitude location of GMRT relatively

Date	June 3, 2005	June 4, 2005
LST range	12–20 hours	10–19 hours
local time ^a range	20:00–04:00	18:00–03:00
Time on target	359 min	397 min
Primary calibrator	3C 286	3C 286
Time on calibrator	94 min	108 min

^a Indian Standard Time (IST) = Universal Time (UT) + 5:30

Table 4.1: Overview of GMRT observations on the Boötes field.

near the geomagnetic equator, results in an increase of ionospheric phase rotations that vary with time and viewing direction.

The Boötes field was observed with the GMRT during two consecutive nights (Table 4.1), with the field centered at $14^{\text{h}}32^{\text{m}}05.75^{\text{s}}$ right ascension and $+34^{\circ}16'47.5''$ declination. Visibilities were recorded each 16.8 seconds in a single sideband of 8.0 MHz centered at 153.1 MHz, comprising 128 channels of 62.5 KHz each, in two circular polarizations (RR and LL). The bandwidth was narrowed to ~ 6 MHz by antenna-based bandpass filters to reduce the effect of RFI at the edges of the observing band. Observing in the spectral channel mode allows for excision of narrow-band RFI in the observing band, and for reducing bandwidth smearing during imaging.

During both nights, the target field was observed in time blocks of 36 minutes, alternated with 8 minute observations on the calibrator (3C 286). The relatively high overhead in calibrator observations was justified by the need to monitor the GMRT system stability, RFI conditions and ionospheric conditions, and to ensure the consistency of the flux scale over time. The directional variation of ionospheric phase rotations between calibrator and target field compromises the astrometric accuracy when transferring the calibrator phase solutions. There were typically 27 antennas available during each observing run. A power failure at the start of the first observation night caused a ~ 1 hour effective loss of observing time.

4.2.2 Data reduction

The data reduction was performed in two stages. The first stage consisted of ‘traditional’ calibration, in which the flux scale, bandpass shapes and phase offsets were determined from the calibrator observations, transferred to the target field data, after which the target field was self-calibrated and imaged for several iterations. During the second stage of the data reduction, we made use of the recent SPAM software package (see Chapters 2 and 3) that incorporates direction-dependent ionospheric phase calibration. A detailed description of these stages follows below.

Traditional calibration

We adopted a point source model for calibration against 3C 286, with a flux density of 31.01 Jy on the Perley–Taylor 1999.2 scale⁵, which is derived from the Baars et al. (1977) scale for 3C 295. The following reduction steps were performed independently on the data sets from both nights.

For the first phase of data reduction, we used the Astronomical Image Processing Software (AIPS; e.g., Bridle & Greisen 1994) package, developed by the National Radio Astronomy Observatory (NRAO). A first round of flagging consisted of removal of dead and malfunctioning antennas and baselines, systematic removal of the first 30 seconds of each observing time blocks due to potential system instabilities, and manual and semi-automated flagging of channels and time ranges on individual baselines, based on excessive (≥ 5 times the RMS) visibility amplitudes. An initial phase calibration was performed on 3C 286 with the highest possible (16.8 sec) time resolution, using a small, (relatively) RFI-free channel range. Bandpass calibration on 3C 286 (normalized to the same channel range) was followed by a combined amplitude and phase (A&P) calibration on the same source on a 10 minute time scale. The bandpass, amplitude and (combined) phase calibration was transferred to the target field data. The outer channels of the target field data were dropped due to excessive noise and RFI, resulting in a 6.75 MHz effective bandwidth.

The target field data of the first night was imaged (see Table 4.2), followed by three rounds of phase-only self-calibration & imaging (60, 30 and 16.8 seconds time resolution, respectively) and one final round of (60 seconds) A&P self-calibration & imaging using gain normalization to preserve the flux scale. The data from both nights were A&P calibrated (normalized, 16.8 sec) against this target field model, after which the target field model was subtracted from the visibilities. The residuals were manually and semi-automatically flagged per baseline for excessive visibility amplitudes, after which the model was added back. The resulting visibility data sets for both nights were combined into one data set and imaged. The RMS of the image background, determined by fitting a gaussian to the pixel values of the inner half of the (uncorrected) primary beam area, is approximately $1.4 \text{ mJy beam}^{-1}$. Near the brightest three sources with apparent flux densities larger than 1 Jy, the background RMS is measured to be $> 2.2 \text{ mJy beam}^{-1}$.

Direction-dependent phase calibration

Despite the good overall quality of the self-calibrated image from the first stage, there were significant artifacts present in the background near the bright sources, limiting the local dynamic range to a few hundred.

The time variations in the antenna-based phase corrections from self-calibration indicated that the ionospheric conditions were relatively quiet during the observations. This conclusion was further strengthened by a visual inspection of the 153 MHz image, which showed many relatively undistorted, compact point sources that match well in source positions to those in the 1.4 GHz NVSS catalog (Condon et al. 1994, 1998). However, the presence of significant image artifacts near the brightest sources indicated that the image quality could be further improved by including direction-dependent phase corrections through SPAM.

The SPAM package uses the ParselTongue interface (Kettenis et al. 2006) to access AIPS

⁵Defined in the ‘VLA Calibrator Manual’, available online through <http://www.vla.nrao.edu/astro/calib/manual/baars.html>

Field diameter	6.8° ^(a)
Pixel size	4''
Weighting	robust 0.5 ^(b)
Wide-field imaging	polyhedron (facet-based) ^c
Number of initial facets	199
Facet diameter	0.57°
Facet separation	0.47°
Deconvolution	Cotton-Schwab CLEAN ^d
CLEAN box threshold	5 σ
CLEAN depth	2 σ
Restoring beam	26'' \times 22'' (78°)

^a We map more than twice the HPBW diameter to allow for deconvolution of nearby bright sources.

^b Briggs (1995)

^c Perley (1989a); Cornwell & Perley (1992)

^d Schwab (1984); Cotton (1999); Cornwell et al. (1999)

Table 4.2: Overview of the wide-field imaging parameters.

tasks and files from the Python programming environment, while providing a collection of high-level tasks for basic calibration and imaging and for calibration of direction-dependent ionospheric phase rotations. SPAM measures the antenna-based, direction-dependent phase rotations by peeling bright sources in the FoV (Noordam 2004), separates (constant) instrumental and (time- and spatially variable) ionospheric phase contributions, combines the ionospheric phases into a consistent phase screen model, and predicts the ionospheric phase corrections in arbitrary viewing directions while imaging the FoV.

For our data sets, we noticed discontinuous phase behaviour in the calibration solutions on several antennas that was clearly of instrumental origin. SPAM is able to correct for slow instrumental phase drifts on a few antennas (see Section 3.4), but not for abrupt transitions. Self-calibration is relatively unconstrained and can solve for antenna-based phase discontinuities, but lacks directional variability. Applying both self-calibration and SPAM would seem to be a logical option, although the combined effect is difficult to predict because self-calibration invalidates the SPAM assumption of constant instrumental phases. Under quiet ionospheric conditions, when the phase structure over the array for different viewing directions is dominated by slowly varying gradients, self-calibration may approximately solve for an overall phase gradient but not for any higher order phase structure. Applying SPAM after self-calibration can be considered as a perturbation to the overall gradient correction.

For the data reduction presented here, complementing self-calibration with SPAM resulted in a significant reduction of background noise, most noticeable near the bright sources. The self-calibrated data set (collapsed into 27 frequency channels & polarizations combined into Stokes I) and source model are used as an initial estimate to start the SPAM calibration cycle, consisting of the following steps:

1. Subtract the target field source model from the visibility data while applying the (direction-dependent) phase calibration corrections (if available). Peel apparently bright sources.

Calibration cycles	2
Peeled sources ^a	24
Number of added facets	24
Layer heights (weights)	100 km (0.25) 200 km (0.50) 400 km (0.25)
Parameter γ^b	5 / 3
Model parameters	20
Model fit phase RMS ^a	$19.2^\circ \pm 3.0^\circ$
Peeling corrections applied	yes
Reference catalog	NVSS ^c

^a Specified for the final (second) calibration cycle only.

^b Power-law slope of the assumed phase structure function.

^c Condon et al. (1994, 1998)

Table 4.3: Overview of the SPAM processing parameters. For more information on the meaning of the parameters, see Chapters 2 and 3).

2. Fit an ionospheric phase model to the peeling solutions.
3. Apply the ionospheric phase model phases during re-imaging of the target field.

The total SPAM calibration consisted of two cycles, for which relevant parameters are given in Table 4.3. We used the same imaging parameters as given in Table 4.2, but centered an additional 24 facets at the locations of the peeled sources to minimize pixellation effects (e.g., Cotton & Uson 2008). The image background RMS in the inner half of the primary beam area is on average $1.0 \text{ mJy beam}^{-1}$, while the local noise near the brightest three sources is $< 1.45 \text{ mJy beam}^{-1}$. Because all three bright sources are located outside the HPBW, we expect that the remaining background artifacts are dominated by visibility amplitude errors due to residual RFI, pointing errors and rotating, non-circular primary beam patterns (e.g., Bhatnagar et al. 2008).

4.3 Catalog construction

In this section we describe the construction of the source catalog that was extracted from the 153 MHz image of the Boötes field. The resulting image after SPAM calibration was scaled down by 4 percent to incorporate a correction to the flux calibrator scale (see Section 4.3.4). Next, the image was corrected for primary beam attenuation with a circular beam model⁶

$$A(\theta, \nu) = 1 - 4.04 \cdot 10^{-3}(\theta\nu)^2 + 76.2 \cdot 10^{-7}(\theta\nu)^4 - 68.8 \cdot 10^{-3}(\theta\nu)^6 + 22.03 \cdot 10^{-3}(\theta\nu)^8, \quad (4.1)$$

where θ is the angular distance from the pointing center in arcminutes and ν the observing frequency in GHz. As the fractional bandwidth is small (< 4 percent), we use same the central

⁶From the GMRT User Manual.

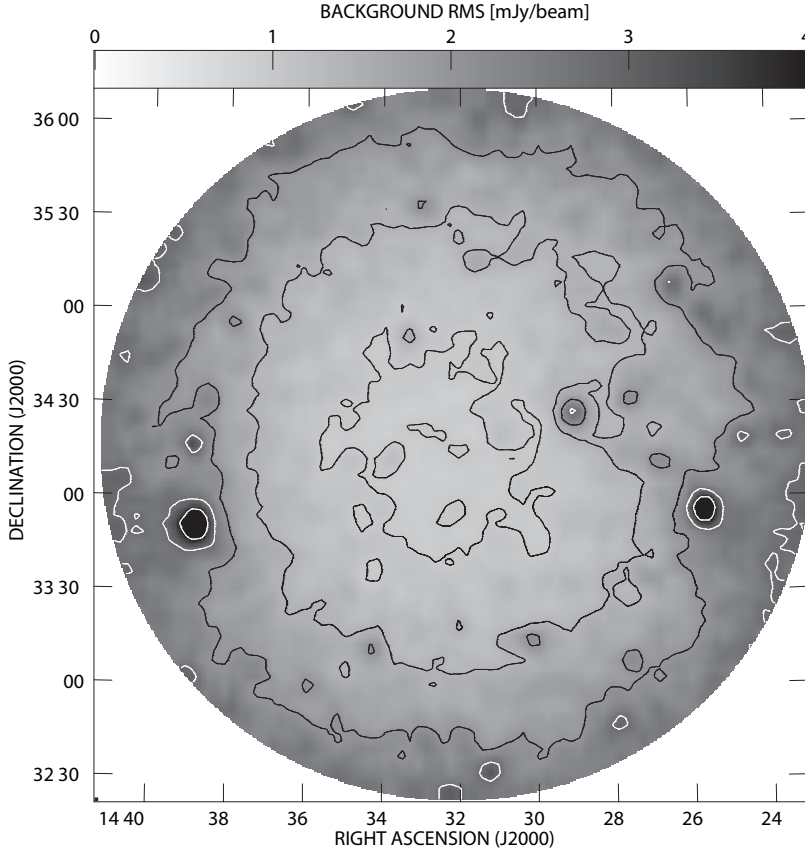


Figure 4.1: The grayscale map represents the local background RMS as measured in the (primary beam corrected) Boötes field image. The overplotted contours mark lines of equal RMS at [1.0, 1.4, 2.0, 2.8, 4.0] mJy beam^{-1} (white above 2.0 mJy beam^{-1}). The local enhancements in RMS coincide with the positions of the brightest sources.

frequency (153.1 MHz) beam model for all frequency channels. The image area is limited to $A(\theta, \nu) > 0.3$ to reduce the propagation of inaccuracies in the primary beam model and to limit the increase of background noise near the edge. This yields a circular survey area of 11.3 square degrees. Figure 4.1 shows a map of the local background RMS of the circular survey area, which has a large central area with a background RMS less than 1.0 mJy beam^{-1} , a global increase of the local noise to 2.0–2.5 mJy beam^{-1} when moving towards the field edge, and several small areas around bright sources where the local noise is approximately twice the surrounding noise level. The overall background RMS was found to be 1.7 mJy beam^{-1} .

For an observation of ~ 10 hours, the theoretical thermal noise level for the GMRT at 153 MHz is estimated to be $\sim 0.2 - 0.3 \text{ mJy beam}^{-1}$ (⁷). For our observation, the measured noise level in the central part of the field is a factor of 3 to 5 larger. We think this discrepancy

⁷Derived from the GMRT User Manual.

is mainly due to the combined result of residual RFI and residual calibration errors, because of the systematic patterns that remain visible in the image background. Pointing errors and non-circular symmetry in the primary beam pattern are likely to be the main cause for the residual sidelobe noise, most apparent around the bright sources (e.g., Bhatnagar et al. 2008).

Although we used multi-frequency synthesis, the 0.25 MHz width of individual frequency channels causes bandwidth smearing during imaging. Applying the standard formula (e.g., Thompson 1999) to our case, the radial broadening of sources at the edge of the field (at 1.9 degree from the pointing center) is estimated to be $\sim 11''$, which is half the minor axis of the restoring beam. Similarly, the visibility time resolution of 16.8 sec causes time average smearing in the order of $\sim 8''$ at the field's edge. This may appear problematic, but the majority of sources are detected within the inner part of the primary beam (both effects scale linearly with radial distance from the pointing center), and the total flux density of smeared sources is conserved.

4.3.1 Source extraction

We used the *Blob Detection & Source Measurement* (BDSM) software package (Mohan 2008) to extract sources from our image. With our settings, BDSM estimates the local background noise level σ_L over the map area, searches for peaks $> 5\sigma_L$, expands the $5\sigma_L$ detections into islands by searching for adjacent pixels $> 3\sigma_L$ (rejecting islands smaller than 4 pixels), fits the emission in the islands with gaussians, and estimates the flux densities, shapes and positions of sources (including error estimates) both by grouping of fitted gaussians into sources and by a direct moments analysis of the island pixels. These detection criteria were found to include very few fake sources (see Section 4.3.2). Uncertainties in the source flux density, position and shape measurements are estimated following Condon (1997).

BDSM detected 644 islands, for which the 935 fitted gaussians were grouped into 696 distinct sources. Of these, 499 sources were fitted with a single gaussian. Visual inspection of the image, complemented with a comparison against a very deep 1.4 GHz map (see Section 4.3.3), resulted in the removal of 16 source detections in the near vicinity of six of the seven brightest sources. We also removed 4 sources that extended beyond the edge of the image. To facilitate total flux density measurements at the high flux end, we combined multiple source detections in single islands, and manually combined 50 additional source detections that were assigned to different islands but appeared to be associated in either the 153 MHz image or the deep 1.4 GHz map. The combined flux density is the sum of the individual components, while the combined position is a flux-weighted average. Error estimates of the positions and flux densities of the components are propagated into error estimates of the combined flux density and position. The final catalog consists of 598 sources.

4.3.2 Completeness and contamination

We estimated the completeness of the 153 MHz catalog by performing Monte-Carlo simulations. The source extraction process generated a residual image from which all detected source flux was subtracted. For our simulation, we inserted 1000 artificial point sources into the residual image, and used the same mechanism as described in Section 4.3.1 to extract them. The artificial source positions were selected randomly, but never within $50''$ of another source, a blanked region (near the image edge) or a > 10 mJy residual. The source peak fluxes S were chosen

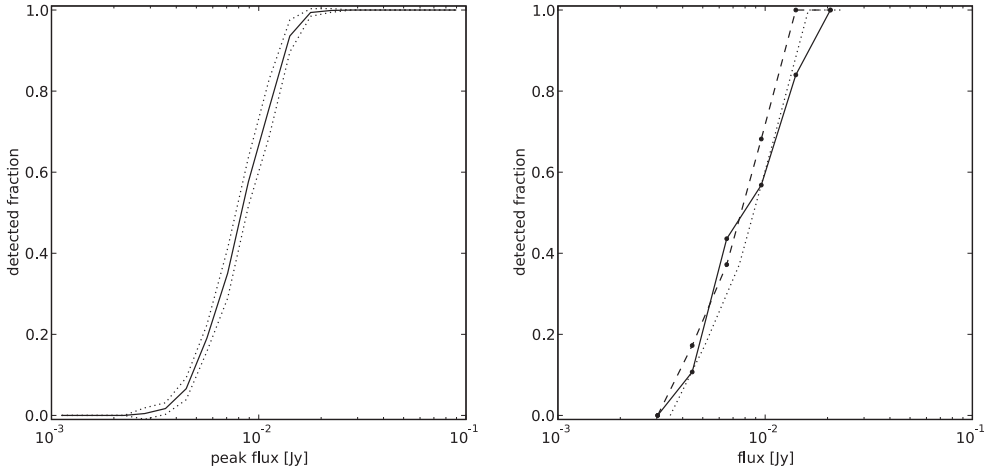


Figure 4.2: Detection fractions as a function of flux. *Left:* Result from 20 Monte-Carlo simulations, in which 1000 point sources with varying fluxes were inserted into the residual image, followed by a source extraction. The horizontal axis denotes the input (peak) flux. The solid line is the average detection fraction, and the dotted lines denote the 1σ uncertainty. *Right:* Result from scaling the peak flux and total flux density of a subset of high S/N sources with varying sizes down to the detection limit, and applying the $5\sigma_L$ detection criteria. The dashed line is the detection fraction as a function of peak flux, the solid line is the detection fraction as a function of total flux density, and the dotted line is the dashed line shifted in flux by 15 percent to approximately match the solid line.

randomly within the range 3 mJy to 3 Jy, while obeying the source count statistic $dN/dS \propto S^{-1.5}$, which produced statistically sufficient detection counts in all logarithmic flux bins (except in the highest flux bins). The simulation was repeated 20 times to improve the accuracy and to derive error estimates. The detection fractions are plotted in Figure 4.2. From this plot, the estimated completeness is ~ 70 percent at 10 mJy and ~ 99 percent at 20 mJy.

In this approach we have ignored several effects that may influence the detectability of sources, such as (i) the intrinsic size of sources, (ii) calibration errors, and (iii) imaging and deconvolution. The source detection algorithm uses a peak detection threshold. Sources that are resolved or are defocussed due to calibration errors will therefore have a decreased probability of detection. We have not attempted to model for the angular size distribution of sources at this frequency. However, previous observations show that the major fraction of low-frequency sources are unresolved at $\sim 25''$ resolution (e.g., Cohen et al. 2004; George & Ishwara-Chandra 2009). In our catalog, more than 90 percent of the sources appear to have simple, near-gaussian morphologies. Assuming the angular size distribution of sources changes slowly with source flux density, and assuming that calibration and imaging smearing affects all sources in a statistically equal way, we can estimate the resolution bias from the catalog itself. For this purpose, we select a subset of 214 high S/N sources with peak fluxes between 12 and $20\sigma_L$ and simple morphologies. The flux densities of these sources were scaled down by a factor of 4 to create an artificial population of sources near the detection threshold. After applying the $5\sigma_L$ detection criterium, we determined the detection fractions, both as a function of peak flux and total (integrated) flux density (Figure 4.2). Although this approach suffers from low number statistics, the

general trend of both detection fraction functions is similar but shifted in flux by ~ 15 percent. We therefore assume that the true completeness is approximated by the point source completeness derived from the Monte-Carlo simulations, shifted upwards in flux by 15 percent.

A known effect that arises from the deconvolution process is CLEAN bias (e.g., Condon et al. 1994, 1998; Becker et al. 1995). This is a systematic negative offset in the recovered flux densities after deconvolution, probably the result of false CLEANing of sidelobe peaks in the dirty beam pattern. One can estimate the CLEAN bias by injecting artificial sources into the visibility data and compare the recovered flux densities after imaging & deconvolution with the injected flux densities. We have not attempted this approach, but instead taken precautions to minimize the CLEAN bias effect. In our case, the dirty beam is well-behaved due to a relatively uniform UV-coverage from two extended observing runs, in combination with multi-frequency synthesis and a robust weighting parameter of 0.5 (slightly towards natural weighting). CLEAN bias is further suppressed through the use of CLEAN boxes in the imaging & deconvolution process.

For an estimate of the contamination of the catalog with fake detections, we compare the GMRT 153 MHz image and extracted source catalog against the results from a deep WSRT 1.4 GHz survey of the Boötes field by de Vries et al. (2002). The 153 MHz and 1.4 GHz observations are well matched in terms of survey area and resolution (~ 7 square degrees and $13'' \times 21''$ for WSRT, respectively). The typical background RMS over the WSRT survey area is $28 \mu\text{Jy beam}^{-1}$. For a spectral index of -0.8 , the 1.4 GHz observations are ~ 10 times more sensitive. We restrict our comparison to a 1.4 degree radius circular area to avoid the noisy edge of the deep 1.4 GHz survey. For all of the 399 sources detected at 153 MHz we find a counterpart in the 1.4 GHz map (383 sources were automatically matched within a $25''$ search radius, while the remaining fraction of sources with complex morphology were confirmed manually). We could not match the full GMRT area, but considering that our source extraction is based on local background RMS and that the false detections only occurred near a few bright sources, we estimate that the contamination of our complete catalog over the full survey area is < 1 percent.

4.3.3 Astrometric accuracy

For an estimate of the astrometric accuracy, we compare the source positions in the GMRT 153 MHz catalog against catalog source positions from the deep WSRT 1.4 GHz map of de Vries et al. (2002). For our position comparison, we only use sources whose flux profile is accurately described by a single gaussian, and whose peak flux S is at least $10\sigma_L$. This bypasses most of the position errors that arise from low signal-to-noise (S/N , or S/σ_L), different grouping of gaussians and spectral variations across sources. Using a search radius of $10''$, we cross-match 126 sources in both catalogs. This number does not change when modifying the search radius between $5 - 60''$. These sources appear to be randomly distributed over the selected area.

Figure 4.3 shows a plot of the position offsets of the 153 MHz sources as compared to their 1.4 GHz counterparts. We measure a small mean position offset in right ascension (RA, or α) and declination (DEC, or δ) of $(\Delta\alpha, \Delta\delta) = (0.11'', 0.09'')$. We correct the catalog positions for this small offset. The estimated RMS scatter around this offset is $\sigma_{\alpha,\delta} = 1.32''$.

Because we are comparing catalogs that both have a limited positional accuracy, the total RMS position scatter is composed of position errors from both. We compared compact sources with high S/N , therefore we may ignore S/N -dependent errors from the fitting process. Under these conditions, the observed scatter can be written as the quadratic sum of the astrometric

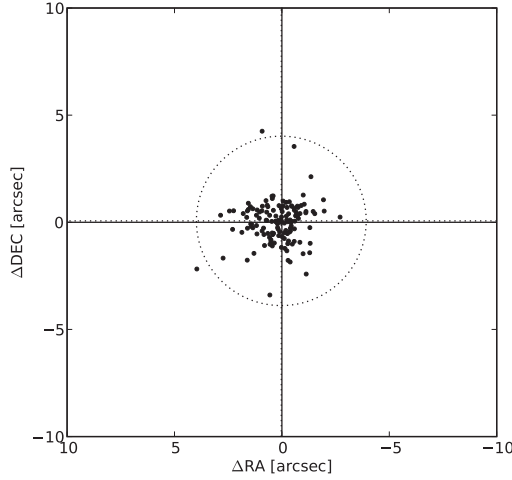


Figure 4.3: Scatter plot of the position offsets of a bright ($> 10 \sigma_L$) subset of 126 sources from the GMRT 153 MHz catalog that have a simple (gaussian) flux profile, using the source catalog of the deep 1.4 GHz WSRT observations as the reference. The dotted lines mark the mean position offset, while the dotted circle marks 3 times the RMS scatter around the offset.

calibration accuracies of each catalog:

$$(\sigma_{\alpha,\delta})^2 = (\sigma_{\alpha,\delta}^{1400})^2 + (\sigma_{\alpha,\delta}^{153})^2 \quad (4.2)$$

The S/N-independent part of the positional accuracy of the 1.4 GHz sources is $0.44''$ (de Vries et al. 2002), therefore we derive an overall astrometric calibration accuracy for the 153 MHz image of $1.24''$. We consider this to be an upper limit, as we did not incorporate the possible position error due to varying spectral indices across sources. We quadratically add this error to the calculated position errors from the source extraction process in the 153 MHz source catalog as determined in Section 4.3.1. The latter errors include the S/N-dependent part of the positional accuracy.

4.3.4 Flux scale

The accuracy of the flux scale transferred from the calibrator 3C 286 to the target Boötes field is influenced by several factors: (i) the quality of the calibrator observational data, (ii) the accuracy of calibrator source model, and (iii) the difference in observing conditions between the calibrator and target field. Here we discuss issues that influence these factors.

The quality of the calibrator data is most noticeably affected by RFI and by ionospheric phase rotations. The repeated observation of 3C 286 every ~ 45 minutes during the observing enabled us to monitor the RFI and ionospheric conditions over time. The mild fluctuations in the initial (short interval) calibration gain phases at the start of the data reduction showed that the ionosphere was very calm during both observing nights, therefore we exclude the possibility of diffraction or focussing effects (e.g., Jacobson & Erickson 1992a). Apparent flux loss due to

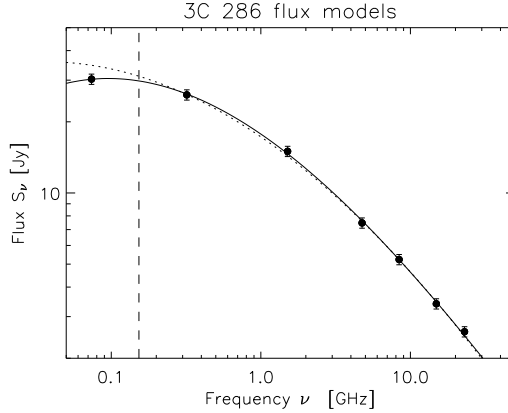


Figure 4.4: Model of the radio spectrum of 3C 286. The measurements (dots) above 153 MHz (dashed line) were used to fit the original Perley–Taylor 1999.2 model (dotted line), which appears to overestimate the flux density at 153 MHz. By adding one measurement at 74 MHz, we fit an alternative model (solid line) that may give a better prediction at 153 MHz.

ionospheric phase rotations was prevented by applying the (short interval) gain phase corrections before bandpass- and amplitude calibration (see Section 4.2.2).

RFI was continuously present during both observing sessions. This mainly consisted of persistent RFI over the full band, most noticeably on the shortest (central square and neighbouring arm antenna) baselines, and of more sporadic events on longer baselines during one or more time stamps and/or narrow frequency ranges. The sporadic events were relatively easy to recognize and excise, but for the persistent RFI this is much more difficult due to a lack of contrast between healthy and affected data on a single baseline. Some of the shortest, most affected baselines were removed completely. On longer baselines, persistent RFI from quasi-stationary sources can average out due to fringe tracking (Athreya 2009), but does add noise. Large magnitude RFI amplitude errors in the visibilities may result in a suppression of the gain amplitude corrections. Because these effects are hard to quantify, we adopt an ad-hoc 2 percent amplitude error due to RFI.

Because 3C 286 is unresolved ($\lesssim 2.5''$) within a $20''$ to $25''$ beam, we used a point source for the calibrator model with a flux density of 31.01 Jy (Section 4.2.2). The utilized Perley–Taylor flux density at 153 MHz is an extrapolation of VLA flux density measurements at 330 MHz and higher, using a fourth order polynomial in log-log space. In Table 4.4 a comparison is presented between flux density measurements of 3C 286 in various sky surveys at low frequencies and the predicted flux densities from the Perley–Taylor model. Although there is a large variation in the flux differences at the different frequencies, there appears to be an overestimation by the Perley–Taylor model below 200 MHz due to a spectral turnover of 3C 286 below ~ 300 MHz. For this reason, we re-fitted the polynomial to the original data points plus the additional 74 MHz VLSS measurement, assuming 5 percent errors for all data points (Figure 4.4). Our new model is given by:

$$\log_{10}(S_\nu) = 1.24922 - 0.434710 \log_{10}(\nu) - 0.174786 (\log_{10}(\nu))^2 + 0.0251542 (\log_{10}(\nu))^3, \quad (4.3)$$

Survey	Catalog flux	Perley–Taylor model flux	New model flux
74 MHz VLSS ^a	30.26 ± 3.08 Jy	34.67 Jy	30.26 Jy
151 MHz 6C ^b	26.31 Jy	31.25 Jy	29.81 Jy
151 MHz 7C ^c	26.53 Jy	”	”
159 MHz 3C ^d	30.0 ± 7.0 Jy	30.94 Jy	29.65 Jy
178 MHz 4C ^e	24.0 Jy	30.22 Jy	29.26 Jy
325 MHz WENSS ^f	27.12 ± 1.63 Jy	25.96 Jy	26.11 Jy

^a Cohen et al. (2007)

^b Hales et al. (1988)

^c Hales et al. (2007) and references therein. Note that we use the peak flux rather than the integrated flux density, as 3C 286 is unresolved on the 7C resolution.

^d Edge et al. (1959); Bennett (1962)

^e Pilkington & Scott (1965); Gower et al. (1967)

^f Rengelink et al. (1997). Note that we use the peak flux rather than the integrated flux, as 3C 286 is unresolved on the WENSS resolution.

Table 4.4: Flux measurements of 3C 286 from different radio survey catalogs at low frequencies.

with ν the frequency in GHz and S_ν the flux density in Jy. This parametrization results in a slightly better fit to the flux densities from the various surveys (Table 4.4), although the large scatter remains. For the center of the GMRT band at 153.1 MHz, the new model predicts a flux density of 29.77 Jy. We have adopted this new model by scaling the image by the ratio 29.77/31.01 before primary beam correction (Section 4.3). The accuracy of this flux scale is closely related to the accuracy of the 74 MHz data point, for which a 10 percent flux error is given. Assuming the error in the 330 MHz is much smaller, and 153 MHz is roughly half way from 74 to 330 MHz in logarithmic frequency, we set an upper limit of 5 percent error on the adopted flux scale of 3C 286 at 153 MHz.

The presence of other sources in the 3.1 degree FoV around 3C 286 further complicates the flux calibration. For example, the total apparent flux density in the Boötes field that was extracted through deconvolution is ~ 46 Jy from ~ 1000 sources, which may be typical lower limit for any blind field. If this flux is distributed over many sources that are individually much fainter than the calibrator, then the net effect of this additional flux is only noticeable on a small subset of the shortest baselines, while calibration utilizes all baselines. Inspection of the 3C 286 field at 74 MHz (VLSS; Cohen et al. 2007) and 325 MHz (WENSS; Rengelink et al. 1997) does identify two relatively bright sources within 0.7 degrees of 3C 286 with estimated apparent GMRT 153 MHz flux densities of 5.3 and 2.7 Jy, respectively. These sources will cause a modulation of the visibility amplitudes across the UV-plane. We performed a simple simulation, in which we replaced the measured 3C 286 visibilities with noise-less model visibilities of three point sources, being 3C 286 and the two nearby sources, and calibrated these visibilities against a single point source model of 3C 286, using the same settings as in the original data reduction. We found that the combined gain amplitude for all antennas and all time intervals was 1.000 ± 0.004 . For individual 10 minute time blocks, the largest deviation from one was 1.00 percent, which indicates the magnitude of the possible error when using a single 10 minute calibrator observation on 3C 286. The small deviations per time block are transferred to the target field data, but these are suppressed by amplitude self-calibration against the target field source model. We set an upper limit of 1 percent due to the presence of other sources in the FoV of the calibrator.

While transferring the flux scale from calibrator to target field, the derived gain amplitudes need to be corrected for differences in sky temperature due to galactic diffuse radio emission (e.g., Tasse et al. 2007), which is detected by individual array antennas but not by the interferometer. The GMRT does not implement a sky temperature measurement, therefore we need to rely on an external source of information. From the Haslam et al. (1982) all-sky map, we find that the mean off-source sky temperatures at 408 MHz as measured in the 3C 286 and Boötes field are both approximately 20 ± 1 degree. Applying the formulae given by Tasse et al. (2007) for the GMRT at 153 MHz⁸, we estimate a gain inaccuracy of ~ 2 percent at most.

Another effect that may influence the gain amplitude transfer between calibrator and target field is an elevation-dependent gain error. This is a combination of effects such as structural deformation of the antenna, atmospheric refraction and changes in system temperature from ground radiation. According to Chandra et al. (2004), the effect on amplitude is rather small, if not negligible, for GMRT frequencies of 610 MHz and below. Furthermore, the relatively short angular distance of 13.4 degrees between 3C 286 and the target field center causes the differential elevation error to be limited. Elevation dependent *phase* errors are not relevant,

⁸We adopted the GMRT system parameters from
http://www.gmrt.ncra.tifr.res.in/gmrt_hpage/Users/doc/manual/UsersManual/node13.html

because we don't rely on the calibrator to restore the astrometry. For our observation, we assume that elevation-dependent effects can be ignored.

To incorporate the effects discussed above plus some margin, we quadratically add a relative flux error of 10 percent to the flux density measurement errors in the source catalog.

4.4 Analysis

The 598 radio sources in our 153 MHz catalog form a statistically significant set, ranging in flux density from 5.1 mJy to 3.9 Jy. Because of the large survey area, cosmic variance is expected to be small. Radio images at 153 MHz of a selection of extended sources are presented in Appendix 4.6. In this section, we discuss two characteristics of the survey: number counts and spectral indices. When properly corrected for incompleteness, the number counts are an objective measure of the 153 MHz source population, that can be compared against models and other surveys. For individual sources, the spectral index can help to classify sources, and identify rare sources such as HzRGs and cluster halos & relics.

4.4.1 Differential source counts

We derived the Euclidean-normalised differential source counts from the catalog. Because the source extraction criteria vary over the survey area, we used Figure 4.2 to correct for the missed fraction per flux bin. This will mainly affect the lowest two bins. Furthermore, the combined effect of random peaks in the background noise and a peak detection criteria causes a selection bias for positively enhanced weak sources (Eddington bias). In general, noise can scatter sources into other flux bins, most noticeably near the detection limit. Our attempts to correct for this effect through Monte-Carlo simulations were numerically unstable due to the low number counts in the lowest flux bin. The effect on the higher bins was minimal, therefore we omit the Eddington bias corrections.

In Figure 4.5 the Euclidean normalized differential source counts are presented, including the lowest flux bin discussed above. The plotted values are tabulated in Table 4.5. Because no accurate source counts are available for 153 MHz at these low flux levels, we compare against the 330 MHz source count model from Wieringa (1991), scaled down to 153 MHz assuming various mean spectral indices. The visual correspondence between model and measurements is best for a mean spectral index of -0.8 .

George & Stevens (2008) have determined Euclidean normalized differential source counts for 153 MHz GMRT observations on a field centered around ϵ Eridanus with a central background RMS value of $3.1 \text{ mJy beam}^{-1}$. They fit a single power-law slope of 0.72 to 113 sources over a flux range of 20 mJy–2 Jy, which is flatter than the value of 0.87 from our data over the range 40–400 mJy. The most likely explanation for this difference is the larger uncertainties on their lower source counts due to the higher background RMS and the smaller survey area that was used for analysis.

The derived source counts agree well with a 151 MHz source count model by Jackson (2005), based on an extrapolation of source counts from the 3CRR and 6C catalogs (Laing et al. 1983; Hales et al. 1988). In this model, the FR_{II} radio sources dominate the counts above $\sim 50 \text{ mJy}$, while below the FR_I sources are the most dominant population. The flattening at low (sub-mJy) flux densities was first seen at 1.4 GHz (Windhorst et al. 1985), and later also at

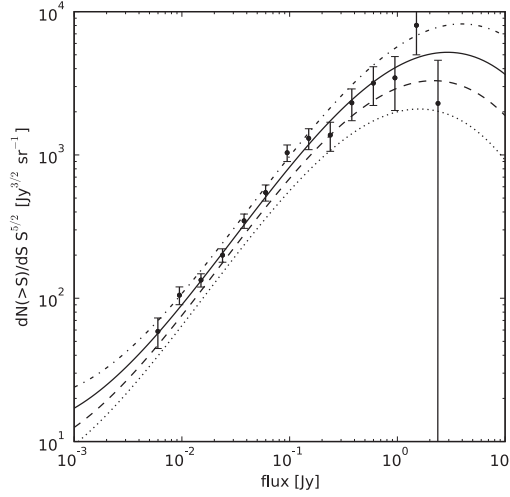


Figure 4.5: Euclidean-normalised differential source counts for the full 153 MHz catalog of ~ 600 sources, distributed over 14 logarithmic flux bins ranging from 4.75 mJy to 3 Jy (black dots plus poissonian error bars). Overplotted are models that were fitted to 325 MHz source counts from Wieringa (1991), scaled down in frequency to 153 MHz by assuming a constant spectral index for the whole source population. The spectral index values used are -0.0 (dotted line), -0.4 (dashed line), -0.8 (solid line) and -1.2 (dot-dash line).

Flux bin center [Jy]	Raw counts	Normalized counts [Jy ^{3/2} sr ⁻¹]
0.00598579	30	58.70 \pm 14.12
0.00948683	89	105.05 \pm 14.92
0.01503562	102	133.90 \pm 14.18
0.02382985	87	199.81 \pm 21.45
0.03776776	76	347.09 \pm 39.81
0.05985787	60	546.74 \pm 70.58
0.09486833	57	1036.35 \pm 137.27
0.15035617	36	1305.98 \pm 217.66
0.23829847	19	1375.27 \pm 315.51
0.37767762	16	2310.75 \pm 577.69
0.59857869	11	3169.75 \pm 955.72
0.94868330	6	3449.72 \pm 1408.34
1.5035617	7	8030.29 \pm 3035.16
2.3829847	1	2288.93 \pm 2288.93

Table 4.5: Euclidean-normalised differential source counts (including error estimates) for the full 153 MHz catalog of 598 sources, distributed over 14 logarithmic flux bins ranging from 4.75 mJy to 3 Jy.

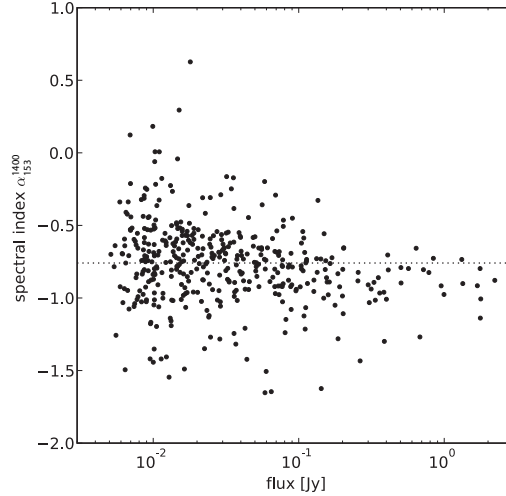


Figure 4.6: Spectral index for 417 sources between 1.4 GHz and 153 MHz. The detection limit is almost fully determined by the 153 MHz survey due to the sensitivity of the 1.4 GHz observations. The median spectral index is -0.76 (dotted line). 16 sources have a spectral index below -1.3 .

frequencies below 1 GHz (e.g., at 610 MHz; Ibar et al. 2009). This population of faint sources is thought to consist of starburst galaxies (e.g., Thuan 1987). The model by Jackson (2005) predicts a flattening in the power-law shape below ~ 10 mJy due to a growing fractional population of starburst galaxies. Our survey depth is not sufficient to detect this flattening.

4.4.2 Spectral indices

Because of the good match in resolution between the GMRT 153 MHz image and the deep WSRT 1.4 GHz image from de Vries et al. (2002), we can accurately determine spectral indices over a decade in frequency. Due to the high detection rate of 1.4 GHz sources at 153 MHz positions (Section 4.3.2), we do an automated search for 1.4 GHz counterparts within $25''$ of the 153 MHz sources and ignore all sources for which we don't find counterparts. The spectral indices of 417 matched sources are plotted in Figure 4.6. We find a median spectral index of -0.76 , which is slightly lower than the median values of -0.79 (Cohen et al. 2004), -0.85 (Ishwara-Chandra & Marathe 2007) and -0.82 (Sirothia et al. 2009) found in similar high-resolution, low-frequency surveys. There is a steepening trend of the mean spectral index towards higher flux densities, indicating an increase of flat-spectrum sources in the source population towards lower flux densities. This effects is also seen between 1.4 GHz and 325 MHz (de Vries et al. 2002; Zhang et al. 2003) and 1.4 GHz and 74 MHz (Cohen et al. 2004), but our measurement confirms this trend towards even lower flux densities.

From Figure 4.6 we highlight a group of 16 USS sources that have a spectral indices lower than -1.3 . Table 4.6 lists these sources in decreasing flux order. Despite the relatively large uncertainty in 153 MHz flux density for the faintest sources, the spectral index is still relatively well constrained due to the large frequency span. The angular distribution of the USS sources is quite peculiar (Figure 4.7). There are 6 sources that form 3 pairs within $6'$ of each other.

ID ^a	RA ^b	DEC ^b	153 MHz flux [mJy]	1.4 GHz flux [mJy]	α_{153}^{1400}
J142656+352230	14 ^h 26 ^m 56.46 ^s	35°22'30.8"	264.2 ± 26.6	11.31 ± 0.46	-1.43 ± 0.05
J143506+350059	14 ^h 35 ^m 06.89 ^s	35°00'58.2"	142.8 ± 14.5	4.02 ± 0.16	-1.62 ± 0.05
J143118+351549	14 ^h 31 ^m 18.29 ^s	35°15'49.5"	64.8 ± 6.9	1.74 ± 0.08	-1.65 ± 0.05
J143500+342531	14 ^h 35 ^m 00.98 ^s	34°25'30.2"	59.7 ± 6.2	2.18 ± 0.09	-1.51 ± 0.05
J143520+345950	14 ^h 35 ^m 20.51 ^s	34°59'49.1"	58.6 ± 6.2	1.55 ± 0.07	-1.65 ± 0.05
J143815+344428	14 ^h 38 ^m 15.28 ^s	34°44'29.8"	44.0 ± 4.8	1.93 ± 0.09	-1.42 ± 0.05
J143331+341012	14 ^h 33 ^m 31.84 ^s	34°10'12.9"	37.0 ± 4.1	2.04 ± 0.09	-1.32 ± 0.05
J142631+341557	14 ^h 26 ^m 31.69 ^s	34°16'00.9"	22.5 ± 3.6	1.16 ± 0.07	-1.35 ± 0.08
J142954+343516	14 ^h 29 ^m 53.90 ^s	34°35'18.8"	16.4 ± 2.4	0.62 ± 0.04	-1.49 ± 0.07
J142724+334714	14 ^h 27 ^m 24.77 ^s	33°47'18.5"	12.8 ± 2.8	0.43 ± 0.04	-1.55 ± 0.11
J143538+335347	14 ^h 35 ^m 38.76 ^s	33°53'44.2"	12.3 ± 2.2	0.56 ± 0.05	-1.41 ± 0.09
J143310+333131	14 ^h 33 ^m 10.42 ^s	33°31'27.7"	11.3 ± 2.2	0.50 ± 0.04	-1.42 ± 0.10
J143230+343449	14 ^h 32 ^m 30.47 ^s	34°34'49.5"	10.1 ± 1.8	0.52 ± 0.04	-1.35 ± 0.09
J142719+352326	14 ^h 27 ^m 19.32 ^s	35°23'29.2"	10.0 ± 3.4	0.42 ± 0.06	-1.44 ± 0.17
J143700+335920	14 ^h 37 ^m 00.74 ^s	33°59'20.2"	9.5 ± 2.5	0.42 ± 0.04	-1.42 ± 0.13
J143249+343915	14 ^h 32 ^m 49.12 ^s	34°39'14.0"	6.4 ± 1.8	0.24 ± 0.04	-1.49 ± 0.15

^a From de Vries et al. (2002).^b Measured at 153 MHz.**Table 4.6:** 153 MHz catalog selection of 16 USS sources with a spectral index below -1.3.

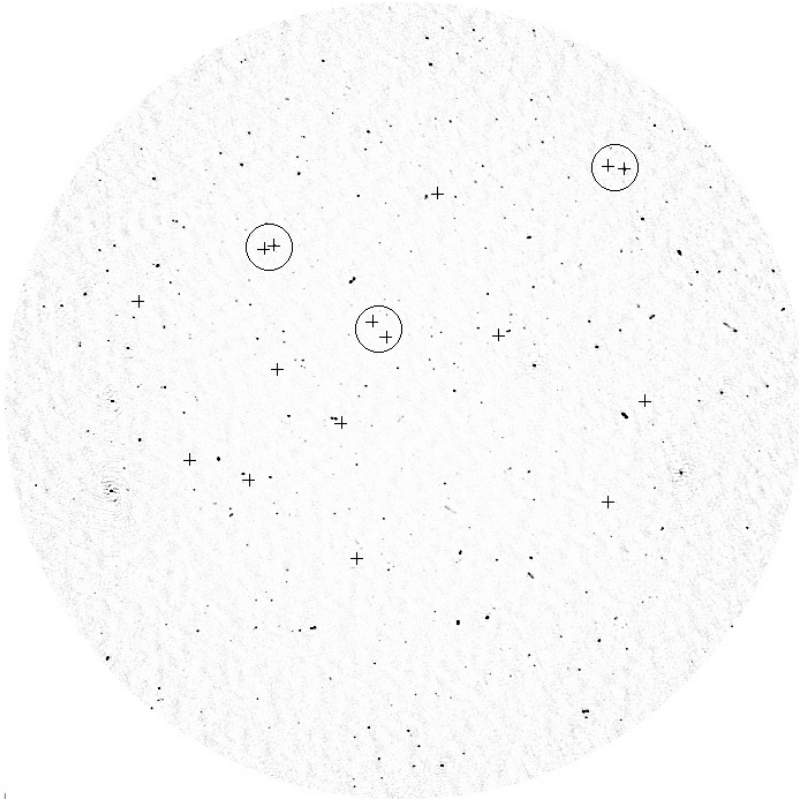


Figure 4.7: Greyscale map of the 153 MHz survey area with the positions of the 16 USS sources marked (plus signs). The angular distribution of USS sources is somewhat peculiar, as 6 sources have a neighbour within $6'$ (marked by circles).

These pairs, together with the remaining 10 single sources, appear to be randomly distributed across the FoV. Visual inspection of the pairs in the images at 153 MHz and 1.4 GHz did not reveal any obvious artifacts in the background near these sources, which makes it less likely that these sources are fake detections. There is no visual evidence in the radio maps that the pair components are physically connected. Through Monte-Carlo simulations we determined that, out of 16 sources with random positions over a 1.5° radius field (which is approximately the 1.4 GHz field radius), the chance of finding 3 pairs within $6'$ is 1.4 ± 0.4 percent. Therefore, it is unlikely that these pairs appeared by chance. Further investigation is needed to establish the true nature of these pairs.

Croft et al. (2008) examine 4 candidate HzRGs (which they labelled A, B, C and E) based on their steep (≤ -0.87) spectral index between 1.4 GHz and 325 MHz. As their candidate sources are also present in the 153 MHz catalog, we complement their data with our new spectral index measurements in Table 4.7. Both sources A and E appear to have fairly straight power-law spectra down to 153 MHz, while sources B and C appear to undergo considerable spectral flattening. Based on our selection criteria for USS sources, only source A would be considered

ID	RA ^a	DEC ^a	α_{325}^{1400} (^b)	α_{153}^{1400} (^c)	z_{phot} (^d)
A	14 ^h 26 ^m 31.75 ^s	+34°15′57.5″	-1.48	-1.35 ± 0.08	4.97
B	14 ^h 26 ^m 47.87 ^s	+34°58′51.0″	-0.89	-0.56 ± 0.06	3.76
C	14 ^h 27 ^m 41.84 ^s	+34°23′24.7″	-0.98	-0.44 ± 0.13	1.21
E	14 ^h 32 ^m 58.44 ^s	+34°20′55.4″	-0.87	-0.95 ± 0.05	4.65

^a As measured at 1.4 GHz; de Vries et al. (2002).

^b The spectral index between 325 MHz and 1.4 GHz as measured by Croft et al. (2008).

^c The spectral index between 153 MHz and 1.4 GHz as measured in this work.

^d Photometric redshift, as measured by Croft et al. (2008).

Table 4.7: Spectral indices between 1.4 GHz and 153 MHz for four candidate HzRGs by Croft et al. (2008).

a candidate HzRG.

4.4.3 Identification fraction of radio sources versus spectral index

We investigate the spectral index-redshift correlation by determining the NIR K -band identification fraction of radio sources as function of spectral index. On average, steep spectrum sources are located at higher redshifts, and therefore more difficult to detect. Using K -band has an advantage over (also available) shorter wavelength bands as this band suffers the least from extinction, and is known to correlate with redshift through the $K - z$ correlation (e.g., Willott et al. 2003).

We have identified possible optical counterparts of the radio sources using the FLAMEX K_S -band catalogue (Elston et al. 2006). This survey covers 7.1 square degrees within the Boötes field. For the NIR identification we use the likelihood ratio technique described by Sutherland & Saunders (1992). This allows us to obtain an association probability for each NIR counterpart, taking into account the NIR magnitudes of the possible counterparts. Before the cross identification, we removed all radio sources located outside the coverage area of the K_S -band images, or located within 20 pixels of the edge or other blanked pixels within individual K_S -band frames.

Following Sutherland & Saunders (1992) and Tasse et al. (2008), the probability that a NIR counterpart with magnitude m is the true NIR counterpart of the radio source is given by the likelihood ratio

$$\text{LR}(r, m) = \frac{\theta(< m) \exp(-r^2/2)}{2\pi \sigma_\alpha \sigma_\delta \rho(< m)}, \quad (4.4)$$

with m the K_S -band magnitude of the NIR candidate, $\theta(< m)$ the a priori probability that the radio source has a NIR counterpart with a magnitude smaller than m , and $\rho(< m)$ the surface number density of NIR sources with a magnitude smaller than m . σ_δ^2 and σ_α^2 are the quadratic sums of the uncertainties in the radio and NIR positions in right ascension and declination, respectively. For the radio source positions and uncertainties we have taken the values from the 1.4 GHz WSRT catalogue, as the astrometric precision is better than the 153 MHz GMRT data. For the FLAMEX survey we have adopted 0.3″ for the position uncertainty. The uncertainty-normalized angular distance is given by the parameter $r = \sqrt{(\Delta_\alpha/\sigma_\alpha)^2 + (\Delta_\delta/\sigma_\delta)^2}$, with Δ the

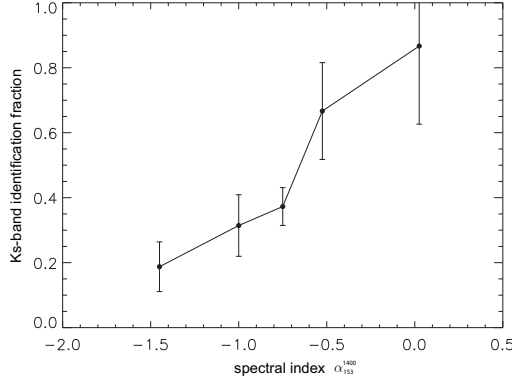


Figure 4.8: Identification fraction of radio sources in the near-infrared K_s -band as a function of spectral index between 1.4 GHz and 153 MHz.

positional difference in either α or δ between the possible NIR counterpart and radio source.

The probability $P(i)$ that candidate i is the true NIR counterpart is

$$P(i) = \frac{\text{LR}_i(r, m)}{\sum_j \text{LR}_j(r, m) + [1 - \theta(m_{\text{lim}})]}, \quad (4.5)$$

with j running over all possible NIR counterparts. $\theta(m_{\text{lim}})$ is the fraction of radio sources having a NIR counterpart at the magnitude limit of the NIR survey. The values for $\rho(< m)$ (surface number density of NIR sources) were estimated from the data itself using bins of 0.1 magnitude across the full survey area. The a-priori identification fraction $\theta(< m)$ was also estimated from the data itself, using the technique described by Ciliegi et al. (2003). This involves counting the surface number density of NIR sources around the radio sources as function of magnitude. This distribution is compared to a distribution of background objects, the overdensity of NIR sources around radio sources gives an estimate of $\theta(< m)$. We found $\theta(m_{\text{lim}})$ to be 0.62.

We selected 368 radio sources that are present within both the 1.4 GHz and 153 MHz catalogs (matched within $6''$) and have a simple morphology (fitted with a single gaussian). We have computed the likelihood ratio of all NIR counterparts located within $20''$ from the radio position. We have defined a radio source to have a NIR counterpart if $\sum_j \text{LR}_j(r, m) > 0.75$. The results are shown in Figure 4.8. The identification fraction is ~ 70 percent for $\alpha_{153}^{1400} < 0.7$, while for $\alpha_{153}^{1400} > 0.7$ the identification fraction drops to about 30 percent. This is in agreement with the spectral index-redshift correlation.

4.5 Conclusions and future plans

We have presented the results from a deep (central RMS < 1.0 mJy), high-resolution ($26'' \times 22''$) radio survey at 153 MHz, covering the full NOAO Boötes field and beyond. This 11.3 square degree survey is among the deepest surveys at this frequency to date (e.g., Sirothia et al. 2009). We produced a catalog of 598 sources detected at 5 times the local background RMS level, with source flux densities ranging from 3.9 Jy down to 5.1 mJy. We estimate our completeness

and contamination to be > 95 percent at 20 mJy and < 1 percent, respectively. The on-source dynamic range (background RMS measured around the source) is limited to ~ 600 , while off-source (background RMS measured in central part of the image, away from bright sources) this rises to > 4000 . We expect that the significantly reduced sidelobe structure around bright sources due to direction-dependent phase calibration (SPAM; see Chapters 2 and 3) is now limited by direction-dependent amplitude errors. The catalog is electronically available in STARBASE format (Roll 1996) at http://www.strw.leidenuniv.nl/~intema/files/bootes_gmrt_153.rdb.

The 153 MHz catalog allows for a detailed study of source populations in a relatively unexplored flux range. We have analyzed the source counts and spectral index distributions for our survey. From this analysis we draw the following conclusions:

- (i) The differential source counts are accurately determined over a flux range of between 20 mJy and 1 Jy. The counts are highly consistent with source counts at 325 MHz of Wieringa (1991), scaled to 153 MHz using a mean spectral index of -0.8 . Using the same spectral index to extrapolate the results from 610 MHz and 1.4 GHz (e.g., Ibar et al. 2009), we expect a flattening of the differential source counts below ~ 5 mJy at 153 MHz. Our survey is not sensitive enough to detect this flattening, which indicates a dominant population of AGN in our catalog (Jackson 2005).
- (ii) The spectral indices of 417 sources between 153 MHz and 1.4 GHz have been determined down to a 153 MHz flux density of ~ 5 mJy. The survey depths at 153 MHz and 1.4 GHz (de Vries et al. 2002) are equal for sources with a spectral index of -1.6 . For our sample, the median spectral index is -0.76 , and the lowest spectral index is -1.65 , which indicates that the sample selection limit is dominated by the 153 MHz survey depth. The unique combination of the very deep 153 MHz and 1.4 GHz survey catalogs shows a continuing trend of average flattening of source spectra towards the lowest 153 MHz flux densities. The inclusion of many very faint sources explains why the median spectral index of -0.76 is slightly higher as compared to other measurements using 74 MHz or 153 MHz observations, that lack either sensitivity at the low-frequency end or at the high-frequency end.
- (iii) We detect 16 out of 417 sources that have an USS with spectral index lower than -1.3 , the lowest having a spectral index of -1.65 . The fraction of USS sources is 3.8 percent, which is mostly dependent on the survey detection limit at 153 MHz. It is not straightforward to compare this fraction with other surveys that have different detection limits at the high- and/or low-frequency end. Possibly the best match is a survey by Sirothia et al. (2009), that includes GMRT 153 MHz observations down to similar sensitivity. Using the same criteria, they find a USS fraction of 3.7 percent (14 out of 374), which is consistent with our result.
- (iv) A statistical analysis of the detection fraction of radio sources in K_S -band images, based on determining likelihood ratios, reproduces the expected (and previously observed) correlation between spectral index and K_S -band identification fraction (e.g., Tielens et al. 1979; Blumenthal & Miley 1979; Wieringa 1991). This links two known correlations together, namely the $K - z$ correlation (e.g., Rocca-Volmerange et al. 2004) and the correlation between spectral index and redshift (Tielens et al. 1979; Blumenthal & Miley 1979).

We plan to continue our analysis of the 153 MHz source survey by comparing it with many other available catalogs at various spectral bands. A high priority task will be to study the properties of the 16 USS sources, to determine if these objects are HzRGs, derive estimates of their redshifts and search the surrounding area for galaxies at similar redshift. This approach has been successful for the identification and study of galaxy cluster formation (e.g., Röttgering et al. 1994b; Venemans et al. 2002).

The observations presented here are part of a larger survey with six additional, partly overlapping flanking fields observed with GMRT at the same frequency, covering a total survey area of ~ 70 square degrees. This same area is also covered by extended WSRT observations using the 8 LFFE⁹ bands between 115–165 MHz. We will combine these observations with the observations presented here to produce a combined high- and low-resolution catalog at ~ 153 MHz to further facilitate the study of the low-frequency sky, and in particular to facilitate the further search for USS radio sources.

Acknowledgements. The authors would like to thank the staff of the GMRT that made these observations possible. GMRT is run by the National Centre for Radio Astrophysics of the Tata Institute of Fundamental Research. This study made use of online available maps and catalogs from the WSRT Boötes Deep Field survey and the FLAMINGOS Extragalactic Survey. HTI acknowledges a grant from the Netherlands Research School for Astronomy (NOVA).

⁹Low Frequency Front-End.

4.6 Appendix: A selection of 153 MHz radio source images

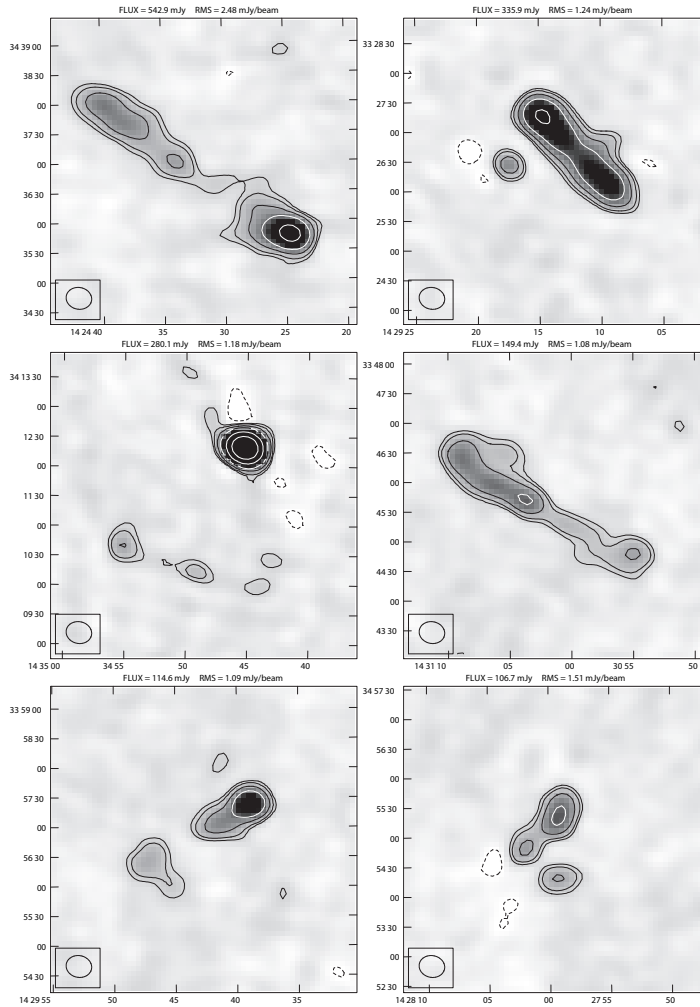
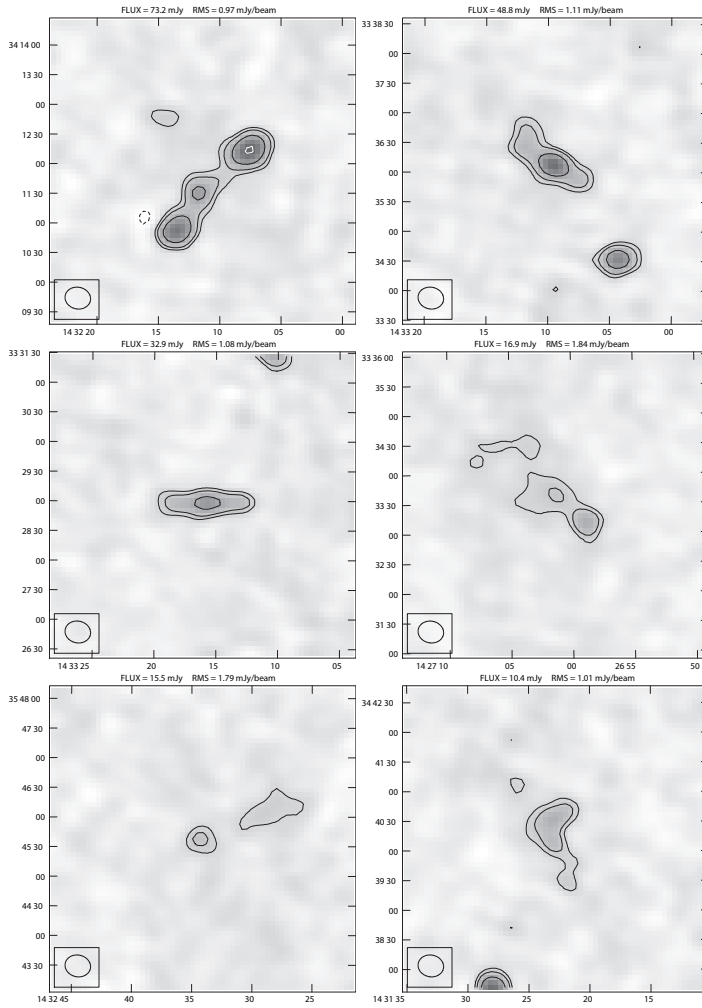


Figure 4.9: Grey-scale images of a selection of resolved 153 MHz sources with an interesting morphology (i.e., not a point source or double point source morphology). Horizontal and vertical axes are RA and DEC, respectively. For each source, the total flux and local background RMS are specified above the $5' \times 5'$ image. Contours are drawn at $[-3, 3, 5, 10, 20, 50, 100]$ times the local background RMS. The grey-scale ranges from -3 to 30 times the local background RMS. This figure continues on the next page.

Figure 4.9: *Continued.*

Low-frequency radio images of the galaxy cluster Abell 2256

Abstract. The galaxy cluster Abell 2256 is a prime target for a study at low radio frequencies, because it possesses an unusually large number of tailed radio sources, and a number of objects with steep radio spectra, including the radio halo, relic and the peculiar ‘source F’ region. We present the results of high-resolution GMRT observations at 153 and 325 MHz, and low-resolution WSRT LFFE observations at 8 frequencies within the range 115–165 MHz. In the low-resolution maps, we detect both the central radio halo and the peripheral radio relic. We confirm the flattening of the spectral index of the relic towards the relic edge. Comparison of the total intensity and spectral index maps at this resolution with earlier 350 MHz and 1.4 GHz observations suggests that the spectral index of the halo emission between 140 MHz and 1.4 GHz flattens from ~ -2 in the center to $\gtrsim -1.4$ towards the southern and eastern boundaries. We use the high-resolution maps to study two complex regions within the cluster. The morphology and steep radio spectrum suggests that the complex ultra-steep spectrum source F at the eastern cluster boundary probably consists of two AGN, of which one ceased activity. The brightest region (F2) fits the profile of a radio ‘phoenix’, old AGN plasma whose synchrotron emission was revived by shock compression. Near the cluster center, we detect a long, steep-spectrum extension of a previously detected head-tail galaxy at higher frequency (source A), at a projected angle of ~ 80 degrees from the high-frequency tail. In the same region we find a steep-spectrum region that may be a radio phoenix as well. These observations support a recent cluster merger scenario, in which disturbances in the ICM strongly influence the appearance of (previously) radio-loud AGN.

H. T. Intema, R. J. van Weeren, H. J. A. Röttgering, J. B. R. Oonk,
D. V. Lal, G. K. Miley, and I. A. G. Snellen
Submitted to Astronomy & Astrophysics

5.1 Introduction

Diffuse synchrotron radio emission from galaxy cluster halos, relics and radio tails provides a unique diagnostic for studying the magnetic field (e.g., Feretti & Johnston-Hollitt 2004), plasma distribution and gas motion within clusters of galaxies. Galaxy clusters containing radio halos appear to have large X-ray luminosities, high intra-cluster medium (ICM) temperatures and large galaxy velocity dispersions (e.g., Feretti et al. 2002). These characteristics of dynamic activity are to be expected if the clusters grow by merging of subclusters, as predicted by models of large-scale structure formation (Kempner & Sarazin 2001, and references therein). A merger scenario is supported by the presence of highly polarized, megaparsec-scale relic structures at the periphery of some X-ray clusters (e.g., Röttgering et al. 1997; Brentjens & de Bruyn 2004), which are thought to be tracers of the shock waves generated by cluster mergers (Enßlin et al. 1998; Miniati et al. 2000). Also the presence of head-tail galaxies in clusters is found to indicate a non-relaxed cluster state (Klamer et al. 2004). Their positions correlate with regions of enhanced X-ray emission and galaxy density (Mao et al. 2009).

Abell 2256 (A2256 from here on) is a nearby, rich galaxy cluster at a mean redshift of $z = 0.0583$ (Miller et al. 2003) that contains both a radio halo and relic, and also several head-tail sources (Bridle et al. 1979; Röttgering et al. 1994a; Clarke & Enßlin 2006; Brentjens 2008). The cluster contains a diffuse X-ray source, consisting of three substructures (Briel et al. 1991; Sun et al. 2002), that roughly coincides with the radio halo. The radial velocity distribution of galaxies has a large dispersion ($> 1200 \text{ km s}^{-1}$; Faber & Dressler 1977; Miller et al. 2003) and also appears to consist of three distinct groups (e.g., Berrington et al. 2002) based on position and velocity. This combined observational evidence has led to the conclusion that A2256 is currently undergoing a cluster merger.

Detailed studies of merging clusters such as A2256 are essential for understanding the formation of the largest structures in the Universe. Diffuse cluster radio emission usually has a very steep radio spectrum ($S_\nu \propto \nu^\alpha$ with $\alpha < -1$), which indicates that the radiating electrons are old and can, in principle, provide a fossil record of the cluster history (e.g., Miley 1980). A study at low ($\lesssim 300 \text{ MHz}$) radio frequencies has the natural benefit of an increased relative brightness of steep-spectrum sources, and provides a view on aged synchrotron sources, complementary to the more recent radio activity as seen at higher ($\gtrsim 1 \text{ GHz}$) frequencies.

The effectiveness of low-frequency observations has been limited, mainly due to: (i) low resolution ($\gtrsim 1'$), (ii) sidelobe confusion from bright outlier sources, (iii) ionosphere-induced phase distortions, and (iv) man-made radio frequency interference (RFI). The construction of larger and/or more sensitive low-frequency arrays (e.g., the WSRT¹ at 115–165 and 325–377 MHz, the VLA² at 74 and 327 MHz and the GMRT³ at 153, 235 and 325 MHz), combined with the recent development of more advanced data reduction and imaging algorithms, has yielded significant improvements in the quality of low-frequency radio maps (e.g., see Chapter 4 and references therein).

In this chapter, we present deep continuum observations of A2256 with the GMRT at 153 and 325 MHz, as well as WSRT LFFE⁴ observations between 115–165 MHz. We use these observations to study the nature of several interesting regions of emission, both on large and small

¹Westerbork Synthesis Radio Telescope.

²Very Large Array.

³Giant Metrewave Radio Telescope.

⁴Low Frequency Front End.

spatial scales. The compact WSRT has a relatively low resolution ($\gtrsim 2'$) at these frequencies, but is very sensitive to large-scale ($\gtrsim 1$ degree) emission from the halo and relic regions. The complementary higher resolution observations with GMRT ($\sim 25''$ and $\sim 15''$ at 153 and 325 MHz, respectively) allow for a detailed study of compact emission regions that have been noted for their entangled or complex morphologies, such as the region containing head-tail sources A & B and the source F region (e.g., Bridle et al. 1979; Röttgering et al. 1994a).

In Section 5.2, we describe the observations and data reduction and present the resulting images. In Section 5.3, we analyze the images, followed by a discussion in Section 5.4. A summary is presented in Section 5.5. Throughout this chapter, source positions are given in epoch J2000 coordinates. We adopt a flat, Λ -dominated cosmology with $\Omega_M = 0.27$, $\Omega_\Lambda = 0.73$ and $H_0 = 100 h \text{ km s}^{-1} \text{ Mpc}^{-1}$ with $h = 0.71$ (Komatsu et al. 2009). For a mean redshift for A2256 of 0.0583 (Miller et al. 2003), the conversion between angular size and proper size is $67 \text{ kpc arcmin}^{-1}$, or $4.0 \text{ Mpc degree}^{-1}$.

5.2 Observations and data reduction

In this section, we describe the observations and data reduction of the GMRT 153 MHz and WSRT 115–165 MHz observations of the A2256 field. The GMRT 325 MHz data reduction is described in van Weeren et al. (*in preparation*). The pointing center for all three observations is at RA $17^{\text{h}}03^{\text{m}}09.06^{\text{s}}$ and DEC $+78^\circ39'59.7''$.

5.2.1 Observations

GMRT 153 MHz

A2256 was observed with the GMRT in a 6 MHz wide protected radio band, centered at 153 MHz (see Table 5.1 for more information). Combining 14 antennas in a central square kilometer and 16 antennas in an extended Y-shape up to 35 km baselines makes GMRT sensitive to a wide range of spatial scales. The field-of-view (FoV) at 153 MHz, defined by the half-power beam width (HPBW), is 3.1 degrees, while the resolution is typically 20–25''. Although the observing band is protected, significant man-made radio frequency interference (RFI) is present within the band at all times. The low-frequency observations are further complicated by ionospheric phase rotations that vary with time and viewing direction, and are relatively strong at the location of the GMRT relatively near the geomagnetic equator. By observing in spectral channel mode with short integration times, the data supports more selective excision of detectable RFI, more accurate (ionospheric phase) calibration, and reduces bandwidth and time-averaging smearing during wide-field imaging. The GMRT observation included a 20 minute calibrator observation on 3C 48 at the end of the observing run.

WSRT 115–165 MHz

A2256 was observed with the WSRT in eight radio bands in the range 115–165 MHz (see Tables 5.1 and 5.2). The eight bands were positioned in frequency to minimize RFI within the observing bands. To improve UV-coverage and sensitivity, and suppress grating lobes due to the regular 144 meter spacings of the 10 fixed antennas, the A2256 field was observed for 12 hours

Observation	Date(s)	Int. Time [sec]	Total Time ^a [hours]	Bandwidth [MHz]	Ch. Width [kHz]	Polarizations
GMRT 153 MHz	June 5, 2005	16.8	8.2	8 ^b	62.5	RR,LL
GMRT 325 MHz	May 25 & 26, 2008	16.8	9.5	2 × 16	125	RR,LL
WSRT 115–165 MHz ^c :						
36 m spacing	Dec. 1, 2004	10.0	10.0	8 × 2.5	19.5	XX,YY,XY,YX
48 m spacing	Dec. 4 & 6, 2004	10.0	10.5	8 × 2.5	19.5	XX,YY,XY,YX
60 m spacing	Dec. 8 & 10, 2004	10.0	11.3	8 × 2.5	19.5	XX,YY,XY,YX
72 m spacing	Dec. 11, 2004	10.0	10.8	8 × 2.5	19.5	XX,YY,XY,YX
84 m spacing	Dec. 15, 2004	10.0	10.8	8 × 2.5	19.5	XX,YY,XY,YX
96 m spacing	Dec. 18, 2004	10.0	10.7	8 × 2.5	19.5	XX,YY,XY,YX

^a Total time on target during the observation.

^b Effectively reduced to 5–6 MHz by antenna-based bandpass filters due to RFI.

^c Observations consist of 6 array configurations, or spacings.

Table 5.1: Overview of observations on the A2256 field.

Frequency	HPBW	Resolution	Pixel Size	Background RMS
116.75 MHz	15.5°	2.9′	50″	14.6 mJy beam ⁻¹
121.75 MHz	14.8°	2.8′	50″	14.3 mJy beam ⁻¹
130.00 MHz	13.9°	2.6′	50″	7.2 mJy beam ⁻¹
139.25 MHz	13.0°	2.45′	40″	7.1 mJy beam ⁻¹
141.75 MHz	12.7°	2.4′	40″	7.1 mJy beam ⁻¹
147.50 MHz	12.2°	2.3′	40″	6.1 mJy beam ⁻¹
157.00 MHz	11.5°	2.2′	40″	5.0 mJy beam ⁻¹
162.50 MHz	11.1°	2.1′	40″	6.0 mJy beam ⁻¹

Table 5.2: Overview of some characteristics of the WSRT LFFE observations.

(full synthesis) in each of six ‘traditional’ configurations⁵ of the four movable antennas. Each observing day (i.e., each spacing) included 15 minute calibrator observations on 3C 295 and 3C 48.

5.2.2 Data reduction

GMRT 153 MHz

Data reduction of the GMRT 153 MHz observations was done using the Astronomical Image Processing Software (AIPS; e.g., Bridle & Greisen 1994) package, developed by the National Radio Astronomy Observatory (NRAO). Furthermore, we used the (recent) SPAM software package (Chapters 2 and 3) to incorporate direction-dependent ionospheric phase calibration. SPAM utilizes AIPS tasks and files through the ParselTongue interface (Kettenis et al. 2006), while providing high-level tasks for basic calibration & imaging and for calibration of direction-dependent ionospheric phase rotations. For the latter, SPAM measures the antenna-based, direction-dependent phase rotations by peeling bright sources in the FoV (Noordam 2004), separates instrumental from ionospheric phase contributions, combines the ionospheric phases into a consistent phase screen model, and predicts the ionospheric phase corrections in arbitrary viewing directions while imaging the FoV.

Following the SPAM recipe for data reduction, we used 3C 48 for flux, bandpass and instrumental phase calibration. Initial flagging of all visibility data included removal of dead and malfunctioning antennas and baselines, systematic removal of the first 30 seconds of each observing time blocks due to potential system instabilities, and manual and semi-automated flagging of channels and time ranges on individual baselines, based on excessive (≥ 5 times the RMS) visibility amplitudes. An initial phase calibration was performed on 3C 48 against a 62.71 Jy point source model (using the Perley–Taylor 1999.2 scale⁶, which is derived from the Baars et al. (1977) scale for 3C 295) using a small, relatively RFI-free channel range (unless stated otherwise, phase-only calibrations are all performed on the visibility time resolution). A single time-constant bandpass calibration on 3C 48, normalized to the same channel range,

⁵See the WSRT Guide to Observations.

⁶Defined in the ‘VLA Calibrator Manual’, available online at <http://www.vla.nrao.edu/astro/calib/manual/baars.html>

was performed while temporarily applying the phase calibration. After excision of 48 noisy channels at both edges of the bandpass, the spectral resolution was reduced to save computing time in further data reduction steps. Averaging every 4 channels into 20 channels of 0.25 MHz yields a total bandwidth of 5 MHz. This was followed by more flagging and a single flux calibration to the point source model while temporarily applying both phase and bandpass calibrations. The RR and LL polarizations were combined into stokes I while applying the bandpass and flux calibration, which was followed by a phase calibration using the full bandwidth. The time-varying calibration phase corrections were filtered to estimate the (presumed) constant instrumental phase offsets, by iterative fitting of time-variant, spatial phase gradients (Cotton et al. 2004, see also Chapter 2).

The flux, bandpass and instrumental phase calibrations were transferred to the A2256 field data, which was flagged and combined in the same way as the 3C 48 data. This data was phase calibrated against a 35 point source model, derived from power-law extrapolation of NVSS and WENSS source flux densities and corrected for primary beam attenuation. This was followed by wide-field imaging of the primary beam area (Table 5.3), followed by 3 rounds of phase-only self-calibration & imaging. After each self-calibration round, the source model was temporarily subtracted from the visibility data, followed by flagging of excessive residual visibility amplitudes. After subtracting the latest source model, the visibility data was inspected for bright, interfering outliers. Images were created from the visibilities at the positions of known bright sources (bright 1.4 GHz NVSS sources within 5 primary beam radii, and 9 distant but extremely bright sources, such as Sun, Cas A, Cyg A, etc.). No significant flux was detected in any of these images.

Self-calibration was followed by two additional rounds of SPAM calibration and imaging (see Table 5.4). In this process we lost ~ 50 percent of the data due to large ionospheric model fit errors (> 40 degrees RMS; e.g., see Section 3.5.2). Despite the data loss, using the remaining data significantly reduced the image artifacts near bright sources, resulting in a final background RMS of $2.1 \text{ mJy beam}^{-1}$, measured over the inner half of the primary beam area.

To enable the detection of the known diffuse radio sources in A2256, we have attempted to conserve as many short baselines as possible during flagging, although the RFI was particularly severe on these baselines. For the final image, we have attempted to boost the contrast of the diffuse emission by applying different weighting schemes (natural weighting, gaussian tapering of the UV-plane). However, this only resulted in enhancing large-scale ripples in the image background, and therefore these attempts were abandoned. As a result, the sensitivity for large-scale emission is compromised, but we retain a good signal on smaller, more compact emission regions.

The final image was corrected for primary beam attenuation with a circular beam model ⁷

$$A(\theta, \nu) = 1 - 4.04 \cdot 10^{-3}(\theta\nu)^2 + 76.2 \cdot 10^{-7}(\theta\nu)^4 - 68.8 \cdot 10^{-3}(\theta\nu)^6 + 22.03 \cdot 10^{-3}(\theta\nu)^8, \quad (5.1)$$

where θ is the angular distance from the pointing center in arcminutes and ν the observing frequency in GHz. The 153 MHz image is presented in Section 5.2.3 together with the other images.

⁷From the GMRT User Manual.

Field diameter	4.9 ^{◦a}
Pixel size	4.2''
Weighting	robust 0.5 ^b
Wide-field imaging	polyhedron (facet-based) ^c
Number of initial facets	109
Facet diameter	0.60 [◦]
Facet separation	0.50 [◦]
Deconvolution	Cotton-Schwab CLEAN ^d
CLEAN box threshold ^e	5 σ
CLEAN depth ^e	2 σ
Restoring beam	22.1'' \times 16.7'' (PA 39.5 [◦])

^a We map more than twice the HPBW diameter to allow for deconvolution of nearby bright sources.

^b Briggs (1995)

^c Perley (1989a); Cornwell & Perley (1992)

^d Schwab (1984); Cotton (1989, 1999); Cornwell et al. (1999)

^e σ is the background RMS, measured in the central part of the image.

Table 5.3: Overview of GMRT imaging parameters.

Calibration cycles	2
Peeled sources ^a	20
Number of added facets	20
Layer heights (weights)	100 km (0.25) 200 km (0.50) 400 km (0.25)
Parameter γ ^b	5 / 3
Model parameters	20
Model fit phase RMS ^{ac}	22.2 [◦] \pm 4.2 [◦]
Peeling corrections applied	yes
Phase drift estimates applied	yes
Reference catalog	NVSS ^d

^a Specified for the final (second) calibration cycle only.

^b Adopted power-law slope of the overall phase structure function.

^c After rejection of excessive model fit errors
> 40 degrees.

^d Condon et al. (1994, 1998)

Table 5.4: Overview of the SPAM processing parameters. For more information on the meaning of the parameters we refer to Chapters 2 and 3.

Field diameter	15.0°
Pixel size	40'' – 50'' ^a
Weighting	robust 0.
Wide-field imaging	polyhedron (facet-based)
Number of facets	200
Facet diameter	85' – 107'
Facet separation	81'
Deconvolution	Cotton-Schwab CLEAN
CLEAN box threshold ^a	–
CLEAN depth	3 σ
Restoring beam ^b	circular 2.1 – 2.9'

^a No CLEAN boxes were used.

^b See Table 5.2 for setting per band.

Table 5.5: Overview of WSRT imaging parameters. See Table 5.3 for more info.

WSRT 115–165 MHz

Because of limitations in the data reduction software to simultaneously image and deconvolve the large WSRT LFFE frequency span (e.g., varying primary beam shapes, resolutions and spectral indices), each of the eight bands was processed independently. Data reduction was performed using the AIPS package, which started with initial flagging of RFI and bad data, excising between 10 and 40 percent of the data per band under varying conditions over time and frequency. The system temperature measurements of the WSRT were bypassed due to the presence of significant RFI in the receiver bands. The calibrator observations on 3C 295 and 3C 48 were used to determine the time-constant, normalized bandpass calibration. After applying the bandpass calibration, more flagging was done, including the flagging of 17 frequency channels at the band's edges. Flux calibration was postponed to a later stage, because of the bypassed system temperature measurements and the uncertainties in the gain amplitude determination from a non-isolated calibrator in the large FoV.

From here on, we will use the term 'subset' for the visibility data of one WSRT frequency band – spacing combination. For all subsets, both 3C 295 and 3C 48 were phase-calibrated using point source models on the highest possible (visibility) time resolution. We selected one subset (139.25 MHz – 36 meter) with little RFI and slowly varying (ionospheric) calibration phase corrections on 3C 295 / 3C 48. This subset was used to generate a target field model. The phase corrections from the calibrators were transferred to the target field. Next, the subset data was imaged over twice the primary beam radius (Table 5.5) to facilitate removal of nearby bright outliers. This was followed by three rounds of self-calibration & imaging, in which the final round also included amplitude calibration.

All other subsets were phase calibrated against the target field model derived above, followed by imaging and one round of (amplitude & phase) self-calibration & imaging. After subtracting the appropriate target field model from each visibility subset (including nearby outliers), the visibility data was imaged at the positions of five extremely bright outlier sources, namely the Sun, Cas A, Cyg A, Vir A and Tau A. Because the apparent flux densities of these sources were

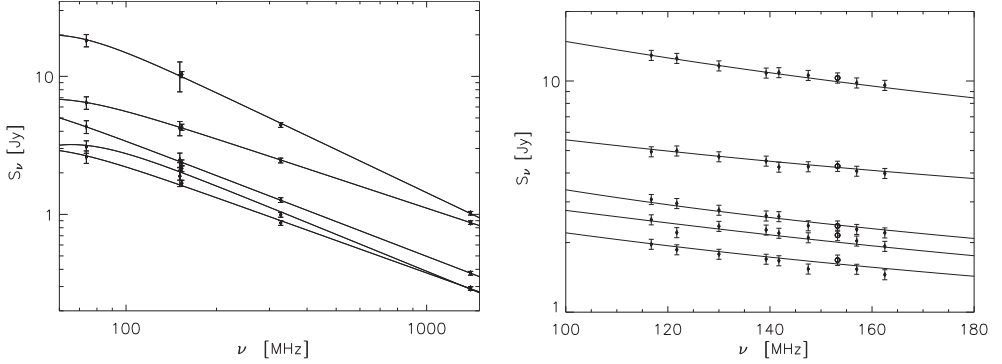


Figure 5.1: Fitted spectra for 5 bright point sources in the vicinity of A2256. *Left:* Fitted spectral models (double power-law; solid lines) based against catalog flux density measurements (filled dots) at 74, 151, 153, 327 and 1400 MHz for sources (top to bottom) 4C 79.17, 4C 79.16, 6C B165417.3+783341., 6C B171152.4+801023. and 6C B170753.6+775949. *Right:* Comparison of the WSRT LFPE corrected flux densities (filled dots) and GMRT 153 MHz flux density (open dot) against the fitted spectral models. Note that the frequency axis is linear instead of logarithmic.

significant, each of these sources was peeled (Noordam 2004). Before adding back the target field source model (excluding nearby outliers), all residual visibility data was re-inspected for RFI and flagged where needed. The visibility data of the different spacings was combined per band into 8 large data sets. The data volume was reduced through spectral and temporal averaging of each 3 channels and 2 time stamps, respectively, resulting in 58.5 KHz channels and a 20 second visibility time resolution. Each band was imaged, followed by one round of (amplitude & phase) self-calibration and imaging.

Each image was corrected for primary beam attenuation with a circular beam model⁸

$$A(\theta, \nu) = \cos^6(0.0192 \theta \nu), \quad (5.2)$$

where θ is the angular distance from the pointing center in arcminutes and ν the observing frequency in GHz. For the absolute flux calibration we used 5 bright point sources in the center of the FoV for which flux density measurements are available in the 74 MHz VLSS, 151 MHz 6C, 327 MHz WENSS and 1.4 GHz NVSS catalogs (Cohen et al. 2007; Hales et al. 1988; Rengelink et al. 1997; Condon et al. 1994, 1998) and are present in the GMRT 153 MHz image (Section 5.2.3). Flux densities of these sources were measured in the GMRT 153 MHz band and WSRT LFPE bands through Gaussian fitting in the images. The catalog flux densities (including GMRT 153 MHz) were fitted per source with a double power-law spectrum, allowing for a possible turn-over at low frequencies (see Figure 5.1). From these fits, we determined the amplitude correction factors per WSRT band, averaged over the 5 sources, and applied these to the images. We adopted an absolute flux calibration uncertainty of 10 percent, but anticipate that the relative flux error between WSRT bands is much smaller (~ 2 percent, based on the scatter of WSRT fluxes in Figure 5.1).

The background RMS of all WSRT images (Table 5.2) is limited by systematic rather

⁸From the WSRT Guide to Observations.

than noise-like fluctuations. Most prominent are residual grating lobes and radial lines around bright sources. From the WSRT Guide to Observations, we estimate that the theoretical thermal noise for these observations ranges from $\sim 2 \text{ mJy beam}^{-1}$ at the lowest frequency to $\sim 1.5 \text{ mJy beam}^{-1}$ at the highest frequency. At the field center, the classical confusion noise is estimated to be $3 - 5 \text{ mJy beam}^{-1}$ (Ger de Bruyn, private communication), which is attenuated with the primary beam and therefore drops towards the field edge. In the WSRT images, the background RMS at the field edge is roughly half the values given in Table 5.2, but still 3 to 4 times as high as the thermal noise. We interpret our significantly higher background RMS values to be a combination of residual RFI, ionospheric phase errors and other calibration errors. We have not attempted direction-dependent ionospheric phase calibration, because the one-dimensional geometry of WSRT complicates ionospheric modeling. Because of the limited size of the WSRT array, it is likely to operate in the ionospheric calibration regime where sources suffer from apparent differential movement without any source deformation (regime 3 in Lonsdale 2005). The resulting ionospheric smearing over 12 hour observations is expected to cause a minor (≤ 2 percent) broadening of the $2' - 3'$ beam (assuming a smearing excess of $< 20''$, based on experience with 74 MHz VLA observations). Although the average effect of calibration errors on the source shape may be minor, the induced background artefacts on individual time stamps do not average out for a one-dimensional array in a 12-hour synthesis. Most of the observing was done during daytime, which is also known to have a negative effect on ionospheric conditions (e.g., Cohen & Röttgering 2009).

The background structure of the final WSRT images results in a varying contrast on the diffuse emission regions in A2256 from band to band. Instead of interpreting the results from ‘noisy’ individual bands, we combined them to reduce the effect of artifacts in individual maps. We excluded two bands (121.75 and 147.50 MHz), in which the image artifacts seem to have a severe effect on the emission of A2256. Because the image combination is a non-trivial operation considering the variation in spectral index across A2256 (e.g., Clarke & Enßlin 2006), we performed this operation after determination of the WSRT spectral index map over the A2256 area (Section 5.2.4). Convolution of the remaining 6 bands to a common resolution of $2.9'$ and resampling to a common $50''$ pixel grid was followed by combining into a single $\sim 140 \text{ MHz}$ map using the mean spectral index (the mean over all pixels in the spectral index map) of -1.65 over the 115–165 MHz range for appropriate flux scaling.

5.2.3 Total intensity maps

In Figures 5.2 and 5.3 we present the total intensity maps from the GMRT 153 and 325 MHz observations, and the combined WSRT intensity map at an equivalent frequency of 140 MHz. The WSRT image was resampled to the $2.2''$ grid of the 325 MHz GMRT observations, using a 4 pixel width interpolation kernel to smooth the image across pixel boundaries. We used the deeper 325 MHz image ($0.20 \text{ mJy beam}^{-1}$ background RMS) to mark various sources as identified by Bridle et al. (1979) and Röttgering et al. (1994a). This map clearly shows several radio features for which this cluster is best known: the head-tail sources A, B, C and I, the steep spectrum source F consisting of several components, the large relic area surrounding sources G and H, and traces of the diffuse halo centered approximately on source D.

In the GMRT 153 MHz map, only parts of the relic area are detected due to poor sensitivity and a loss of short baselines to RFI. There is no significant detection of halo emission above two times the local background RMS. Sources with more compact emission, such as sources A, B,

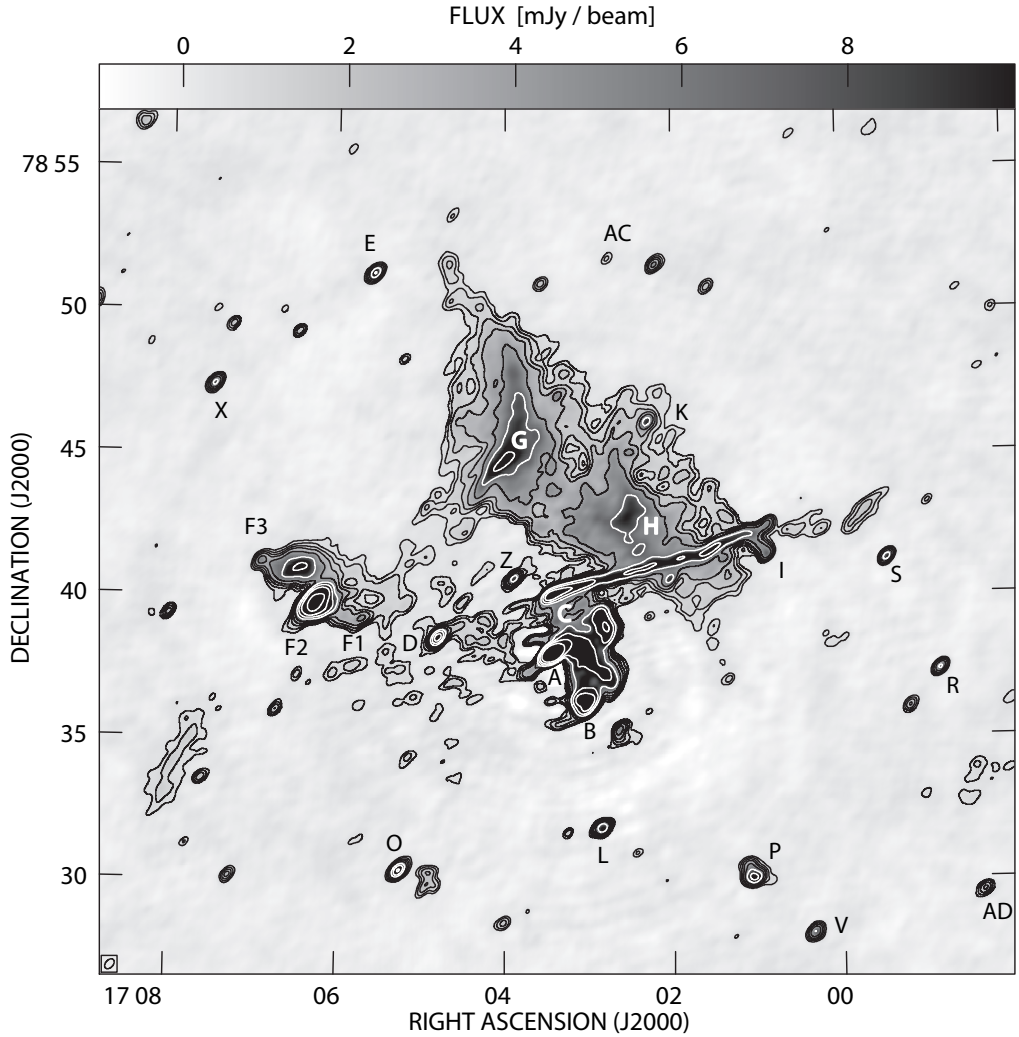


Figure 5.2: Combined grayscale and contour plot of A2256 at 325 MHz as observed with GMRT. The background RMS is $0.20 \text{ mJy beam}^{-1}$. The synthesized beam width of $24'' \times 16''$ is depicted in the bottom-left corner. Contours are drawn at $[3, 5, 8, 12, 20, 36, 60, 100, 200] \times$ the background RMS. The capital letters are source labels as defined by Bridle et al. (1979) and Röttgering et al. (1994a).

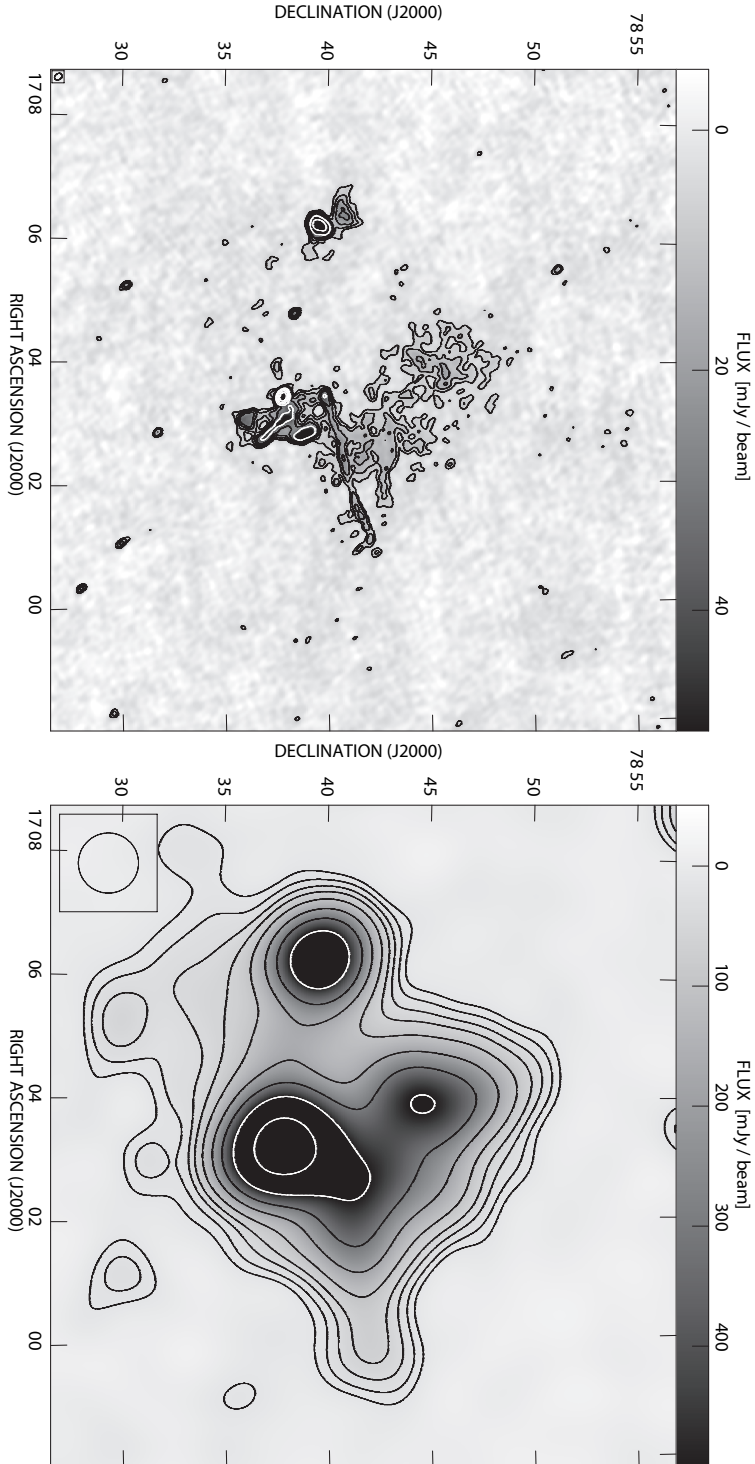


Figure 5.3: Combined grayscale and contour plots of A2256. *Left:* Result of GMRT 153 MHz observations, yielding a synthesized beam width of $22.1'' \times 16.7''$ and a background RMS of $2.1 \text{ mJy beam}^{-1}$. *Right:* Combined WSRT map at an equivalent frequency of 140 MHz, with a circular beam width of $2.9''$ and a background RMS is $5.5 \text{ mJy beam}^{-1}$. Contours in both maps are drawn at $[3, 5, 8, 12, 20, 36, 60, 100, 200] \times$ the background RMS.

C and F, are clearly detected, as well as several of the point-like sources farther out. We discuss the source complex A & B and source F in more detail in Sections 5.3.4 and 5.3.5.

The peaks of the emission in the WSRT 140 MHz map coincide with the source combination A, B and C, the source F and the relic source G, while smaller peaks in the south coincide with sources O and L. The extended relic area is detected at high S/N, while the halo emission is clearly detected in the area between sources D and O. The 140 MHz halo shape roughly agrees with the halo detections at 350 MHz (Brentjens 2008) and 1.4 GHz (Clarke & Enßlin 2006), but does not continue as far southward (beyond sources O and L) as is seen in the 350 MHz and 1.4 GHz maps.

There are two interesting extensions in the WSRT map at the edges of the diffuse halo & relic regions, one extending westward of the tail end of source C ($17^{\text{h}}00^{\text{m}}, +78^{\circ}43'$) and one extending eastward from the halo area below source F ($17^{\text{h}}08^{\text{m}}, +78^{\circ}34'$), that coincide with three filamentary radio sources in the GMRT 325 MHz map. These sources are also visible in the 350 MHz map by Brentjens (2008), but not noted. The western extension also coincides with a very steep spectrum region in the WSRT spectral index map (Section 5.2.4). Van Weeren et al. (*in preparation*) discusses these two regions in further detail.

5.2.4 Spectral index maps

In Figure 5.4 we present two spectral index maps of the full A2256 region. The low-resolution spectral index map was created from the 6 WSRT bands, by fitting a power-law to the (band-dependent) values of each common ($50''$) pixel, and blanking those pixels that had less than 4 values above 3 times the background RMS. As with the total intensity map, the spectral index map was resampled to the GMRT 325 MHz pixel grid. The original $50''$ pixels have a spectral index fit uncertainty of ~ 1 , which explains the presence of several green/blue noise blobs along the edges. Beyond, the uncertainty rapidly drops to 0.2–0.3 for typical regions and < 0.1 for peak regions. The uncertainty includes the effect of map noise in individual bands. UV-coverage has little effect on the spectral index accuracy, because even at the highest frequency the WSRT array is sensitive to spatial scales $\gtrsim 0.5$ degrees.

The high-resolution spectral index map was created from the 153 and 325 MHz GMRT maps. Fitting gaussians to 10 common point sources in both images and comparing peak positions showed that the systematic astrometric offset between both maps was less than $2''$. Both images were convolved to a circular $24''$ beamsize, after which the 153 MHz map was resampled to the $2.2''$ grid of the 325 MHz map. The spectral index was calculated per pixel, again only using pixels above 3 times the background RMS. Because of the better sensitivity of the 325 MHz map, the spectral index determinations are mainly limited by the 153 MHz pixels. In this case, the effects of UV coverage are important, because both at 153 and 325 MHz the GMRT resolves the large-scale emission. Convolution to the same resolution does help to create a better match in coverage in the outer UV-plane, but does little for matching the inner UV-plane where the large-scale sensitivity is defined. This means that the high-resolution map is accurate in representing the changes in spectral index on smaller scales ($< 1'$), but less accurate in determining the absolute spectral index in large-scale ($> 1'$) diffuse emission areas.

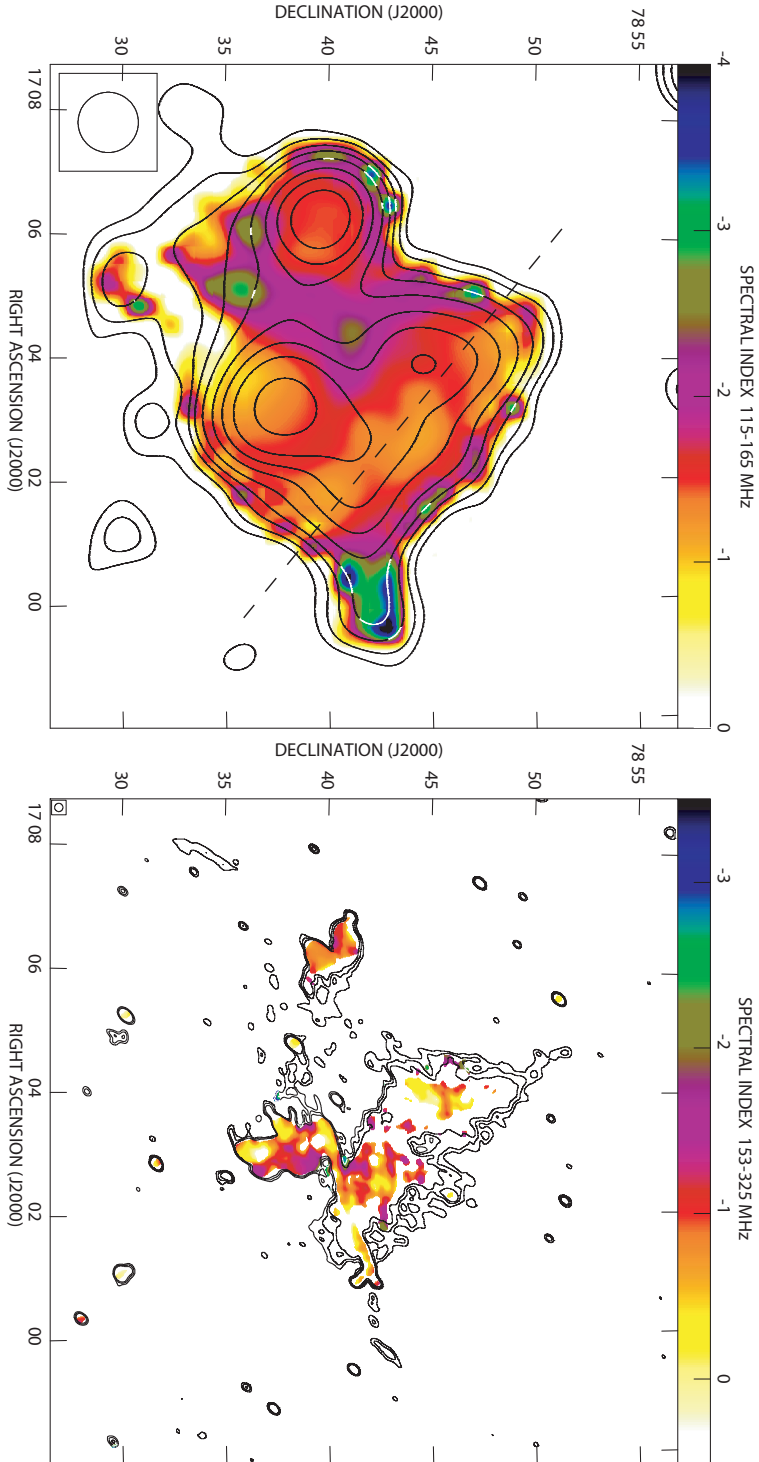


Figure 5.4: Spectral index maps of A2256. *Left:* Smoothed low-resolution spectral index map, measured across 6 WSRT bands between 115–165 MHz. The overlaid contours are taken from the total intensity map in Figure 5.3. Note that the uncertainty in spectral index is large (~ 1) along the outer 50'. *Right:* High-resolution spectral index map, measured between 153–325 MHz. The overlaid contours are 325 MHz total intensity contours (Figure 5.2) at $[5, 8, 12] \times$ the background RMS. Note that the spectral index color bar is shifted by 0.5 between maps.

5.3 Results

The large-scale sensitivity of the WSRT observations detects diffuse emission of A2256 out to the largest scales. Flux measurements of the megaparsec-sized halo and relic in the WSRT map are expected to include all flux. However, the low resolution causes a blending of the more compact sources (e.g. sources A, B, C, F, etc.) with the extended emission. The loss of short baselines in the GMRT 153 MHz data due to RFI prevents an accurate combination of WSRT and GMRT data, as there is little overlap in baseline lengths (e.g., Stanimirovic 2002). For the relic and halo, we have restricted our study to examining the spectral index across these sources in areas that are not contaminated. The high resolution and smaller-scale sensitivity of the GMRT observations at 153 and 325 MHz allow for a detailed study of cluster regions with a complex emission structure. In this work, we use these observations to study the source complex A & B, and complex source F.

5.3.1 Large-scale flux distribution

We estimated the combined flux density of all sources in the cluster by hand-drawing an outer contour around the continuous flux area in the low-resolution WSRT 140 MHz map (Figure 5.3) and summing the flux within. Repeating this process for more strict and more wide areas gave similar values, which we combined into a single estimate of 7.0 ± 0.9 Jy. This includes a ~ 10 percent uncertainty in the determination of the absolute flux scale. This estimate is consistent (within error margins) with the 151 MHz flux density estimate of 8.1 ± 0.8 Jy by Masson & Mayer (1978) (converted to the Perley–Taylor scale by Brentjens 2008), but less so with the double power-law model flux density of 8.7 ± 0.4 Jy at 140 MHz by Brentjens (2008). As a check, we have measured the total flux density of A2256 in the images of individual WSRT bands and find that the flux model $S_\nu = 7.0(\nu/140 \text{ MHz})^{-1.65}$ Jy is a good representation of the individual measurements, where we have taken the mean frequency and mean spectral index that were used for the construction of the total intensity map in Section 5.2.3.

5.3.2 Peripheral relic

In the low-resolution spectral index map (Figure 5.4) there is mixing of emission from different regions. The relic and halo regions are extended enough to have little contamination over substantial parts of their area. Away from sources A to C and the western extension, the relic area appears to have a rather uniform large-scale spectral index distribution. We identify two distinct transitions in the emission area, between the relic and the western extension and between the relic and the halo. These transitions coincide with relic boundaries as seen in the 325 MHz GMRT total intensity map and at higher frequency (e.g., Röttgering et al. 1994a; Clarke & Enßlin 2006). Avoiding the noisy edges, we observe a steepening of the mean spectral index from north-west ($\alpha \approx -1$) to south-east ($\alpha \approx -1.5$). Due to the poor resolution, part of the steepening is probably caused by the gradual transition towards the steeper halo emission ($\alpha \approx -2$; see below). The steepening trend is similar to that observed at 1.4 GHz by Clarke & Enßlin (2006). The mean spectral index, measured along a line running from NW to SE parallel to the relic edges (dashed line in Figure 5.4), is -1.2 ± 0.1 . This is slightly steeper, but consistent within error margins, with the value of -1.0 ± 0.1 at 1.4 GHz. The spectral index map at 350 MHz by Brentjens (2008) shows much more variation across the relic, with no clear

steepening trend.

5.3.3 Central halo

In the low-resolution intensity map (Figure 5.3), between sources A & B, source F and the relic region, there is a relatively uncontaminated view of part of the halo emission (we ignore source D based on the GMRT 153 MHz map in Figure 5.3). This region has a rather uniform spectral index $\alpha \approx -2$ (Figure 5.4), clearly steeper than the emission from the relic and compact source regions. The spectral index map between 1.37 and 1.71 GHz by Clarke & Enßlin (2006) also shows a significant steepening of the halo emission (possible < -3) as compared to other emission regions, although this result is stated to be possibly affected by UV-coverage. For the southern part of the halo we lack sensitivity for accurate spectral index determinations. Our spectral index measurement of the halo is similar to other low-frequency estimates of -1.9 between 22.25 and 81.5 MHz (Costain et al. 1972) and -1.8 between 151 and 610 MHz (Bridle et al. 1979), although the latter estimate is uncertain (Brentjens 2008) because it is based on a resolved halo map at 610 MHz.

From the previous radio halo maps at 350 MHz and 1.4 GHz we notice that the halo emission extends beyond our detection limit in the low-resolution spectral index map, therefore we miss a fraction of the total flux density. From the noise levels of the 350 MHz and 1.4 GHz maps we derive that both are approximately equally sensitive for a spectral index of -1.4 . We observe that the 1.4 GHz halo extends further eastward than the 350 MHz halo, which suggests that the spectral index flattens to > -1.4 in this region. The model radio spectrum of A2256 by Brentjens (2008) assumes a single mean spectral index of -1.61 ± 0.04 for the halo. This can be made consistent with the observations above when assuming that the spectral index varies across the halo, flattens considerably towards the southern and eastern edge, and assign total flux differences to limitations in sensitivity. We do note that the fitted model spectral index for the halo by Brentjens (2008) depends strongly on their estimated halo flux density at 350 MHz and the estimate at 1.4 GHz by Clarke & Enßlin (2006), which may be affected by their estimates of hidden halo flux coinciding with bright emission from relic and the more compact sources (A to D, F, etc.).

5.3.4 Sources A & B

Previous high-resolution observations at 1.4 GHz and 2.7 GHz depict source A as a point-like source that coincides with an optical galaxy at redshift $z = 0.0586$ (Miller et al. 2003), with an $30'' - 40''$ extending tail to the west (Bridle & Fomalont 1976; Röttgering et al. 1994a; Miller et al. 2003). At lower resolution, the 1.4 GHz and 330 MHz maps (Röttgering et al. 1994a) show that the tail extends further west and possibly bends southwards, but its appearance becomes confused with the tail extending from source B. Miller et al. (2003) also detect an extension eastwards of the emission peak, which they identify as independent radio emission from the western nucleus of neighbouring galaxy NGC 6331. Deep, lower resolution images at 350 MHz (Brentjens 2008) and 1.4 GHz (Clarke & Enßlin 2006) show that the whole source complex A & B is embedded in diffuse emission from the halo. No apparent morphological relation exists between sources A & B and the diffuse relic area.

Previous high-resolution observations of source B shows the classical morphology of a head-tail galaxy with a double tail (Röttgering et al. 1994a), similar to NGC 1265 in the Perseus

cluster (Miley 1973). From the core emission that coincides with an optical galaxy counterpart at $z = 0.0548$ (Miller et al. 2003), two radio lobes emerge on the east- and west-side and bend northwards. The length of the brightest part of the head-tail is $40 - 50''$ along a north-south line, but fainter emission continues further north (see also Clarke & Enßlin 2006). In the lower resolution 1.4 GHz and 330 MHz maps from Röttgering et al. (1994a) it appears that the tail emission continues northward beyond source A towards the extremely long head-tail source C. Because of this apparent morphological connection, it seems unlikely that the apparent tail extension is halo emission.

We attempt to disentangle the emission seen in this area by assuming a minimal number of (previously) radio-loud AGN involved. Figure 5.5 shows magnifications of the source A & B area from the two GMRT maps at 153 and 325 MHz (Figures 5.2 and 5.3), as well as a uniform-weighted map at 325 MHz to boost the resolution (which is not used for flux density measurements). Similar to Section 5.3.1, we estimate the flux density of the compact, bright regions of sources A and B at 153 and 325 MHz by drawing image contours around their core areas and summing the flux within. For source A, we find flux densities of 0.53 ± 0.02 Jy at 153 MHz and 0.41 ± 0.02 at 325 MHz, and for source B we find 0.15 ± 0.04 Jy at 153 MHz and 0.13 ± 0.01 at 325 MHz. The specified uncertainties do not include systematic uncertainties in the absolute flux scale.

In all GMRT maps there is a $\sim 2.5'$ (~ 170 kpc projected) tail of visible emission that runs from SW to NE, which appears to connect to source A under a ~ 80 degree angle. The connection between this tail and source A is strengthened by the 1.4 and 2.7 GHz observations of source A (Bridle & Fomalont 1976; Röttgering et al. 1994a; Miller et al. 2003) in which the visible tail from source A overlaps with the low-frequency tail and appears to have a bend in the direction of the low-frequency tail. For sake of convenience, we call this tail source A2. Bridle & Fomalont (1976) noticed a spectral steepening in westward direction, which they found to be consistent with a head-tail configuration. The emission from the long ($\sim 2'$) low-frequency source A2 is confused with emission that appears to originate from source B, except for a small length at the SW end of the tail. When considering the 153 MHz and uniform-weighted 325 MHz maps, the strongest emission originates from a rather well-confined $\sim 30''$ thin strip (≈ 35 kpc), therefore it seems reasonable to assume that source A2 is intrinsically narrow. The tail end has a significantly steeper spectrum (-1.6) than near source A (-0.3), which fits the typical profile of spectral steepening along a radio tail (e.g., Jaffe & Perola 1973). Ignoring the smallest variations, the spectral index along source A2 in the overlap region with source B is rather constant (-1 to -1.2). The measured total flux density within the thin strip over the $2'$ tail length is 0.35 ± 0.05 Jy at 153 MHz and 0.14 ± 0.06 Jy at 325 MHz, which includes some flux contamination from the surrounding diffuse emission of source B.

In addition to the long tail, the 325 MHz map also contains a small extension of emission at the opposite side (south-east) of source A. We note that dynamic range limitations from calibration and imaging cause some artifacts near bright source A. The apparently significant $> 15\sigma$ detection in the robust weighted 325 MHz map is therefore more likely a $2 - 3\sigma$ detection when considering the local noise. We cannot be sure if this feature is real or an image artifact. However, if real, the small tail overlaps with the radio source just eastward of source A, which Miller et al. (2003) associated with NGC 6331, although our detection extends $\sim 50''$ further east. This implies a spectral steepening of the small tail away from source A, which we cannot confirm in our spectral index map due to the non-detection at 153 MHz. It is tempting to associate the small tail with source A as well, which would provide source A with the typical double-lobe morphol-

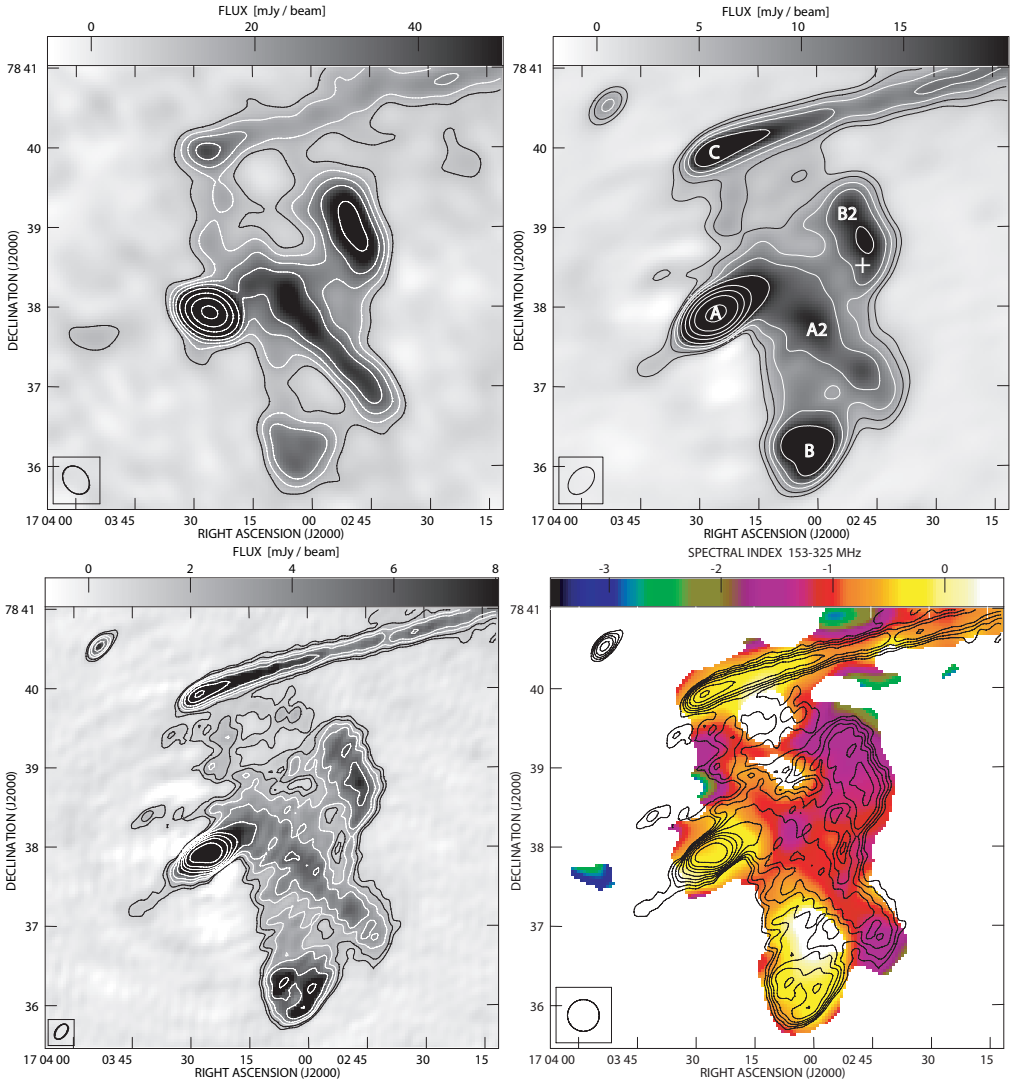


Figure 5.5: Detailed maps of the confused region of sources A & B in A2256. *Top Left:* Magnification of the GMRT 153 MHz map in Figure 5.3. Contours are drawn at $[5, 8, 12, 18, 30, 54, 90, 150, 300] \times$ the background RMS. *Top Right:* Magnification of the GMRT 325 MHz map in Figure 5.2. Contours are drawn at $[15, 25, 40, 60, 100, 180, 300, 500, 1000] \times$ the background RMS. Several of the labelled sources are discussed in the text. The plus-sign marks the position of the cluster galaxy nearest (in projection) to source B2. *Bottom Left:* Uniform weighted map (instead of robust weighted) of the GMRT 325 MHz map, yielding a beam width of $13.1'' \times 7.8''$ and a background RMS of $0.12 \mu\text{Jy beam}^{-1}$. Contours are drawn at $[7, 12, 20, 28, 50, 90, 150, 250, 500] \times$ the background RMS. *Bottom Right:* Spectral index map of the GMRT observations between 153 and 325 MHz, convolved to a common beam width of $24'' \times 24''$. Contours are taken from the uniform weighted 325 MHz map.

ogy of an AGN rather than a head-tail morphology, with relativistic beaming being responsible for the contrast between the two lobes.

The low-frequency morphology of source B corresponds to the head-tail radio source observed at higher frequencies, with wide tail emission that (partly) merges north of the head into a single diffuse emission region. The view of the wide tail is confused by source A (and source A2, but for the discussion here we simply assume the narrow tail is part of source A). Assuming the emission from source A is confined to the bright emission areas, the tail of source B appears to extend beyond source A towards source C. This apparent connection is supported by (i) the apparent continuity of the wide tail across source A in terms of flux level and boundary contours, (ii) the apparent presence of two tail extensions north of source A in the 153 MHz map, (iii) the steepening of the spectral index between source B and the apparent tail extension(s), and (iv) the extent of the tail in 1.4 GHz images (Röttgering et al. 1994a; Clarke & Enßlin 2006), in which source A2 is not visible. If the diffuse emission north of source A is indeed part of the tail of source B, the total length of the tail would be $\geq 4'$, which corresponds to a projected length of ≥ 270 kpc, similar to the ~ 280 kpc length of NGC 1265 (Feretti et al. 1996) and over half the length of the long head-tail galaxy source C. This tail is slightly bent and widens from $1'$ at the head to $\sim 2.5'$ at the tail end.

There are two regions of emission for which we discuss alternative origins. A region of faint emission lies at the end of the (assumed) tail of source B at $17^{\text{h}}03^{\text{m}}15^{\text{s}}$, $+78^{\circ}39'30''$, which connects to source C (in projection; see Figure 5.5). Twin-tail sources such as source B are known to have tails that fade towards the tail end, but a morphological connection to another source may be possible. Based on the total intensity maps alone it may seem that some of the faint emission extends southwards from source C. However, this is inconsistent with the required large velocity (relative to the ICM) of the galaxy found in the head of source C to create the extremely straight, narrow-tail morphology (Röttgering et al. 1994a). There is no known cluster galaxy in the catalogs by Fabricant et al. (1989), Berrington et al. (2002) or Miller et al. (2003) that lies in this area and generates this emission. In the absence of plausible alternatives, we assume that the low-frequency tail of source B extends all the way up to source C.

The second region for which the origin is unclear is the bright emission region that appears to be connected to the western end of the wide tail of source B at $17^{\text{h}}02^{\text{m}}50^{\text{s}}$, $+78^{\circ}39'00''$, which we will call source B2. The dimensions of this region are approximately $1.2' \times 0.7'$, which corresponds to 80×47 kpc² at the cluster distance. The total flux density estimates for source B2 at 153 and 325 MHz are 0.27 ± 0.05 Jy and 0.12 ± 0.01 Jy, respectively, which yields a spectral index estimate of -1.08 ± 0.36 between 153 and 325 MHz. It is unclear whether source B2 is a distinct source or part of source A or B. From the catalog of Berrington et al. (2002) we identify a confirmed cluster galaxy near (in projection) the southern edge of source B2 (see Figure 5.5). If this galaxy is responsible for the bright emission region, it must have ceased its radio-loud phase, as there is no detection of radio emission from this source in the deep maps at 1.4 GHz (Röttgering et al. 1994a; Miller et al. 2003). The apparent alignment of source B2 with the tail from source A before the bend could indicate a physical relation, but this would require the narrow tail to be either unrelated to source A or to be displaced over a significant distance.

5.3.5 Source F

Source F has been noticed for its peculiar Z-shape and ultra-steep spectrum (e.g., Masson & Mayer 1978; Bridle et al. 1979). Based on the morphology at 1.4 GHz, source F was divided

into three parts: the central bright region F2, the emission region F3 north-east of F2 and the faint emission region F1 south-west of F2. At 1.4 GHz, the region F3 has the appearance of a head-tail radio source (Röttgering et al. 1994a), with an optical counterpart at the eastern head at redshift $z = 0.0563$ (Miller et al. 2003) and considerable steepening of the spectrum from the head towards the tail end (-0.7 to -1.9) near source F2. Source F1 also resembles a head-tail source with spectral steepening along the tail (-1 to -1.6 , ending at source F2) but at much fainter flux levels and without an optical counterpart at the head.

The emission of source F2 could be connected to both F1 and F3, but its true origin is unclear. In the absence of confirmed optical counterpart for source F2, it has been speculated that sources F1, F2 and F3 are all part of the same source (Bridle et al. 1979), originating from the head of source F1. High-resolution 1.4 GHz imaging reveals filamentary structure inside source F2 (Röttgering et al. 1994a; Miller et al. 2003), which has been noted to bear resemblance to the cluster relic source in Abell 85 at J004127-092300 (e.g., Slee et al. 2001). If source F2 resides at the cluster distance, the $1.4' \times 0.8'$ dimensions correspond to a proper size of $94 \times 54 \text{ kpc}^2$. The spectral index of source F2 between 350 MHz and 1.4 GHz is estimated at -1.71 ± 0.08 (Brentjens 2008).

Magnifications of the source F region from the GMRT 153 and 325 MHz maps are presented in Figure 5.6. Similar to Section 5.3.1, we estimate the flux density of the source F components at 153 and 325 MHz by drawing image contours around their areas and summing the flux within. The resulting flux determination of source F1 is very uncertain, therefore omitted. For source F2, we find flux densities of $0.53 \pm 0.02 \text{ Jy}$ at 153 MHz and 0.30 ± 0.01 at 325 MHz, and for source F3 we find $0.18 \pm 0.02 \text{ Jy}$ at 153 MHz and 0.13 ± 0.01 at 325 MHz. The 325 MHz flux density of source F2 is a good match to the 325 MHz estimate of 0.29 ± 0.07 from the power-law model between 350 MHz and 1.4 GHz by Brentjens (2008). Our flux density measurements at 325 MHz are significantly higher than the 327 MHz flux densities of $0.250 \pm 0.018 \text{ Jy}$ for source F2 and $0.078 \pm 0.010 \text{ Jy}$ for source F3 by Röttgering et al. (1994a). While both maps have similar resolution, our background RMS is a factor ~ 2 lower. A visual comparison of the relic area in both maps clearly shows that our map is more sensitive to large-scale emission. These differences lead us to conclude that our 325 MHz flux density measurements include a diffuse component that is not detected in the 327 MHz map by Röttgering et al. (1994a). Our flux density measurement of source F2 at 153 MHz is lower than the 151 MHz estimate of 0.65 Jy (no error estimate quoted) by Bridle et al. (1979), but their estimate is based on differencing a low-resolution map against an extrapolated map from higher frequencies, which includes many assumptions and uncertainties. When adding a 20 percent uncertainty to this estimate, both measurements agree within error bars.

From the total flux density measurements we find that the spectral index between 153 and 325 MHz is -0.76 ± 0.09 for source F2 and -0.43 ± 0.15 for source F3. Figure 5.6 also contains a spectral index map of the source F region over the same frequency range. There is a good match between the spectral index map of source F2 and the spectral index of -0.76 based on the total flux densities. For source F3, the spectral map is on average much steeper than -0.43 , which indicates that the total flux density measurement of source F3 includes a component at 325 MHz that is not detected at 153 MHz. Most likely, the 325 MHz measurement includes a diffuse component not seen at 153 MHz due to differences in sensitivity and UV-coverage, which becomes more important for fainter sources such as source F3. Fortunately, except for the tail of source B, the regions in the spectral maps we discussed so far are all regions with strong emission at 153 MHz. The combined spectral index results for source F2 from Brentjens (2008)

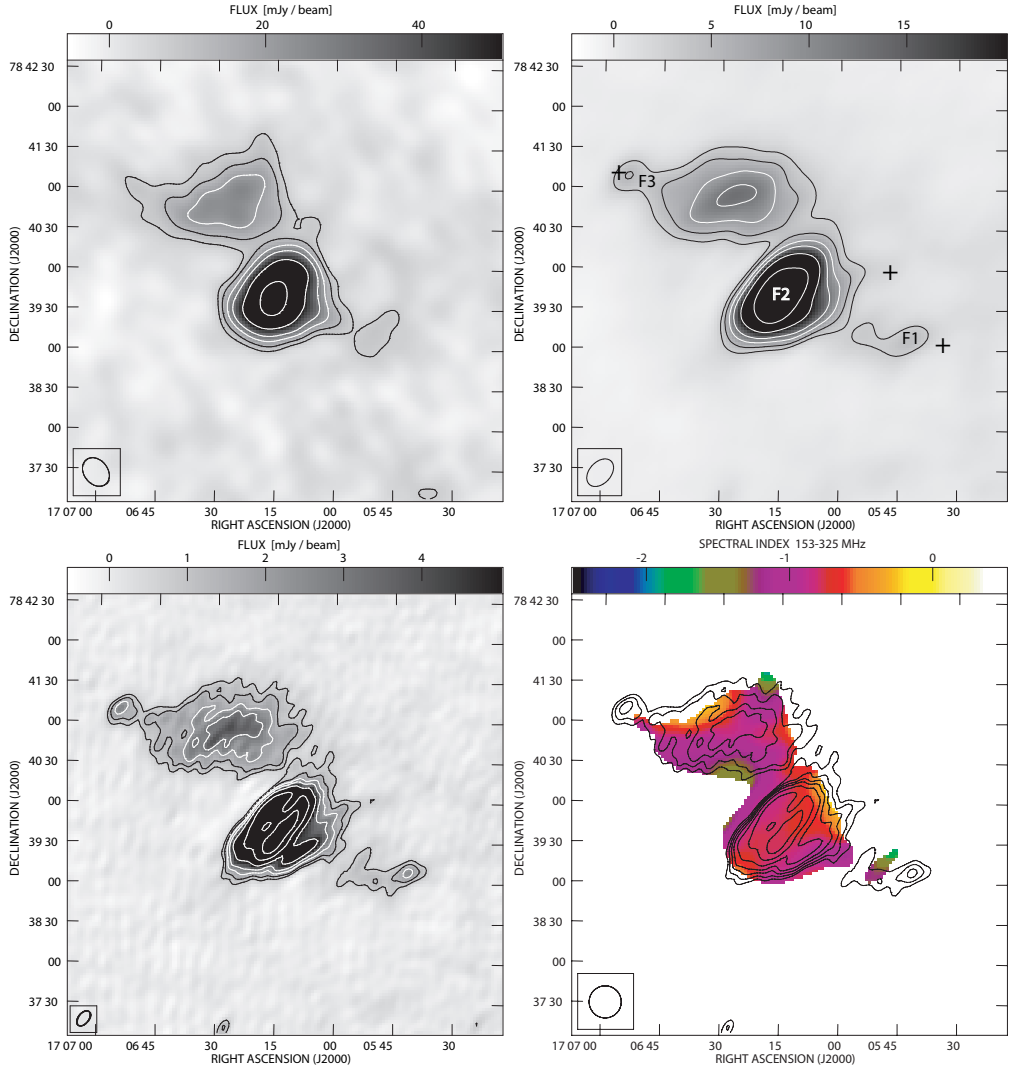


Figure 5.6: Detailed maps of the complex source F in A2256, similar to Figure 5.5. *Top Left:* Magnification of the GMRT 153 MHz map. Contours are drawn at $[4, 6, 10, 15, 24, 42, 72, 120, 240] \times$ the background RMS. *Top Right:* Magnification of the robust weighted GMRT 325 MHz map. Contours are drawn at $[15, 25, 40, 60, 100, 180, 300, 500, 1000] \times$ the background RMS. Several of the labelled sources are discussed in the text. The plus-signs mark the positions of the cluster galaxies nearest (in projection) to sources F1, F2 and F3. *Bottom Left:* Uniform weighted map of the GMRT 325 MHz observations. Contours are drawn at $[6, 10, 16, 25, 42, 75, 125, 210, 420] \times$ the background RMS. *Bottom Right:* Spectral index map of the GMRT observations between 153 and 325 MHz. Contours are taken from the uniform weighted 325 MHz map.

and this work implies a large spectral index change from -0.76 between 153 and 327 MHz to -1.71 between 327 MHz and 1.4 GHz.

5.4 Discussion

Cluster mergers are known to have an effect on the appearance of radio sources in the cluster. Using the low-frequency observations from WSRT and GMRT we have presented a complementary radio view on several remarkable sources in A2256. The low-resolution images confirmed the presence and steep spectra of the large-scale emission regions, namely the radio halo and relic. The high-resolution imaging yielded several interesting results that we discuss further in this section.

5.4.1 A radio phoenix in the cluster periphery

Source F2 is located at the western edge of the radio halo, which coincides with the edge of the observed X-ray emission (e.g., Clarke & Enßlin 2006; Sun et al. 2002). In the nomenclature of Kempner et al. (2004), its steep spectrum, apparent size, apparent detachment from its origin (most likely an AGN) qualifies source F2 as either a *radio phoenix* or an *AGN relic*, depending on whether or not the ICM has compressed the region to revive the aged AGN plasma emission. Given the geometry of source F (see Figure 5.6), it seems reasonable to assume source F2 originates from the AGN associated with source F3, or possibly with an AGN previously associated with source F1. Reasons for assuming that source F2 is a radio phoenix that has been revived by a shock wave from the ICM are (i) the extreme steepening of the spectrum towards higher frequencies, (ii) its relative brightness, and (iii) the shell-like filamentary structure. Through semi-analytical modeling of compression of fossil radio plasma, Enßlin & Gopal-Krishna (2001) showed that compression of a radio cocoon with a steepened spectrum of aged synchrotron emission can result in a flux enhancement while preserving the steep spectrum. Furthermore, numerical magneto-hydrodynamical (MHD) simulations by Enßlin & Brüggen (2002) showed that adiabatic shock compression of radio cocoons can produce radio sources with a shell-like filamentary appearance.

With the help of the synchrotron aging / revival model of Enßlin & Gopal-Krishna (2001) we investigated two scenarios for the origin of source F2: (1) the AGN relic scenario, in which the synchrotron emitting volume aged, but is not shocked, and (2) the radio phoenix scenario, in which the aged synchrotron volume has been adiabatically compressed by a (cluster merger) shock wave. The model includes many assumptions, therefore the outcome should be interpreted as an order of magnitude estimation. We adopt the model parameter values from the ‘smoking gun’ scenario by Enßlin & Gopal-Krishna (2001), as this describes the evolution of a small synchrotron emitting volume in the cluster periphery. Two important model input parameters are the current (observed) synchrotron volume and the magnetic field strength within. For source F2 we adopted a cylindrical volume of $V = \pi d^2 l / 4 \approx 2 \cdot 10^{-4} \text{ Mpc}^3$, where we used the projected dimensions $l \times d = 94 \times 54 \text{ kpc}^2$ from Section 5.3.5. Using the revised minimum energy formulae by Beck & Krause (2005)⁹, we estimated the magnetic field strength in source F2. From our flux density measurement at 153 MHz, and assuming an injection spectral index of $\alpha_{\text{inj}} = -0.7$, we

⁹For the calculation we used the BFIELD code (version 10feb2006), available through the same authors.

derive a total magnetic field strength $B \sim 6 \mu\text{G}$, which is similar to the estimates by Brentjens (2008).

In scenario 1, an AGN that was assumed to be active for ~ 0.015 Gyr has injected relativistic electrons with an energy spectrum $N(E) \propto E^{2\alpha_{\text{inj}}-1}$ into a volume V_0 , permeated with a magnetic field B_0 . After the AGN ceased activity, the volume expanded further due to an over-pressure in the volume as compared to the surrounding gas at the cluster boundary. While expanding, the radio luminosity drops. Pressure equilibrium is reached on a time scale on the order of ~ 0.01 Gyr. We used the model to calculate the observable radio spectrum during the volume expansion after the AGN activity ceased. Similar to Kale & Dwarakanath (2009), we manually varied the shock compression factor $C = V_0/V$ and the expansion time Δt_1 to obtain a good fit for the spectrum, normalized to the GMRT 153 MHz flux density measurement $S_{153} = 0.53$ Jy, as well as a good reproduction of the observed volume and magnetic field strength. Our fit included the GMRT 153 MHz and 325 MHz flux density measurements, as well as the compiled flux points by Brentjens (2008), but we excluded the rather uncertain 151 MHz estimate from Bridle et al. (1979). The best fit is given by $C = 0.23$ and $\Delta t_1 = 24$ Myr, which implies $V_0 = 5 \cdot 10^{-5} \text{ Mpc}^3$, $B_0 = 16 \mu\text{G}$ and an initial 153 MHz flux density of $S_{153} = 8.3$ Jy.

In scenario 2, we continue the ‘smoking gun’ scenario by assuming pressure equilibrium is reached after $\Delta t_1 = 32$ Myr. The initial volume has expanded by a factor of ~ 5 and is slowly losing energy through synchrotron radiation over a period of $\Delta t_2 = 100$ Myr. During the next $\Delta t_3 = 130$ Myr, the volume is adiabatically compressed by a shock wave, reducing the volume to less than its initial size. The post-shock volume is again in pressure equilibrium with its environment, and continues to lose energy through synchrotron radiation. Similar to scenario 1, we manually varied the compression factor C and the spectral aging time Δt_4 after compression to obtain a good fit for the spectrum, observed volume and magnetic field strength. The best fit is given by $C = 3.2$ and $\Delta t_4 = 20$ Myr, which implies $V_0 = 7 \cdot 10^{-4} \text{ Mpc}^3$, $B_0 = 2.8 \mu\text{G}$ and an initial 153 MHz flux density of $S_{153} = 0.12$ Jy.

Figure 5.7 shows plots of the model spectra for both scenarios. In both cases, our GMRT 325 MHz flux density measurement lies significantly above the fitted curve. There was no parameter combination for which the 325 MHz measurement could be fitted accurately in combination with the 153 MHz and 1.4 GHz measurements. The models are consistent with all other measurements, given the uncertainties.

Due to the volume expansion, the AGN relic scenario requires an initial volume that is larger than the observed volume, while the initial magnetic field strength is required to be stronger than the observed value. Furthermore, this scenario puts a strict time constraint on the age of the volume since the AGN turned off. For the radio phoenix scenario the requirements are less strict, because they do not only depend on age since the AGN turned off, but also on the time and strength of the shock compression. If, like assumed above, the compression factor is larger than one, the initial volume is larger than the observed volume, and the magnetic field strength is initially smaller.

For the following discussion, we assume that our model and the derived initial conditions are reasonably accurate. The magnetic field strength in galaxy clusters is typically found to be in the order of 0.5 to $5 \mu\text{G}$, depending on the location in the cluster, and the method and assumptions used for determining the magnetic field strength (Carilli & Taylor 2002, and references therein). The magnetic field strength in lobes of AGN are roughly an order of magnitude larger (e.g., Croston et al. 2005). A required initial field strength of $16 \mu\text{G}$ for the AGN relic scenario is therefore as likely as the $2.8 \mu\text{G}$ for the radio phoenix scenario. Based on radio number counts

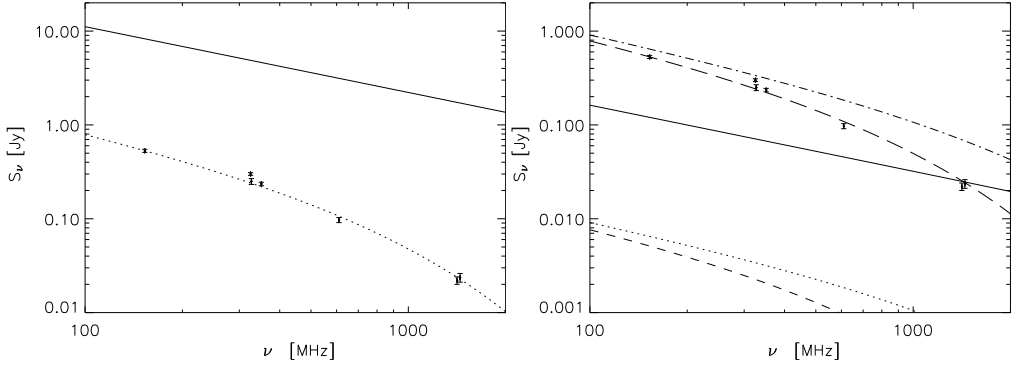


Figure 5.7: Fits of the synchrotron aging / revival model of Enßlin & Gopal-Krishna (2001) to the GMRT 153 MHz and 325 MHz flux density measurements of source F2, complemented with the compiled flux points by Brentjens (2008). *Left:* Scenario 1 (AGN relic scenario), in which the injected synchrotron emitting volume (solid line) ages to become an AGN relic (dotted line) before reaching pressure balance with its environment. *Right:* Scenario 2 (radio phoenix scenario), in which the injected synchrotron emission (solid line) reaches pressure balance (dotted line), continues to lose energy through radiation (dashed line), gets adiabatically compressed (dot-dash line), and again continues to lose energy through radiation (long dashed line). See the text for more information.

(e.g., Chapter 4), an AGN with an initial 153 MHz flux density of 8.3 Jy indicates a more rare type of source than the rather common 0.12 Jy for the radio phoenix. When considering an age of 24 Myr for the AGN relic, this requires the AGN to be present in the near vicinity. Taking the velocity dispersion of 1350 km s^{-1} (Faber & Dressler 1977) as a typical velocity value, the angular displacement of the AGN galaxy in the sky plane is $\lesssim 25''$. Based on the age requirement, there is no discrepancy if source F2 is physically associated with source F3, but a physical association between source F1 and source F3 would be unlikely. Alternatively, there may be another, yet unidentified, galaxy involved. The less strict age requirement for the radio phoenix allows for many more options for the originating AGN galaxy.

Although not conclusive, the combined evidence presented here and in literature favours an explanation in which source F2 is a radio phoenix rather than an AGN relic. Revival of aged, steep-spectrum synchrotron emission through merger shock compression may be one of the mechanisms that is causing the detectable presence of this and several other steep-spectrum radio sources, as it can ‘simultaneously wake’ the fossil radio lobes that have been created in relatively short (~ 0.01 Gyr) AGN lifetimes and have been accumulating over a very long (sub-)cluster lifetime (few Gyr). This can also explain the appearance of the newly discovered filamentary structures on the edge of the halo & relic area by van Weeren et al. (*in preparation*).

5.4.2 A radio phoenix at the cluster center?

The bright emission region near source A and B that we named source B2 is similar to source F2 in terms of angular size, shape, relative brightness and unknown origin, but differs in other observed properties: it is located (in projection) near the brightest of three X-ray peaks, the centers of possible merging subclusters that form the larger A2256 cluster (Sun et al. 2002), its

153–325 MHz spectrum is steeper, and there are no clear filamentary structures visible (but this could be a resolution issue). Source B2 also qualifies as an AGN relic or radio phoenix, for much of the same reasons as source F2. The indirect evidence for shock compression comes from the cluster merger scenario that has been proposed for A2256, based on radio and X-ray observations (Sun et al. 2002; Clarke & Enßlin 2006).

To extend the measured spectrum of source B2 to three points, we make an estimate of the 1.4 GHz flux density by defining a rectangular area of $1.2' \times 0.7'$ and using the average between the first and second contour ($225 \mu\text{Jy beam}^{-1}$ for a $17.3'' \times 13.7''$ beam) in the map by Röttgering et al. (1994a) as the mean flux level. Assuming a 25 percent uncertainty, this yields 3.7 ± 0.9 mJy. The spectral index between 325 MHz and 1.4 GHz is -2.3 ± 0.2 . Recalling the spectral index estimate of -1.08 ± 0.36 between 153 and 325 MHz (Section 5.3.4), this implies a large spectral steepening towards high frequency, similar to source F2.

Again, we use the synchrotron aging / revival model of Enßlin & Gopal-Krishna (2001), now to investigate the origin of source B2. We adopt most of their model parameter values from the ‘cocoon at the cluster center’ scenario. We assume a cylindrical volume of $V = \pi d^2 l / 4 \approx 1.4 \cdot 10^{-4} \text{ Mpc}^3$ (using the projected dimensions $l \times d = 80 \times 47 \text{ kpc}^2$ from Section 5.3.4), and a total magnetic field strength $B \sim 6 \mu\text{G}$ from the revised minimum energy formulae by Beck & Krause (2005), assuming an injection spectral index of $\alpha = -0.7$.

For scenario 1 (AGN relic), we obtain the best model fit in the phase where the unshocked volume is in pressure equilibrium with the surrounding gas, with $C = 0.60$ and $\Delta t_2 = 105 \text{ Myr}$, which implies $V_0 = 8 \cdot 10^{-5} \text{ Mpc}^3$, $B_0 = 8.5 \mu\text{G}$ and an initial 153 MHz flux density of $S_{153} = 1.1 \text{ Jy}$.

For scenario 2 (radio phoenix), we obtain the best model fit for the phase in which the shocked volume is in pressure equilibrium with the surrounding gas, with $C = 3.8$ and $\Delta t_4 = 105 \text{ Myr}$, which implies $V_0 = 5 \cdot 10^{-4} \text{ Mpc}^3$, $B_0 = 2.5 \mu\text{G}$ and an initial 153 MHz flux density of $S_{153} = 57 \text{ mJy}$.

The model fits for both scenarios and the flux density measurements are plotted in Figure 5.8. Given that the spectra were scaled to the 153 MHz measurement, it was not possible to find model parameters that would create an accurate fit to both the 325 MHz and 1.4 GHz flux density measurements. Similar to Section 5.4.1, this could be resolved if the 325 MHz flux density was scaled down, but there are too few data points to be conclusive about the origin of this apparent discrepancy.

Similar to source F2, the requirements on the initial conditions of source B2 are more strict for the AGN relic scenario than for the radio phoenix scenario, but less extreme. In the AGN relic scenario, the total age (expansion plus equilibrium) $\Delta t_1 + \Delta t_2 = 5.4 + 105 \approx 110 \text{ Myr}$ would provide a galaxy displacement radius of $\lesssim 100''$. Alternatively, if source B2 is part of the tail of source B, the question rises why source B2 is much brighter than the rest of the tail. If it is shocked, why not the rest of the tail? The alignment and correspondance in brightness of source B2 with source A may indicate a physical relation, but we cannot proceed beyond speculation.

5.4.3 Bent head-tail galaxies at the cluster center

If the low-frequency tail that we named source A2 in Section 5.3.4 is physically related to source A, it may belong to a class of bent head-tail galaxies in clusters, such as 3C 129 in 4U 0446+44 (Miley 1973) and 4C 21.05 in Abell 84 (Giovannini & Feretti 2000). Mao et al.

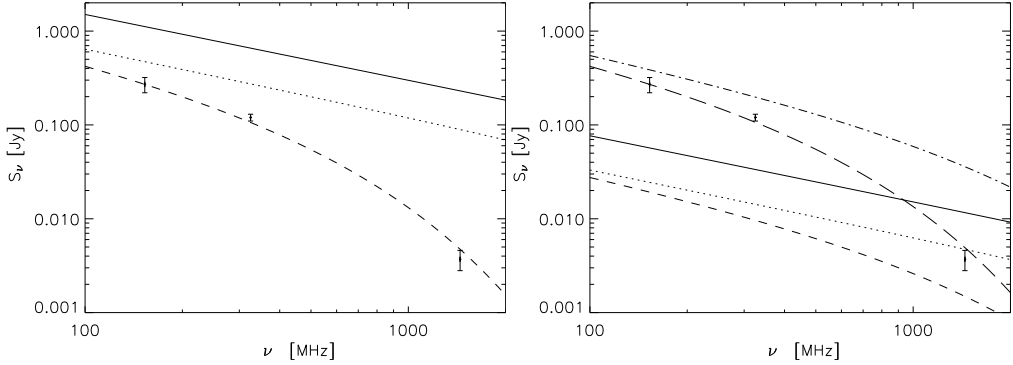


Figure 5.8: Fits of the synchrotron aging / revival model of Enßlin & Gopal-Krishna (2001) to the GMRT 153 MHz and 325 MHz flux density measurements of source B2, complemented with a 1.4 GHz flux density estimate using the map from Röttgering et al. (1994a). *Left:* Scenario 1, in which the injected synchrotron emission (solid line) reaches pressure balance (dotted line) and continues to lose energy through radiation (dashed line). *Right:* Scenario 2, in which the injected synchrotron emission (solid line) reaches pressure balance (dotted line), continues to lose energy through radiation (dashed line), gets adiabatically compressed (dot-dash line), and again continues to lose energy through radiation (long dashed line). See the text for more information.

(2009) found that 5 head-tail galaxies in the merging A3125–A3128 supercluster live in regions of very high galaxy density ($> 100 \text{ Mpc}^{-3}$) in the vicinity of peaks in the X-ray emission. They argue that the radial peculiar velocities of their head-tail galaxies with respect to the supercluster average are too low to cause the bends in the tails, therefore bulk motion of the ICM must be responsible. We compare the radial velocities of sources A and B (the latter also appears to have a slightly bent tail) against the A2256 cluster velocity distribution. Miller et al. (2003) found $cz = 17565 \pm 54 \text{ km s}^{-1}$ and $16417 \pm 39 \text{ km s}^{-1}$ for sources A and B, respectively, and quote a systematic radial velocity of $cz_0 = 17490 \pm 74 \text{ km s}^{-1}$ and a dispersion $\sigma_{cz} = 1269^{+56}_{-49} \text{ km s}^{-1}$. The peculiar radial velocity / dispersion ratios of sources A and B are $+0.06$ and -0.85 , respectively, indicating that neither of both has a particularly large velocity along the line-of sight.

The low peculiar radial velocity, combined with the possible double lobe morphology, suggests that source A has a low 3-dimensional velocity as compared to the cluster center. This implies that the bend in the low-frequency tail A2 (or rather, lobe A2) is indeed the result of bulk movement of the ICM, which could result from the cluster merger. The negative velocity as compared to the cluster center, combined with the approximate north–south orientation of the tail, suggests that source B may have passed closer to the cluster center, i.e. closer to source A. Any displacement of the ICM may have affected the tail of source B as well.

5.5 Summary

We have presented deep, low-frequency radio observations of the galaxy cluster Abell 2256. In deep WSRT observations at 115–165 MHz we clearly detect the diffuse halo and relic emission,

and measure a 140 MHz flux density of 7.0 ± 0.9 Jy for the whole cluster. The mean spectral indices over the same frequency range for the relic and halo are estimated at ~ -1.2 and ~ -2 , respectively. We suggest that the flatter halo spectral index of -1.6 found by Brentjens (2008) can be the result of an over-estimation of hidden halo flux at 350 MHz and 1.4 GHz, the inaccuracy of several older flux density measurements below 300 MHz, or a spectral flattening of the halo towards the southern and eastern boundary.

We used the deep GMRT observations at 153 and 325 MHz to study the regions containing sources A & B and the complex source F. We detected a tail of low-frequency emission (which we named source A2) that appears to connect to the tail of source A at higher frequencies, which implies a (projected) bend of ~ 80 degrees. In the same area, we detected an emission region, which we named source B2. We speculated on the possible connection with either source A or B. Similar to source F2, source B2 also has no clear origin. The results of applying semi-analytical models for synchrotron aging / revival (Enßlin & Gopal-Krishna 2001) favour a scenario in which source F2 is revived by shock compression. The outcome for source B2 is less clear.

The presence of revived synchrotron emission regions and sources with a bend tail (or lobe) are indicators of cluster merger activity (e.g., Enßlin & Gopal-Krishna 2001; Klammer et al. 2004; Mao et al. 2009). Taken together, the results presented in this chapter support the hypothesis that the ICM of A2256 is disturbed by recent merger activity (e.g., Clarke & Enßlin 2006; Brentjens 2008).

Acknowledgements. The authors would like to thank both the staff of the WSRT and GMRT that made these observations possible. The WSRT is operated by the Netherlands Foundation for Research in Astronomy (ASTRON) with support from the Netherlands Foundation for Scientific Research (NWO). The GMRT is run by the National Centre for Radio Astrophysics (NCRA) of the Tata Institute of Fundamental Research (TIFR). HTI acknowledges a grant from the Netherlands Research School for Astronomy (NOVA).

Large-scale structure of Lyman break galaxies around a radio galaxy protocluster at $z \sim 4$

Abstract. We present broad-band imaging with the Subaru Telescope of a $25' \times 25'$ field surrounding the radio galaxy TN J1338–1942 at redshift $z = 4.1$. The field contains excesses of Lyman- α emitters (LAEs) and Lyman break galaxies (LBGs) identified with a protocluster surrounding the radio galaxy. Our new wide-field images provide information about the boundary of the protocluster and its surroundings. There are 874 candidate LBGs within our field, having redshifts in the range $z = 3.5 - 4.5$. An examination of the brightest of these (with $i' < 25.0$) shows that the most prominent concentration coincides with the previously discovered protocluster. The diameter of this galaxy overdensity corresponds to ~ 2 Mpc at $z = 4$, consistent with the previous estimation using LAEs. Several other concentrations of LBGs are observed in the field, some of which may well be physically connected with the $z = 4.1$ protocluster. The observed structure in the smoothed LBG distribution can be explained as the projection of large-scale structure, within the redshift range $z = 3.5 - 4.5$, comprising compact overdensities and prominent larger voids. If the 5 to 8 observed compact overdensities are associated with protoclusters, the observed protocluster volume density is $\sim 5 \times 10^{-6} \text{ Mpc}^{-3}$, similar to the volume density of rich clusters in the local Universe.

H. T. Intema, B. P. Venemans, J. D. Kurk, M. Ouchi, T. Kodama,
H. J. A. Röttgering, G. K. Miley, and R. A. Overzier
Astronomy & Astrophysics, **456**, 433 (2006)

6.1 Introduction

There is considerable evidence for galaxy overdensities at high redshifts ($z > 2$; e.g. Steidel et al. 1998; Møller & Fynbo 2001; Shimasaku et al. 2003; Palunas et al. 2004; Ouchi et al. 2005). In many cases these overdensities have been presumed to be associated with the ancestors of rich local clusters. At $z > 2$ the Universe is $\lesssim 3$ Gyr old, too short for these structures to have virialized (e.g., Venemans 2005). Hence these structures are often called *protoclusters*. Most searches for protoclusters have been limited by relatively small fields (typically smaller than $10' \times 10'$).

An efficient way of finding protoclusters is to use high redshift radio galaxies (HzRGs; e.g. Röttgering et al. 1994b) as tracers (Venemans et al. 2002; Kurk et al. 2004). HzRGs are large massive objects with many of the properties expected of forming dominant cluster (cD) galaxies (West 1994). Although most protoclusters are not radio-loud, radio-selected protoclusters may be typical. Because radio-sources are relatively short-lived ($\sim 10^7$ years; Blundell & Rawlings 1999), the statistics are consistent with the progenitor of every rich local cluster having harboured a luminous radio galaxy at some stage in its existence.

Using the VLT, Venemans et al. (2002) spectroscopically confirmed 20 Lyman- α emitters (LAEs) in a $7' \times 7'$ field around HzRG TN J1338–1942 at a redshift of $z = 4.1$ and identified these LAEs with a $z = 4.1$ protocluster. Further evidence that this LAE overdensity was indeed associated with a protocluster was provided by observations with the HST/ACS that revealed an excess and non-uniform distribution of candidate Lyman break galaxies (LBGs) around the HzRG (Miley et al. 2004; Overzier et al. 2008).

Although the LAE search around TN J1338–1942 was extended with a second $7' \times 7'$ field (Venemans 2005), this was insufficient to determine the boundary of the protocluster. Here we present the results of a multi-color study of candidate LBGs from a $25' \times 25'$ region surrounding TN J1338–1942. The large field-of-view (FoV) facilitates searches for LBGs out to the boundary of the protocluster structure and beyond. The data also provide new information about large-scale structure and voids at $z \sim 4$.

Throughout this chapter, we use AB-magnitudes, 1σ errors and adopt a flat, Λ -dominated cosmology with $\Omega_M = 0.3$, $\Omega_\Lambda = 0.7$ and $H_0 = 100 h \text{ km s}^{-1} \text{ Mpc}^{-1}$ with $h = 0.7$.

6.2 Data reduction and sample selection

Deep multi-color imaging of the TN J1338–1942 field was carried out using the Subaru Suprime-Cam instrument (Miyazaki et al. 2002) on January 31st and February 1st, 2003. Data reduction on the B -, R_C - and i' -band images was performed in a manner similar to that of the SDF and SXDF fields (Ouchi et al. 2001, 2004a). The FoV was $24.7' \times 24.2'$ and the seeing had an equivalent FWHM of $0.98''$. Source extraction and photometry was done using SExtractor (Bertin & Arnouts 1996). Fluxes were measured in a $2''$ circular aperture with 3σ limiting magnitudes of 27.2, 26.9 and 26.5, respectively. Extending the observed power-law estimation for bright source counts (e.g., see Palunas et al. 2004), the initial object sample was limited to $i' \leq 26.5$ to obtain a photometric completeness of ~ 72 percent for the highest magnitude bin ($\Delta i' = 0.5$).

LBGs in an approximate redshift range $z = 3.5 - 4.5$ were selected using color selection criteria by Ouchi et al. (2004a), resulting in a sample of 874 LBGs. Based on the same work, the estimated contamination by interlopers and stars is ~ 6 percent, while the estimated com-

pleteness distribution function over redshift has an approximate gaussian function shape with a FWHM of 0.8, centered at $z = 4$ with a peak value of ~ 45 percent. In addition, a bright subsample of LBGs was constructed having $i' < 25.0$. For this subsample of 125 objects, the galaxy colors at the corresponding LBG redshift range are well constrained. The completeness distribution function for this subsample has a FWHM of 0.8, centered at $z = 4.1$ with a peak value of ~ 90 percent, while the estimated contamination is < 1 percent.

6.3 Analysis

6.3.1 Projected density distribution of bright LBGs

We first investigated the projected distribution of bright LBGs by smoothing the spatial distribution of our bright subsample with a gaussian kernel. Structure identification is dependent on the size of the smoothing kernel. The FWHM of $5'$ was chosen to match the average distance between neighbouring bright LBGs, thereby optimizing the contrast between overdense and underdense regions. This FWHM is also similar to the angular size of LAE proto-clusters at $z = 3 - 6$ (Shimasaku et al. 2003; Ouchi et al. 2005; Venemans 2005), which improves the chance of detecting such structures in the bright LBG distribution. The smoothed LBG map was divided by a normalisation map to correct for undetected bright LBGs behind foreground objects and FoV boundaries, which causes some dense areas near the border to be overemphasized. The result is shown in Figure 6.1.

The most significant projected overdensity in this LBG structure map (away from the border) contains the HzRG TN J1338–1942. We associate this overdensity with the protocluster at $z = 4.1$ previously discovered in the smaller fields accessed by the VLT (LAEs in two $7' \times 7'$ fields; Venemans et al. 2002; Venemans 2005) and ACS/HST (LBGs in a $3' \times 3'$ field; Miley et al. 2004; Overzier et al. 2008). Taking $\Delta = 0.5$ as the boundary (with $\Delta = (\Sigma - \langle \Sigma \rangle) / \langle \Sigma \rangle$, where Σ and $\langle \Sigma \rangle$ are the local and average projected LBG densities, respectively), (i) the diameter of the overdensity is $\sim 5'$, corresponding to a (proper) size of ~ 2 Mpc at $z = 4$ and (ii) the location of the HzRG is in the western part of the structure. The protocluster size and the relative location of the HzRG are similar to those found by Venemans et al. (2002) and Venemans (2005) for LAEs. The choice the convolution kernel width may seem to effect the measured angular size of the overdensity (both $5'$), but the underlying group of bright LBG candidates can be seen to agree with this estimate.

6.3.2 LBG overdensity in redshift space

We determined the overlap between the whole LBG sample and the LAE sample by Venemans et al. (2002) and Venemans (2005) to obtain spectroscopic redshifts for several LBGs. There were 86 LAE candidates found in a narrow redshift range $\Delta z = 4.087 - 4.119$ surrounding TN J1338–1942 (fields plotted in Figures 6.1 and 6.2). Spectroscopic confirmation of redshift followed for 38 LAEs, including TN J1338–1942 (Venemans 2005).

Within the same area, we identified 104 candidate LBGs (out of the whole LBG sample). Of these LBGs, 7 are also spectroscopically confirmed LAEs, thus obtaining a redshift for these 7 LBGs within the redshift range mentioned above. Based on the contamination fraction, we expect 6 of the 104 candidate LBGs to be interlopers. To see whether the 7 confirmed LBGs represent a significant overdensity, we estimated the expected number of LBGs in the redshift

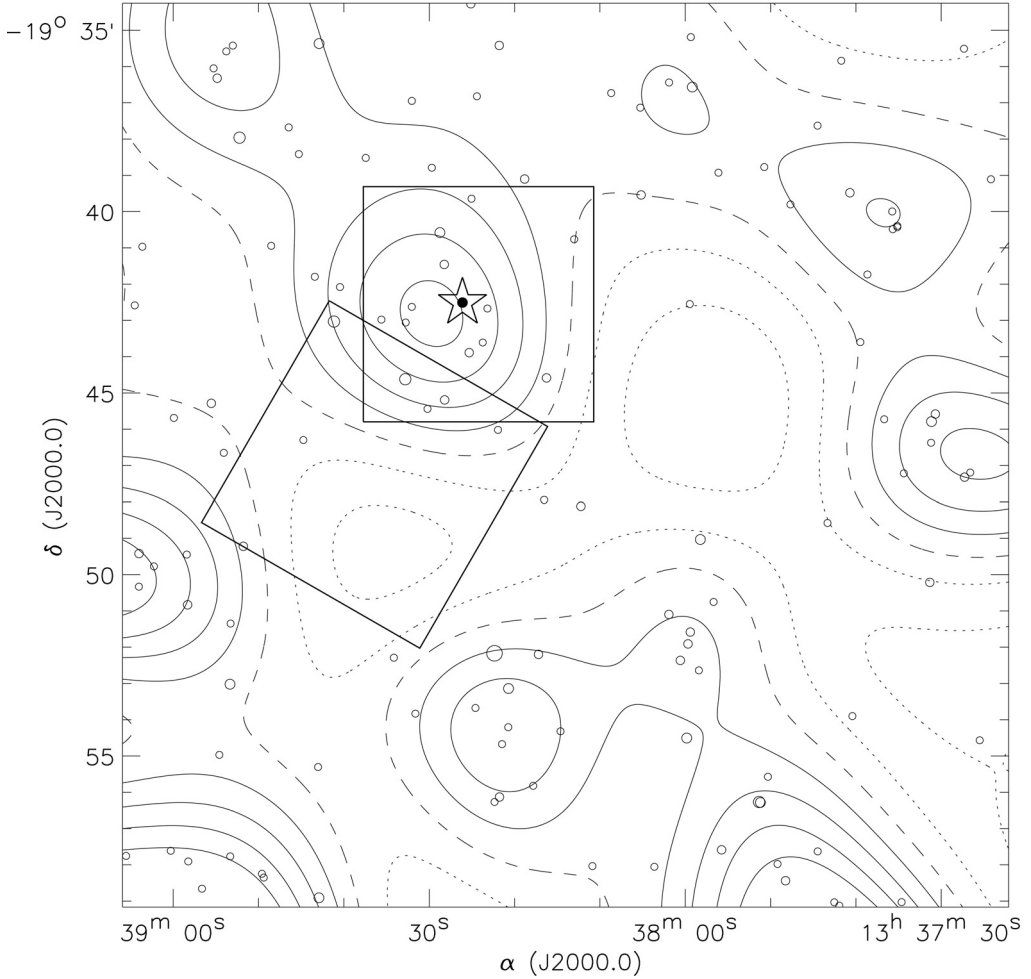


Figure 6.1: Projected distribution of 125 bright LBGs (open circles; diameter scales with brightness; $21.5 < i' < 25.0$) in the TN J1338–1942 field, including TN J1338–1942 (filled circle within star). The projected density contours (curved lines), obtained by gaussian smoothing, reveal overdense (solid lines; $\Delta = 0.25, 0.50, 0.75, 1.00$ from edge to center) and underdense regions (dotted lines; $\Delta = -0.25, -0.50, -0.75$ from edge to center) relative to a mean density of 0.21 per square arcminute (dashed line). TN J1338–1942 inhabits a significant overdense area, probably associated with the protocluster found by Venemans et al. (2002). The rectangles represent the two fields that were used by Venemans et al. (2002) and Venemans (2005) to search for LAEs.

range Δz using Monte-Carlo simulations. We randomly assigned redshifts to 98 objects, using the completeness distribution function as redshift distribution, and counted the number of objects in Δz . We repeated this procedure 10,000 times and found that the expected number of LBGs in redshift range Δz is 3.6 ± 1.9 . As a result, the 7 spectroscopically confirmed LBGs might indicate a modest LBG volume overdensity of $\delta = 1.0 \pm 1.0$ (with $\delta = (\rho - \langle \rho \rangle) / \langle \rho \rangle$, where ρ and $\langle \rho \rangle$ are the local and average LBG volume density, respectively) in close vicinity of TN J1338–1942.

The estimated overdensity above is a lower limit, because not all high redshift galaxies have Ly- α emission. Steidel et al. (2000) found that at $z = 3$ only 20 – 25 percent of the LBGs satisfy typical LAE selection criteria. Assuming that this is also true at $z = 4$, this implies that the 7 confirmed LBGs represent a true number of at least 28 LBGs within Δz . As these are expected to be part of the 104 observed LBGs, the LBG volume overdensity within Δz is increased to at least $\delta = 7 \pm 4$. Note that still ~ 70 percent of the LBGs lie outside Δz . This excess of LBGs in redshift space is consistent with the location of the protocluster that harbours TN J1338–1942.

6.3.3 Projected density distribution of all LBGs

Using the same technique as in Section 6.3.1 (but using a FWHM of $2'$ to match the average distance between neighbouring LBGs), the whole sample of 874 LBGs was used to make a second structure map, which is shown in Figure 6.2. In this map, TN J1338–1942 also inhabits a clear but less prominent projected overdensity of galaxies as compared to Figure 6.1. In addition to this overdensity associated with the previously known protocluster, 4 – 7 other intriguing peaks are seen in the large-scale structure distribution, surrounded by larger regions of relatively empty space. These overdensities may be associated with protoclusters within the redshift range $z = 3.5 - 4.5$, while the underdense regions indicate the presence of large voids. The typical transverse size of the overdensities is $\sim 5'$, which corresponds to ~ 2 Mpc at $z = 4$, while the underdensities are more than twice this size. Without spectroscopic data, we cannot establish whether the other overdensities are physically linked to the protocluster.

The overdensity surrounding TN J1338–1942 contains relatively many bright LBGs compared to the other overdensities, which suggests that the TN J1338–1942 protocluster is the most massive structure within the observed volume. The strong clustering of bright LBGs at one particular position within the FoV agrees with the observation that at $z \sim 4$, brighter LBGs have larger clustering lengths than fainter LBGs (Allen et al. 2005; Ouchi et al. 2004b).

Similar structure maps were created for 20 mock samples of 874 random points each with the same positional constraints as the LBG sample. Visual comparison between the detailed LBG map and the mock maps shows that for the latter, the overdensities are larger but lower in amplitude, while the underdensities are smaller and more isolated. Basically, these over- and underdensities have similar sizes and amplitudes, very different from what is observed in the LBG map.

Figure 6.3 shows the projected density distribution function (PDDF) of the detailed LBG map and the mean PDDF of the mock maps. Using a Kolmogorov-Smirnov test (e.g., Press et al. 1992), we found that the probability that the PDDF of the LBG map is drawn from an underlying distribution equal to the mean PDDF of the mock maps is 43 percent. For the 20 mock maps, the probability that they are drawn from the mean PDDF is much higher (> 99.9 percent). In Figure 6.3, it can be seen that for the LBG sample there is significantly ($> 3\sigma$) more area with $-0.75 < \Delta < -0.5$ and $\Delta > 0.65$ than for the mock samples. This is consistent with the underdensities (presumably voids) being larger than the more strongly peaked overdensities

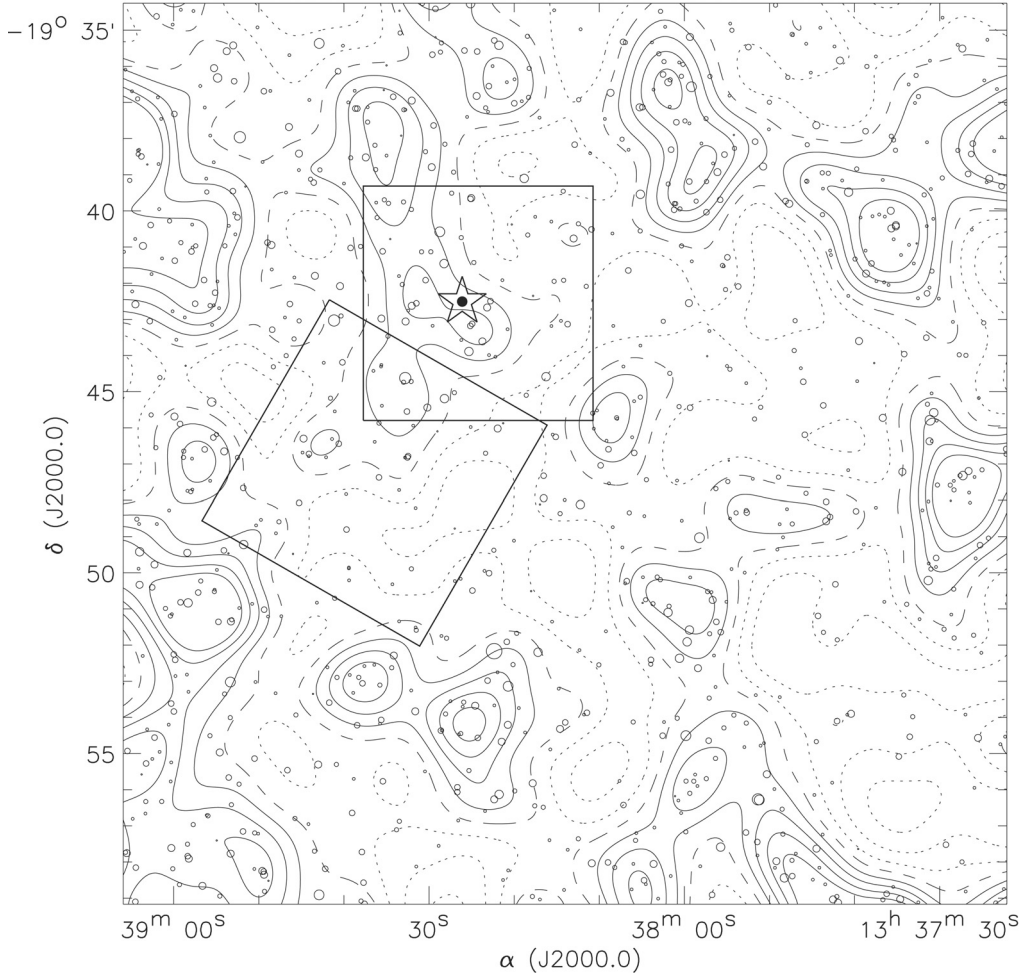


Figure 6.2: Projected distribution of 874 LBGs with $21.5 < i' < 26.5$ in the TN J1338–1942 field, similar to Figure 6.1. The contours are relative to a mean density of 1.47 per square arcminute (dashed line). Like in Figure 6.1, TN J1338–1942 inhabits a significant overdense area, probably associated with the protocluster found by Venemans et al. (2002).

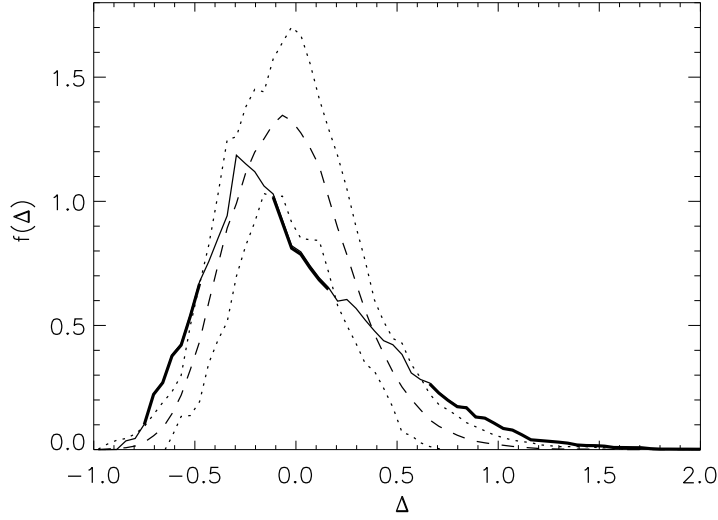


Figure 6.3: Plotted here are the (normalised) projected density distribution function (PDDF) of the whole sample of 874 LBGs (solid line) and the combined PDDF of 20 equally sized mock samples (dashed line is mean, dotted lines are mean $\pm 3\sigma$, where σ is the standard deviation between the mock samples). At several intervals, the PDDF of the LBG sample deviates from the mock samples by more than 3σ (thick solid line). The smoothed LBG distribution has relatively less area with a density close to mean, relatively more area out to higher densities and relatively more area with lower densities, which characterizes the presence of compact overdensities with high peaks and extended underdensities.

(presumably protoclusters).

6.3.4 LBG angular and spatial correlation

The two-point angular correlation function (ACF; Peebles 1973, 1980) of the whole LBG sample was calculated, using estimators by Landy & Szalay (1993) and Hamilton (1993), which gave practically identical results. The estimators are negatively offset from the true ACF due to the difference between the measured average and the true average LBG density in the restricted FoV (the ‘integral constraint’). When assuming a power-law form $\omega(\theta) = A_\omega \theta^{-\beta}$ for the true ACF, the offset can be estimated following Roche et al. (2002). Iteratively fitting a power-law and estimating the offset converged to solutions for both a variable ($\beta = 1.1 \pm 0.1$) and a fixed slope ($\beta = 0.8$; e.g., Peebles 1980) power-law. We found that for all cases the clustering amplitude A_ω is significantly larger than its uncertainty ($\geq 6\sigma$), confirming that there is a non-random clustering signal present in our LBG distribution.

After correcting the clustering amplitude for contamination (Ouchi et al. 2004b), the inverse Limber transformation (Efsthathiou et al. 1991) was used to calculate the (comoving) spatial correlation length. We found correlation lengths of $r_0 = (3.7 \pm 0.7) h^{-1}$ Mpc and $r_0 = (4.6 \pm 0.4) h^{-1}$ Mpc for the variable and fixed slope fit, respectively. These results are similar to those found by Ouchi et al. (2004b), indicating that (within the observed volume) the clustering properties of LBGs in the HzRG field are not significantly different from blank fields.

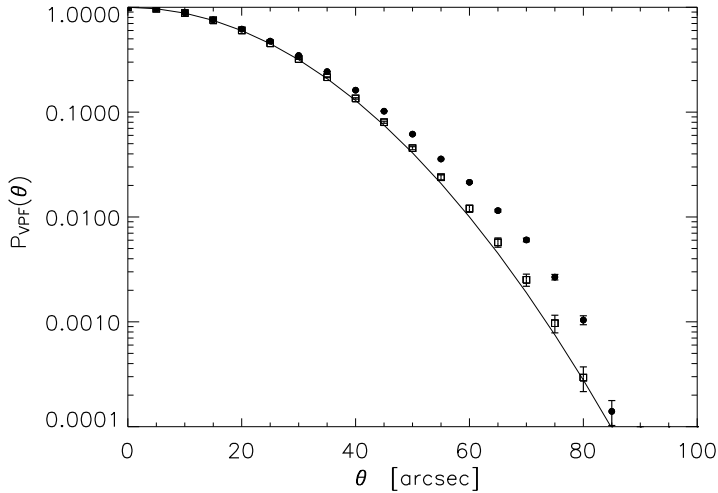


Figure 6.4: The two-dimensional void probability function (VPF) of the LBG sample (filled dots; error bar is poissonian error), compared with the mean VPF of 20 mock samples (open squares; error bar is combination of poissonian error and standard deviation between mock catalogs) and the theoretical VPF for poissonian distributions (solid line). For radii $\theta > 40''$, the underdensities in the projected LBG distribution are significantly larger than the underdensities in mock and poissonian distributions.

6.3.5 LBG void probability function

A disadvantage of using the two-point ACF for detecting clustering in galaxy distributions is that it is less sensitive to non-gaussian density fluctuations. One can use n -point ACFs to improve the detection of the latter, but error-bars becomes exceedingly large with higher n when the number of galaxies is fixed. A complementary approach is to focus on voids instead. The two-dimensional void probability function (VPF; White 1979) defines the fraction of circular areas at random positions in the FoV which contain no galaxies. The VPF was calculated for both the whole LBG sample and the 20 mock samples from Section 6.3.3 and plotted in Figure 6.4. The mean VPF of the mock samples is very similar to the theoretical VPF for poissonian distributions (which is $P_{\text{VPF}}(\theta) = \exp[-\pi\theta^2\langle\Sigma\rangle]$). At larger radii, the VPF of the full LBG sample is significantly higher than both the mean mock VPF and the theoretical VPF, meaning that the underdensities in the projected LBG distribution are relatively large compared to underdensities found in random distributions. This result is similar to the result of Palunas et al. (2004) at $z = 2.34$, using a sample of 34 LAEs in a FoV similar to ours.

6.3.6 Protocluster volume density

The comoving volume that is observed using the LBG selection criteria by Ouchi et al. (2004a) has a size of approximately $1.8 \times 10^6 \text{ Mpc}^3$. Assuming that the 5 to 8 observed overdensities in the LBG map are indeed associated with protoclusters, the volume density of protoclusters within $z = 3.5 - 4.5$ is $\sim 5 \times 10^{-6} \text{ Mpc}^{-3}$. This agrees with the estimate of Venemans (2005), who found a density of $\sim 6 \times 10^{-6} \text{ Mpc}^{-3}$ for LAE protoclusters at $z = 2 - 5.2$. They also report

on similar results from Steidel et al. (1998), based on LBGs at $z = 2.7 - 3.4$ ($3 \times 10^{-6} \text{ Mpc}^{-3}$), Shimasaku et al. (2003), based on LAEs at $z = 4.9$ ($7 \times 10^{-6} \text{ Mpc}^{-3}$) and Ouchi et al. (2005), based on LAEs at $z = 5.7$ ($> 2 \times 10^{-6} \text{ Mpc}^{-3}$).

Our estimated volume density of protoclusters can be compared with the volume density of local rich clusters. Values found for rich cluster density at low redshift ($z < 0.1$) lie in the range $(2 - 4) \times 10^{-6} \text{ Mpc}^{-3}$ (Bahcall & Soneira 1983; Postman et al. 1992; Peacock & West 1992; Zabludoff et al. 1993; Mazure et al. 1996). Our result is consistent with this number range, providing further evidence that the observed overdensities at high redshift are progenitors of rich clusters in the local Universe.

6.4 Conclusions

We draw several conclusions from the present observations:

- (i) TN J1338–1942 is located in an overdensity of LBGs, both in projection and in redshift space. The new wide-field results are consistent with previous observations which revealed the presence of a protocluster through the overdensities of LAEs (Venemans et al. 2002; Venemans 2005) and LBGs (Miley et al. 2004; Overzier et al. 2008). This further supports the hypothesis that HzRGs are located in dense environments. The apparent size of the overdensity and the relative position of TN J1338–1942 within the overdensity are similar to that found by Venemans et al. (2002) and Venemans (2005) for LAEs.
- (ii) There are 4 – 7 additional overdensities in the projected LBG distribution, similar to the one harbouring TN J1338–1942. These may well be due to protoclusters at $z = 3.5 - 4.5$ and one or more of these overdensities could well be physically related to the TN J1338–1942 protocluster.
- (iii) The spatial distribution of our complete LBG sample is consistent with a Universe at $z \sim 4$ that comprises a web of compact galaxy overdensities (protoclusters) embedded in larger regions of galaxy underdensities (voids). The statistics of the overdensities are consistent with the local volume density of rich clusters.

Spectroscopic measurements are needed to investigate whether there is a physical connection between some of the outlying observed galaxy overdensities and the overdensity corresponding to the TN J1338–1942 protocluster. Such observations could enable the cosmic web at $z = 4.1$ to be traced over distances of tens of megaparsec. Furthermore, similar measurements on other $z > 2$ protoclusters would be useful for constraining the development of large-scale structure in the early Universe.

Acknowledgements. This chapter is based on data collected at the Subaru Telescope, which is operated by the National Astronomical Observatory of Japan. We are grateful to the staff of the Subaru Telescope Facility at Mauna Kea, Hawaii, for their support. We wish to recognize and acknowledge the very significant cultural role and reverence that the summit of Mauna Kea has always had within the indigenous Hawaiian community. We are most fortunate to have the opportunity to conduct observations from this mountain. HTI acknowledges a grant from the Netherlands Research School for Astronomy (NOVA). GKM acknowledges a grant from the Royal Netherlands Academy of Arts and Sciences (KNAW).

Bibliography

- Abazajian, K. N., Adelman-McCarthy, J. K., Agüeros, M. A., et al. 2009, *ApJS*, 182, 543
- Allen, P. D., Moustakas, L. A., Dalton, G., et al. 2005, *MNRAS*, 360, 1244
- Anderson, J., van Langevelde, H., & Campbell, R. 2005, in *URSI General Assembly*, New Delhi, India, [http://www.ursi.org/Proceedings/ProcGA05/pdf/J03-P.8\(01310\).pdf](http://www.ursi.org/Proceedings/ProcGA05/pdf/J03-P.8(01310).pdf)
- Athreya, R. 2009, *ApJ*, 696, 885
- Baars, J. W. M., Genzel, R., Pauliny-Toth, I. I. K., & Witzel, A. 1977, *A&A*, 61, 99
- Bahcall, N. A. & Soneira, R. M. 1983, *ApJ*, 270, 20
- Bahcall, N. A. 1988, *ARA&A*, 26, 631
- Beck, R. & Krause, M. 2005, *Astronomische Nachrichten*, 326, 414
- Becker, R. H., White, R. L., & Helfand, D. J. 1995, *ApJ*, 450, 559
- Bennett, A. 1962, *MmRAS*, 68, 163
- Berrington, R. C., Lugger, P. M., & Cohn, H. N. 2002, *AJ*, 123, 2261
- Bertin, E. & Arnouts, S. 1996, *A&AS*, 117, 393
- Bhatnagar, S., Cornwell, T. J., Golap, K., & Uson, J. M. 2008, *A&A*, 487, 419
- Bilitza, D. & Reinisch, B. W. 2008, *Advances in Space Research*, 42, 599
- Blanch, J., Walter, T., & Enge, P. 2004, in *National Technical Meeting of the Institute of Navigation*, San Diego, CA, USA
- Blandford, R. D. & Payne, D. G. 1982, *MNRAS*, 199, 883
- Blumenthal, G. & Miley, G. 1979, *A&A*, 80, 13

- Blundell, K. M. & Rawlings, S. 1999, *Nature*, 399, 330
- Braude, S. Y., Rashkovsky, S. L., Sidorchuk, K. M., et al. 2002, *Ap&SS*, 280, 235
- Brentjens, M. A. & de Bruyn, A. G. 2004, in *The Riddle of Cooling Flows in Galaxies and Clusters of galaxies*, ed. T. Reiprich, J. Kempner, & N. Soker, 7
- Brentjens, M. A. 2008, *A&A*, 489, 69
- Bridle, A. H. & Fomalont, E. B. 1976, *A&A*, 52, 107
- Bridle, A. H., Fomalont, E. B., Miley, G. K., & Valentijn, E. A. 1979, *A&A*, 80, 201
- Bridle, A. & Greisen, E. 1994, *The NRAO AIPS Project – A Summary*, AIPS Memo 87, Tech. rep., NRAO
- Briel, U. G., Henry, J. P., Schwarz, R. A., et al. 1991, *A&A*, 246, L10
- Briggs, D. S. & Cornwell, T. J. 1992, in *ASPC Series, Vol. 25, ADASS I*, ed. D. M. Worrall, C. Biemesderfer, & J. Barnes, 170
- Briggs, D. 1995, PhD thesis, New Mexico Institute of Mining Technology, Socorro, New Mexico, USA
- Bust, G. S. & Mitchell, C. N. 2008, *Rev. Geophys.*, 46, RG1003
- Carilli, C. L. & Taylor, G. B. 2002, *ARA&A*, 40, 319
- Cassano, R., Brunetti, G., & Setti, G. 2006, *MNRAS*, 369, 1577
- Chandra, P., Ray, A., & Bhatnagar, S. 2004, *ApJ*, 612, 974
- Ciliegi, P., Zamorani, G., Hasinger, G., et al. 2003, *A&A*, 398, 901
- Clark, B. G. 1980, *A&A*, 89, 377
- Clarke, T. E. & Enßlin, T. A. 2006, *AJ*, 131, 2900
- Cohen, A. S., Röttgering, H. J. A., Kassim, N. E., et al. 2003, *ApJ*, 591, 640
- Cohen, A. S., Röttgering, H. J. A., Jarvis, M. J., Kassim, N. E., & Lazio, T. J. W. 2004, *ApJS*, 150, 417
- Cohen, A. S., Lane, W. M., Cotton, W. D., et al. 2007, *AJ*, 134, 1245
- Cohen, A. S. & Röttgering, H. J. A. 2009, *arXiv:0905.4501*
- Colless, M., Dalton, G., Maddox, S., et al. 2001, *MNRAS*, 328, 1039
- Condon, J. J., Cotton, W. D., Greisen, E. W., et al. 1994, in *ASPC Series, Vol. 61, ADASS III*, ed. D. R. Crabtree, R. J. Hanisch, & J. Barnes, 155
- Condon, J. J. 1997, *PASP*, 109, 166
- Condon, J. J., Cotton, W. D., Greisen, E. W., et al. 1998, *AJ*, 115, 1693

- Cool, R. J., Kochanek, C. S., Eisenstein, D. J., et al. 2006, *AJ*, 132, 823
- Cool, R. J. 2007, *ApJS*, 169, 21
- Cornwell, T. J. & Perley, R. A. 1992, *A&A*, 261, 353
- Cornwell, T., Braun, R., & Briggs, D. S. 1999, in *ASPC Series*, Vol. 180, *Synthesis Imaging in Radio Astronomy II*, ed. G. B. Taylor, C. L. Carilli, & R. A. Perley, 151
- Costain, C. H., Bridle, A. H., & Feldman, P. A. 1972, *ApJ*, 175, L15
- Cotton, W. D. 1989, in *ASPC Series*, Vol. 6, *Synthesis Imaging in Radio Astronomy*, ed. R. A. Perley, F. R. Schwab, & A. H. Bridle, 233
- Cotton, W. D. 1999, in *ASPC Series*, Vol. 180, *Synthesis Imaging in Radio Astronomy II*, ed. G. B. Taylor, C. L. Carilli, & R. A. Perley, 357
- Cotton, W. D. & Condon, J. 2002, in *URSI General Assembly*, Maastricht, The Netherlands
- Cotton, W. D., Condon, J. J., Perley, R. A., et al. 2004, in *SPIE Conference Series*, ed. J. M. Oschmann, Jr., Vol. 5489, 180
- Cotton, W. D. & Uson, J. M. 2008, *A&A*, 490, 455
- Croft, S., van Breugel, W., Brown, M. J. I., et al. 2008, *AJ*, 135, 1793
- Croston, J. H., Hardcastle, M. J., Harris, D. E., et al. 2005, *ApJ*, 626, 733
- Croton, D. J., Springel, V., White, S. D. M., et al. 2006, *MNRAS*, 365, 11
- Davies, K. 1990, *Ionospheric Radio* (Stevenage, UK: Institution of Engineering and Technology)
- De Breuck, C., van Breugel, W., Röttgering, H. J. A., & Miley, G. 2000, *A&AS*, 143, 303
- De Breuck, C., van Breugel, W., Stanford, S. A., et al. 2002, *AJ*, 123, 637
- De Breuck, C., van Breugel, W., Röttgering, H., et al. 2001, *AJ*, 121, 1241
- de Vries, W. H., Morganti, R., Röttgering, H. J. A., et al. 2002, *AJ*, 123, 1784
- Edge, D. O., Shakeshaft, J. R., McAdam, W. B., Baldwin, J. E., & Archer, S. 1959, *MmRAS*, 68, 37
- Efstathiou, G., Bernstein, G., Tyson, J. A., Katz, N., & Guhathakurta, P. 1991, *ApJ*, 380, L47
- Eisenhardt, P. R., Stern, D., Brodwin, M., et al. 2004, *ApJS*, 154, 48
- Elston, R. J., Gonzalez, A. H., McKenzie, E., et al. 2006, *ApJ*, 639, 816
- Enßlin, T. A., Biermann, P. L., Klein, U., & Kohle, S. 1998, *A&A*, 332, 395
- Enßlin, T. A. & Gopal-Krishna. 2001, *A&A*, 366, 26
- Enßlin, T. A. & Brüggen, M. 2002, *MNRAS*, 331, 1011

- Enßlin, T. A. & Röttgering, H. 2002, *A&A*, 396, 83
- Esposito, S. 2005, *Comptes Rendus Physique*, 6, 1039
- Faber, S. M. & Dressler, A. 1977, *AJ*, 82, 187
- Fabian, A. C., Sanders, J. S., Crawford, C. S., & Ettori, S. 2003, *MNRAS*, 341, 729
- Fabricant, D. G., Kent, S. M., & Kurtz, M. J. 1989, *ApJ*, 336, 77
- Fan, X., Strauss, M. A., Schneider, D. P., et al. 2003, *AJ*, 125, 1649
- Feretti, L., Giovannini, C., Klein, U., Mack, K.-H., & Sijbring, L. G. 1996, in *IAU Symposium*, Vol. 175, *Extragalactic Radio Sources*, ed. R. D. Ekers, C. Fanti, & L. Padrielli, 347
- Feretti, L., Gioia, I. M., & Giovannini, G., eds. 2002, *Astrophysics and Space Science Library*, Vol. 272, *Merging Processes in Galaxy Clusters*
- Feretti, L. & Johnston-Hollitt, M. 2004, *New Astronomy Review*, 48, 1145
- Ferrari, C., Govoni, F., Schindler, S., Bykov, A. M., & Rephaeli, Y. 2008, *Space Science Reviews*, 134, 93
- Fuller-Rowell, T., Araujo-Pradere, E., Minter, C., et al. 2006, *Radio Science*, 41, RS6003
- George, S. J. & Stevens, I. R. 2008, *MNRAS*, 390, 741
- George, S. J. & Ishwara-Chandra, C. H. 2009, *arXiv:0903.2726*
- Giovannini, G. & Feretti, L. 2000, *New Astronomy*, 5, 335
- Gizani, N. A. B., Cohen, A., & Kassim, N. E. 2005, *MNRAS*, 358, 1061
- Gower, J. F. R., Scott, P. F., & Wills, D. 1967, *MmRAS*, 71, 49
- Hales, S. E. G., Baldwin, J. E., & Warner, P. J. 1988, *MNRAS*, 234, 919
- Hales, S. E. G., Riley, J. M., Waldram, E. M., Warner, P. J., & Baldwin, J. E. 2007, *MNRAS*, 382, 1639
- Hamilton, A. J. S. 1993, *ApJ*, 417, 19
- Hanisch, R. J. 1982, *A&A*, 116, 137
- Hardy, J. W. 1998, *Adaptive Optics for Astronomical Telescopes* (New York, NY, USA: Oxford University Press)
- Haslam, C. G. T., Salter, C. J., Stoffel, H., & Wilson, W. E. 1982, *A&AS*, 47, 1
- Hinshaw, G., Weiland, J. L., Hill, R. S., et al. 2009, *ApJS*, 180, 225
- Hogbom, J. 1974, *A&AS*, 15, 417
- Houck, J. R., Soifer, B. T., Weedman, D., et al. 2005, *ApJ*, 622, L105

- Hwang, C.-Y. & Chang, M.-Y. 2009, *ApJS*, 181, 233
- Ibar, E., Ivison, R. J., Biggs, A. D., et al. 2009, arXiv:0903.3600
- Ishwara-Chandra, C. H. & Marathe, R. 2007, in *ASPC Series*, Vol. 380, *Deepest Astronomical Surveys*, ed. J. Afonso, H. C. Ferguson, B. Mobasher, & R. Norris, 237
- Iye, M., Ota, K., Kashikawa, N., et al. 2006, *Nature*, 443, 186
- Jackson, C. 2005, *Publications of the Astronomical Society of Australia*, 22, 36
- Jacobson, A. R. & Erickson, W. C. 1992a, *A&A*, 257, 401
- Jacobson, A. R. & Erickson, W. C. 1992b, *Planet. Space Sci.*, 40, 447
- Jaffe, W. J. & Perola, G. C. 1973, *A&A*, 26, 423
- Jannuzi, B. T. & Dey, A. 1999, in *ASPC Series*, Vol. 191, *Photometric Redshifts and the Detection of High Redshift Galaxies*, ed. R. Weymann, L. Storrie-Lombardi, M. Sawicki, & R. Brunner, 111
- Jarvis, M. J., Rawlings, S., Willott, C. J., et al. 2001, *MNRAS*, 327, 907
- Kale, R. & Dwarakanath, K. S. 2009, arXiv:0905.0966
- Kassim, N. E., Perley, R. A., Erickson, W. C., & Dwarakanath, K. S. 1993, *AJ*, 106, 2218
- Kassim, N. E., Lazio, T. J. W., Erickson, W. C., et al. 2007, *ApJS*, 172, 686
- Kempner, J. C., Blanton, E. L., Clarke, T. E., et al. 2004, in *The Riddle of Cooling Flows in Galaxies and Clusters of galaxies*, ed. T. Reiprich, J. Kempner, & N. Soker, 335
- Kempner, J. C. & Sarazin, C. L. 2001, *ApJ*, 548, 639
- Kenter, A., Murray, S. S., Forman, W. R., et al. 2005, *ApJS*, 161, 9
- Kettenis, M., van Langevelde, H. J., Reynolds, C., & Cotton, B. 2006, in *ASPC Series*, Vol. 351, *ADASS XV*, ed. C. Gabriel, C. Arviset, D. Ponz, & S. Enrique, 497
- Klamer, I., Subrahmanyam, R., & Hunstead, R. W. 2004, *MNRAS*, 351, 101
- Klamer, I. J., Ekers, R. D., Bryant, J. J., et al. 2006, *MNRAS*, 371, 852
- Komatsu, E., Dunkley, J., Nolte, M. R., et al. 2009, *ApJS*, 180, 330
- Kurk, J. D., Pentericci, L., Röttgering, H. J. A., & Miley, G. K. 2004, *A&A*, 428, 793
- Laing, R. A., Riley, J. M., & Longair, M. S. 1983, *MNRAS*, 204, 151
- Landy, S. D. & Szalay, A. S. 1993, *ApJ*, 412, 64
- Lazio, T., Kassim, N., & Perley, R. 2005, *Low-Frequency Data Reduction at the VLA: A Tutorial for New Users*, version 1.13, Tech. rep., NRAO

- Lonsdale, C. J. 2005, in ASPC Series, ed. N. Kassim, M. Perez, W. Junor, & P. Henning, Vol. 345, 399
- Mao, M. Y., Johnston-Hollitt, M., Stevens, J. B., & Wotherspoon, S. J. 2009, MNRAS, 392, 1070
- Marchetti, E., Brast, R., Delabre, B., et al. 2007, The Messenger, 129, 8
- Markwardt, C. B. 2009, arXiv:0902.2850
- Masson, C. R. & Mayer, C. J. 1978, MNRAS, 185, 607
- Matheron, G. 1973, Advances in Applied Probability, 5, 439
- Mazure, A., Katgert, P., den Hartog, R., et al. 1996, A&A, 310, 31
- McGreer, I. D., Becker, R. H., Helfand, D. J., & White, R. L. 2006, ApJ, 652, 157
- Miley, G. K. 1973, A&A, 26, 413
- Miley, G. 1980, ARA&A, 18, 165
- Miley, G. K., Overzier, R. A., Tsvetanov, Z. I., et al. 2004, Nature, 427, 47
- Miley, G. & De Breuck, C. 2008, A&A Rev., 15, 67
- Miller, N. A., Owen, F. N., & Hill, J. M. 2003, AJ, 125, 2393
- Miniati, F., Ryu, D., Kang, H., et al. 2000, ApJ, 542, 608
- Miyazaki, S., Komiyama, Y., Sekiguchi, M., et al. 2002, PASJ, 54, 833
- Mohan, N. R. 2008, ANAAMIKA manual – version 2.1, Tech. rep., Leiden Observatory, http://www.strw.leidenuniv.nl/~mohan/anaamika_manual.pdf
- Møller, P. & Fynbo, J. U. 2001, A&A, 372, L57
- Murray, S. S., Kenter, A., Forman, W. R., et al. 2005, ApJS, 161, 1
- NIMA 1984, DoD World Geodetic System, Tech. Rep. TR8350.2
- Nityananda, R. 2003, in ASPC Series, Vol. 289, The Proceedings of the IAU 8th Asian-Pacific Regional Meeting, Volume I, ed. S. Ikeuchi, J. Hearnshaw, & T. Hanawa, 29
- Noordam, J. E. 2004, in Proceedings of the SPIE, Vol. 5489, 817
- Noordam, J. E. 2008, The MIM principle – version 2.0, Tech. rep., ASTRON, available on request through noordam@astron.nl
- Ouchi, M., Shimasaku, K., Okamura, S., et al. 2001, ApJ, 558, L83
- Ouchi, M., Shimasaku, K., Okamura, S., et al. 2004a, ApJ, 611, 660
- Ouchi, M., Shimasaku, K., Okamura, S., et al. 2004b, ApJ, 611, 685

- Ouchi, M., Shimasaku, K., Akiyama, M., et al. 2005, *ApJ*, 620, L1
- Overzier, R. A., Bouwens, R. J., Cross, N. J. G., et al. 2008, *ApJ*, 673, 143
- Palunas, P., Teplitz, H. I., Francis, P. J., Williger, G. M., & Woodgate, B. E. 2004, *ApJ*, 602, 545
- Pandey, V. N. & Shankar, N. U. 2007, *Highlights of Astronomy*, 14, 385
- Peacock, J. A. & West, M. J. 1992, *MNRAS*, 259, 494
- Peacock, J. A. 2001, *Cosmological Physics* (Cambridge, UK: Cambridge University Press)
- Pearson, T. J. & Readhead, A. C. S. 1984, *ARA&A*, 22, 97
- Peebles, P. J. E. 1973, *ApJ*, 185, 413
- Peebles, P. J. E. 1980, *The large-scale structure of the universe* (Princeton, NJ, USA: Princeton University Press)
- Pentericci, L., Röttgering, H. J. A., Miley, G. K., et al. 1999, *A&A*, 341, 329
- Perley, R. A. 1989a, in *ASPC Series*, Vol. 6, *Synthesis Imaging in Radio Astronomy*, ed. R. A. Perley, F. R. Schwab, & A. H. Bridle, 259
- Perley, R. A. 1989b, in *ASPC Series*, Vol. 6, *Synthesis Imaging in Radio Astronomy*, ed. R. A. Perley, F. R. Schwab, & A. H. Bridle, 287
- Pilkington, J. D. H. & Scott, P. F. 1965, *MmRAS*, 69, 183
- Postman, M., Huchra, J. P., & Geller, M. J. 1992, *ApJ*, 384, 404
- Press, W., Teukolsky, S., Vetterling, W., & B.P., F. 1992, *Numerical Recipes in C*, Second Edition (Cambridge, UK: Cambridge University Press)
- Rees, M. J. 1978, *Nature*, 275, 516
- Rengelink, R. B., Tang, Y., de Bruyn, A. G., et al. 1997, *A&AS*, 124, 259
- Rocca-Volmerange, B., Le Borgne, D., De Breuck, C., Fioc, M., & Moy, E. 2004, *A&A*, 415, 931
- Roche, N. D., Almaini, O., Dunlop, J., Ivison, R. J., & Willott, C. J. 2002, *MNRAS*, 337, 1282
- Roddier, F. 1981, *Progress in Optics*, 19, 281
- Roettgering, H. J. A., van Ojik, R., Miley, G. K., et al. 1997, *A&A*, 326, 505
- Roll, J. 1996, in *ASPC Series*, Vol. 101, *ADASS V*, ed. G. H. Jacoby & J. Barnes, 536
- Röttgering, H., Snellen, I., Miley, G., et al. 1994a, *ApJ*, 436, 654
- Röttgering, H. J. A., Lacy, M., Miley, G. K., Chambers, K. C., & Saunders, R. 1994b, *A&AS*, 108, 79

- Röttgering, H. J. A., Wieringa, M. H., Hunstead, R. W., & Ekers, R. D. 1997, *MNRAS*, 290, 577
- Röttgering, H. J. A., Braun, R., Barthel, P. D., et al. 2006, arXiv:astro-ph/0610596
- Rybicki, G. B. & Lightman, A. P. 1979, *Radiative processes in astrophysics* (Malden, MA, USA: Wiley-Interscience)
- Schwab, F. 1981, VLA Scientific Memo 136, Tech. rep., NRAO
- Schwab, F. R. 1984, *AJ*, 89, 1076
- Shimasaku, K., Ouchi, M., Okamura, S., et al. 2003, *ApJ*, 586, L111
- Sirothia, S. K., Saikia, D. J., Ishwara-Chandra, C. H., & Kantharia, N. G. 2009, *MNRAS*, 392, 1403
- Slee, O. B., Roy, A. L., Murgia, M., Andernach, H., & Ehle, M. 2001, *AJ*, 122, 1172
- Smith, D. A., Araujo-Pradere, E. A., Minter, C., & Fuller-Rowell, T. 2008, *Radio Science*, 43, RS6008
- Spoelstra, T. A. T. & Yang Yi-pei. 1995, *Journal of Atmospheric and Terrestrial Physics*, 57, 85
- Springel, V., White, S. D. M., Jenkins, A., et al. 2005, *Nature*, 435, 629
- Stanimirovic, S. 2002, in *ASPC Series*, Vol. 278, *Single-Dish Radio Astronomy: Techniques and Applications*, ed. S. Stanimirovic, D. Altschuler, P. Goldsmith, & C. Salter, 375
- Steidel, C. C., Adelberger, K. L., Dickinson, M., et al. 1998, *ApJ*, 492, 428
- Steidel, C. C., Adelberger, K. L., Shapley, A. E., et al. 2000, *ApJ*, 532, 170
- Subrahmanya, C. R. 1991, in *ASPC Series*, Vol. 19, *IAU Colloq. 131: Radio Interferometry. Theory, Techniques, and Applications*, ed. T. J. Cornwell & R. A. Perley, 218
- Sun, M., Murray, S. S., Markevitch, M., & Vikhlinin, A. 2002, *ApJ*, 565, 867
- Sutherland, W. & Saunders, W. 1992, *MNRAS*, 259, 413
- Swarup, G. 1991, in *ASPC Series*, Vol. 19, *IAU Colloq. 131: Radio Interferometry. Theory, Techniques, and Applications*, ed. T. J. Cornwell & R. A. Perley, 376
- Tasse, C., Röttgering, H. J. A., Best, P. N., et al. 2007, *A&A*, 471, 1105
- Tasse, C., Le Borgne, D., Röttgering, H., et al. 2008, *A&A*, 490, 879
- Taylor, G. B. 2007, *Highlights of Astronomy*, 14, 388
- Thompson, A. R. 1999, in *ASPC Series*, Vol. 180, *Synthesis Imaging in Radio Astronomy II*, ed. G. B. Taylor, C. L. Carilli, & R. A. Perley, 11
- Thompson, A. R., Moran, J. M., & Swenson Jr., G. W. 2001, *Interferometry and Synthesis in Radio Astronomy*, Second Edition (Malden, MA, USA: Wiley-Interscience)

- Thuan, T. X. 1987, in *High Redshift and Primeval Galaxies*, ed. J. Bergeron, D. Kunth, B. Rocca-Volmerange, & J. Tran Thanh van, 125
- Tielens, A. G. G. M., Miley, G. K., & Willis, A. G. 1979, *A&AS*, 35, 153
- van Breugel, W., De Breuck, C., Stanford, S. A., et al. 1999, *ApJ*, 518, L61
- van der Tol, S., Jeffs, B., & van der Veen, A.-J. 2007, *IEEE Transactions on Signal Processing*, 55, 4497
- van der Tol, S. & van der Veen, A.-J. 2007, in *International Symposium on Signals, Circuits and Systems*, Vol. 2, Iasi, Romania, 1
- van Velthoven, P. F. J. 1990, PhD thesis, University of Eindhoven, Eindhoven, The Netherlands
- Venemans, B. P., Kurk, J. D., Miley, G. K., et al. 2002, *ApJ*, 569, L11
- Venemans, B. P. 2005, PhD thesis, Leiden University, Leiden, The Netherlands
- Venemans, B. P., Röttgering, H. J. A., Miley, G. K., et al. 2007, *A&A*, 461, 823
- Voronkov, M. A. & Wieringa, M. H. 2004, *Experimental Astronomy*, 18, 13
- West, M. J. 1994, *MNRAS*, 268, 79
- White, S. D. M. 1979, *MNRAS*, 186, 145
- Wieringa, M. H. 1991, PhD thesis, Leiden University, Leiden, The Netherlands
- Wieringa, M. 1992, *Experimental Astronomy*, 2, 203
- Willott, C. J., Rawlings, S., Jarvis, M. J., & Blundell, K. M. 2003, *MNRAS*, 339, 173
- Windhorst, R. A., Miley, G. K., Owen, F. N., Kron, R. G., & Koo, D. C. 1985, *ApJ*, 289, 494
- Yoshida, N. 2009, [arXiv:0906.4372](https://arxiv.org/abs/0906.4372)
- Zabludoff, A. I., Geller, M. J., Huchra, J. P., & Vogeley, M. S. 1993, *AJ*, 106, 1273
- Zhang, X.-Z., Reich, W., Reich, P., & Wielebinski, R. 2003, *Chinese Journal of Astronomy and Astrophysics*, 3, 347

Nederlandse samenvatting

Het waarnemen van sterrenstelsels en clusters

Straling reist met een snelheid van bijna 300.000 kilometer per seconde door het heelal. Met deze hoge snelheid doet het licht van Proxima Centauri, de eerste ster na de zon, er toch meer dan vier jaar over om ons te bereiken. Deze 4.3 lichtjaren komen overeen met een afstand van ongeveer 40 biljoen kilometer. Voor andere sterren binnen ons sterrenstelsel (de Melkweg), bestaande uit ongeveer 300 miljard sterren, kan dit oplopen tot ongeveer 70 duizend lichtjaar. In het heelal bevinden zich miljarden sterrenstelsels die elk weer bestaan uit miljarden sterren. Naast sterren bevat een sterrenstelsel ook gas en stof. Ook vermoedt men dat er zich in het centrum van ieder sterrenstelsel een zeer zwaar zwart gat bevindt. Dit is een bijzonder compacte samenklontering van materie die zoveel zwaartekracht uitoefent op zijn nabije omgeving dat zelfs straling niet aan de greep van de zwaartekracht kan ontsnappen. De afstand tot de Andromedanevel, het dichtstbijzijnde sterrenstelsel dat qua grootte vergelijkbaar is met de Melkweg, is ongeveer 2.5 miljoen lichtjaar. De meest afgelegen sterrenstelsels die zijn waargenomen liggen op afstanden van bijna 13 miljard lichtjaar.

Sterrenstelsels worden beschouwd als de bouwstenen van ons heelal. De verdeling van sterrenstelsels over het nabije heelal is verre van gelijkmatig, maar lijkt geconcentreerd te zijn in een sponsachtige structuur. De meest prominente componenten zijn de *clusters*, min-of-meer bolvormige groepen van vele honderden sterrenstelsels, de *filaments*, draadachtige structuren met relatief minder sterrenstelsels die de clusters onderling verbinden, en de *voids*, grote leegtes tussen de clusters en filaments in. Computersimulaties laten zien dat de sponsachtige verdeling van sterrenstelsels kan zijn ontstaan uit een zeer gelijkmatige, oorspronkelijke verdeling van materie. De belangrijkste drijfveren zijn de zwaartekracht die de sterrenstelsels naar elkaar toetrekt en de uitdijende ruimte van het heelal die de sterrenstelsels uit elkaar drijft. Van clusters is bekend dat zij naast sterrenstelsels ook gas bevatten en zogenaamde *donkere materie*, een onzichtbare component die de massa-inhoud van de clusters (en sterrenstelsels) domineert. Zowel sterrenstelsels als clusters groeien in massa door samensmeltingen, wat vaak gepaard gaat met een tijdelijk sterke toename in stralingsintensiteit.

Astronomen proberen door middel van waarnemingen met telescopen het ontstaan en de ontwikkeling van de inhoud van het heelal te doorgronden. Veel van de veranderingen in sterrenstelsels en clusters vinden plaats op een tijdschaal van miljoenen of soms miljarden jaren, waardoor het heelal in onze ogen lijkt stil te staan. De straling die door deze objecten wordt uitgezonden is zo oud als het aantal lichtjaren dat deze heeft afgelegd, daarom kijken we met

toenemende afstand verder terug in het verleden van het heelal. Door op verschillende afstanden in het heelal te kijken, proberen astronomen af te leiden hoe sterrenstelsels en clusters zich ontwikkelen in de tijd.

De meest bekende straling is het zichtbare licht (optische straling) waar onze ogen gevoelig voor zijn, maar dit beslaat slechts een smal bereik van golflengtes in het totale spectrum van elektromagnetische straling. Voorbeelden van straling met een langere golflengte zijn infrarode straling, microgolfstraling en radiostraling, terwijl ultraviolette straling, röntgenstraling en gammastraling een kortere golflengte hebben. Het heelal ziet er bij verschillende golflengtes steeds anders uit. Dat komt door verschillen in de natuurkundige processen die verantwoordelijk zijn voor het opwekken van de straling (zoals kernfusie in sterren) en voor het veranderen van reeds uitgezonden straling (zoals verstrooiing en absorptie door gas en stof). Een doorsnee ster als de zon genereert naast optische straling ook alle andere bovengenoemde vormen.

De stralingsintensiteit van de zon varieert per golflengte; dit wordt het *spectrum* genoemd. Het spectrum geeft informatie over de fysische toestand waarin de ster zich bevindt. Ook gas en stof kunnen straling uitzenden, elk met hun eigen spectrum. Het spectrum van een heel sterrenstelsel is de som van de spectra van alle sterren, gas en stof tussen de sterren en andere bronnen die straling uitzenden, plus alle veranderingen die de straling op weg van het sterrenstelsel naar de telescoop ondervindt. Op grotere schaal zendt ook het ijle clustergas tussen de sterrenstelsels straling uit. Het spectrum van bronnen uit het verre heelal wordt naast verstrooiing en absorptie ook door de uitdijning van het heelal veranderd, doordat de golflengte van straling wordt opgerekt. Voor optische straling geldt dat deze naar de rode kant van het regenboog-spectrum verschuift, vandaar dat dit effect algemeen wordt aangeduid met de term *roodverschuiving*.

De twee meest gangbare soorten sterrenkundige waarnemingen zijn afbeeldingen van stukken van de hemel op één golflengte (of een klein golflengte-bereik) en spectra van individuele objecten. Met behulp van een afbeelding kan de hemelpositie en het uiterlijk van een sterrenstelsel worden bepaald, maar niet de afstand tussen het sterrenstelsel en ons. Door het meten van het spectrum van een sterrenstelsel kan in veel gevallen de roodverschuiving nauwkeurig worden bepaald, waaruit de afstand tot het sterrenstelsel kan worden afgeleid.

Radiotelescopen

Radiostraling is alle straling met een golflengte langer dan één millimeter. Ter vergelijking: optische straling heeft een golflengte tussen ongeveer één-duizendste tot drie-duizendste van een millimeter. Radiosterrenkunde is in 1931 'ontdekt' doordat er op een transatlantische radioverbinding (15 meter golflengte) een onverklaarbare ruis werd gevonden. De Amerikaan Karl Jansky stelde vast dat deze niet afkomstig was van de aarde, maar kwam uit de richting van het centrum van de Melkweg. In 1941 is de radiohemel door de Amerikaan Grote Reber voor het eerst in kaart gebracht bij een golflengte van 2 meter, waarop duidelijk de contouren van de Melkweg te zien zijn.

Net als bij optische telescopen wordt voor radiotelescopen veelal gebruik gemaakt van een reflecterende schotel om de straling te bundelen. De resolutie (de mate van detail) van de eerste radiohemelkaarten was zeer laag, wat wordt veroorzaakt door de fundamentele relatie tussen de resolutie, de golflengte en de diameter van de schotel. Hoe langer de golflengte, hoe lager de resolutie, maar ook hoe kleiner de schotel, hoe lager de resolutie. Met de vooruitgang van de technologie is voor sterrenkundig onderzoek in toenemende mate gebruik gemaakt van kortere golflengtes en grotere schotels om de resolutie en het contrast van hemelkaarten te verbeteren.

De grootste draaibare schotels zijn rond de 100 meter in diameter, terwijl de grootste vaste schotel een diameter heeft van ongeveer 300 meter.

Radio-interferometrie is een techniek waarbij meerdere radioantennes (schotels of ander type antennes) worden gecombineerd tot één grote, virtuele telescoop. De resolutie hangt hierbij niet meer af van de afmeting van individuele antennes, maar van de langste afstand tussen twee antennes. Hierdoor kunnen veel hogere resolutie afbeeldingen van de hemel worden gemaakt dan mogelijk is met een enkele schotel. Vanaf ongeveer 1960 is deze techniek in toenemende mate gebruikt, bijvoorbeeld voor de Nederlandse Westerbork Synthesis Radio Telescope (WSRT) in Drenthe, die bestaat uit 14 draaibare schotels van elk 25 meter in doorsnede, verspreid langs een oost-west lijn van ongeveer 3 kilometer. Twee andere voorbeelden zijn de Amerikaanse Very Large Array (VLA; 27 draaibare schotels van 25 meter in een Y-vorm van maximaal 35 kilometer) en de Indiase Giant Metrewave Radio Telescope (GMRT; 30 draaibare schotels van 45 meter in een Y-vorm van 30 kilometer). Voor sommige projecten gebruiken astronomen radiotelescopen die honderden of duizenden kilometers uit elkaar staan, maar dit kan vaak alleen worden toegepast als de radiobron waarnaar gekeken wordt bijzonder compact en helder is.

Radiostraling uit het heelal

Vanwege de relatief lange golflengte heeft radiostraling in vergelijking met andere soorten straling minder last van verstrooiing en absorptie door gas en stof in het heelal, wat resulteert in een vrijwel onverstoorde blik op zowel het nabije als het verre, jonge heelal. Dit, in combinatie met de enorme afmetingen van veel radiobronnen, maakt radiostraling een krachtig hulpmiddel bij het bestuderen van de vorming en ontwikkeling van de grootste structuren in het heelal.

Waterstof, het meest voorkomende gas in het heelal, zendt straling uit op een karakteristieke golflengte van 21 cm. Waterstof is aanwezig in sterren, in sterrenstelsels in de ruimte tussen de sterren en waarschijnlijk ook in de extreem lege ruimte tussen sterrenstelsels. Er zijn ook andere soorten gas die op verschillende karakteristieke golflengtes radiostraling uitzenden, maar niet vergelijkbaar in hoeveelheid en intensiteit met waterstof. Een tweede belangrijke soort radiostraling is de *kosmische achtergrondstraling*, het afgekoelde restant van energierijke straling (straling met een veel kortere golflengte) uit een zeer vroege fase van het heelal. Deze straling heeft een golflengtebereik van ongeveer 1 tot 2 millimeter.

Een derde, veel voorkomende soort radiostraling komt van geladen deeltjes waarvan de snelheid wordt veranderd. Deze straling heeft niet één karakteristieke golflengte, maar is met variabele intensiteit aanwezig over het heel bereik van golflengtes. De belangrijkste radio-variant is *synchrotron-straling* waarbij elektronen rondom magnetische veldlijnen cirkelen met snelheden dicht bij de lichtsnelheid. Voor een typisch synchrotron-spectrum neemt de intensiteit toe met toenemende radiogolflengte tot een zeker maximum, waarna de intensiteit weer afneemt. Voorbeelden van bronnen met een karakteristiek synchrotron-spectrum zijn de Melkweg, supernova restanten, actieve sterrenstelsels en diffuus, geschokt gas in clusters. Elk van deze bronnen wordt hier kort toegelicht.

Net als in andere sterrenstelsels is in de Melkweg een magneetveld aanwezig. De oorsprong van dit magneetveld is niet duidelijk, evenmin als de elektronen die nodig zijn voor de synchrotron-straling. Toch is het overduidelijk dat het hier synchrotron-straling betreft, zowel door de vorm van het spectrum als door de grootte van de synchrotron-gebieden aan de hemel.

Een supernova restant is een vaak bolvormig restant van een geëxplodeerde zware ster na-

dat deze al zijn brandstof heeft verbruikt. De explosie genereert de voor synchrotron-straling benodigde elektronen en een schok die het omringende magneetveld in het sterrenstelsel samendrukt en daardoor versterkt. In de Melkweg vindt naar schatting één keer per 50 jaar een supernova-explosie plaats, die honderden jaren zichtbaar kan blijven. In zogenaamde *starburst*-sterrenstelsels, waarin bovenmatig veel zware sterren worden gevormd in zeer korte tijd, kan het aantal supernova-explosies oplopen tot enkelen per jaar, waardoor deze sterrenstelsels relatief veel radiostraling uitzenden.

Een actief sterrenstelsel is een sterrenstelsel waarbij materie in een schijf rond het centrale zwarte gat draait voordat dit wordt opgeslokt. De extreme omstandigheden nabij het zwarte gat zorgen ervoor dat elektronen extreem versneld worden en ontsnappen in een richting haaks op de roterende schijf, waarschijnlijk met behulp van sterke magneetvelden die lokaal worden opgewekt. Deze elektronen kunnen soms miljoenen lichtjaren afleggen voordat ze afremmen door botsingen met ijl gas tussen de sterrenstelsels, waardoor gigantische *radiolobben* ontstaan.

De aanwezigheid van radiostraling van diffuus gas in clusters wordt in vele gevallen in verband gebracht met recente samenvoegingen van subclusters tot een groter cluster. Met computersimulaties is aangetoond dat deze samenvoegingen gepaard gaan met de opwekking van schokgolven in het ijle clustergas. Net als bij supernova's zullen de schokgolven een reeds aanwezig magnetisch veld kunnen versterken. Schokgolven worden ook genoemd als de mogelijke bron van snelle elektronen, maar dit is onzeker.

Lange golflengtes

Voor veel synchrotron-bronnen ligt het maximum van het spectrum bij golflengtes van een meter of meer (wat overeenkomt met een radiofrequentie van 300 MHz of minder). Het is daarom makkelijk om deze bronnen op lange golflengtes waar te nemen, omdat de bronnen dan relatief helder zijn. *Steil-spectrum bronnen* zijn radiobronnen die bij een verdubbeling van de golflengte meer dan verdubbelen in helderheid. Voorbeelden van steil-spectrum radiobronnen zijn de Melkweg, het ijle gas in clusters, actieve sterrenstelsels in het jonge heelal en oude radiolobben van inmiddels inactieve sterrenstelsels. Waarnemen op lange golflengtes met een interferometer heeft als bijkomend voordeel dat het blikveld van de telescoop groot is, waardoor het makkelijker wordt om grote gebieden aan de radiohemel in kaart te brengen. Ook is het detecteren en registreren van lange radiogolven technologisch gezien zeer eenvoudig.

Tegenover deze voordelen staan ook belangrijke nadelen die het volledig benutten van deze waarnemingen belemmeren. Ten eerste is het grote blikveld naast een voordeel ook een nadeel, omdat het voor het bereiken van het hoogst mogelijke contrast in de hemelkaarten nodig is om van alle zichtbare bronnen afbeeldingen te maken, ook al beslaat het doelwit van de waarneming een zeer klein deel van het totale blikveld. Een tweede nadeel is dat de golflengtes waarop de zeer gevoelige telescopen proberen de relatief zwakke hemelbronnen waar te nemen, vaak ook allerlei ongewenste, door de mens opgewekte signalen kunnen bevatten. Voorbeelden zijn FM-radiozenders, analoge TV-zenders, portofoons, luchtvaartcommunicatie en satelliet-signalen, maar ook stoorsignalen van bijvoorbeeld computers, hoogspanningskabels en elektrische ontstekingen in motorvoertuigen. Een derde nadeel is dat de ionosfeer, de bovenste laag van de aardse atmosfeer, de radiogolven beïnvloedt wanneer zij passeren. De passerende straling kan worden gereflecteerd, vertraagd, afgebogen, verstrooid en (deels) worden geabsorbeerd. De sterkte van deze effecten neemt toe met de golflengte, daarom is het lastig om scherpe, hoge resolutie afbeeldingen te maken van de hemel op lange golflengtes.

Door de vooruitgang in technologie en algoritme-ontwikkeling zijn voor verschillende van deze problemen oplossingen beschikbaar. Aan het verminderen van de verstoringen door de ionosfeer wordt momenteel actief gewerkt (waaronder in dit proefschrift). In het vooruitzicht van deze verbeteringen zijn de bestaande WSRT, VLA en GMRT telescopen uitgerust met ontvangers voor lange golflengtes. Wereldwijd zijn er verschillende telescopen voor lange golflengtes in verschillende stadia van ontwerp en ontwikkeling, wat duidt op een hernieuwde interesse voor het lange golflengte-bereik waar de radiosterrenkunde ooit is begonnen.

Voorop in deze ontwikkeling loopt de Low Frequency Array (LOFAR), een nieuwe radiotelescoop die momenteel in aanbouw is in Nederland. LOFAR is specifiek ontworpen voor het doen van waarnemingen op lange golflengtes tussen 1 en 10 meter. In plaats van draaibare schotels wordt gebruik gemaakt van *stations*. Ieder van de 36 geplande stations bestaat uit tientallen vaste antennes die elektronisch worden gekoppeld tot een virtuele, draaibare schotel. Binnen Nederland wordt de maximale afmeting van de telescoop ongeveer 50 km. Er worden ook enkele stations gebouwd in andere Europese landen (E-LOFAR), waardoor de totale telescoop een afmeting van duizenden kilometers krijgt. Door de unieke combinatie van zeer hoge gevoeligheid en zeer hoge resolutie zal het sterrenkundig onderzoek op lange golflengtes met LOFAR een grote sprong voorwaarts kunnen maken. De verwachting is dat LOFAR ten opzichte van de huidige radiotelescopen veel meer radiobronnen op grote afstand zal kunnen detecteren, maar ook radiobronnen zal vinden die op nog grotere afstand staan. Voor het behalen van deze doelstellingen is het van essentieel belang dat er op korte termijn nieuwe algoritmes beschikbaar komen voor het bewerken van de waarnemingen.

Dit proefschrift

Het centrale thema van dit proefschrift is het bestuderen van de grote-schaal structuur van het heelal door middel van radiostraling met golflengtes langer dan een meter. Er is gewerkt aan twee onderwerpen: het verbeteren van de kwaliteit van hemelkaarten en het bestuderen van actieve sterrenstelsels en clusters van sterrenstelsels. In de wetenschappelijke hoofdstukken van dit proefschrift wordt het onderzoek naar specifieke aspecten van deze twee onderwerpen gepresenteerd, elk met zijn eigen conclusies. Hieronder volgt een samenvatting per hoofdstuk.

Voor het uitvoeren van radiowaarnemingen op langere golflengtes is het van essentieel belang dat de effecten van de ionosfeer op de waarnemingen worden onderdrukt. Het meest dominante effect is een vertraging van de radiogolf, waardoor er een *fasedraaiing* van de radiogolf optreedt. De inhoud van de ionosfeer verandert met plaats en tijd. Daarom hangt de fasedraaiing af van de locatie van de antenne, de hoek waaronder de antenne door de ionosfeer kijkt en het tijdstip waarop de waarneming plaatsvindt. Bij een waarneming van een bron met een radio-interferometer kijkt iedere antenne door een ander stuk van de ionosfeer en ervaart dus een andere fasedraaiing. Het *verschil* in fasedraaiingen tussen antennes resulteert in onscherpe afbeeldingen van de radiohemel. In **hoofdstuk 2** wordt een nieuwe kalibratietechniek gepresenteerd om de effecten van ionosferische fasedraaiingen te onderdrukken. Deze techniek bepaalt de ionosferische fasedraaiing per antenne in de richting van een aantal beschikbare, heldere radiobronnen in het blikveld van de telescoop. Deze metingen worden gecombineerd in een model van de ionosfeer waarin deze wordt voorgesteld als een dunne, turbulente laag op 200 kilometer boven het aardoppervlak. Het model kan vervolgens worden gebruikt om fasedraaiingen per antenne in de richting van willekeurige radiobronnen te berekenen en te verwijderen. Voor twee testcases, waarnemingen bij een golflengte van 4 meter uit het data-archief van de VLA tele-

scoop onder variërende ionosferische omstandigheden, leidt toepassing van de nieuwe kalibratietechniek tot een significante verbetering van de kwaliteit van de hemelkaarten in vergelijking met andere bestaande kalibratietechnieken.

De nieuwe kalibratietechniek werkt onder een veelvoud van aannames, waaronder de aanname dat de telescoop zelf geen extra fasedraaiingen veroorzaakt en de aanname dat de dominante verschillen in ionosferische fasedraaiing ontstaan in één dunne laag. In **hoofdstuk 3** worden deze specifieke aannames afgezwakt door de uitbreiding van het ionosfeermodel met meerdere turbulente lagen op verschillende hoogtes en door toevoeging van een filter waarmee langzaam variërende, instrumentele fasedraaiingen worden gedetecteerd en verwijderd. Toepassing van het filter op 4 meter waarnemingen van de VLA telescoop in de grootste configuratie (35 km) verwijderde een significante instrumentele fasedraaiing voor tenminste één van de antennes. Toepassen van het meerlaags-model op dezelfde waarnemingen leidt (ten opzichte van het oorspronkelijke éénlaags-model) tot een kleine verbetering van de gemiddelde positienauwkeurigheid van radiobronnen in de resulterende hemelkaarten.

Hoofdstuk 4 beschrijft de toepassing van de kalibratietechniek op een zeer lange waarneming met de GMRT telescoop van een specifiek stuk van de hemel, het zogenaamde Boötes-veld. Dit resulteert in één van de meest gedetailleerde hemelkaarten die tot nu toe zijn gemaakt op 2 meter golflengte. Van de ongeveer 600 gedetecteerde radiobronnen in het Boötes-veld zijn nauwkeurig de positie, de helderheid en de vorm gemeten en in een catalogus opgeslagen. De afmetingen van het veld en het aantal bronnen zijn groot genoeg om een statistische vergelijking met andere velden uit te voeren. Een eerste stap in de analyse is het tellen van radiobronnen met een bepaalde helderheid, wat aanwijzingen geeft over de samenstelling van de bronpopulatie. Brontellingen op 2 meter golflengte zijn nog niet eerder met vergelijkbare precisie bij zulke lage helderheden uitgevoerd. Er is een goede overeenkomst tussen deze brontellingen en brontellingen uit hemelkaarten op kortere golflengte. Hieruit volgt dat de bronpopulatie vooral uit actieve sterrenstelsels bestaat. Door de 2 meter catalogus te combineren met een eerder gepubliceerde 21 cm catalogus is de steilheid van het spectrum van ongeveer 400 bronnen bepaald. Gemiddeld is een bron op 2 meter golflengte 5.4 keer zo helder als op 21 cm, maar de werkelijke helderheidsverhouding varieert van bron tot bron. Met behulp van reeds beschikbare infrarood-waarnemingen kan een eerder gevonden statistische relatie tussen de steilheid van het radiospectrum en de afstand van de radiobron indirect worden bevestigd. Er is een kleine groep van 16 zogenaamde steil-spectrum bronnen, waarbij de helderheidsverhouding tussen 2 meter en 21 cm meer dan drie keer zo groot is als bovengenoemd gemiddelde. Dit zijn mogelijk actieve sterrenstelsels op zeer grote afstand. Verder onderzoek is nodig om dit te bevestigen.

Hoofdstuk 5 bevat een studie van een cluster in het nabije heelal, Abell 2256 genaamd. Er zijn sterke aanwijzingen gevonden dat het hier een cluster betreft dat recentelijk is ontstaan door de samenvoeging van twee of drie kleinere clusters. De schokgolven die hierbij zijn opgewekt hebben het gas in de cluster flink verstoord, waardoor de intrinsieke hoge temperatuur van het gas nog verder is verhoogd. Hierdoor wordt door het gas relatief veel radiostraling en röntgenstraling uitgezonden. Met behulp van radiowaarnemingen met de WSRT en GMRT telescopen is de structuur van Abell 2256 bestudeerd op golflengtes van 1 en 2 meter, waarbij deels gebruik is gemaakt van de nieuwe kalibratietechniek. De WSRT waarnemingen bevestigen de aanwezigheid van twee gigantische gebieden van miljoenen lichtjaren in doorsnede waaruit diffuse radiostraling afkomstig is met een zeer steil spectrum. De GMRT hemelkaarten op golflengtes van 1 en 2 meter hebben een hogere resolutie dan de WSRT hemelkaart. In vergelijking met eerdere waarnemingen op kortere golflengtes is in deze hemelkaarten een aantal

nieuwe bronnen zichtbaar waarvan de oorsprong niet duidelijk is. Het steile spectrum van deze bronnen suggereert dat het hier vermoedelijk gaat om oude radiolobben van sterrenstelsels die in het verleden actief zijn geweest. De relatieve helderheid van de bronnen en het uiterlijk van één van de bronnen kunnen goed worden verklaard wanneer deze bronnen door schokgolven in het clustergas zijn samengedrukt.

Voor het bestuderen van het ontstaan van clusters moet ver terug worden gekeken in het heelal. Voor het lokaliseren van jonge clusters kan gebruik worden gemaakt van radiobronnen. Actieve sterrenstelsels in het jonge heelal zijn relatief zwaar, waardoor zij zich veelal in of nabij de centra van clusters bevinden. Deze stelsels zijn vaak zeer heldere radiobronnen en hebben veelal een zeer steil radiospectrum. Hierdoor zijn ze eenvoudiger te detecteren op lange radiogolflengtes. Van één zo'n sterrenstelsel, TN J1338-1942 genaamd, is eerder via meting van de roodverschuiving vastgesteld dat de straling is uitgezonden toen de leeftijd van het heelal slechts een tiende was van de geschatte huidige leeftijd van 13.7 miljard jaar. Ook is via eerdere waarnemingen een verdichting van het aantal sterrenstelsels gevonden rondom dit sterrenstelsel, wat duidt op de aanwezigheid van een cluster in aanbouw. In **hoofdstuk 6** worden waarnemingen van dit cluster gepresenteerd die zijn gemaakt met behulp van een speciale breedbeeldcamera op de Japanse Subaru-telescoop op Hawaï. Drie zeer lange opnames, één in het zichtbare licht en twee in het infrarood, dekken een gebied af dat veel groter is dan het cluster. Door de helderheid van de sterrenstelsels in de drie opnames te vergelijken worden ongeveer 900 sterrenstelsels geselecteerd die grofweg op dezelfde afstand staan als TN J1338-1942. De verdeling van deze sterrenstelsels aan de hemel is, zoals verwacht, geconcentreerd rondom TN J1338-1942, maar ook rondom een aantal andere posities. Deze concentraties zijn ieder ongeveer 10 miljoen lichtjaar in doorsnede. Het aantal concentraties is ongeveer gelijk aan het aantal grote clusters in het nabije heelal in een vergelijkbaar volume. Dit is goed te verklaren als iedere concentratie inderdaad een jong cluster is. De totale verdeling van sterrenstelsels over het blikveld heeft qua structuur overeenkomsten met het uiterlijk van het nabije heelal, waarin sterrenstelsels geconcentreerd zijn in clusters en filaments rondom lege voids.

Curriculum vitae

Ik ben geboren op 2 april 1971 te Leiden. Zes weken na mijn geboorte verhuisden mijn ouders, mijn twee zussen en ik van Leiden naar Alphen aan den Rijn, waar ik een groot deel van mijn leven heb gewoond. Vooral mijn vader heeft mijn jeugdige interesse in techniek en wetenschap gestimuleerd, onder andere door mij mee te nemen naar bijeenkomsten van de Koninklijke Nederlandse Vereniging voor Weer- en Sterrenkunde (KNVWS) en door de aanschaf van een kleine telescoop.

In juni 1989 behaalde ik mijn VWO diploma aan het Ashram College te Alphen aan den Rijn, waarna ik elektrotechniek ben gaan studeren aan de Technische Universiteit te Delft. Na een succesvol eerste jaar, leidde de grootschaligheid en afstandelijkheid van deze opleiding uiteindelijk tot een gebrek aan motivatie. Na het staken van de studie heb ik in 1993 in één van de laatste lichtingen de militaire dienstplicht vervuld. Gedurende 6 maanden was ik als soldaat gestationeerd in Donauwörth (Duitsland). Gemotiveerd door het inzicht dat mij zonder diploma een sombere toekomst stond te wachten, heb ik mijn studie elektrotechniek voortgezet aan de Hogeschool Utrecht, resulterend in een HTS-diploma in juni 1996. Tijdens deze studie, in december 1994, is mijn moeder overleden.

Van juli 1996 tot augustus 2000 heb ik gewerkt als technisch programmeur bij High Tech Automation. Gedurende deze periode heb ik op projectbasis gewerkt bij het TNO Fysisch & Elektronisch Laboratorium (FEL) te Den Haag, bij Philips Digital Video Systems (DVS) te Hilversum en bij de TNO Technische & Fysische Dienst (TPD) te Delft. In deze periode heb ik verschillende vakinhoudelijke cursussen gevolgd over embedded en real-time software, maar ook een aantal cursussen over persoonlijke ontwikkeling. Op deze zoektocht heb ik niet alleen mezelf, maar ook mijn vrouw Joanca gevonden. In december 1999 zijn wij gaan samenwonen in Haarlem. Op 1 augustus 2000 zijn wij getrouwd.

Sinds de aanschaf van een 20 cm Schmidt-Cassegrain telescoop in 1998 is mijn interesse in de sterrenkunde opnieuw opgeleefd. Met de onmisbare steun van Joanca heb ik een grote verandering in mijn leven gerealiseerd, door mijn werk als programmeur te stoppen en per september 2000 sterrenkunde te gaan studeren aan de Universiteit Leiden. Mede dankzij een aantal vrijstellingen heb ik in één jaar het curriculum van de eerste twee studiejaar afgerond. Tijdens de doctoraalfase heb ik onder leiding van dr. Garrelt Mellema onderzoek gedaan naar gravitationele instorting van wolken gas in het heelal door middel van computersimulaties. Mijn afstudeeronderzoek bij dr. Huub Röttgering richtte zich op het zoeken naar groepen sterrenstelsels (clusters) in het jonge heelal met behulp van zeer gevoelige optische afbeeldingen van de Japanse Subaru-

telescoop op Hawaïi. In juni 2004, gedurende mijn laatste studiejaar, is onze dochter Emma geboren. In december 2004 behaalde ik mijn doctoraalexamen sterrenkunde.

Met behulp van subsidie van de Nederlandse Onderzoeksschool voor Astronomie (NOVA) startte in februari 2005 mijn promotie-onderzoek onder begeleiding van (inmiddels) prof. dr. Huub Röttgering en prof. dr. George Miley. Dit onderzoek had als voornaamste drijfveer de toekomstige ingebruikname van de Low Frequency Array (LOFAR), een nieuwe radiotelescoop die voornamelijk in Nederland wordt ontwikkeld en gebouwd.

Ik heb gedurende mijn onderzoek twee maal waarnemingen verricht met de Giant Metre-wave Radio Telescope (GMRT) in India en één maal met de Very Large Array (VLA) in de Verenigde Staten. Verder heb ik gewerkt met waarnemingen van de Nederlandse Westerbork Synthesis Radio Telescope (WSRT). Ik heb werkbezoeken gebracht aan de stichting Astronomisch Onderzoek Nederland (ASTRON) in Dwingeloo, het Amerikaanse National Radio Astronomy Observatory (NRAO) in Charlottesville (Virginia) en Socorro (New Mexico), het Naval Research Laboratory (NRL) in Washington DC, het Center for Astrophysics (CfA) van Harvard University in Cambridge (Massachusetts) en het Department of Physics and Astronomy (Panda) van de University of New Mexico in Albuquerque (New Mexico). Ik presenteerde mijn onderzoeksresultaten bij alle bovengenoemde instituten, bij verschillende meetings en workshops in Leiden en bij conferenties in Manchester (Verenigd Koninkrijk), Sintra (Portugal) en Perth (Australië). Ik heb verder twee 'schools' bijgewoond in Obergurgl (Oostenrijk) en Manchester en twee conferenties in Emmen en Praag (Tsjechië).

In Leiden heb ik het master-college Radio Astronomy en het bachelor-college Modern Onderzoek geassisteerd. Tevens was ik gedurende een jaar lid van de opleidingscommissie sterrenkunde. Ter popularisering van de sterrenkunde heb ik een tiental lezingen verzorgd voor verschillende afdelingen van de KNVWS. Ook publiceerde ik een populair wetenschappelijk artikel in het Leidse faculteitsblad 'Eureka!'. In maart 2006, tijdens het tweede jaar van mijn promotie-onderzoek, is onze tweede dochter Sophie geboren.

Ter afsluiting van het promotie-onderzoek verdedig ik op 26 augustus 2009 dit proefschrift. Na mijn promotie zal ik als Jansky Fellow verbonden zijn aan het Amerikaanse National Radio Astronomy Observatory in Charlottesville, Virginia.

Nawoord / Acknowledgements

De totstandkoming van dit proefschrift is geen solo-actie, maar het resultaat van vele interacties tussen mijzelf en anderen. Jaron en Bram, mede dankzij jullie heb ik mijn eerste grote stap in de wetenschapswereld kunnen zetten: mijn eerste publicatie in een vaktijdschrift. For more than four years I enjoyed the discussion and interaction with the members of our radio-group in Leiden: Amitesh, Bas, Ilse, Mamta, Niruj, Oleksandr and Reinout, and part-time members Sridhar, Ignas, Rudolf en Raymond. I would like to thank my international collaborators Aaron, Bill, Dharam and Masami for their invaluable support. De leden van de LIONS groep, Ger, Hans, James, Jan, Maaijke en Ronald wil ik bedanken voor de opbouwende kritiek op mijn werk tijdens onze bijeenkomsten. De ontwikkeling van de python-interface ParselTongue heeft een cruciale rol gespeeld in het mogelijk maken van ionosferische calibratie met AIPS, waarvoor ik vooral Mark en Huib-Jan verantwoordelijk acht. Also many thanks to Niruj for developing and supporting the source extraction package BDSM.

Ik heb tijdens mijn onderzoek dankbaar gebruik gemaakt van de financiële steun door de Nederlandse Onderzoeksschool voor Astronomie, de Sterrewacht Leiden, het Leids Kerkhoven-Bosscha Fonds en het Leidse Sterrewacht Fonds. I am grateful for the support from the NCRA, GMRT, NRAO and VLA staff during my working visits and observing sessions. Voor de ondersteuning op het gebied van computers en software ben ik dank verschuldigd aan Erik, David, Tycho en Aart. De gesmeerde organisatie en gezellige sfeer op de Sterrewacht Leiden is in mijn mening grotendeels het resultaat van de secretariële ondersteuning van Kirsten, Jeanne, Liesbeth en Anita. In general, thanks to all the past and present people at the Observatory for making it such an inspiring environment to work in. Franco, dank je dat je het zes jaar hebt uitgehouden als mijn kamergenoot op de Sterrewacht, en al langer als vriend. Het was altijd fijn om te weten dat er een promovendus rondliep die nog ouder was dan ik.

Ik wil mijn familie, schoonfamilie en vrienden bedanken voor hun interesse in en betrokkenheid bij mijn werk als sterrenkundig onderzoeker.

Lieve Joanca, zonder jou was ik er niet aan begonnen, zonder jou had ik het niet volgehouden en zonder jou had ik het niet af weten te ronden. Deze laatste woorden zijn daarom voor jou. MTW

